DESIGN AND VALIDATION OF AN ADVANCED PROTOTYPE FOR THE QUANTITATIVE CHARACTERIZATION OF IRON OXIDES PELLET FLOW BEHAVIOUR UNDER EXTREME OPERATIVE CONDITIONS AND CONTROLLED ATMOSPHERE

Salvatore La Manna

UNIVERSITY OF SALERNO

DEPARTMENT OF INDUSTRIAL ENGINEERING

Ph.D. Course in Industrial Engineering
Curriculum in Chemical Engineering - XXXVIII Cycle

DESIGN AND VALIDATION OF AN ADVANCED PROTOTYPE FOR THE QUANTITATIVE CHARACTERIZATION OF IRON OXIDES PELLET FLOW BEHAVIOUR UNDER EXTREME OPERATIVE CONDITIONS AND CONTROLLED ATMOSPHERE

Supervisor
Prof. Massimo Poletto

Ph.D. student
Salvatore La Manna

Scientific Referees
Prof. Diego Barletta
Prof. Vincenzo Vaiano

Ph.D. Course Coordinator
Prof. Massimo De Santo

Publication List

1. Qyteti, K., La Manna, S., Illana, E., Barletta, D., Poletto, M. and Scherer, V. (2025), Discrete element modeling of shear cell experiments with cohesive wooden spheres. Particuology, 107, pp. 300–312. doi: 10.1016/j.partic.2025.10.006.
2. La Manna, S., Zinatlou Ajabshir, S., Barletta, D. and Poletto, M. (2025), Le proprietà di flusso di solidi particellari per processi avanzati ad alta temperatura ed elevata pressione. La Termotecnica, 7, pp. 20–22.
3. La Manna, S., Zinatlou Ajabshir, S., Barletta, D. and Poletto, M. (2025) ,An Innovative Setup to Investigate High-temperature and High-stress Flow Properties for Industrial Processes Particles. Chemical Engineering Transactions, 117, pp. 763–768.

Acknowledgements

This work was funded by the European Commission under the "Horizon Europe (Grant agreement 101058429)" project, specifically within the "Maximise H2 Enrichment in Direct Reduction Shaft Furnaces" (MaxH2DR) project. [1]

1. E. C. CORDIS, “Maximise H2 Enrichment in Direct Reduction Shaft Furnaces (MaxH2DR).” Accessed: Feb. 10, 2025. [Online]. Available: https://cordis.europa.eu/project/id/101058429

Contents

Figure Index

Table Index

Abstract

The steel industry is one of the most energy-intensive sectors and contributes nearly 30% of global industrial CO_2 emissions [1]. A promising strategy to mitigate this impact is to replace conventional carbon-based gaseous reagents with hydrogen via direct reduction. This reaction process takes place in the shaft furnace, which operates at temperatures up to 1000°C and gas pressures of 1-2 bar. Inside the furnace, gaseous reactants flow counter-current to the solid phase, composed of pellets or sinters containing oxidized iron forms. Despite its potential, the transition to hydrogen-based reduction still lacks comprehensive predictive models capable of describing the coupled thermodynamics, reaction kinetics, fluid dynamics, and solid mechanics of the system. The solid phase plays a decisive role, since its mechanical and physicochemical properties strongly influence overall process efficiency. In addition, the material undergoes progressive transformations driven by operating conditions such as temperature gradients and mechanical load, as well as by the chemical reduction itself. These transformations can induce softening, cohesion, and agglomeration, making it essential to quantify such phenomena and to understand the frictional interactions between iron oxide particles. Accurate characterization of these effects is fundamental to ensuring efficient solid phase movement and complete conversion, while preventing operational instabilities that could compromise process performance and efficiency.

The behaviour of iron oxides and pellets has long been a subject of scientific investigation. Numerous studies have examined the reduction of iron ores in blast furnaces, yet most focus on isolated aspects rather than capturing the full sequence of phenomena occurring during reduction. For instance, Lan et al. [2] analysed the fluidity of cement at temperatures up to 850 °C, while Maarup et al. [3] investigated the softening and melting of iron ores at 1500 °C. Xiao et al. [4] explored the effect of varying hydrogen fractions (0%, 5%, 10%, 15%) in blast furnaces, concentrating on the softening–melting zone between 1200 °C and 1500 °C, and demonstrated that hydrogen accelerated reduction and improved efficiency. Although these contributions provide valuable insights, they remain constrained to specific conditions and do not encompass the broader range of operating variables relevant to industrial practice. Advancing predictive models for hydrogen-based direct reduction, therefore, requires a deeper understanding of solid behaviour under process conditions. This task is hindered by two major limitations: laboratory-scale equipment cannot replicate the extreme operating environment of shaft furnaces, and conventional methods are inadequate for studying coarse particles such as

pellets. An illustrative case is the work of Tomasetta et al. [5], who investigated the influence of temperature on the flow properties of fine powders using a modified Schulze annular shear cell. Their experiments, conducted on fluid cracking catalyst powder, corundum, and fly ash with mean particle sizes of 70 μm, 23 μm, and 10 μm, respectively, covered a temperature range from ambient to 500 °C. While this research underscores the importance of precise temperature control in optimizing powder flow, the particle sizes and thermal conditions examined are clearly different from those encountered in direct reduction processes, highlighting the need for dedicated methodologies tailored to industrially relevant scales.

The objective of this work is to reproduce, at laboratory scale, the conditions in the DR shaft furnace experienced by the solid phase during processing, namely temperatures approaching 1000 °C and maximum estimated normal stresses on the order of 800 kPa, within highly reactive environments. To achieve this, an analysis protocol tailored to the particle dimensions was defined, enabling the measurement of the flow behaviour of iron ore pellets under representative operating conditions. This approach enables investigation of how pellets respond to combined thermal, mechanical loads and chemical reactions, thereby taking the first steps towards bridging the existing theoretical and practical gaps in the characterization of granular solids under harsh conditions.

To address these challenges, a dedicated prototype was designed and constructed. The device integrates a shear cell capable of operating under conditions comparable to those occurring in commercial reduction equipment. In particular, able to apply controlled normal stresses up to 800 kPa and reach temperatures as high as 1000 °C. Its development required several essential steps: the careful selection of building materials resistant to hydrogen attack; the design and integration of mechanical components using SolidWorks; the definition and incorporation of a sensor system within the structure; the implementation of LabView-based code for data acquisition, processing, and interaction with the prototype; and, finally, the calibration and validation of the acquired data.

During the design phase of the prototype, preliminary tests were conducted at room temperature using a commercial apparatus, the Schulze rotational cell, to obtain initial information on material behaviour and to evaluate possible design options. Two types of samples were examined: monodisperse wood particles, used as a simplified model, and iron oxide pellets with diameters between 10 and 13 mm. The results obtained with the pellets guided the optimal design of the new setup, refining the shear cell geometry and underscoring the limitations of conventional data analysis methods in deriving frictional and cohesive properties for coarse solids.

Further investigations were carried out on powders derived from the pellets, with particle sizes between 125 and 180 μm, tested in a modified Schulze cell at elevated temperatures up to 660 °C. These initial high-temperature tests

revealed the sensitivity of the solid phase to temperature, showing a marked increase in interparticle cohesion beginning at approximately 400 °C. Collectively, these preliminary studies provided critical insights for prototype development, while also highlighting the need to move beyond traditional continuum mechanics approaches towards discrete element modelling (DEM) to capture the behaviour of granular solids under harsh conditions.

Once the prototype was validated, the experimental program focused on two distinct classes of materials, both subjected to combined normal and shear loads. The first class comprised the solid materials processed in the shaft furnace, namely reduced and unreduced iron oxides, characterized by non-standard dimensions and variable densities. Due to their size, a custom protocol was defined, applying a single normal stress of 50 kPa to mitigate excessive fragmentation, while testing across a wide temperature range from 25 to 1000 °C. The mechanical data obtained with such coarse particulates cannot be adequately interpreted using traditional continuum mechanics, and were planned to be used to calibrate DEM models. Although the tests primarily yielded descriptive information on pellet behaviour under the applied stresses, these results proved essential for DEM calibration. Importantly, the experiments highlighted the decisive role of the reduction degree in governing pellet strength and integrity: microfractures and fragmentation were observed at intermediate reduction levels, whereas highly reduced pellets exhibited pronounced brittleness, potentially induced by isothermal laboratory reduction, even under relatively modest compressive stresses.

Quartz sand was selected as the second material, serving as both a standard reference medium and an ideal case study for prototype validation. Its characterization was carried out in accordance with ASTM D6773, through alternating consolidation phases with varying anomalous loads while the sample was subjected to shear stresses. The experimental data confirmed that quartz sand displays temperature-insensitive behaviour across the investigated range (25–800 °C) under compressive stresses up to 800 kPa. The results showed remarkable consistency, with internal friction angles and cohesion values closely matching those reported in the literature. The absence of significant thermal effects demonstrated that stress transmission and failure response are governed primarily by particle geometry, packing density, and intergranular friction, rather than by temperature-induced changes in cohesion or strength. This mechanical stability and reproducibility ensured that the influence of the apparatus and measurement protocol could be distinguished from material-specific effects, thereby validating the reliability of the experimental prototype.

Although the apparatus was conceived to withstand the aggressive action of hydrogen under extreme conditions, these capabilities have not yet been explored and will be the subject of future studies. In its current configuration, the prototype has demonstrated validity and reliability, enabling analyses with

conventional approaches on standard materials while offering the versatility to adapt methodologies according to the properties of the tested solids. This flexibility opens the way to investigating new operating conditions and broadening the scope of granular material characterization.

I. Introduction and Overview of the problem

Steel is one of the most widely utilized materials in modern age due to its exceptional versatility and robust mechanical, physical and chemical properties. Its strength, durability, recyclability, and adaptability make it indispensable across a range of sectors, including automotive, medical, structural engineering and aerospace. As a cornerstone of technological advancement and infrastructure, steel plays a vital role in both societal progress and human resilience.

Steel is a generic term encompassing a family of iron-based alloys with a carbon content between 0.02 % and 2.14 % by weight, together with elements such as manganese, silicon, sulphur, and oxygen. It is this ability to form controlled alloys that endows steel with a diverse spectrum of properties suited to myriad applications. For example, adding chromium or nickel enhances corrosion resistance, allows service at extreme temperatures, and maintains structural integrity in highly reactive environments.

Iron (Fe) is the most abundant metallic element on Earth, comprising roughly 32.1 % of the planet's mass, with concentration increasing toward the core. About 5 % of the Earth's crust consists of iron and its compounds. Metallic iron is extremely rare in nature due to its high reactivity; instead, iron occurs primarily as compounds: combined with oxygen (~46 %), silicon (~28 %), aluminium (~8 %), and in various hydrated or oxygenated forms. Consequently, iron is obtained from ores rather than mined in elemental form [1]. The principal iron ores are oxidized minerals such as magnetite ($\alpha - Fe_3O_4$), hematite (Fe_2O_3), goethite ($\alpha - FeOOH$) and maghemite ($\beta - Fe_3O_4$) [2]. These must be reduced from a molar O/Fe ratio of about 0.43, in the most oxidized case, to nearly zero to produce metallic iron. Two main industrial routes achieve this iron ore reduction, basically classified according to the physical state of the iron produced:

- The integrated blast furnace–basic oxygen furnace (BF–BOF) process.

- The direct reduced iron (DRI) followed by the electric arc furnace (EAF) process.

Both categories rely on gaseous reducing agents to reduce iron oxides to iron. Regardless of the chosen pathway, the reduction involves:

- Gas flow through the oxide layer to the gas–solid interface.
- Diffusion through macro and micropores to the reaction sites.
- Adsorption of reducing species at the oxide interface.
- Removal of oxygen from iron ions and formation of gaseous products.
- Desorption and diffusion of these gaseous products back through the pore network.
- Solid-state diffusion, nucleation, and growth of metallic nuclei.
- Mass transfer across the boundary layer into the bulk gas stream.

Process kinetics may be reaction-controlled at lower temperatures or mass transfer-controlled at higher temperatures, where chemical kinetics are favoured. Furthermore, not all of the phenomena indicated necessarily occur, depending on the degree of porosity of the solid phase. [3]

In both the BF-BOF and DRI-EAF processes, the reduction of iron oxides is intrinsically linked to the use of carbon- or hydrogen-based gases, which directly affects the environmental impact of the process. The most commonly used route is the blast furnace, which makes extensive use of coke as both a reducing agent and an energy source, resulting in significant CO_2 emissions. Even in the DRI-EAF route, unless hydrogen is used as the primary reducing agent, syngas derived from natural gas contributes to carbon production. As a result, steel production remains one of the most carbon-intensive industrial activities, accounting for 7-9% of global CO_2 emissions.

I.1. Integrated Iron and Steel process

The integrated iron-and-steel process has dominated global steel production for more than two centuries and remains the industry's primary route. It typically comprises sintering and pelletizing units, coke-making ovens, and - at its heart - the blast furnace (BF), where iron oxides are reduced by contacting mixed feeds of coke and ore with oxygen-bearing gases. This pathway is often paired with the Basic Oxygen Furnace (BOF) for downstream steelmaking. Continuous technological refinements have transformed the blast furnace into a highly efficient chemical reactor capable of stable operation with a wide variety of feed materials.

The blast furnace operates as a counter-current reactor: solid burdens - iron ore, sinter, and coke - are charged from the top, while a preheated air blast enters through tuyeres at the bottom [6]. Carbon, introduced primarily as coke, is layered with the solid phase during charging of the process to provide both thermal and chemical energy. On one side, it is used to carry out the combustion reaction needed to release the energy required to maintain the

system temperature; on the other side, it is combined with oxygen to produce carbon monoxide (CO), the effective reducing agent of the process.
The robustness of this complex system arises from its exceptional mass and heat transfer efficiency between solids and the gaseous stream. Due to the enormous complexity of reactions and phenomena in the furnace, the schematic partitioning of the unit may differ, for example, by referring to structural regions or local temperatures, but the representation of interest for this work is based on the description of the solid behaviour. According to this criterion, a schematic representation of the Blast furnace is reported in Figure I.1, showing the four regions defined. Starting from the top, the sequence includes the lumpy zone, cohesive zone, active coke zone, raceway, as well as the hearth and stagnant coke zone (Lu, 2022)(Lu, 2022). The geometry of each part has been improved and refined over time, primarily by experience. Consequently, the dimensions and the proportionality between each part are essentially empirical and adapted to the behaviour of the system according to the operative conditions. Modern blast furnaces stand about 30 m tall, with internal diameters reaching over 10 m at their widest section.

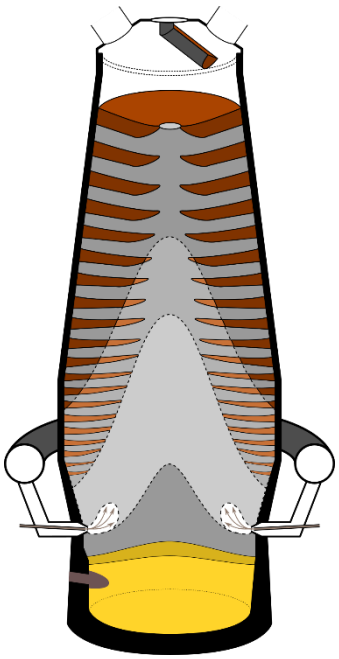

Figure I.1 Cross-sectional representation of the shaft furnace, adapted from the work of Y. Kaymak et al. [7] The upper section shows the alternating layers of solid iron oxides and coke. Beneath the reaction zone lie the air-inlet levels, while the lower region illustrates the collection and downward flow of the converted material.

I.1.1. Raceway

The raceway is the critical zone of the blast furnace, located immediately around the tuyeres, where intense heat and key chemical reactions convert the solid burden into a molten phase. Tuyeres are arranged radially along the furnace shell and inject an oxygen-enriched gas stream at temperatures above 1000 °C. Within the raceway, combustion and gasification of carbon occur through reactions such as:

$$C + O_2 = CO_2 \qquad \Delta H^o_{298} = -393.5\ kJ/mol \qquad (1)$$

$$C + CO_2 = 2CO \qquad \Delta H^o_{298} = +172.5\ kJ/mol \qquad (2)$$

$$C + H_2O = H_2 + CO \qquad \Delta H^o_{298} = +131.3\ kJ/mol \qquad (3)$$

These reactions illustrate carbon's dual role, which primarily supplies most of the thermal energy through combustion, and also produces CO, the reducing agent capable of extracting oxygen from iron-containing minerals. As a result of these reactions, temperatures in the raceway can approach 2000 °C, fully liquefying iron and slag for withdrawal at the ground. The ascending gas stream - primarily N_2, CO, and H_2 - flows upward through the burden, preheating and progressively reducing iron oxides. The reducing power of the gas phase is often characterized by its O/C ratio, which decreases from the raceway toward the top of the furnace as oxygen is consumed and carbon content rises. Advanced control of raceway shape, depth, and gas composition through tuyere design, blast parameters, and pulverized-coal or oxygen injection directly impacts furnace efficiency, fuel consumption, and overall productivity. Computational fluid dynamics and optical diagnostics are increasingly used today to model and optimize these raceway phenomena.

I.1.2. Lumpy zone

The lumpy zone extends from the top of the BF downward to the cohesive zone, where the iron ores start to soften and deform. Under gravity, the solid load descends while exchanging heat with the rising gas, driving off free water and desorbed moisture. Figure I.2 maps the evolution of the reaction network and the stability of iron oxides as a function of temperature and gas composition in terms of CO/CO_2 and H_2/H_2O ratios (Seetharaman et al., 2014)(Seetharaman et al., 2014). At temperatures above 570°C, reduction proceeds in three sequential reactions. According to the oxidation number of the iron, passing from $Fe_2^{+3}O_3$, through $Fe^{+2}Fe^{+3}O_4$ and $Fe^{+2}O$ to Fe. Each step follows its own equilibrium line and kinetic regime.

$$3Fe_2O_3 + CO = 2Fe_3O_4 + CO_2 \qquad \Delta H^o_{298} = -47.2\ kJ/mol \qquad (4)$$

$$3Fe_2O_3 + H_2 = 2Fe_3O_4 + H_2O \qquad \Delta H^o_{298} = -6.0\ kJ/mol \qquad (5)$$

$$Fe_3O_4 + CO = 3FeO + CO_2 \qquad \Delta H^o_{298} = +19.4\ kJ/mol \quad (6)$$

$$Fe_3O_4 + H_2 = 3FeO + H_2O \qquad \Delta H^o_{298} = +60.6\ kJ/mol \quad (7)$$

$$FeO + CO = Fe + CO_2 \qquad \Delta H^o_{298} = -11.0\ kJ/mol \quad (8)$$

$$FeO + H_2 = Fe + H_2O \qquad \Delta H^o_{298} = +30.2\ kJ/mol \quad (9)$$

As the reducing gas ascends, it transfers heat and consumes its reducing potential. The molar O/C ratio (O_2 relative to C in the gas) quantifies this: a higher O/C implies more CO_2 produced and thus weaker reductive capacity.

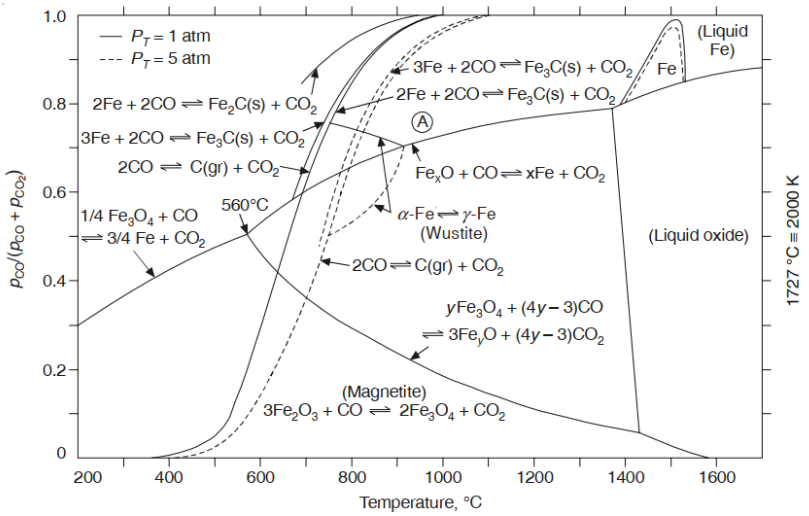

Figure I.2 Equilibrium pCO/(pCO + pCO2) ratios in gas as a function of temperature for reactions in the Fe–C–O system. The lines are for equilibria of reactions as indicated. [7]

In the upper part of the BF, known as the chemical reserve zone, the O/C ratio in the reducing gas and the O/Fe ratio in the solids remain relatively constant at approximately 1.75. An O/Fe ratio of 1.08 indicates that iron oxides are nearly fully reduced to FeO in this region. However, further reduction of FeO to metallic iron cannot take place in this condition because it requires an O/C ratio below 1.3 at 1475°C, which is not present. Due to the minimal chemical activity, the temperature in this zone remains stable, and the gas and solid compositions change slightly. Above this reserve zone, the O/C ratio exceeds 1.3, insufficient to reduce FeO to Fe but adequate to convert Fe_2O_3 to FeO, provided the O/C ratio is below 1.75 at 850°C. As the gas continues to rise, its temperature and reducing power diminish further due to the endothermic nature of the reactions converting Fe_3O_4 to FeO. Near the furnace top (200–700°C), Fe_2O_3 is reduced to Fe_3O_4. This reaction is largely unaffected by temperature and can proceed even at low CO concentrations, as suggested by the equilibrium line's position near the temperature axis.

For this reason, much of the reduction unit has been designed and optimized to bring the solid phase to conditions suitable for the complete reduction of iron oxides. Furthermore, the geometry of this region has been improved and adapted over time to account for phenomena associated with iron ores, such as expansion and agglomeration. Then, the lumpy zone is designed as a frustrum cone, reaching its maximum diameter in correspondence with the cohesion zone. Therefore, to facilitate the gravitational descent of the solid and preserve the gas permeability along the unit, the BF cross-section increases with temperature, approximately doubling, from the lumpy zone to the tuyere region (Ghosh and Chatterjee, 2008)(Ghosh and Chatterjee, 2008)(Ghosh and Chatterjee, 2008).
If the solid phase at the lower part of the lumpy zone is softening, the gas at the top leaves the BF with temperatures around 100 - 150°C and is composed primarily of nitrogen (50 - 60%), carbon dioxide (18 - 20%), hydrogen (2 - 4%), and the remainder mostly carbon monoxide.

I.1.3. Cohesive zone

In the cohesive zone of a blast furnace, iron ores are in a semi-solid, plastic state rather than fully solid or fully liquid. As these softened particles deform and press together, the interstitial voids narrow sharply, severely restricting gas permeability. In this region, coke typo remain solid and provide narrow flow channels for the ascending gases, making the coke a crucial component for keeping the cohesive zone as narrow as possible to facilitate gas flow and preserve the gas pressure in the equipment reaction regions. Partial melting of ore particles produces slag composed of FeO and gangue oxides such as CaO, SiO_2, Al_2O_3, and MgO. As this plastic mixture descends, it continues to absorb heat from the rising gases, and although the process is slow, the carburization of solid iron begins. Carbon is incorporated into the structure via the reaction between Fe and CO, which typically results in carbon content below 1%wt.

$$3Fe + 2CO = Fe_3C + CO_2 \qquad \Delta H^o_{298} = -147.4\ kJ/mol \quad (10)$$

The dissolution of carbon lowers iron's melting point, enabling the formation of a liquid metal and slag. Once sufficient liquid accumulates, droplets of molten iron and slag coalesce and drain downward. This dripping marks the lower boundary of the cohesive zone and the transition into the fully molten region, where metal and slag collect in the hearth.

I.1.4. Active Coke, Hearth, and Stagnant Coke Zone

The semi-molten mixture exiting the cohesive zone descends into the active coke zone, where residual wüstite (FeO) undergoes final reduction. Here, iron droplets further carburize through intimate contact with coke and carbon monoxide, attaining carbon levels of 3.0 - 3.5%wt.

Below, the hearth and stagnant coke zone consist of a densely packed coke bed through which molten iron and slag percolate. As the iron descends, it absorbs additional carbon, reaching saturation at around 4.5%wt at 1500°C. Upon entering the hearth, differences in density cause slag and iron to separate into distinct layers, enabling efficient recovery of molten iron with minimal impurity levels.
Overall, the blast furnace operates as a two-stage reactor. The upper, low-temperature zone handles drying, preheating, and reduction to wustite. The lower, high-temperature zone - comprising the cohesive zone, active coke zone, raceway, and hearth - facilitates smelting, metalloid reduction, slag formation, and iron melting.

I.1.5. High-grade metallurgical coke

The quality of the steel and iron produced in a blast furnace depends critically on the properties of the solid raw materials.
The coke exerts a decisive influence on final product quality. It can comprise up to 60 % of the blast furnace burden by mass, and its huge quantity is justified by the fulfilment of three essential roles:

- Supplying the heat energy via combustion reactions directly within the furnace
- Maintaining bed permeability and structural support in the cohesive zone
- Generating carbon monoxide (CO), the primary gaseous reducing agent

To deliver these functions, steelmaking includes a carbonization step based on destructive distillation of coal into metallurgical coke in coke ovens. In oxygen-free conditions, coal is heated to about 1100 °C, yielding a porous, heterogeneous solid. Coke performance is assessed by its high-temperature mechanical strength, reactivity, low ash content, and consistent chemistry, governing both the fuel's reactivity and overall furnace productivity. Ideally, metallurgical coke should:

- Withstand handling and charging stresses without significant breakage.
- Resist compression and abrasion under the burden's weight.
- Exhibit minimal shrinkage during reaction to preserve gas flow channels.
- React sufficiently to produce CO at a controlled rate.

The first three coke requirements are intrinsically linked to bed permeability: a critical factor in furnace performance. As molten iron forms, it spreads over the surfaces of coke, which is the only material remaining solid under blast-furnace conditions, and percolates through the voids. High permeability, characterized by excessively large coke particles, results in inadequate interaction between the phases. In fact, the gas would tend to bypass the solid

bed through preferential paths, rather than distributing itself throughout it. This tendency reduces the amount of heat produced and the concentration of CO in the gas phase. For these reasons, coke is fundamental throughout the entire process, and its integrity, understood as its ability to resist volume changes, is an essential aspect for the overall efficiency of the unit.
Coke properties derive from coal quality, coking conditions, and post-carbonization treatments, all of which shape its microstructure, morphology, and physical behaviour (Ghosh and Chatterjee, 2008)(Ghosh and Chatterjee, 2008)(Ghosh and Chatterjee, 2008). In addition to mechanical strength and reactivity, low ash content is vital. Ash absorbs useful thermal energy, increases fuel consumption, generates excess slag, and introduces impurities (e.g., sulphur) into the melt. Minimizing ash thus enhances energy efficiency, reduces slag volumes, and improves the purity of the iron phase.
Meeting these combined demands, such as high strength, controlled reactivity, and low impurity levels, has driven interest in alternative ironmaking routes. Direct-reduction processes, which produce porous "sponge iron" without coke, offer a promising path to reduce reliance on metallurgical coke while achieving stringent product specifications.

I.2. Direct reduction iron (DRI) and electric arc furnace (EAF) process

Direct Reduction (DR) is a solid-state reaction in which oxygen is removed from the solid ore using reductants such as coal or reformed natural gas. During the entire reaction network, the main product preserves its solid-state due to the fact that reactions take place in an environment where the maximum temperature is kept below the iron melting temperature, 1535°C, and the end product is highly metallized direct reduced iron (DRI), or "sponge iron," reflecting its retained morphology, a 27-30% mass loss from deoxygenation, and a porous, sponge-like structure.
Based on the type of reductant, DR processes are classified as:

- Coal-based DR process: solid carbon sources (e.g., coal, gasified coal, coke breeze) supply both thermal energy and the reducing agent.
- Gas-based DR process: gaseous reductants (H_2, CO, or reformed natural gas such as CH_4) remove oxygen from the ore.

Despite the reagent, the final product is in a solid state and requires subsequent processing to achieve the desired composition, such as using the Electric Arc Furnace (EAF).
This thesis focuses exclusively on gas-based DR; for this reason, the following discussion will address only the gas-based DR process for which different technologies have been developed over time and four different reactors have been designed in the form of shaft furnaces, fluidised beds or retorts.

I.2.1. Gas-based DR process

From a chemical perspective, natural gas is composed predominantly of alkanes, hydrocarbon chains described by the general formula C_nH_{2n+2}. Methane (CH_4) is the principal component, although heavier paraffins (ethane, propane, butane) and inert or impurity gases (N_2, CO_2, H_2S) are also present.
Natural gas cannot be used directly in the rector to conduct the reduction of iron ores because its hydrocarbons react too slowly with iron oxides and tend to decompose into carbon soot. Instead, it must first be converted in a reformer, named for its main reaction: steam reforming. According to Figure I.2, the equilibria between CO and CO_2 is favoured for the first one at high temperature. Therefore, the conversion happens at a temperature of the order of 1000°C, to obtain a mixture composed essentially of H_2 and CO. These reactions, reported in eqs. (11) and (12), are known as reforming and describe the conversion of methane into a mixture composed of about 75% of hydrogen and 25% carbon monoxide. To balance energy demand with endothermic steam reforming reaction, the gas is mixed with an oxygen steam to conduct an exothermic partial combustion reactions:

$$CH_4 + H_2O = CO + 3H_2 \qquad \Delta H^o_{298} = +206.1\ kJ/mol \qquad (11)$$

$$CH_4 + CO_2 = 2CO + 2H_2 \qquad \Delta H^o_{298} = +247.3\ kJ/mol \qquad (12)$$

$$CH_4 + \frac{3}{2}O_2 = CO + 2H_2O \qquad \Delta H^o_{298} = -519.3\ kJ/mol \qquad (13)$$

$$CH_4 + H_2O = CO_2 + H_2 \qquad \Delta H^o_{298} = +164.9\ kJ/mol \qquad (14)$$

To achieve industrially viable rates, these reactions are catalysed and operated at temperatures above 700 °C. The product gas must then be heated to 1000–1100 °C to preserve its reforming composition and satisfy the thermochemical demands of iron-ore reduction. Under these conditions, the syngas stream contains about 85–90 % H_2 + CO (in a near 1:1 molar ratio) and 10–15 % CO_2 + H_2O (with CO_2:H_2O around 4:1). [9]
Additional advantages of on-site stream reforming include:

- The reformer reactor is smaller, making it easier to produce the reduction mixture in situ.
- The reducing mixture can be obtained from a wide range of sources, such as gases from coal or coke gasification, hydrogen, and hydrocarbon gases like gasoline, fuel oil, and naphtha.
- Unit integration can be easily performed to recover energy from offset gases.
- Long catalyst life is allowed since the impurities are not fed to the reforming reactor.

- The possibility of generating electricity from the process by sending the steam produced to be used in the gas reforming reactions to a turbo generator. This integration enables a drastic reduction in the plant's energy requirements from an external electricity supply.

Typically, gas-based DR reaction to produce sponge iron takes place in a shaft furnace (SF): a vertical, counter-current reactor. Iron ore (in lump or pellet form) is charged from the top, while preheated reforming gas enters through tuyeres at the bottom. This configuration mirrors a blast furnace, but the main product remains solid throughout the reduction.

Among DR technologies, the most widely adopted is the MIDREX® process, pioneered in the USA in 1967. MIDREX exemplifies high metallization efficiency, energy integration, and product consistency. The reforming unit, the shaft furnace, and the energy integration are the fundamentals of this process. Usually, the reformer unit operates on natural gas, using a nickel catalyst to produce the reducing agent in situ. Although shaft furnaces can accommodate lump ore, pellets, or blends, pellets are preferred for their uniform size distribution, superior permeability, and consistent metallization performance.

As the hot reducing gas flow ascends, it transfers heat to the descending solids and reacts continuously, converting CO and H_2 into CO_2 and H_2O, and modifying its composition. The offset gas, which leaves the unit from the top, exits the furnace at a temperature around 400 - 450°C. After particulate removal, approximately 60% of this sensible heat is recovered in gas-to-gas exchangers to reheat fresh syngas to about 900 °C, while the gasses is combusted to supply supplementary process heat.

The full suite of reduction reactions, which progressively strip oxygen from the iron ore, is summarized in eqs. (15-31):

Hematite Fe_2O_3	$Fe_2O_3 + 3CO = 2Fe + 3CO_2$	$\Delta H^o_{298} = -24.8\ kJ/mol$	(15)
	$3Fe_2O_3 + CO = 2Fe_3O_4 + CO_2$	$\Delta H^o_{298} = -47.2\ kJ/mol$	(16)
	$3Fe_2O_3 + H_2 = 2Fe_3O_4 + H_2O$	$\Delta H^o_{298} = -6.0\ kJ/mol$	(17)
	$Fe_2O_3 + 3H_2 = 2Fe + 3H_2O$	$\Delta H^o_{298} = +98.8\ kJ/mol$	(18)
	$3Fe_2O_3 + C = 2Fe_3O_4 + CO$	$\Delta H^o_{298} = +125.3\ kJ/mol$	(19)
Magnetite Fe_3O_4	$Fe_3O_4 + C = 3FeO + CO$	$\Delta H^o_{298} = +191.9\ kJ/mol$	(20)
	$Fe_3O_4 + CO = 3FeO + CO_2$	$\Delta H^o_{298} = +19.4\ kJ/mol$	(21)
	$Fe_3O_4 + H_2 = 3FeO + H_2O$	$\Delta H^o_{298} = +60.6\ kJ/mol$	(22)
	$Fe_3O_4 + 4CO = 3Fe + 4CO_2$	$\Delta H^o_{298} = -13.6\ kJ/mol$	(23)
	$Fe_3O_4 + 4H_2 = 3Fe + 4H_2O$	$\Delta H^o_{298} = +151.2 kJ/mol$	(24)
Wustite FeO	$FeO + C = Fe + CO$	$\Delta H^o_{298} = +161.5\ kJ/mol$	(25)
	$FeO + CO = Fe + CO_2$	$\Delta H^o_{298} = -11.0\ kJ/mol$	(26)
	$FeO + H_2 = Fe + H_2O$	$\Delta H^o_{298} = +30.2\ kJ/mol$	(27)
Metallic iron Fe	$3Fe + CH_4 = Fe_3C + 2H_2$	$\Delta H^o_{298} = +99.9\ kJ/mol$	(28)
	$3Fe + 2CO = Fe_3C + CO_2$	$\Delta H^o_{298} = -147.4\ kJ/mol$	(29)
	$3Fe + CO + H_2 = Fe_3C + 2H_2O$	$\Delta H^o_{298} = -106.2\ kJ/mol$	(30)
	$Fe + CO + H_2 = Fe(C_{free}) + H_2O$	$\Delta H^o_{298} = -131.3\ kJ/mol$	(31)

This reaction sequence (eqs. 15–27) converts iron oxides stepwise into metallic iron, while the final four equations describe carbon uptake into the solid phase. A direct comparison shows that hydrogen-driven reductions are overall endothermic, whereas CO-based reductions release heat. Consequently, hydrogen-rich gas mixtures often require an external heat source to sustain reaction temperatures.

By overlapping Figure I.3, which maps solid-phase equilibrium as a function of H_2 volumetric fraction, with Figure I.2, it is also possible to perform a thermodynamic analysis. In the case of CO and CO_2 (Figure I.2), the stability region for metallic iron is extremely narrow and occurs at high CO

concentrations and high temperatures. In the case of hydrogen, on the other hand, the region of stability of metallic iron is much wider and far from the conditions of liquefaction, occurring with concentrations of H_2 above than 60%. The Fe/oxide boundary shifts to lower temperatures as H_2 concentration increases. From the graph, it can be seen that thermodynamically, iron reduction is feasible at temperatures as low as ~500 °C when H_2 exceeds ~70%. However, the sluggish reaction kinetics under these mild conditions render such operations impractical at an industrial scale.

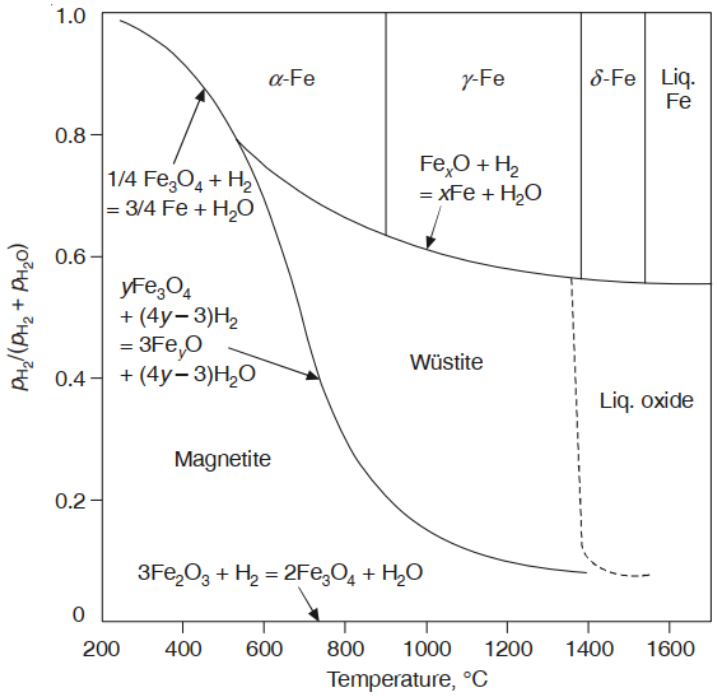

Figure I.3 Equilibrium [pH2/(pH2 + pH2O)] ratios in gas as a function of temperature for reactions in Fe–H–O system. The lines are for equilibria of reactions as indicated.[9]

This comparison elucidates why blast furnaces operate under severe, high-temperature, CO-rich conditions, yet highlights the broader, less energy-intensive operating window available to gas-based DR processes with adjustable H_2/CO ratios.

I.3. Lamps, sinters, and pellets

Regardless of the reduction route, the chemical composition, geometric and physical properties of the solid critically determine the process efficiency. Among the multitude of variables, supplying feedstock with favourable chemical and physical characteristics is essential for stable reactor operation. Three types of solid feed materials are commonly used: lamp ores, pellets, and

sinters. Each kind of feed has a distinct impact on product quality and energy requirements.

Starting with minerals, the solid extracted is processed to reduce its size using various types of crushers. In general, there are three main products of the crushing process according to the product dimension:

- The coarsest fraction (10 to 40 mm): direct-shipping lump ore is mined, crushed, and screened to size for furnace feed without further processing. Its minimal treatment makes it cost-effective, but its irregular shape, broad size distribution, and native impurity levels can impair permeability, reduce overall efficiency, and increase production costs.
- The intermediate fraction (0.1 to 10 mm): the sinter feed comprises fine iron ore and recycled fines too small for direct charging. In a sinter plant, these fines are agglomerated into clinker-like aggregates (sinter) with controlled size and porosity to optimize gas flow and reducibility.
- The finest (< 0.1 mm): when ore fines exhibit sufficiently high iron content, they serve as pellet feed; otherwise, they are discarded or sent to beneficiation. Because fines tend to concentrate gangue minerals, stringent screening is required to avoid excessive impurities.

Regardless of particle size, furnace feed typically consists of hematite (Fe_2O_3) and magnetite (Fe_3O_4), with iron contents preferably higher than 55%. In DRI use, the higher the iron content in the feed, the lower the impurity content at the end of the process. In blast furnaces, the higher the iron content in the feed, the lower the slag volume produced, which corresponds to an increase in productivity and a reduction in the coke rate. For the same reason, lump iron ores that contain less than 55% iron are often beneficiated - i.e. by magnetic separation, flotation, or roasting - to enrich the iron content.

I.3.1. Sinter making

The term “sinter” indicates an agglomerated mixture of fine iron ore, recycled ironmaking by-product, and fluxes (e.g., dolomite or limestone), processed with solid fuels like coke breeze. Sinter comprises roughly 60% of the blast-furnace charge and is used to overcome the low permeability of fine particles. “Sintering” refers to the partial fusion of these fines at temperatures just below the iron-ore melting point, bonding adjacent particles into porous agglomerates.

Sintering is therefore an ideal way to recycle materials that are unsuitable for direct processing due to their small size. The quality of the sinter directly affects the quality of the final product and production costs, so it is necessary to mix the various materials in the optimal proportions. Figure I.4 shows a schematic representation of a sinter-making plant. The materials, coming from various storage silos, are transported on conveyor belts and mixed before

being sent to the sintering machines. The feed must be mixed as uniformly as possible in order to obtain a more homogeneous final product. The solid phase is sent to the mixing drum, where it is mixed with water to achieve an optimal moisture content (~6-8 %) for granulation. The drum rotation promotes the formation and growth of spheres/granules. Here, the fundamental parameter is time: 3-4 minutes of mixing prevents granules from exceeding 10 mm. The granules obtained are spread onto a strand or grate and pass through preheating, ignition, and sintering zones (up to 1200-1300 °C) using gas or coke-fired burners.

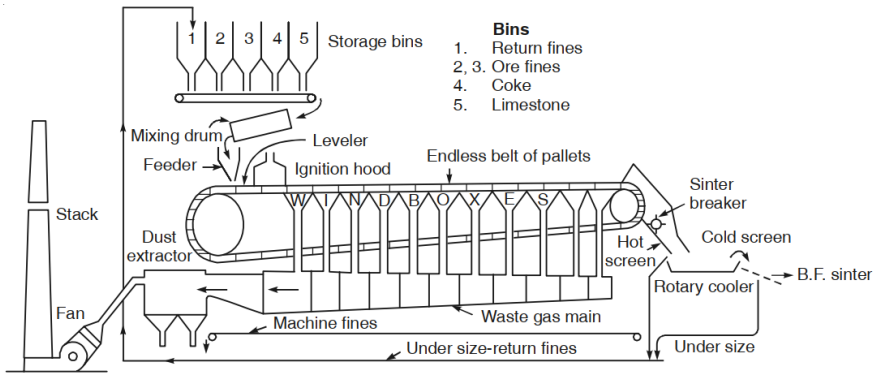

Figure I.4 Sinter making plans scheme.

The solid phase tends to agglomerate due to the partial melting of the outer layers and the formation of a slag that acts as a binder between the particles. However, what is obtained is a single layer of material, which is then cooled and crushed. Subsequent screening allows aggregates smaller than 5 mm to be removed and reused as raw material for the production of other sintered solids (Ghosh and Chatterjee, 2008)(Ghosh and Chatterjee, 2008)(Ghosh and Chatterjee, 2008). Optimizing each stage by adjusting blend ratios, moisture, granule size, bed thickness, and thermal profile yields sinter with the strength, porosity, and reducibility required for efficient, stable blast-furnace operation.

I.3.2. Pelletisation

Particles that are too fine for the sintering process are used to make spherical compacts called pellets. Pelletizing begins by blending iron-oxide fines with fluxes (limestone or dolomite) and a binder, typically bentonite, to reach a moisture content of about 10 %. The material is sent to either 45° inclined rotating pans or rotating drums for pellet production. The pelletizer runs at around 10-15 rpm, and the final product is called green pellets. In the process, capillary forces, mediated by the water, drive the agglomeration of fine particles into “green” pellets. Precise moisture control is vital: too little water prevents adequate growth, while excess moisture yields oversized, irregular clumps. After roughly 3 minutes of tumbling, the emerging pellets are

screened; those between 10 and 16 mm are fired, while undersized fragments are recycled for regrinding.

Before final hardening, green pellets undergo staged heating for both drying and thermal integration. The process scheme for a pelletising plant is reported in Figure I.8. First, they pass through a preheating zone at 600 - 700°C, fuelled by exhaust gases from the subsequent rotary kiln, to remove residual moisture and prevent breakage. This step is essential to prevent pellet disintegration during the subsequent firing. Next, the pellets enter the rotary kiln, where temperatures rise to 1250 - 1300°C to sinter the oxide matrix. In this way, the pellets achieved the physical and metallurgical requirements for handling, transportation, and final use. The mechanical properties of the produced pellets should be suitable for use in both BF and DRI processes.

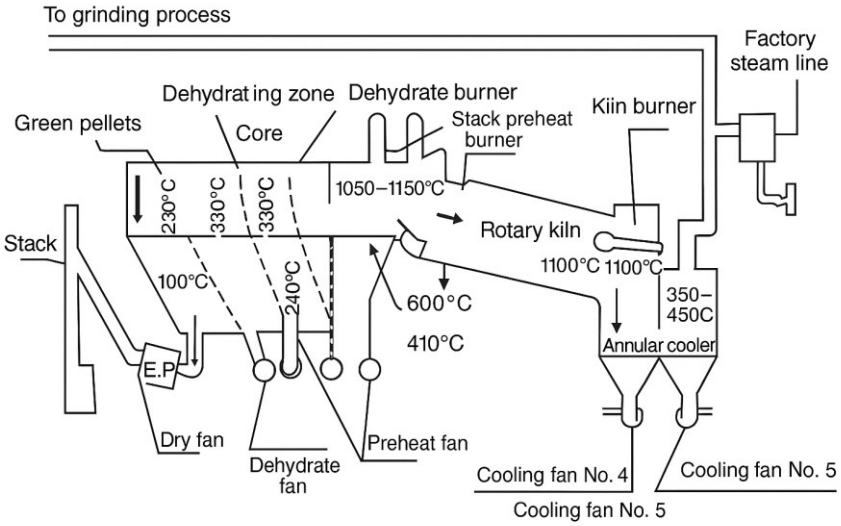

Figure I.5 Pelletizing plans scheme.

Unlike sinter, where partial melting bonds particles, pellet strength derives from solid-state diffusion and recrystallization, yielding a robust product optimized for blast-furnace or DRI service.

I.4. The Decarbonization of the Steel Industry

Iron and steel are among the most versatile and indispensable materials in the global economy, underpinning everything from infrastructure to consumer goods, leading to an explosion in steel production over the last 10 years.

According to the World Steel Association, global crude-steel production reached 1886.3 million tonnes (Mt) in 2024 [10], showing stability over the last five years. Figure I.6 illustrates this steady output, with world production

shown in orange and China's share in blue. China alone accounts for nearly half of total steel output, underscoring its dominant role.

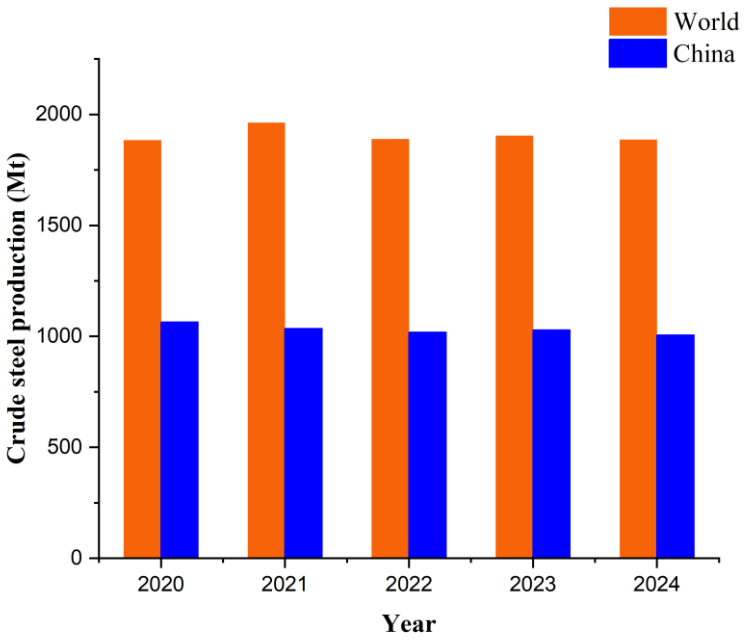

Figure I.6 Comparison between global steel production (in blue) and steel production in China (in purple) for the years 2020 to 2024.

Despite its critical importance, the metallurgical sector is increasingly criticised for its environmental impact. As we have seen in the previous paragraphs, both the blast-furnace (BF) and direct-reduction (DR) routes emit significant CO_2 into the atmosphere, even if to different degrees, thereby exacerbating the well-known impact on Earth's climate. Metallurgical sectors contribute substantially to global carbon emissions, with steel manufacturing accounting for approximately 7-9% of total CO_2 worldwide emissions. The strong chemical bonds in iron ores require very high temperatures and energy inputs, making decarbonization particularly challenging and bringing metallurgy into the category of sectors "hard to adapt," as replacing traditional processes with innovative, lower-emission methods is not straightforward.
The previous paragraphs described the two main processes currently used to produce iron in metallic form. Of the two main ironmaking routes, the BF-basic-oxygen-furnace (BOF) process remains preeminent, accounting for about 70 % of production. Section I.1 demonstrated that the reaction network is intrinsically linked to CO_2 production, driven by excessive use of coke. In the BF process, carbon primarily meets the energy requirements of the operation, allowing high temperatures, high loads of material to the process, and enabling reduction reactions to take place with the production of CO.

Therefore, the system is self-sustaining, as it does not require external energy sources. However to improve the kinetics and the stability of metallic iron, it is necessary to work at the highest possible temperature [3]. The combination of these phenomena leads to immense CO_2 emissions, with estimates suggesting that producing 1 tonne of crude steel emits about 1.9 tonnes of CO_2. Attention is therefore focused on these two aspects to identify possible alternatives from both environmental and economic perspectives. In response, the direct-reduction process (DRP) followed by electric-arc-furnace (EAF) route is gaining attention. It is a less energy-intensive process, since it requires less demanding operating conditions and no longer requires melting the solid phase. So, it turns out to be less intensive in terms of CO_2 emissions,it is estimated that, using current technologies and processes, for every tonne of steel produced using natural gas based DRI-EAF, 0.6 tonnes of CO_2 are released into the atmosphere, resulting in an estimated reduction of over 60% in emissions [11] [12] [13]. As steel demand continues to grow, efforts are underway to develop more sustainable production methods, including recycling, energy-efficient technologies, and carbon-neutral initiatives aimed at reducing the industry's environmental footprint. In this scenario, DR represents a preliminary step in the right direction.

I.4.1. European countermeasures to CO_2 emissions

The European Union (EU) has designed a multisectoral offensive, placing research at the forefront of its efforts to address CO_2 emissions, with a particular focus on the decarbonization of heavy and energy-intensive industries, such as steelmaking. Through ambitious policy frameworks and substantial financial instruments, the EU is accelerating the development and deployment of green technologies. Flagship programs, such as the Innovation Fund and Horizon Europe, the EU's main funding program for research and innovation, are channelling these resources into demonstration and implementation projects for low-carbon processes. The steel industry, one of the largest emitters, is a primary target of this support. Evidence of this growing interest in modernizing a key sector like steel is the Clean Steel Partnership, a collaboration between the European Commission and the steel sector under Horizon Europe - represented by the European Steel Technology Platform (ESTEP). With a budget of approximately €700 million, it aims to drive research and innovation toward zero-carbon steelmaking. Its targets are to slash CO_2 emissions by 55% by 2030 and by 95% by 2050, laying the groundwork for a climate-neutral steel industry [14], [15].
Three main pathways are under development:

- Carbon Direct Avoidance (CDA): Designing production processes that prevent CO_2 formation, primarily by replacing coal with green hydrogen as the reductant or involving electricity as energy source.

- Smart Carbon Usage (SCU): Enhancing carbon efficiency through carbon capture, utilization, and storage (CCUS) and tighter process integration to optimize energy use.
- Circular Economy: Promoting steel recycling and the valorisation of production cycle by-products [16].

I.4.2. Maximise H2 Enrichment in Direct Reduction

A prime example of a Horizon Europe-funded initiative, and the cornerstone of this thesis, is the MaxH2DR (Maximise H_2 Enrichment in Direct Reduction Shaft Furnaces) project [17]. This initiative directly addresses the challenge of using hydrogen to produce "green" steel, which falls into the CDA category. The project, active from 2022 to 2026, aims to develop and optimize the direct reduction of iron ore using a high concentration of hydrogen in the reduction gas. It therefore aims to investigate the key aspects of H_2-enriched direct reduction, answering the fundamental questions for the correct design of the plant's main unit - the shaft furnace - and filling the knowledge gaps in this innovative approach. Although hydrogen-enriched DR is practiced internationally, little is known about operation under extremely high H_2 concentrations (greater than 80%). MaxH2DR aims to fill these knowledge gaps by combining laboratory experiments, pilot trials, and modelling to unlock the full potential of H_2-DR, understanding and overcoming the technical hurdles of high-hydrogen direct reduction, including process stability, energy balance, and the properties of the resulting direct reduced iron (DRI).

The rationale for prioritizing the DR route over the traditional blast-furnace (BF) pathway stems from a comparative analysis of their strengths and limitations. Although BF is still one of the main production processes, it has several weaknesses:

- Although it offers greater flexibility than DR, the quality of the final product depends heavily on the properties of the raw materials used. BF requires iron oxide minerals with high-quality metallurgical properties, and high-quality coke as both fuel and permeability agent, and an on-site coking plant.
- Economic viability only at large scales, resulting in a return on investment within an acceptable timeframe.
- Extensive auxiliary infrastructure (e.g., raw material handling and preparation systems, sintering plants, coke ovens with rigorous environmental control systems, pellet hardening furnaces) adds capital and operational complexity.
- A heavy carbon and energy footprint, driven by high-temperature, coal-based reduction reactions [18].

By contrast, the DR process already has intrinsic benefits that allow it to significantly reduce CO_2 emissions for the same amount of steel or iron

produced. In addition, it presents different advantages, such as requiring fewer production support units, lower initial investment costs, and less energy-intensive.In addition, the major privilege is the potential to reduce oxides without carbon compounds, freeing production from the use of solid materials such as coke or fossil fuels.

H_2-based direct reduction, however, introduces several critical challenges, foremost among them the strongly endothermic nature of the reduction reactions. Unlike CO-driven processes, the hydrogen route cannot sustain its heat demand internally, so external heating must be integrated. Moreover, the new reaction network influences morphology, diffusion, and kinetics, which remain unknown. The end-product is a sponge solid that retains all feedstock impurities and undergoes negligible volumetric change. The absence of carbon in the structure entails two aspects: first, under the process conditions, the material cannot melt, as it is essentially composed of iron; second, to achieve a specific carbon concentration and obtain a steel with given properties, additional processes are necessary.

Because the solid phase traverses the full height of the shaft furnace, it is vital to understand how particle properties and flow behaviour evolve with operating conditions and conversion degree. Small shifts in gas composition can trigger unpredictable effects: local temperature variations, changing adhesion/cohesion between pellets, or evolving surface chemistries can all degrade bed permeability. Should the porous structure collapse or particles coalesce, gas will channel through preferred routes, dramatically reducing gas-solid contact, slowing reduction rates, destabilizing the process, and compromising product quality.

These intertwined phenomena and parameters must be systematically clarified to reliably predict furnace behaviour, maximize metallization efficiency, minimize energy and capital costs, and appropriately size new reactors. The MaxH2DR project addresses precisely these gaps, generating the fundamental data and mechanistic insights needed to realize commercial-scale, hydrogen-driven green steelmaking. Such knowledge will be instrumental in meeting the EU's ambitious decarbonization targets and in charting alternative, low-carbon pathways for the steel industry.

I.4.3. Scope of thesis

The European MaxH2DR project is an evident example of synergy and cooperation between industrial partners, research institutions, and universities, involving experts in the steel industry, simulation, characterization, modelling, and process analysis. Among the 10 partners involved, from 7 different countries, there is the University of Salerno (UniSa), represented by its Powder Technology Laboratory of the Department of Industrial Engineering.

UniSa contribution is to characterise how pellet-scale physical properties evolve with process variables and conversion degree. Temperature (between 600 and 1000°C), compressive stress, and H_2 concentration have to be systematically investigated to quantify their influence on pellet morphology, strength, and the flow behaviour of the solid phase. The main objective of this thesis is the design and development of a novel prototype shear testing device for high-temperature, controlled-atmosphere applications, capable of replicating at a laboratory scale the extreme conditions encountered in a shaft furnace. Conditions that cannot be reproduced using commercial shear testing equipment.

This custom shear cell generates time-series of shear stress and normal stress data as functions of temperature and metallization degree of pellets. Those datasets are used by another partner of the consortium to calibrate a DEM-CFD code by modelling the experimental observations through simulations. This mutual integration is a key aspect in designing experimental tests that allow the extraction of parameters that are fundamental to defining pellet flow, such as friction, cohesion, and softening coefficients, under high H_2 concentration, high-temperature, and compressive conditions.

Figure I.7 illustrates the conceptual layout of the high-temperature shear cell prototype. At the center of this proptotype, there is a shear cell which consists of a trough that contains the sample and a lid to which the measuring elements are mechanically linked. Figure I.7.a highlights the essential components of the testing apparatus. At the top of the structure, a normal-force sensor and a torque sensor are mounted and connected to the lid of the shear cell through a central rod.At the base of the trough, a rotary motor provides controlled rotation, enabling the application of shear to the material and allowing the combined measurement of normal load and torque during the test. Once the lid is secured, the trough is rotated to generate internal shear in the compacted sample. The entire assembly sits inside a sealed containment chamber, where temperature and gas composition are precisely regulated. Figure I.7.b shows the entire assemply in sectional view.

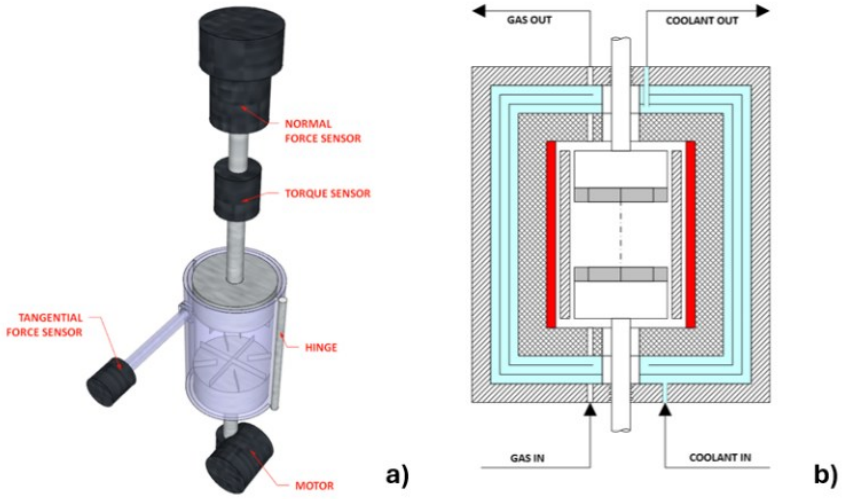

Figure I.7 Preliminar design of the setup: (a) the 3D representation of the trough, lid, and main mechanical components; (b) the cross-sectional view of the setup, in the centre the the trough and the lid surrounded by an insulated and heating system.

This rigorous, experiment-driven simulation framework will not only demonstrate the technical and economic viability of green steelmaking but also enhance the precision of pilot plant design and scale-up studies for a truly low-carbon steel industry.

II. Literature review

II.1. Principles of the mechanics of solid particulates

The study of particulate flowability, along with the identification and quantification of the factors governing the flow of bulk solids, represents a fundamental aspect not only in mineral processing but in any industrial sector where the motion of a solid phase is involved. The discharge of bulk solids entails complex interactions among particles and granules, which remain in continuous contact throughout the process. As a result, a thorough understanding of bulk behaviour is essential to accurately predict and control flow dynamics [19], [20].

The flow properties of bulk solids are significantly influenced by a range of physical parameters, including particle size distribution, shape, surface roughness, interparticle cohesion, moisture content, and apparent density [19], [21], [22]. These characteristics directly affect the relative motion between particles and, consequently, the overall flowability of the material. However, their influence is not isolated, rather it emerges from the interplay among these factors and the chemical composition of the solid phase. This multifactorial dependency can lead to complex and sometimes unpredictable flow behaviour, especially under varying process conditions.

For this reason, the characterization of bulk solids is not merely advisable but essential when the solid phase plays a dominant role in the process. A rigorous and context-specific characterization enables the optimization of operational parameters, improves process efficiency, and helps define the expected flow pattern and throughput. Moreover, it allows for preventing and mitigating the undesirable phenomena such as particle interlocking or arching, which may occur when the applied stress is insufficient to overcome internal resistance, resulting in sudden flow interruptions or reductions. Addressing these challenges through proper material characterization is therefore critical to ensuring the reliability and performance of bulk handling systems.

II.1.1. Continuum mechanics

The characterization of flow behaviour, aimed at predicting the response of solid materials under operative conditions, is conducted on the bulk solid phase. For this reason, a clear definition of bulk solid is essential. A bulk solid can be described as an assembly of discrete solid particles that remain in contact with one another, forming a collective phase whose macroscopic behaviour differs significantly from that of its individual constituents.

The methodologies adopted for flow description are based on two principal approaches that have been consolidated over time: the discrete element method (DEM) and the continuum approach.

The discrete element method relies on numerical simulation tools that model particle–particle interactions by solving the force balance equations for each particle or small clusters of particles [23], [24], [25]. Although this approach offers considerable potential for detailed analysis, it is subject to several limitations. The number of particles that can be realistically simulated is restricted by computational capacity, and the geometric complexity of particle shapes often requires simplification. Furthermore, the high computational effort and extended processing time required to solve the governing equations, combined with the difficulty in accurately reproducing key particle characteristics such as shape and surface texture, limit the applicability of DEM for rapid or large-scale estimation of flow properties [26], [27].

In contrast, the continuum approach represents the classical framework for characterizing the flow behaviour of bulk solids and serves as the foundation for the prototype and analytical developments presented in this thesis. This method assumes that the solid phase behaves as a continuous medium, thereby shifting the focus from individual particle interactions to the analysis of forces and deformations acting on defined boundary areas of representative volume elements. For the continuum assumption to hold, the volume under investigation must be sufficiently large relative to the particle size, such that the discrete nature of the material and the multitude of contact points between particles can be neglected. Within this framework, flow properties are typically assessed by measuring stress and strain fields in the tested bulk material, which also brings the development of calculation procedures and design approaches.

To better illustrate the principles of continuum theory, it is useful to consider the stress distribution that arises when a bulk powder system is subjected to uniaxial compression. Under such conditions, the magnitude of compressive stress may vary depending on the direction of observation. This directional dependence reflects the internal redistribution of forces within the bulk material.

A representative example involves a bulk solid confined within a trough and compressed by a force applied vertically through a lid. The application of this compressive load induces internal stress within the sample, even in the absence of macroscopic motion. Specifically, both normal stresses (denoted

as σ) and tangential or shear stresses (denoted as τ) can be identified throughout the material. These stresses arise from particle-particle contact interactions and the constraints imposed by the system's boundaries.
To describe the mechanical state of the system, a force balance can be formulated by considering both vertical and horizontal components. The adopted convention assumes that normal stress is positive when it acts along the inward normal direction, corresponding to a compressive force. Shear stress is considered positive when it acts perpendicular to the inward normal and is oriented in a counterclockwise direction [19], [20], [28].

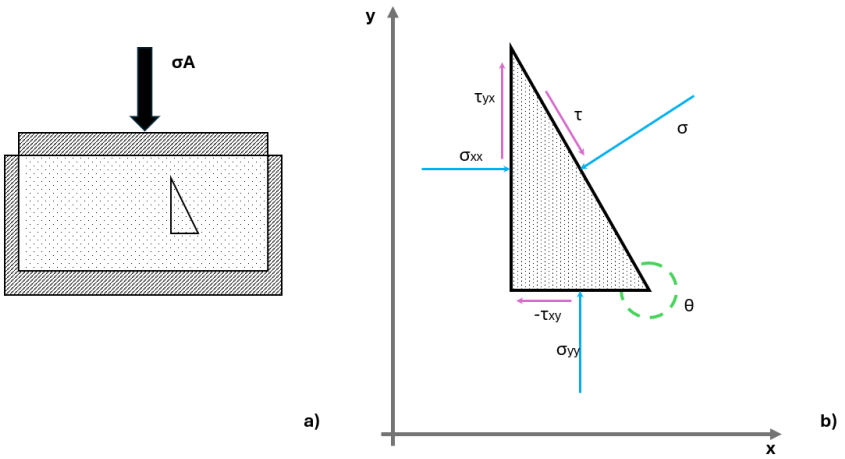

Figure II.1 (a) Sectional view of the cell containing the solid specimen, compressed by a lid applying a normal force. (b) Force distribution within a generic triangular element of the sample: normal stresses shown in blue, shear stresses in purple.

Figure II.1 presents a sectional view of the trough (a), where a rectangular cross-section of the sample is selected for analysis (b). A force balance is applied to a triangular volume element within this section. The stresses acting on the hypotenuse are represented by σ and τ. For the orthogonal faces aligned with the x-y coordinate system, a double subscript notation is used to identify the stress components: the first letter indicates the direction of the stress vector, while the second refers to the orientation of the plane on which the stress acts.
Given that the powder within the triangular element is assumed to be in static equilibrium, the force balance allows for the determination of the stresses exerted by the surrounding material on the element itself. The application of the force balance and trigonometric relationships leads to the expression of the stress components acting on the inclined plane in terms of the original coordinate system.

$$l \cdot \sigma = -l \cdot sin\theta \left(\sigma_{xx} \cos\left(\theta - \frac{3\pi}{2}\right) + \tau_{xy} \cos(2\pi - \theta) \right) + \tag{32}$$

$$+ l \cdot cos\theta \left(\sigma_{yy} \cos(2\pi - \theta) + \tau_{xy} \cos\left(\theta - \frac{3\pi}{2} \right) \right)$$

$$\sigma = \frac{1}{2}(\sigma_{xx} + \sigma_{yy}) - \frac{1}{2}(\sigma_{xx} - \sigma_{yy}) \cos 2\theta - \frac{1}{2}(\tau_{xy} + \tau_{yx}) \sin 2\theta \quad (33)$$

A similar procedure can be applied by considering the direction of the shear stress τ, leading to an analogous formulation of the stress components along the inclined interface.

$$\tau = \frac{1}{2}(\sigma_{xx} - \sigma_{yy}) \sin 2\theta + \frac{1}{2}(\tau_{xy} + \tau_{yx}) - \frac{1}{2}(\tau_{xy} + \tau_{yx}) \cos 2\theta \quad (34)$$

By solving the moment equilibrium equations around the centroid of the bulk solid element, it becomes evident that the shear stresses τ_{xy} and τ_{yx} are equal in modulus, reflecting the internal symmetry of the stress tensor and is consistent with the conditions of static equilibrium:

$$\tau_{xy} = \tau_{yx} \quad (35)$$

Using this observation, the stresses on a plane at angle θ is expressed in terms of the orthogonal planes x and y as:

$$\sigma = \frac{1}{2}(\sigma_{xx} + \sigma_{yy}) - \frac{1}{2}(\sigma_{xx} - \sigma_{yy}) \cos 2\theta - \tau_{xy} sin2\theta \quad (36)$$

$$\tau = \frac{1}{2}(\sigma_{xx} - \sigma_{yy}) \sin 2\theta - \tau_{xy} cos2\theta \quad (37)$$

Although the derivation of eqs. (36) and (37) was performed with reference to the orthogonal planes x and y, the resulting expressions do not explicitly depend on the orientation of these coordinate axes. This observation allows for a generalization of the stress state at a point, which can be stated as follows:

- The stresses acting along any pair of mutually perpendicular directions are sufficient to fully define the state of stress at their point of intersection.
- The shear stresses associated with any pair of perpendicular directions are equal in magnitude but opposite in sign, reflecting the equilibrium of internal moments and the antisymmetric nature of the shear stress components.

These stress pairs of eqs. (36) and (37) can be represented graphically on a $\sigma - \tau$ diagram, where σ is plotted along the horizontal axis and τ along the vertical axis. By plotting the stress states for a range of θ values and connecting the resulting points, a circular locus emerges. This graphical representation, known as the Mohr stress circle [29], encompasses all possible stress states within the material for a given applied compressive load [30],

[31]. Each point on the circle corresponds to the stress state acting on a plane inclined at an angle θ with respect to the reference axis.
It is important to note that, according to the underlying equations, a physical rotation of the cutting plane by an angle θ corresponds to a rotation of 2θ on the Mohr circle. This geometric amplification is a distinctive feature of the Mohr representation and facilitates the analysis of stress transformations.
The Mohr circle is always centred along the σ-axis, with its centre located at the point $(d, 0)$, and the radius r can be estimated as follows [28]:

$$r = \left[\frac{\left(\sigma_{xx} - \sigma_{yy}\right)^2}{4} + \tau_{xy}^2\right]^{\frac{1}{2}} \tag{38}$$

$$d = \frac{\sigma_{xx} + \sigma_{yy}}{2} \tag{39}$$

The peculiarity of parameters d and r is that they are invariant with respect to the orientation of the coordinate system. This invariance allows for a generalized description of the stress state that is independent of the chosen reference system. In addition, it is possible to demonstrate that there exists a plane inclined by an angle of ϕ from the vertical axis for which the shear stress action is equal to zero.
Therefore, from eqs (38) and (39), the following relation is obtained:

$$tan2\phi = \frac{2\tau_{xy}}{\sigma_{xx} - \sigma_{yy}} \tag{40}$$

Using this new set of variables, the equations describing the normal and shear stresses on any inclined plane can be reformulated in terms of d and r, providing a more intuitive and geometrically consistent framework for stress analysis.

$$\sigma = d - r \cdot \cos(2\theta - 2\phi - 2\pi) \tag{41}$$

$$\tau = r \cdot \sin(2\theta - 2\phi - 2\pi) \tag{42}$$

This formulation allows for a consistent representation of the stress state across all orientations of the cutting plane. The behaviour of both normal and shear stresses under these limiting conditions is illustrated in eqs (43) and (44) and further visualized in Figure II.2.

$$\begin{cases} \theta = 2\pi \\ \sigma = d + r \cdot \cos 2\phi \\ \tau = r \cdot \sin 2\phi \end{cases} \tag{43}$$

$$\begin{cases} \theta = \dfrac{3\pi}{2} \\ \sigma = d + r \cdot \cos(\pi + 2\phi) \\ \tau = r \cdot \sin(\pi + 2\phi) \end{cases} \tag{44}$$

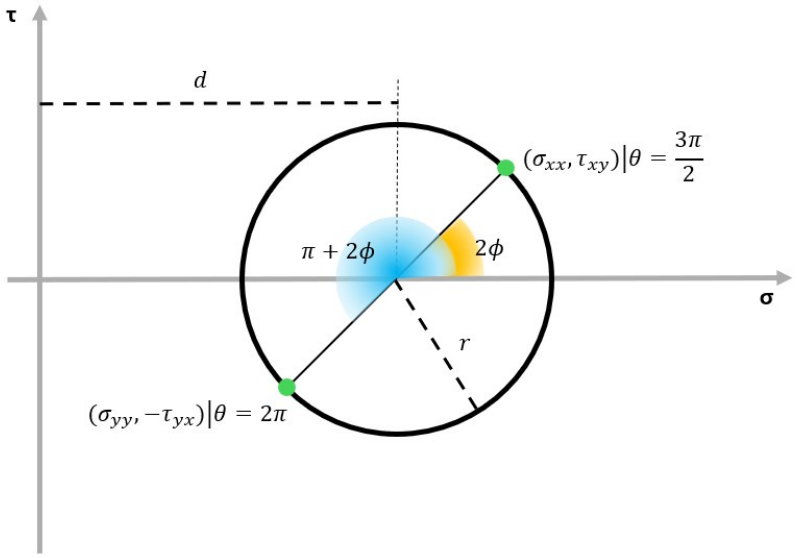

Figure II.2 Graphical representation of the force balance equation along inclined cutting planes, evaluated involving the angle θ equal to 3π / 2 and 2π

The Mohr circle intersects the horizontal axis at two distinct points, corresponding to the stresses acting on the principal planes. These planes are orthogonal to one another, since on the Mohr circle, they are placed at an angle π on the circle of Mohr and are characterized by the absence of shear stresses. The normal stresses acting on these planes are referred to as principal stresses. The larger of the two is termed the major principal stress, denoted by σ_1, while the smaller is the minor principal stress, denoted by σ_2. These values can be obtained directly from eqs. (43) and (44).

$$\sigma_1 = d + r \tag{45}$$

$$\sigma_2 = d - r \tag{46}$$

It should be emphasized that the orientation of the principal planes is not fixed; rather, it may evolve over time in response to the deformation or movement of the solid. This dynamic behaviour must be considered when analysing stress distributions in materials subjected to varying load conditions.
To construct a Mohr stress circle, it is essential to define at least two numerical values: the major principal stress σ_1 and the minor principal stress σ_2. The position and size of the circle depend directly on the magnitude of the applied

normal load, which influences the value of σ_1, the radius of the circle, and consequently σ_2. It is important to recognize that for any given value of σ_1, an infinite number of circles could theoretically pass through that point unless a second stress value is specified. Therefore, the Mohr circle can only be uniquely defined when both principal stresses are known.
From a practical standpoint, determining both principal stresses may be challenging, particularly in experimental setups. For this reason, it is common practice to refer only to the major principal stress when characterizing the stress state. In the procedure developed within this thesis, a simplification is introduced during the compression of the sample, as depicted in Figure II.1. Since the lid applies only to normal stress and no shear stress, it is assumed that the major principal stress corresponds to the vertical load exerted by the weight of the applied mass, divided by the cross-sectional area of the lid. This assumption allows for a direct and unambiguous determination of the major principal stress and its associated principal plane.

II.1.2. Solid mobilization

Within the same $\sigma - \tau$ diagram, which plots normal stress against shear stress, it is possible to represent the conditions under which a solid begins to flow, that is, the transition from elastic to plastic bulk deformation. Experimentally, these conditions can be estimated by identifying the point at which the applied shear stress equals the shear strength of the material. When this threshold is reached, sliding occurs along a specific internal plane, initiating flow. The yield condition of the material varies depending on the magnitude of the applied normal stress. If the relationship between normal stress and shear strength follows a linear trend, the material is classified as a Coulomb material. The line that connects the yield points under varying normal stresses is referred to as the yield locus.
A linear yield locus can be described by its slope, represented by $\tan\alpha$, where α is called the angle of internal friction, and the intersection between the yield locus and the vertical axes, the corresponding value of τ is called cohesion, indicated in this labour with the capital letter C, and they can be connected to normal stress and the shear stress following the linear eq. (47).

$$\tau = \tan\alpha \cdot \sigma + C \tag{47}$$

The angle of internal friction represents a key index of a solid's resistance to flow. It is one of the principal parameters required in the design and engineering of equipment for handling bulk solids, as it provides critical information about the shear stress necessary to maintain particle movement under a given compressive load. This parameter is influenced by several intrinsic properties of the material, including particle shape, size distribution, surface roughness, and packing density. In general, materials composed of irregularly shaped and densely packed particles exhibit a greater tendency to

interlock compared to those composed of lighter, more spherical particles. This interlocking effect increases frictional resistance and, consequently, the slope steepness of the yield locus.
Cohesion is another fundamental parameter in the design and analysis of bulk solid handling systems. It is defined as the shear strength of the material in the absence of any externally applied normal stress and serves as an indicator of the interparticle forces that promote structural integrity within the bulk phase. In most cases, cohesion arises from van der Waals forces, electrostatic interactions, and capillary bridges formed in the presence of moisture [32], [33]. The significance of cohesion becomes particularly pronounced as particle size decreases, due to increased surface area and proximity between particles. Additionally, cohesion is sensitive to temperature variations, which may activate or suppress secondary phenomena that influence interparticle bonding. A more detailed discussion of these effects is provided in Section II.1.4.

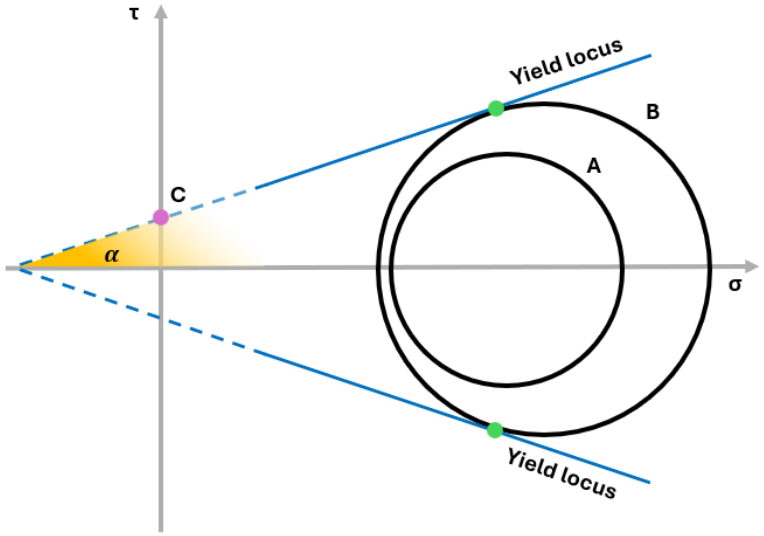

*Figure II.3 Yield locus and Mohr circles representation on $\sigma - \tau$ diagram. **A)** Graphical representation of the state of stresses in an elastically deformed solid condition **B)** Configuration required for a plastic transition and the onset of flow. Green dots indicate the two solutions for incipient flow. The purple dot is the yield locus intercept at the cohesion value. Orange filling marks the angle of internal friction.*

Figure II.3 illustrates the yield locus alongside two Mohr circles. The dotted portion of the yield locus represents a region where deviations from linearity may occur in real material. The relative position of the Mohr circle and the yield locus is related to the mechanical response of the solid under stress.
In the figure, the Mohr circles depicted correspond to the stress states at two distinct mechanical behaviors of the bulk solid. Circle A does not touch the yield locus, indicating that the shear stress in any plane is insufficient to initiate flow. The material behaves as an elastic solid.

In contrast, Circle B is tangent to the yield locus, meaning that the shear stress on the shear plane corresponding to the tangence points is equal to the shear strength of the material. This tangency implies the existence of a cutting plane oriented at an angle 2ϕ with respect to the direction of the major principal stress, along which the material is fully mobilized. In this state, the solid undergoes deformation and flow. In other words, the shear stress applied is equal to the shear strength of the material, and therefore the solid is fully mobilised along this plane.
It is important to emphasize that a Mohr circle intersecting the yield locus is physically inadmissible. Once the shear stress exceeds the yield strength, the material transitions into a flowing state, thereby preventing the persistence of a stress condition that would correspond to an intersection. The onset of flow inherently alters the stress distribution, ensuring that such a configuration cannot be achieved within the solid.

II.1.3. Measurement of flow properties

From the combined analysis of yield loci and Mohr stress circles, several key parameters governing the flow behaviour of bulk solids can be determined. These include the unconfined yield strength, the angle of internal friction, the effective angle of internal friction, cohesion, and bulk density [34], [35], [36]. Each of these parameters is strongly influenced by intrinsic material properties such as particle size distribution, particle morphology [37], chemical composition, moisture content [38], temperature[5], and the duration of consolidation [38], [39], [40]. These factors represent the principal variables affecting flowability, and their individual quantification is often complex and time-consuming [41], [42], [43]. For this reason, simplified methodologies and appropriately designed devices are essential for the effective characterization of a solid's resistance to flow.
Underlying the experimental and theoretical approaches to flow characterization are two fundamental principles: the principle of dilatancy and the principle of friction mobilization [44], [45], [46].
The principle of dilatancy asserts that shear deformation of a bulk solid cannot occur without a corresponding volumetric expansion of the specimen. When shear stress is applied, particles that were previously in contact must rearrange and move relative to one another, creating conditions for particle motion. This rearrangement leads to an increase in void space and a reduction in bulk density, which is a prerequisite for sustained deformation .
The principle of friction mobilization states that, in a static bulk solid, the frictional forces between any two particles can vary from zero up to a threshold value determined by the normal force acting at the contact point. This threshold is related to the degree of consolidation of the material. Once the applied shear stress equals this threshold, relative motion between particles begins, initiating flow while maintaining contact. This transition marks the

onset of sliding along internal cutting planes and allows for further classification of the material's mechanical state. If the applied shear stress is insufficient to induce motion, the material remains in an elastic state. In this condition, particles retain their configuration, and the stress state can return to its original form upon removal of the load, without permanent deformation. Once flow begins, the material transitions from an elastic to a plastic regime, and deformation proceeds along with the activated cutting planes.
In conclusion, for the material to flow, the stress state must reach the threshold defined by the yield locus, and for flow to occur, the material must undergo expansion. This interdependence underscores the importance of both stress analysis and volumetric response in the study of bulk solid mechanics. These principles are used extensively in Section II.1.5.

II.1.4. Uniaxial compression tests

The experimental integration of Mohr stress circles and the yield locus can be effectively realized through a uniaxial compression test [47]. The complete procedure and the corresponding $\sigma - \tau$ diagram are illustrated in Figure II.4. A distinctive feature of this approach is that a single compressive force is applied vertically via a lid placed on the free surface of the solid specimen. During the test, a hollow cylinder with a cross-section area A is filled with a granular solid and subsequently compressed by a vertical load.
Assuming negligible gravitational effects and the absence of friction between the solid and the container walls or the lid, the vertical normal stress can be considered the major principal stress, while the horizontal normal stress, perpendicular to the direction of loading, represents the minor principal stress. This frictionless condition ensures that no shear forces act on the boundaries, allowing for a uniform stress distribution within the specimen. As a result, the stress state at any point inside the material can be represented by a unique Mohr circle. Following the consolidation phase, Figure II.5.A, the applied normal stress is reduced to zero before proceeding to the next steps.

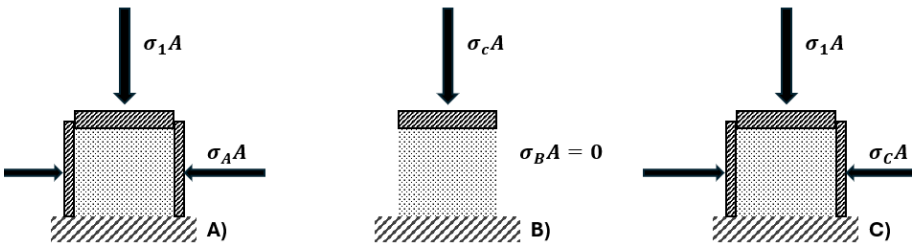

Figure II.4 Schematic representation of the uniaxial compression test. ***A)*** *Consolidation of the solid under the maximum compressive stress to be investigated.* ***B)*** *Flow condition of the unconfined material.* ***C)*** *Testing configuration to determine internal shear conditions for a consolidation stress between the maximum and the unconfined limit.*

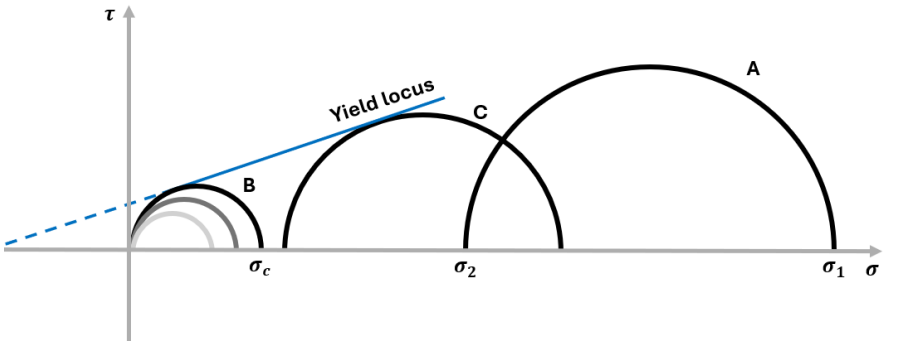

*Figure II.5 Stress representation of the consolidation and flow conditions illustrated in Figure I.4. . **A)** Consolidation state of stress of the material. **B)** State of stress in an unconfined sample, with grey Mohr circles indicating stress states not involving material flow. **C)** state of stress in an internal shear under horizontal constraint in the uniaxial experiment*

Case B in Figure II.5 depicts the condition in which, after consolidation, the cylinder is removed, and the specimen is subjected to an increasing vertical load. This results in a progressive increase in the diameter of the corresponding Mohr circle. Under these conditions, both the normal and shear stresses acting along the vertical surface are zero, and the representative point on the Mohr circle passes through the origin of the $\sigma - \tau$ diagram, corresponding to the minor principal stress.

As the load increases, the Mohr circle expands until it eventually becomes tangent to the yield locus. Prior to reaching this state the Mohr circles lie entirely beneath the yield locus, indicating that the material is undergoing plastic deformation without initiating flow. When the Mohr circle touches the yield locus, the material begins to flow along an internal cutting plane inclined at an angle α, marking the onset of plastic deformation of the specimen.

In the literature, the condition marking the onset of flow in a bulk solid is called incipient flow [34], [48]. According to the principles outlined in Section II.1.3, this transition is characterized by a progressive volumetric expansion of the material. In its initial phase, the deformation is elastic, allowing the particles to slightly separate and increase the interstitial space without altering their relative configuration. As the applied stress continues to increase and reaches the yield locus, the material begins to deform plastically. This results in the activation of internal cutting planes along which the solid flows, realizing a full mobilization. In addition, the major principal stress at which flow begins in a specimen that is not laterally confined is termed the unconfined yield strength, denoted as σ_c. This parameter is one of the most critical descriptors of a solid's flow behaviour and is essential for the design and analysis of bulk handling systems.

Case C in Figure II.5 illustrates the condition in which, in addition to the vertical compressive stress, a horizontal stress is also applied to the specimen. As in the previous configuration, the vertical stress is progressively increased

until the onset of yielding is observed, once a horizontal stress, lower than σ_2 applied during consolidation, is fixed. The presence of horizontal confinement alters the internal stress distribution, resulting in a modified stress state that influences both the shape and position of the corresponding Mohr circle.
Uniaxial compression tests performed under varying consolidation stresses yield distinct yield loci and associated Mohr circles. Each test reflects a unique combination of principal stresses, and the resulting data provide insight into the material's shear strength under different consolidation conditions, thereby aiding comprehension of solid flow behaviour and the determination of key parameters such as cohesion and internal friction.

II.1.5. Shear tester procedure

The uniaxial compression method, while conceptually straightforward, is not practical for precise sample preparation nor for accurately measuring low values of unconfined yield strength. To overcome these limitations, various devices and procedures have been developed and refined over time to achieve the same objective. These methods follow a standardized sequence of two shear-based steps: the consolidation phase, commonly referred to as preshear, and the subsequent shear to failure phase.
Depending on the geometry of the device and the direction of applied shear, it is assumed that particle movement occurs predominantly within a defined planar region known as the shear zone [49], and since we apply both a normal and a shear stress on the same surface, the vertical stress can no longer be considered the greater principal stress. Throughout the procedure, shear stress is recorded as a function of time [50]. Figure II.7 provides a schematic representation of this testing sequence.

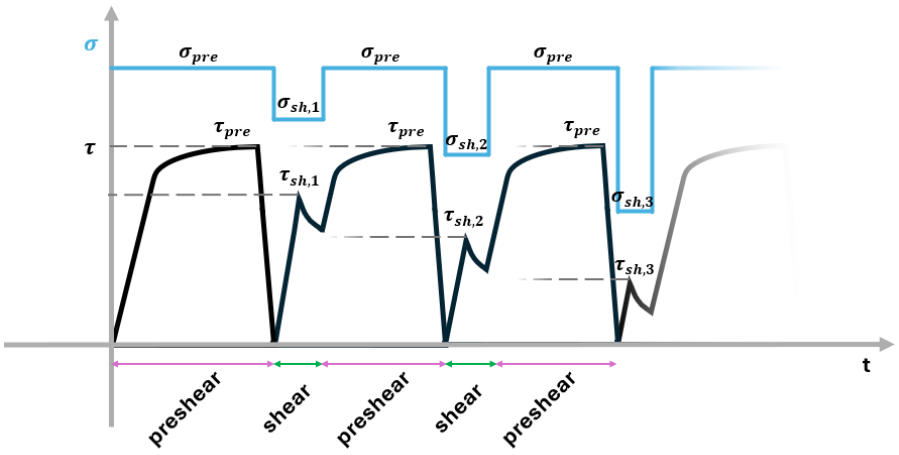

Figure II.6 Time-dependent representation of normal and shear stress during shear tests. Normal stress is shown in blue, shear stress in black. The graph illustrates both pre-shear and shear phases, with compressive loading applied during the decreasing shear phase.

In the typical setup, the granular material is placed within a trough and compressed vertically by a load applied through a lid on the free surface. Shear is then induced by applying a horizontal force to the lid [51]. Initially, the specimen is loosely packed, allowing particles to rearrange and rotate freely. As a result, the measured shear stress and, consequently, the frictional resistance are initially low. With continued shear, the material is progressively compacted, increasing interparticle contact and frictional forces. This process leads to a rise in both shear stress and bulk density until a steady-state condition is reached. At this point, the particles along the cutting plane are fully mobilized, and the frictional resistance reaches its maximum relative to the applied normal load. This condition indicates plastic deformation and defines an underconsolidated specimen. Typically, higher normal loads result in higher steady-state shear stresses. The pair of values representing the normal stress during preshear σ_{pre} and the corresponding steady-state shear stress τ_{pre} can be plotted on a $\sigma - \tau$ diagram.

Once consolidation is complete, the shear stress is reduced to zero before initiating the shear-to-failure step. During this phase, the previously consolidated specimen is subjected to a lower normal load $\sigma_{sh} < \sigma_{pre}$ resulting in a reduced shear force requirement. Initially, the measured shear stress reaches a peak due to the residual internal structure formed during consolidation. This peak reflects the frictional resistance needed to overcome the equilibrium configuration established under the higher consolidation stress. The point at which this maximum is reached marks the failure condition, indicating the onset of particle motion and the transition from elastic to plastic behaviour.

Following failure, the material expands and rearranges under the reduced normal load, establishing a new steady-state flow condition along the cutting plane. This phase is characterized by lower shear stress and a decrease in bulk density. The stress pair at failure, comprising the applied normal load σ_{sh} and the corresponding shear stress τ_{sh}, can also be plotted on the $\sigma - \tau$ chart.

It is well established that the flow behaviour of bulk solids is history dependent. The consolidation phase determines the internal structure, contact network, and shear strength of the specimen. Repeating the preshear step under identical conditions yields reproducible steady-state behaviour, making preshear an essential procedure for eliminating variability due to sample preparation, such as non-homogeneity, and ensuring comparability across tests.

To construct a complete yield locus, a series of tests must be conducted by alternating the preshear and shear-to-failure steps. Each test explores a different failure condition by varying the normal stress applied during the shear phase. The curve connecting the failure points on the $\sigma - \tau$ diagram defines the yield locus, which is specific to the consolidation state established during preshear.

II.1.6. Experimental estimation of flow parameters

As previously discussed, several parameters describing the frictional behaviour and flowability of bulk solids can be estimated or extrapolated from the $\sigma - \tau$ diagram. Among these, the unconfined yield strength σ_c is particularly significant. It is defined as the compressive stress at failure during a uniaxial compression test. Although this parameter cannot be measured directly through shear testing because true uniaxial conditions cannot be replicated, it can be extrapolated from the yield locus by constructing a Mohr circle that passes through the origin of the $\sigma - \tau$ axes and is tangent to the yield locus. The resulting value of σ_c represents one of the key indicators of a material's resistance to flow. Once σ_c is determined, a derivative parameter, known as flow factor ff_c, can be calculated. It is defined as the ratio between the major principal stress applied during the preshear phase and the unconfined yield strength. For each yield locus, a unique value of ff_c exists. According to the Jenike classification, presented in Table II.1, particulate solids can be categorized into five distinct classes based on their flowability.

Table II.1 Flow property behaviour for powders according to Jenike's classification [47].

Flow behaviour	Flowability
Not flowing	$ff_c < 1$
Very cohesive	$1 < ff_c < 2$
Cohesive	$2 < ff_c < 4$
Easy flowing	$4 < ff_c < 10$
Free flowing	$10 < ff_c$

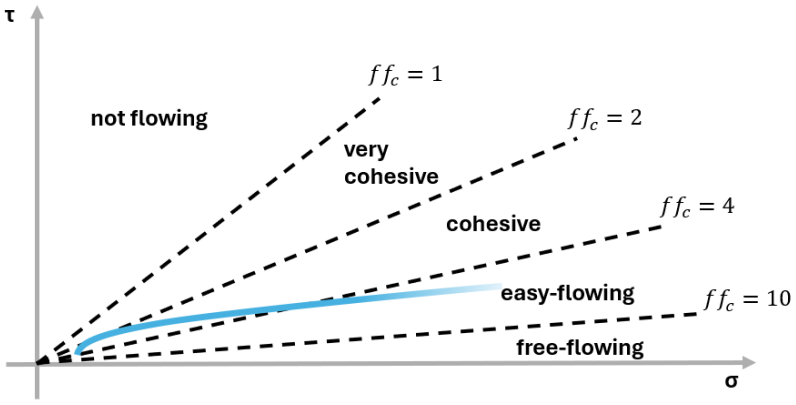

Figure II.7 Jenike powder flow classes represented on the $\sigma - \tau$ diagram. The blue curve illustrates a possible flow function curve for a generic material.

Materials exhibiting easy-flowing or free-flowing behaviour under the relevant process conditions are straightforward to handle, ensuring reliable

flow and efficient material management. In contrast, materials with lower flow factors may require additional design considerations or preventive measures to avoid flow obstructions, arching, or other undesirable phenomena that compromise process performance. For a given material, different values of ff_c can be obtained by varying the consolidation conditions during testing. These values can be plotted on a $\sigma_c - \sigma_1$ diagram, where σ_1 represents the major principal stress during preshear. The curve connecting these points is referred to as the flow function, which characterizes the material's behaviour under different stress states. The flow function provides valuable insight into the material's response to consolidation and shear, and, although extrapolation must be approached with caution, it can be used to estimate flow behaviour under untested conditions. An example of a flow function is illustrated in Figure II.8. In summary, flowability provides a direct and practical measure of a solid's handling characteristics, serving also as a critical parameter in the design and optimization of bulk material processing systems.

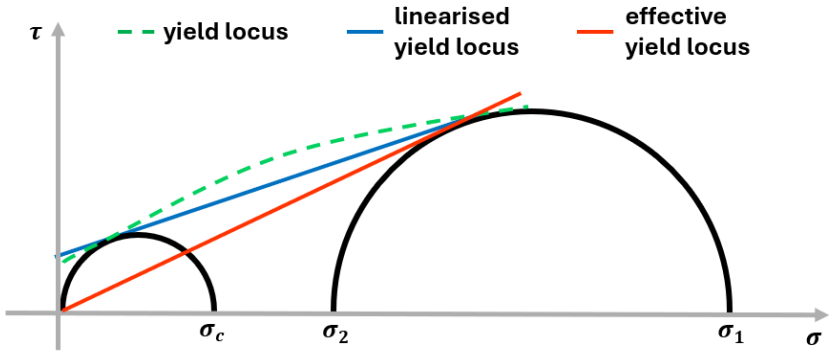

Figure II.8 Schematic representation of yield locus processing based on observed experimental behaviour (in green).

The angle of internal friction, denoted as α, is defined as the slope of the yield locus. In general, the yield locus exhibits a convex shape, which implies that the angle of internal friction varies depending on the position along the curve. For this reason, the most accurate definition considers α as the local slope of the yield locus with respect to the normal stress. However, for practical applications, the yield locus is often approximated by a straight line, the linearized yield locus, and the corresponding angle is used as a representative value of internal friction for design and analysis purposes.

A further simplification involves the construction of a straight line that passes through the origin and is tangent to the Mohr circle associated with the consolidation phase. This line is known as the effective yield locus, and its slope is termed the effective angle of internal friction, denoted as ϕ_e. Since the Mohr circle used in this construction represents the stress state during steady-state flow under consolidation, ϕ_e serves as an index of the internal

friction during flow. It also defines the relationship between the major and minor principal stresses of the consolidation Mohr circle, as expressed in eq. (49).

$$\sin \phi_e = \frac{\sigma_1 - \sigma_2}{\sigma_1 + \sigma_2} \tag{48}$$

$$\frac{\sigma_1}{\sigma_2} = \frac{1 - \sin \phi_e}{1 + \sin \phi_e} \tag{49}$$

In addition to internal friction, other parameters such as tensile strength and cohesion play a significant role in characterizing the mechanical behaviour of bulk solids. These parameters are more challenging to measure directly using standard experimental apparatus.

Tensile strength is defined as the stress required to separate a layer of material in the absence of shear forces. The tensile strength is higher when the cohesion between particles is higher. In fact, the forces that tend to hold them together resist traction. Due to the inherent difficulty in applying tensile loads to granular or powdered systems, where particles tend to separate rather than sustain traction, this parameter is typically extrapolated from the yield locus. Specifically, it corresponds to the intercept of the yield locus with the horizontal axis of the $\sigma - \tau$ diagram.

Cohesion, on the other hand, has been defined as the intercept of the yield locus with the shear stress axis, and it is a measure of the interparticle forces that maintain structural integrity within the bulk phase. These cohesive forces arise from a combination of physical and physicochemical interactions [52], including van der Waals attractions, electrostatic forces [53], and capillary bridges [54] formed in the presence of moisture. The magnitude of cohesion is highly sensitive to particle size: as particle size decreases, the surface area-to-volume ratio increases, enhancing the relative contribution of surface forces [55]. Consequently, fine powders tend to exhibit higher cohesion than coarser granular materials.

Environmental conditions also play a critical role in determining cohesion. Elevated humidity levels facilitate the formation of liquid bridges between particles, enhancing capillary forces and increasing overall cohesion. Temperature fluctuations can either promote or inhibit bonding mechanisms, depending on the material and the surrounding atmosphere. Additionally, the degree of compaction influences cohesion: greater compaction increases particle contact area, thereby strengthening interparticle interactions.

It is important to note that cohesion inversely affects flowability. As cohesion increases, the resistance to particle movement increases, making the material more prone to arching, rat-holing, or other flow obstructions. Therefore, understanding and controlling cohesion is essential for the design of efficient bulk handling systems, especially when dealing with fine powders or materials sensitive to environmental conditions.

II.2. Effects of the Temperature on the flowability of iron ore pellets

An increase in temperature can significantly alter the flowability of a bulk solid, depending on its chemical composition and structural characteristics. In the region of interest for pelletized materials, characterized by elevated temperatures and compressive stresses, both interparticle friction and, consequently, the angle of internal friction may vary due to surface transformations, particle degradation, and mechanical breakage. Cohesion may also change under these conditions.

As discussed in Paragraph 2.1.2, cohesion plays a critical role in the flow behaviour of fine powders due to their small particle size. One might assume that, given the relatively large size of the treated pellets (typically 10–16 mm), cohesion becomes negligible. This assumption is based on the fact that cohesive forces, primarily van der Waals, electrostatic, and capillary interactions, are surface-dependent and tend to be overshadowed by volume forces as particle size increases. However, this simplification does not hold at high temperatures. In reality, additional thermally activated phenomena such as sticking, clustering, sintering, neck growth, softening, and partial melting can occur, significantly influencing the cohesive behaviour of industrial-scale iron ore pellets.

Regarding the behaviour of iron ore pellets under operating conditions relevant to the direct reduction (DR) process, extensive research has been conducted on various aspects, including reaction kinetics, fluid dynamics, and thermodynamics, both for individual particles and bulk systems. Surface properties of reduced and unreduced pellets have also been examined. However, despite this body of work, a comprehensive and systematic investigation into the flow properties of solids under DR conditions, particularly at elevated temperature, remains lacking in the literature. The study by Man et al. [56] provides a valuable example of how elevated temperatures influence the quality and microstructure of iron ore pellets. Specifically, the research examined the effect of pellet size on the properties of pellets produced from a mixed hematite-magnetite ore. Pelletising tests were performed on samples within the 10-12.5 mm size range, and advanced imaging techniques, including electron and optical microscopy, were employed to characterize hematite distribution, pore density, and silicate melt behaviour. The experiments were carried out under controlled conditions at 1300 °C and 0.21 atm oxygen partial pressure. The results revealed significant variations in pellet quality depending on both particle size and processing parameters. These findings underscore the critical importance of precise control over pellet dimensions and thermal treatment during the pelletisation process, which directly impacts the structural integrity and reactivity of the pellets. Optimizing these variables is essential for enhancing the overall

efficiency of the reduction process, particularly under the severe thermal and mechanical conditions typical of industrial operations.

Complementary insights were provided by Lu et al. [57], who investigated the role of high-temperature interactions in enhancing the softening and melting behaviour of iron ore materials within the blast furnace cohesive zone. Their study involved five single iron ores and four mixed charges of the reactor, tested at temperatures up to 1600 °C. Results demonstrated that thermally induced interactions increase the extension of the cohesive zone by modifying its thickness, position, and shape. These findings highlight the critical role of temperature and material composition in governing the mechanical and thermal response of iron-bearing materials under extreme conditions.

Further research by Matsumura et al. [58] investigated the influence of raw material composition on the softening behaviour and reducibility of sinters at high temperatures. By systematically varying the concentrations of key oxides, CaO, SiO_2, Al_2O_3, MgO, and FeO, the study identified critical relationships between chemical composition and the mechanical response of sinters during reduction. These insights offer valuable guidance for tailoring sinter formulations to enhance performance in thermally demanding environments. The experimental campaign included sinter samples produced with varying proportions of limestone, serpentine, and coke breeze, as well as different iron ore sources. Tests were conducted under controlled conditions to precisely evaluate the impact of compositional changes. The methodology involved a detailed analysis of sinter permeability and the rate of reducing agent consumption. By optimizing the chemical makeup, the researchers aimed to improve sinter behaviour in blast furnace operations, ultimately contributing to increased productivity and process efficiency. The findings underscore the importance of precise control over raw material composition to improve softening and melting characteristics, parameters that are linked to the stability and efficiency of the cohesive zone within the furnace.

A complementary work by Xiao et al. [4] focused on the role of hydrogen in modifying the softening–melting behaviour of iron-bearing materials in the blast furnace. The study explored the effect of varying hydrogen volume fractions (0%, 5%, 10%, 15%) within a simulated furnace atmosphere, targeting the softening-melting zone typically ranging from 1200 °C to 1500 °C. Coke was introduced into the iron ore charge, and hydrogen was added to the standard gas mixture, replacing nitrogen, to create a hydrogen-rich environment. Using a Softening and Melting apparatus, the researchers observed that hydrogen accelerated the reduction process from Fe_2O_3 to Fe_3O_4, promoted the formation of low-melting-point phases, and lowered the softening onset temperature. Additionally, hydrogen improved the dynamics of slag formation, contributing to more efficient melting behaviour. These results demonstrate that hydrogen can effectively enhance blast furnace performance, particularly in the softening-melting zone. The study highlights the transformative potential of hydrogen-rich atmospheres in improving

thermal efficiency, reducing energy consumption, and enabling more controlled material behaviour under extreme conditions.

Wu et al. addressed the issue of raw material suitability for modern blast furnace operations (Wu et al., 2009)(Wu et al., 2009), who evaluated the performance of natural lump ores within a mixed feedstock. The study assessed various metallurgical properties of lump ores and found that, while they generally meet the operational requirements of contemporary blast furnaces, their softening and melting behaviours remain suboptimal. Experiments were conducted under high-temperature conditions representative of the upper zones of the blast furnace, with particular attention to the interaction between sinter and lump ores. A key finding of the study was that combining lump ores with sinter significantly improved the softening and melting characteristics of the lump fraction. This enhancement was attributed to the formation of a more cohesive and thermally stable structure of the solids inventory, which facilitated better heat transfer and mechanical integrity. The results suggest that, despite initial limitations, lump ores can be effectively integrated into modern blast furnace operations when used in conjunction with sinter. The study concludes that mixed feedstock practice offers a viable strategy for optimizing furnace performance and material utilization.

In a related investigation, Silvia et al. [60] explored the effect of ternary basicity on the softening and melting behaviour of iron ore–fluxed pellets. The researchers examined pellets with varying basicity levels (0.8, 1.0, and 1.2) and conducted high-temperature experiments ranging from 1200 °C to 1500 °C to simulate blast furnace conditions. Advanced analytical techniques were employed to measure key parameters, including softening temperature, reduction degree, and gas pressure drop across the burden. The study revealed that increasing the MgO content in the pellet matrix improved high-temperature performance, particularly in terms of reduction kinetics and resistance to deformation. The presence of basic fluxes, especially CaO and MgO, enhanced the structural stability of the pellets, resulting in a more cohesive and resilient burden. Compared to acidic pellets, basic fluxed pellets exhibited superior softening and melting characteristics, making them more suitable for demanding furnace environments. The authors concluded that optimizing ternary basicity is a critical factor in improving blast furnace efficiency, burden integrity, and overall process reliability.

The role of hydrogen in enhancing the reduction and softening-melting behaviour of ferrous charges was investigated by Qie et al. [61], who examined the impact of hydrogen addition in a gas-injection blast furnace setup. The study explored hydrogen concentrations ranging from 0% to 15%, with experiments conducted at temperatures between 1200 °C and 1500 °C to simulate operational furnace conditions. Key parameters measured included softening temperature, melting temperature, and reduction degree. The results demonstrated that increasing hydrogen content significantly improved the reduction rate of iron oxides, with optimal performance observed in the 10-

15% hydrogen range. Hydrogen addition was found to widen the softening zone and narrow the melting zone: an effect beneficial for smelting efficiency. These findings suggest that future blast furnace designs should incorporate hydrogen injection systems to optimize reduction kinetics and thermal behaviour. However, such integration would require adjustments to temperature control strategies and the development of advanced equipment capable of handling variable gas compositions. The improved reduction efficiency associated with hydrogen use also contributes to lower fuel consumption and reduced CO_2 emissions, aligning with broader sustainability objectives in metallurgical processing.

In a complementary study, Natsui et al. [62] developed a dynamic model to investigate the plastic deformation behaviour of sintered iron ore under high-temperature reduction conditions. The researchers focused on temperatures ranging from 1200 °C to 1400 °C and employed a Bingham plastic fluid model enhanced with a structural force term to simulate the softening response of sintered ore. The material exhibited a dual-phase structure, with a low-melting-point molten slag core surrounded by a solid iron-rich shell. Experiments were conducted in a high-temperature furnace, using a reduction gas mixture containing CO and H_2 to replicate blast furnace atmospheres. By varying the degree of reduction, the study revealed that higher reduction levels led to increased plastic deformation of the sintered ore. The model accurately predicted deformation behaviour across different conditions, offering valuable insights into the mechanical evolution of burden materials during reduction. These findings underscore the importance of understanding the interplay between reduction degree and deformation mechanics, which is essential for improving the stability and efficiency of blast furnace operations.

The kinetics of iron ore pellet reduction using hydrogen were recently investigated by Patisson et al. [63], who explored its application in steelmaking processes. Reduction experiments were conducted at temperatures ranging from 800 °C to 1000 °C, employing pure hydrogen as the reducing agent. The study demonstrated that hydrogen enables significantly faster reduction kinetics compared to conventional carbon monoxide, achieving complete metallisation of iron ore. This acceleration simplifies the direct reduction process and supports the feasibility of a more compact shaft furnace design. The authors provided a detailed physicochemical analysis of the mechanisms of iron oxide reduction, identifying key factors that influence industrial scalability. Mathematical modelling at both the pellet and reactor scales further validated the efficiency and practicality of hydrogen-based reduction, reinforcing its potential for future low-carbon steelmaking technologies.

Despite extensive research on iron ore pellets under various thermal and chemical conditions, a comprehensive understanding of how these factors jointly affect flow behaviour during shaft furnace processing is still lacking. This thesis aims to address that gap by focusing on the combined influence of

temperature, material composition, and interparticle forces; elements that are critical to both the environmental and operational efficiency of steelmaking.
As reported, hydrogen-based reduction offers a promising alternative to traditional carbon monoxide processes. It enables faster reaction kinetics, improved energy efficiency, and produces water vapour as the only byproduct. These advantages make hydrogen steelmaking a sustainable and forward-looking solution for reducing the carbon footprint of the industry. While existing research provides valuable insights into microstructural evolution, softening behaviour, and reduction mechanisms, it often overlooks the operational flow properties of bulk solids, especially under the dynamic conditions of the direct reduction (DR) process. As discussed, high-temperature phenomena such as sintering, clustering, and surface transformations can significantly alter cohesion and internal friction, directly impacting flowability. A systematic investigation into these thermally activated mechanisms, particularly their influence on cutting plane activation, bulk density evolution, and yield locus behaviour, is essential for advancing predictive control of solid flow in both the DR shaft furnace and other systems that require the use of iron ore pellets.

II.3. Commercial apparatus limitations

To characterize the flow properties of powders, a wide range of equipment and procedures has been developed and continuously refined. Among these, shear testers are the most commonly used and are typically classified into two main categories based on the direction of applied motion: translational and rotational shear testers.
Regardless of the device type, the testing procedure follows the two-step approach described in Section 2.1.5, comprising a consolidation (preshear) phase followed by a shear-to-failure phase. This methodology is adapted to suit the specific mechanical configuration and operating principles of each device.
Despite their differences, both types share a common core component: the shear cell. This typically consists of a trough that holds the powder sample and a lid that applies a compressive load to the material. The direction of relative motion between the trough and the lid determines the type of shear applied: translational or rotational.

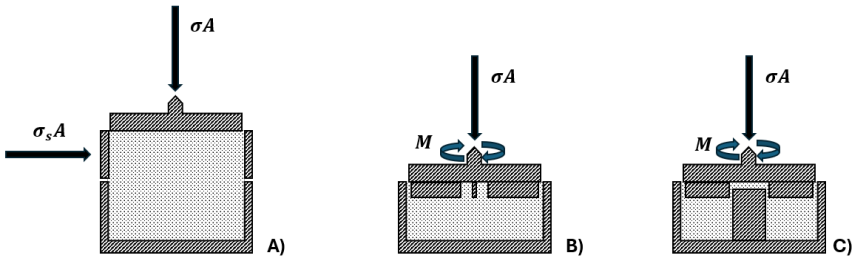

Figure II.9 Cross-sectional view of different shear cell configurations. ***A)*** *Jenike's translational shear cell.* ***B)*** *Rotational shear cell with cylindrical section.* ***C)*** *Rotational shear cell with annular section. The product σA denotes the applied normal force, while M indicates the torque measured during the test.*

A well-known example of a translational shear tester is the Jenike shear cell, one of the earliest devices developed to assess the flowability of bulk solids [64], [65], [66]. As illustrated in Figure II.9.A, the Jenike cell comprises a cylindrical trough and a coaxial ring with identical internal and external diameters, stacked vertically. The powder sample is placed between these rings, and a lid is positioned on the free surface to distribute the applied load uniformly via a hanger mechanism.

During sample preparation, the two rings of the Jenike shear cell are spaced at least 0.2 mm apart to prevent mechanical interference and friction between components. This spacing is achieved by slightly rotating and lifting the upper ring after the trough has been filled with the powder sample. Once the setup is complete, the measurement begins by applying a normal force to the wall of the upper ring using a stem that moves at a constant speed. This procedure induces relative motion between the two rings. Throughout the test, it is assumed that a shear plane forms at the horizontal interface between the rings, allowing for controlled evaluation of the material's shear response.

One of the main limitations of the Jenike shear cell is the limited shear displacement achievable during testing. Specifically, the maximum displacement before the specimen exits the trough is approximately twice the thickness of the trough wall. As a result, each point on the yield locus requires a separate sample preparation, making the process highly time-consuming and labour-intensive.

Due to these constraints, attention has progressively shifted from translational to rotational shear testers, which offer greater flexibility and efficiency. Rotational devices overcome the displacement limitation by enabling continuous shear deformation, allowing for the determination of a complete yield locus using a single sample.

In rotational shear testers, the shear cell typically consists of a cylindrical trough that rotates at a constant angular velocity and a stationary lid that applies a uniform normal stress to the powder specimen. The rotation induces

shear deformation within the material, and the resulting torque M, which corresponds to the shear stress, is measured via load cells connected to the lid. Because of the cylindrical geometry, the shear stress varies with radial distance: being zero at the centre and increasing toward the periphery. To improve measurement accuracy, a toroidal trough and an annular lid are commonly used. When the ratio of the inner to outer diameters of the lid approaches 0.5, and the procedure is properly executed, the results closely match those obtained with the Jenike cell.
Among the most widely adopted rotational shear testers on the market are the Schulze Ring Shear Tester [50], the Brookfield Powder Flow Tester [67], and the Anton Paar Powder Shear Tester [68]. These devices, widely used and compared in literature [51], [69], allow for effectively unlimited shear displacement, which is essential for reaching steady-state flow conditions and constructing a complete yield locus from a single specimen.

*Figure II.10 Photographic images of three major commercial instruments used to characterize solid flow properties. **A** Schulze Ring Shear Tester. **B** the Brookfield Powder Flow Tester. **C** and the Anton Paar Powder Shear Tester.*

The Schulze Ring Shear Tester, available in models such as the RST-01 and RST-XS, represents a modern evolution of the Jenike methodology, adapted for rotational shear testing. At the heart of the device is an annular shear cell, composed of a toroidal trough that holds the powder sample and a matching annular lid. The lid of the Schulze shear cell is equipped with radially arranged vanes that play a critical role in the measurement process. These vanes typically have a rectangular cross-section, approximately 1 mm thick and 5 mm high, with their width determined by the specific lid geometry. Positioned on the surface in contact with the powder sample, the vanes create localized zones of stagnant material between them. This design ensures that the measured torque corresponds primarily to the shear deformation occurring at the tip of the vanes, where the active shear plane is assumed to form. By isolating the deformation zone in this manner, the system minimizes interference from peripheral material movement and enhances the accuracy of shear stress measurements. Unlike the trough, the lid remains stationary as it is mechanically decoupled from the drive system and linked to two load cells.

This configuration allows precise application of a uniform vertical stress across the specimen and torque measurement using only the lid.

The Schulze shear testers are widely recognized for their ability to simulate a broad range of operating conditions, particularly due to their capacity to apply high compressive stresses. The larger RST-01 model, despite its compact shear cell design, can reach normal stresses up to 55 kPa, exceeding the capabilities of most commercially available devices. This feature makes it well-suited for replicating the medium-to-high pressure environments typical of industrial hoppers and storage systems. Cell volumes vary depending on the model and intended application. The RST-XS, designed for research and testing with limited material availability, accommodates sample volumes from 3.5 mL to 70 mL, with 30 mL being the standard. In contrast, the RST-01 supports larger-scale testing with cell capacities up to 900 mL, making it ideal for bulk material characterization. While standard models are configured for ambient temperature operation, specialized versions have been developed to extend the testing range to elevated temperatures up to 600 °C.

The Brookfield Powder Flow Tester (PFT) is designed to evaluate powder flow properties under low to medium compressive stress conditions. Like other rotational shear devices, it features an annular trough to contain the powder sample, with two available cell volumes: a standard 263 mL cell and a small-volume 43 mL option for limited material availability. What distinguishes the PFT is its specialized shear head, which has a vaned or V-shaped profile and is directly connected to the main drive. During testing, this head performs a helical motion, combining vertical compression with rotational shear. This dual-action movement consolidates the sample while simultaneously inducing shear deformation, simulating realistic handling conditions. The device is primarily configured for ambient temperature operation, and its stress application range is more limited compared to high-pressure testers like the Schulze RST series. The maximum normal stress achievable depends on the cell configuration: approximately 13 kPa with the small-volume vane lid and approximately 5 kPa with the large-volume vane lid.

The Anton Paar Powder Shear Cell is designed for high-resolution powder flow characterization using minimal sample volumes, typically 4.3 mL or 18.9 mL, depending on the cell configuration. The system integrates with the Modular Compact Rheometer (MCR) series, which features an ultra-sensitive motor to drive the rotor and a highly accurate sensor to apply and monitor vertical compressive stress. A distinctive feature of this setup is its ability to apply high compaction stresses up to 110 kPa, suitable for simulating dense packing conditions. However, during the shear-to-failure phase, the system operates under lower normal stresses, typically up to 30 kPa, which is significantly below the capabilities of devices such as the Schulze Ring Shear Tester, which can reach up to 55 kPa. This feature limits the applicability of this tester for high-pressure industrial scenarios.

In terms of environmental control, the MCR series offers exceptionally precise temperature regulation, with accessories enabling testing from –160 °C to +980 °C. Additionally, the system supports active humidity control from 5% to 95% relative humidity, allowing researchers to simulate a wide spectrum of storage and processing conditions. This capability is particularly valuable for studying moisture-sensitive powders and caking phenomena. Despite its advanced environmental features and precision, the Anton Paar Powder Shear Cell is best suited for fundamental research, material development, and quality control under controlled laboratory conditions. Its limited shear stress range during failure testing makes it less appropriate for direct application in high-load industrial design, where devices like the Schulze RST series remain the preferred choice.

As discussed in subsequent sections, the operating conditions achievable with commercial shear testing equipment are insufficient to replicate the extreme environments associated with iron oxide reduction processes. Laboratory-scale devices currently available cannot simultaneously reproduce the combination of high normal stress, elevated temperatures, and large sample volumes, all of which are essential for investigating the flow behaviour of particulate materials under realistic process conditions. To bridge this gap, the development of a custom-built apparatus is necessary. Such a system must be capable of precisely controlling severe thermal and mechanical parameters, enabling the study of powder flow under conditions representative of industrial reduction processes. This need includes simulating the intense compaction, thermal gradients, and cohesive transformations that occur during direct reduction or blast furnace operations. Phenomena that cannot be adequately captured using existing commercial devices.

II.3.1. Effect of the Temperature on flow properties of solid materials

Research on powder flowability has traditionally relied on rotational shear cells, providing the benchmark for reproducible measurements of yield loci, flow functions, and unconfined yield strength under ambient conditions. Because of the limitations of commercial equipment, either it has been adapted or new prototypes have been presented. An example of the first category is the work of Tomasetta et al. [70], who developed the High Temperature Annular Shear Cell, a Schulze-like annular geometry capable of operating at temperatures up to 500 °C. Powders are confined in an annular ring, a lid applies normal load in the tens to hundreds of kilopascals, and the trough rotates quasi-statically. This innovation enabled direct measurement of yield loci, flow functions, and unconfined yield strength under realistic high-temperature conditions, applying the standard procedure and exceeding the limits of commercial equipment.

The same apparatus was used for further investigations involving FCC catalysts, corundum, and fly ash (materials with average particle sizes of 70 µm, 23 µm, and 10 µm, respectively), using a heated annular shear cell and subjecting the materials to a maximum temperature of 500°C [5]. They showed that changes in moisture content and surface forces significantly altered yield loci and flow functions. In a subsequent study [71], they linked measured cohesion and tensile strength to models of van der Waals and capillary forces, demonstrating that increased interparticle attraction at higher temperature directly translated into higher bulk strength and reduced flowability. Therefore, their findings revealed that increasing temperature generally reduces powder flowability by increasing interparticle cohesive forces. However, the magnitude of this effect varied significantly depending on the material's composition and morphology.

These observations are supported by the work of Ripp and Ripperger [72] who expanded the range of materials tested to include industrial powders, polymers, and food products in a Schulze ring shear cell with an integrated heating and cooling system. Operating with temperature from below ambient to above 200 °C, they found that warming reduced cohesion in some powders by eliminating capillary bridges, while in others it increased strength through softening or sintering. In addition, the experimental campaigns reveal a consistent trend of increased material strength at elevated temperatures.

Macrí et al. [73], using the High Temperature Annular Shear Cell, demonstrated that for synthetic rutile, with dimensions from 50 µm to 126 µm, cohesion values rose from approximately 1 kPa at ambient temperature to 3-4 kPa at 500 °C. This change was accompanied by an increase in the effective friction angle, shifting the material classification from "easy-flowing" to "cohesive".

Chirone et al. [74] analysed fine ceramic fractions (with dimensions between 40 µm and 50 µm) using the High Temperature Annular Shear Cell, observing that cohesion increased from a baseline between 2-3 kPa at ambient conditions to 5–6 kPa at 500 °C, resulting in flow function indices dropping below 4.

Using the same apparatus and materials, Macrí et al. [75] confirmed that under reactor-like conditions (up to 500 °C), both cohesion and tensile strength generally increased by factors of 2-3.

Testing at even higher temperatures, Gannoun et al. [76] examined $CaCO_3$ and CaO with mean particle size 20-50 µm up to 600 °C using the High Temperature Seville Powder Tester (HTSPT). Instead of relying on mechanical shearing, the HTSPT measures tensile strength using gas dynamics. The particle bed, placed on a distributor immersed in a furnace, is compacted by a downward gas flow or by gravity. By applying an upward gas flow, the force required to 'break' the bed is measured, thus measuring the tensile strength. This operates at temperatures up to 600°C and normal stresses less than 5kPa. They recorded a substantial rise in cohesion from about 1 kPa at ambient to 6 - 7 kPa at maximum temperature; where, consistent with

theory, finer particle fractions showed significantly higher cohesion and lower flowability than coarser fractions.
The major finding is represented by the effectiveness of dry coating additives. The addition of nanosilica coatings could reduce cohesion by 30-40%, improving the flowability of the solid.
Manokaran et al. [77] utilized both the Schulze ring shear tester and the Anton Paar Powder Cell to quantify the interplay between particle size and heat. Their data indicated that reducing particle size increased cohesion by approximately 20% and the friction angle of about 5°, with these effects further amplified by heating.
With a view to overcoming the conditions that can be tested with conventional equipment, in terms of flow properties, there is the work of Castellanos et al. [78] which introduces a centrifugal avalanche tester capable of probing flow properties at effective normal stresses below 1 kPa: a regime inaccessible to conventional shear cells. In this device, a vertical annulus of unconsolidated powder is rotated until centrifugal forces trigger avalanching, from which cohesion and friction are back-calculated using Coulomb's wedge theory. Tests were performed on spherical steel, ferrite, and magnetite beads to validate the method. Operating conditions allowed precise measurement of intrinsic cohesion values between 0.1 and 0.5 kPa and internal friction angles of 25-35°, far below the ranges accessible with standard testers. Results showed that even dry granular materials exhibit measurable cohesion at low loads, dictating whether they flow smoothly as avalanches or fail as cohesive clumps, and predictions of angle of repose matched independent drum experiments, confirming the accuracy of the approach.
Zoet et al. [79] extended ring shear testing to cryogenic regimes. The cryogenic ring shear device was developed to replicate the boundary conditions at the base of a glacier, where ice and sediment interact at the pressure-melting point, a regime that standard geotechnical shear testers cannot reproduce. The apparatus consists of a large annular shear cell housed in a walk-in freezer, shearing ice rings of 20 cm inner diameter, 60 cm outer diameter, and 20–30 cm height over a fixed bed of sediment or rock. It operates under vertical loads ranging from about 5 kPa to 915 kPa, simulating the overburden pressure of ice sheets, and shear velocities between 0.01 and 1000 m per year (equivalent to 3×10^{-10} - 3×10^{-5} m/s), covering both slow creep and surge events. Thermal control is achieved by submerging the chamber in a fluid bath that maintains the interface at the pressure-melting point, while transparent acrylic walls allow direct visualization of cavitation and till deformation. Experiments demonstrated the device's ability to transition from drained, frictional conditions to undrained states where meltwater accumulates, leading to liquefaction of subglacial till and catastrophic strength loss. Long-duration tests lasting weeks to months captured slow processes such as ice sintering and bed deformation. Overall, the instrument provides a controlled laboratory platform for deriving physical

laws of glacier sliding by independently varying stress, velocity, and temperature, offering critical insights for modelling glacier surges and ice sheet stability in climate projections.

Taken together, these studies provide a comprehensive picture of the development and design of equipment created to simulate specific conditions that cannot be replicated using conventional equipment, as well as the importance of such measurements. In fact, the materials studied, the configurations, the operating temperatures from below 0 °C to 600 °C, and the particle sizes from 40 µm to 250 µm lead to results that consistently demonstrate that cohesion, friction angle, tensile strength, and torque increase with finer particle size, higher temperature or greater consolidation, while coatings or moisture reduction can mitigate these effects.

II.3.2. Evolution of Pellet Properties Under Varying Operating Conditions

Within the metallurgical field, considerable attention has been devoted to understanding the phenomena governing the behaviour of pellets, sinters and lump ores, particularly with respect to temperature effects and the composition of the reacting gas mixture during their reduction inside the furnace. The literature has identified several operating conditions that trigger critical issues such as loss of mechanical strength, swelling, or the development of inter-particle cohesion. In contrast, the compressive load exerted on the burden during reduction, that arises from the weight of the overlying layers, has received comparatively little attention, despite its potential to modify the characteristic temperatures and gas compositions associated with these phenomena. A comprehensive description of the solid behaviour remains challenging, as the response depends not only on the chemical nature of the material but also on the specific characteristics imparted during pelletisation. The fragmentation, defined as pellets brackage as a consequence of stress concentration inside lattice during transition from a form to another due to the reductions, is the topic of Yi et al [80]. They investigate the disintegration behaviour of industrial hematite pellets during low-temperature reduction under conditions representative of shaft-furnace operation. Commercial pellets with diameters between 12.5 and 16 mm and an average crushing strength of approximately 2973 N were reduced for 60 minutes at temperatures between 450 and 600 °C, under a compressive load of of about 40 Pa and with gas mixtures typical of industrial processes. The gas flow rate was maintained at 0.6 m^3/h, while the $H_2/(H_2+CO)$ ratio was varied from 0 to 1. Pellet degradation was quantified through the mass of fines generated at the end of the test (particles smaller than 3.15 mm). Although the overall fines production remained low (0.4–3.2 %), a pronounced maximum occurred at 550 °C, corresponding to the temperature at which the hematite-to-magnetite transformation induces the highest lattice-expansion stresses. At 500 °C the

pellet structure remained essentially intact, whereas at 550 °C coarse cracks initiated at pore surfaces and propagated through the newly formed magnetite, leading to severe degradation; crack initiation was experimentally observed to begin near 400 °C and to follow a characteristic propagation pattern [81]. At 600 °C, increased slag and binder plasticity mitigated crack formation, resulting in reduced disintegration. Gas composition exerted a strong influence on behaviour: hydrogen displayed a dual effect, initially intensifying disintegration at intermediate proportions (notably at $H_2/CO = 0.8$) due to its high diffusivity and the rapid reduction it promotes, which increases lattice-transition stresses. When hydrogen became the dominant reductant, however, the reduction proceeded more uniformly, producing magnetite with lower internal strain and markedly reducing crack formation and fine genenration. The composition of the pellet blend also played a decisive role. Pellets produced from pure magnetite exhibited severe degradation (about 20.4 %), whereas additions of SiO_2 or CaO significantly improved resistance, lowering the mass of fines to 9.8 % and 5.2 %, respectively. Crack-density measurements confirmed that SiO_2 and CaO effectively suppressed crack formation, an effect attributed to the formation of low-melting phases such as fayalite ($2FeO \cdot SiO_2$) and calcium ferrite ($CaO \cdot Fe_2O_3$), which act as stress-absorbing binders during reduction. Overall, the most severe disintegration occurred at 550 °C and $H_2/CO = 0.8$, driven by lattice-transition stresses and crack propagation, while higher reduction degrees consistently correlated with increased degradation. Therefore, this work underlines the role of gasses on the formation of fines, at high proportions or in pure hydrogen, it instead reduces disintegration by producing a more uniform, low-strain magnetite layer. Information that can be considered as an index of the mechanical properties' variation due to temperature and reactions.

Nabeel M. et al [82] investigated pellet fragmentation caused by frictional interactions within a compact bed of iron-ore pellets, identifying how these mechanisms contribute to mechanical wear and the generation of dust (defined as material smaller than 0.5 mm). Their experimental setup consisted of approximately 700 g of commercial MPBO pellets of different size classes (small: < 12 mm; medium: 12–14 mm; large: > 13.5 mm) placed in a cylindrical container between two plates, in a configuration similar to the Schulze shear cell. The lower plate was rotated at 240 rpm for ten minutes, while the upper plate applied vertical loads between 1 and 3 kg at room temperature. The frictional force transmitted through the pellet bed was transferred to the loading rod and measured by a load cell. A constant airflow of 8 L/min transported airborne particles to an ELPI+ analyser: an Electrical Low-Pressure Impactor capable of classifying airborne particles by aerodynamic diameter in real time. This enabled the authors to distinguish between coarse "heavy" dust retained in the container and fine "light" dust

carried by the gas stream. Tests were performed both on the as-received pellet mixture and on size-classified fractions.

The results showed a clear linear increase in both wear rate and frictional force with applied load: raising the load from 1 to 3 kg produced an increase of approximately 67 % in friction and dust formation. Under the sliding-dominated conditions of the experiment, pellet size had only a minor influence on wear. The particle-size distribution of the heavy dust fraction was largely insensitive to load, although slightly more fines in the 1–5 μm range appeared at higher loads. In contrast, the airborne dust fraction was strongly load-dependent, with concentrations rising sharply and peaking around 0.5 μm, indicating that abrasion is particularly effective at generating very fine, easily entrainable particles.

The study demonstrates that frictional abrasion within a pellet bed is a significant source of fine dust, especially under higher compressive loads. These particles are sufficiently small to remain airborne and, in industrial furnaces, can accumulate within the voids of the burden, reducing gas permeability and impairing reduction efficiency. Moreover, as will be discussed later, such fines can also promote sticking phenomena between adjacent pellets.

If the stresses to which the pellets are subjected play a fundamental role in fragmentation, the effect of temperature is equally important, a topic widely discussed in the work of Wang et al. [83].Their study examines how the thermal compressive strength of carbon-bearing iron ore pellets prepared without binders evolves during reduction, showing that temperature, pellet size, and reducing-agent dosage interact in a highly non-linear way. The authors prepared pellets composed solely of magnetite concentrate and anthracite (2–18 wt% addition) and subjected them to controlled reduction between 300 and 1150 °C. The reduction tests were performed using a dedicated thermal-strength testing apparatus, consisting of a resistance-heated furnace with a flat-temperature zone, an automatic lifting and rotating sample table, a servo-driven compression system, and an argon-controlled atmosphere. Pellets were heated at 8 °C/min under a constant argon flow of 5 L/min, held at the target temperature for 15-60 minutes, and then compressed in situ and by a load cell the thermal compressive strength was cell continuously recorded. By measuring strength directly at the reduction temperature, the apparatus prevents the microstructural relaxation and phase changes associated with cooling, ensuring that the recorded values reflect the true mechanical state of the pellet during reduction.

The results demonstrate that strength development is governed by a balance between particle fragmentation, interparticle meshing, carbon gasification, and the phase transformations of iron oxides. During the low-temperature reduction stage (300-500 °C), the thermal compressive strength increases with pellet size but decreases with higher anthracite content. At 300 °C and 60 min, pellets containing 8% anthracite show a strength increase from 13.24 N to

31.88 N when pellet size increases from 8.04 mm to 12.78 mm. Conversely, at 500°C, increasing the anthracite ratio from 2% to 8% causes strength to drop from 41.47 N to 8.94 N after 60 min of reduction. Microstructural observations reveal that at these temperatures, magnetite and hematite remain the dominant phases, and strength is controlled by the interplay between fragmentation (which increases contact area and enhances meshing) and the expansion associated with early-stage reduction. When anthracite content is low, fragmentation dominates and strengthens the pellet; when anthracite is high, accelerated reduction and the associated volume expansion disrupt the internal structure and weaken the pellet.

In the high-temperature reduction stage (600-1150°C), the thermal compressive strength exhibits a characteristic rise-and-fall behaviour. For pellets containing 2% anthracite, strength increases from 102 N at 600 °C to a maximum of 226.7 N at 1050 °C, before decreasing to 147.5 N at 1150 °C. With 8 % anthracite, the maximum strength is lower and occurs earlier, rising from 36.4 N at 600 °C to 69.4 N at 1020 °C, then falling to 19.5 N at 1150 °C. When anthracite content reaches 18%, the pellet becomes extremely sensitive to temperature: strength peaks at 35 N at 800 °C but collapses to 8.6 N at 1050 °C. XRD analysis shows progressive transformation from Fe_2O_3 to Fe_3O_4 and FeO, along with the formation of Fe-Si-O phases at elevated temperatures. These transformations, combined with carbon gasification, modify the pore structure and interparticle bonding, explaining the observed strength evolution, demostrating that the thermal compressive strength of binder-free carbon-bearing pellets is highly sensitive to pellet size, anthracite dosage, and reduction temperature. Strength improvements at moderate temperatures arise from enhanced particle meshing and controlled fragmentation, whereas excessive reduction, carbon gasification, and high-temperature phase transformations lead to structural expansion, pore coarsening, and eventual weakening. The work provides a mechanistic basis for optimising carbon-bearing pellet formulations and reduction conditions, offering valuable guidance for their potential use in non-blast-furnace ironmaking technologies where both self-reduction capability and sufficient thermal strength are required.

It has been seen that additives plays a fundamental role in limiting the formation and propagation of cracks, primarily through the development of gangue phases that stabilise the pellet structure during thermal and chemical cycling [80]. Beyond their structural contribution, additives also influence key metallurgical phenomena such as reducibility, dynamic swelling, softening under load, low-temperature disintegration (LTD), and cold crushing strength (CCS). LTD quantifies the tendency of pellets to break down into fines during the Fe_2O_3 to Fe_3O_4 transition; while CCS measures the mechanical load required to fracture an individual pellets at room temperature afther their exposure to thermal and reactive conditions, providing an indication of its robustness during handling and charging. The addition of such as fluxing

agents (i.e. limestone, dolomite, or olivine) can further modify and, in some cases, enhance the mechanical behaviour of iron ore pellets. A representative example is provided by the work of Iljana et al. [84], who examined how reducibility, dynamic swelling, softening under load, LTD, and CCS evolve when limestone is added to acidic pellets. Their results show that even starting from acidic pellets, the introduction of CaO improves reaction kinetics and stabilises the pellet structure across different stages of reduction. Limestone addition ($CaCO_3$) increases the shrinkage capacity of the solid and systematically alters its metallurgical response. Two pellet types were compared: non-fluxed pellets containing approximately 0.5 wt% CaO and fluxed pellets containing about 3.2 wt% CaO. The fluxed pellets exhibited superior reducibility in both dynamic and softening-under-load tests, a behaviour attributed to the formation of low-melting calcium–silicate phases that facilitate reduction. This improvement, however, was accompanied by moderate drawbacks: a slight increase in swelling and cracking during dynamic reduction, an earlier onset of softening by roughly 35 °C, and a reduction in CCS (≈214 daN compared to 265 daN). Resistance to low-temperature degradation also declined, passing from 10.9% to 26.7%, indicating greater fines formation during the Fe_2O_3 to Fe_3O_4 transition. Despite these effects, all mechanical parameters remained within acceptable limits for blast-furnace operation. Overall, the study concludes that limestone addition enhances reducibility and high-temperature performance, while inducing moderate but manageable reductions in low-temperature mechanical stability.

Further insights into the role of pellet chemistry were provided by Umadevi et al. [85], who demonstrated that the mechanical properties of iron ore pellets can be significantly improved by adjusting their basicity through the controlled addition of CaO and SiO_2 as fluxing additives. At very low basicity (about 0.08), the pellets consisted predominantly of hematite and exhibited numerous open, interconnected pores with weak crystal bonding. Increasing basicity to around 0.33 promoted the formation of silicate slag phases, which enhanced inter-granular bonding and reduced porosity. At higher basicity levels (0.78–1.15), the microstructure evolved further through the formation of calcium ferrites and calcium-rich glassy phases, producing denser and mechanically stronger pellets [86]. These transformations were reflected in the physical properties: the cold crushing strength rose from 176 to 264 kg/p as basicity increased. The metallurgical response, however, displayed a non-linear trend. The fragmentation decreased from 16.3% to a minimum of 10.9% at a basicity of 0.33, due to the stabilising effect of silicate glass during reduction, but increased again at high basicity (1.15) because the calcium-rich glass transformed into wollastonite, promoting crack formation; identifying a basicity of approximately 0.33 as the optimal compromise, providing mechanically robust pellets with low degradation and a stable microstructure during reduction.

Huang et al. [87] investigated the mechanisms responsible for the rapid loss of mechanical strength observed in iron-ore oxide pellets during the initial stages of gas-based reduction. The study focused on industrial hematite pellets of approximately 12 mm in diameter, containing about 64.2 wt% total Fe (much larger than the composition largely involved in DR), 0.24 wt% FeO, 5.31 wt% SiO_2 and 0.56 wt% CaO, with an initial cold-crushing strength of roughly 2973 N per pellet. Reduction tests were carried out at 900 °C in a thermogravimetric furnace using a gas mixture composed of 34% H_2, 34% CO, 2% CO_2 and 30% N_2 at a flow rate of 3 L/min. After heating under nitrogen, the pellets were exposed to the reducing gas while mass loss was continuously monitored. Post-reduction characterisation included compressive-strength measurements, optical and electron microscopy, and porosity analysis. To follow the progression of structural changes, each pellet was sectioned into periphery, mantle and core.

The study provides a clear mechanistic explanation for the abrupt deterioration of pellet strength at the onset of reduction. The authors show that the early phase transitions (hematite to magnetite, magnetite to wüstite and eventually to metallic iron) are accompanied by substantial volumetric changes, with the Fe_2O_3 to Fe_3O_4 transformation alone producing an expansion of approximately 24%. These transformations generate internal stresses capable of fracturing grains and weakening inter-particle bonding. At the same time, thermal gradients between the rapidly heated periphery and the cooler core induce tensile stresses at the surface, promoting crack initiation even before significant oxygen removal has occurred.

The experimental results confirm the dominant role of these mechanisms. Within the first minute of reduction, pellet strength decreases from 2973 N to 742 N (almost 75% loss) despite the reduction degree being only about 11%. Porosity also increases sharply during this stage, rising from about 38% in the fresh pellet to nearly 46% in the periphery after one minute. SEM observations show extensive fine cracking and the formation of a loose magnetite network, confirming that the hematite-to-magnetite transition is the primary cause of structural collapse. As reduction advances, the magnetite-to-wüstite transformation enlarges pores and cracks, causing a further but less dramatic strength decrease. Only with the onset of metallic iron formation, after approximately seven minutes, does the periphery begin to densify again through iron whisker sintering, partially restoring hardness. Whiskers are elongated, filament-like metallic iron structures that develop during the wüstite-to-iron transformation, typically growing outward from pore surfaces or crack walls as reduction progresses. Their formation results from rapid nucleation and strongly directional growth under reducing conditions, producing thin iron protrusions capable of filling voids and locally densifying the microstructure. Beyond their contribution to strengthening the pellet periphery and partially healing early-stage cracks, the additional roles played by these whiskers will be discussed in the following sections. In conclusion

the study demonstrates that the earliest stage of reduction is the most critical for pellet integrity, with strength degradation governed by the combined effects of phase-transition-induced volume expansion, thermal stresses, porosity development and crack propagation, all originating at the periphery and advancing toward the core as reduction progresses.

Understanding the swelling behaviour of iron ore pellets requires moving beyond macroscopic indices and examining the microstructural processes that govern deformation during reduction. Among these processes, the formation and growth of metallic "whiskers" at the wüstite–iron transition have emerged as the dominant mechanism linking reduction conditions to pellet expansion, cracking, and eventual disintegration. Over several decades, a coherent body of research has progressively clarified how these filaments nucleate, how they propagate through the pore network, and how their growth is influenced by both intrinsic pellet properties and external operating variables. The classical studies of Sharma and co-workers laid the foundation by demonstrating that swelling is not an empirical anomaly but the direct consequence of whisker-driven internal damage. Subsequent investigations, such as those by Hayashi and Iguchi, expanded this framework by showing how trace gas-phase species—particularly sulphur—can dramatically alter whisker formation and, in extreme cases, trigger abnormal swelling. More recent microstructure-engineering approaches, exemplified by the work of Dong et al., have shifted the focus toward designing pellet structures that suppress whisker growth altogether. Taken together, these contributions form a continuous narrative: from identifying the microscopic origin of swelling, to quantifying the conditions that promote or inhibit whisker formation, to deliberately tailoring pellet microstructures to improve reduction-swelling performance.

The body of work on the swelling of iron ore pellets converges on a central microstructural mechanism: the formation of iron or ferric "whiskers" during gas reduction, particularly near the wüstite–iron transition. A coherent argument emerges when one reads the classical experiments of Sharma and co-workers [88], [89], [90], [91] alongside Hayashi and Iguchi's sulphur-assisted abnormal-swelling study [92] and the more recent, industrially oriented microstructure-engineering work of Dong et al. [93]. Taken together, these contributions trace a clear progression: from the identification of whiskers as the root cause of catastrophic swelling, through the quantification of how operating variables govern whisker formation, to the deliberate design of pellet microstructures that suppress whisker growth and thereby improve reduction-swelling performance.

The starting point is the work of T. Sharma and colleagues on the role of porosity and reduction conditions in swelling. In their paper, Sharma et al. [88] investigated how porosity influences the swelling behaviour of iron ore pellets, briquettes, and lump ores. The authors prepared agglomerates from natural iron ores (and, by analogy with their later work, likely also from

chemically pure Fe_2O_3), systematically varying porosity through pelletisation and firing practice. These samples were then reduced in controlled gas atmospheres within the temperature range characteristic of blast-furnace shaft reactions, and both the swelling index and the degree of disintegration were measured. Microstructural examination complemented the macroscopic observations. The crucial methodological feature is that porosity was treated as the primary structural variable, while reduction temperature and gas composition were kept within ranges known to produce wüstite and metallic iron. The results were unequivocal: higher porosity led to greater volumetric swelling and more severe disintegration. Sharma et al. explicitly attributed this behaviour to the growth of iron whiskers within the pore network, arguing that these filaments nucleate on oxide surfaces, extend into pore cavities, and act as internal wedges that open cracks and ultimately cause fragmentation [88]. In doing so, they shifted the discussion from "swelling as an empirical property" to "swelling as the macroscopic manifestation of whisker-driven internal damage," and they identified porosity as a key structural facilitator of this mechanism.

Having established porosity as a potent control parameter, Sharma and co-workers next turned their attention to the influence of the reduction rate. They examined pellets produced from two Indian iron-ore fines (Bailadila and Noamundi) as well as from chemically pure Fe_2O_3 [91]. Their experimental strategy was to perform isothermal gas-reduction tests in which reduction temperature, reduction time, gas partial pressure, and gas flow rate were systematically varied, thereby generating a broad spectrum of effective reduction rates. Swelling indices were then measured for each condition. The results demonstrated that swelling is not a simple monotonic function of temperature or gas strength; instead, it is governed by the overall rate at which reduction proceeds. For every pellet type, the authors identified a critical reduction rate at which the swelling index reached a maximum. Below this threshold, swelling remained moderate; above it, swelling could again diminish, likely because densification and rapid phase transformation outpaced the development of long, intrusive whiskers. Crucially, Sharma et al. emphasised that whisker growth itself is controlled by the reduction rate, meaning that the conditions which drive the reaction into this critical kinetic window are precisely those that most strongly promote whisker formation. This represents a conceptual advance: whiskers are no longer viewed as an unavoidable by-product of reduction, but as a rate-dependent instability that can, in principle, be mitigated by controlling the velocity of the reaction front.

To quantify these dependencies more rigorously, Sharma's group adopted a statistical design-of-experiments approach in their subsequent work. In the isothermal swelling study [89], they fabricated pellets from chemically pure Fe_2O_3 and from natural Bailadila ore, again adjusting porosity by varying firing temperature and time, and introducing controlled additions of basic oxides (CaO, MgO, SiO_2, Al_2O_3). These pellets were then reduced

isothermally in H_2/CO-containing atmospheres, and the authors treated reduction temperature, reduction time, gas partial pressures, gas flow rate, firing temperature, firing time, porosity, and additive type as independent variables within a statistically designed experimental matrix. Swelling indices were recorded for each run. The resulting analysis produced regression equations in which the swelling index appears as a linear, and in some cases higher-order, function of coded variables representing thermal conditions, gas composition, flow rate, and structural parameters. The trends were fully consistent with their earlier mechanistic interpretation: increasing reduction temperature, gas partial pressure and flow, and porosity all tended to increase swelling, whereas additions of CaO, MgO, and SiO_2 suppressed it. The underlying explanation remained firmly centred on whisker formation. High reduction rates combined with open porosity favour rapid nucleation and growth of iron whiskers, while the gangue phases introduced by these additives partially occupy pore space and modify local thermodynamics in ways that inhibit whisker development.

Sharma et al. [90] extended this parametric framework to more realistic, non-isothermal conditions. Using a tube furnace, the authors heated pellets in CO-containing atmospheres from approximately 800 to 1000 °C at controlled heating rates, while systematically varying the CO partial pressure and gas flow rate according to a statistical design. Swelling indices were measured at the end of each non-isothermal run, and the effects of heating rate, CO partial pressure, flow rate, porosity, and gangue content on swelling were quantified through regression analysis. The resulting trends sharpened the kinetic and structural interpretation developed in their earlier work: faster heating, higher CO partial pressure, and higher gas flow rates all produced larger swelling indices, whereas increased gangue content consistently reduced swelling. Even without isothermal control, the combined effect of rapid heating and a strong reducing atmosphere was to drive the system into the critical reduction-rate regime in which whisker growth is most aggressive. At the same time, gangue phases acted as a microstructural “brake” on whisker development by occupying pore space and strengthening grain contacts. Methodologically, this study is significant because it moves beyond idealised isothermal tests and demonstrates that the same whisker-driven mechanism persists under dynamic heating conditions that more closely resemble those in the blast-furnace shaft.

The sulfur-assisted abnormal-swelling work of S. Hayashi and Y. Iguchi [92] introduces an essential chemical dimension into what had previously been an essentially structural–kinetic framework. Their study examined binder-bonded iron ore pellets reduced in CO-CO_2 gas mixtures containing low partial pressures of COS over a temperature range of 700-1000 °C. Pellets were prepared using different binders (portland cement, bentonite, and limestone) and then reduced under carefully controlled sulfur activities, adjusted relative to the Fe–FeS equilibrium. Swelling indices were measured

after reduction, the gas phase was analysed by gas chromatography to track sulfur species, and microstructures were examined for evidence of fibrous iron. Hayashi and Iguchi found that pronounced abnormal swelling occurred in cement-bonded pellets when sulfur was present and the sulfur activity in the gas was below the Fe–FeS equilibrium level; moreover, cement-bonded pellets could exhibit moderate abnormal swelling even without external COS due to sulfur species released from the cement itself. Crucially, they observed that this abnormal swelling was “mostly accompanied with the formation of fibrous irons”—that is, iron whiskers—within the pellet microstructure. The binder type and sulfur environment therefore played decisive roles in determining whether whisker networks would proliferate and drive catastrophic expansion. This work underscores that whisker formation is not only sensitive to macroscopic kinetic parameters but can also be significantly modulated by trace chemistry and by the nature of the bonding phase, with sulfur exerting a particularly strong influence.

The contribution by Dong X. et al. [94] demonstrates that a deliberate attempt to control whisker formation through microstructural design can yield measurable improvements in industrial pellet performance. Their study focused on low-silicon fluxed pellets with a basicity of approximately 1.1, produced for high-proportion pellet operation in blast furnaces. The authors systematically incorporated 5–15% of finely ground blast-furnace return ore into the pellet feed, then prepared and fired the pellets under plant-relevant conditions. In the laboratory, they conducted standard reduction-swelling index (RSI) tests, employing a fixed reduction temperature and a controlled gas composition consistent with RSI protocols, and quantified the resulting volume expansion. In parallel, they performed SEM–EDS analyses to characterise the distribution of calcium ferrite, magnesium ferrite, and liquid phases in the fired pellets, with particular attention to how these phases were arranged between hematite grains. Finally, the optimised mix containing fine return ore was implemented at the Shougang Jingtang works from 2020 onward, where the authors monitored both pellet quality and blast-furnace performance under industrial conditions.

The results were striking. The baseline RSI of 23.5% for the reference low-Si fluxed pellets dropped to 14.3% when 5–15% fine blast-furnace return ore was incorporated into the mix. Microstructurally, the modified pellets exhibited a pronounced increase in calcium ferrite, magnesium ferrite, and liquid phases, with these phases distributed more uniformly within the intergranular regions separating hematite grains. Dong et al. argued that this more homogeneous network of ferrite and liquid phases “tended to be homogenized,” and that such a structure was particularly effective in inhibiting the generation of ferric whiskers during the reduction of the hematite phase. By occupying and reinforcing pore space and grain boundaries, this continuous skeleton constrains the local expansions associated with whisker growth. Industrial implementation confirmed the laboratory findings: pellets produced with this

optimised recipe maintained high quality in service, demonstrating that microstructures deliberately engineered to suppress whisker formation translate directly into improved swelling behaviour under real blast-furnace operating conditions.

Taken together, these seven studies [88], [89], [90], [91], [92], [93], [94] support a coherent, mechanistic argument about the role of whiskers in the swelling of iron ore pellets. Sharma and co-workers demonstrate, through systematic laboratory experimentation and statistical modelling, that swelling is maximised at a critical reduction rate and that both high porosity and aggressive reduction conditions create the internal environment in which iron whiskers can grow unimpeded. They further show that additions of basic oxides and higher gangue contents suppress swelling, strongly suggesting that microstructures enriched in ferrite and silicate bonding phases physically obstruct whisker development. Hayashi and Iguchi add a crucial chemical dimension by showing that local sulfur activity and binder chemistry can trigger abnormal whisker formation and extreme swelling, even when other parameters remain comparable, highlighting that control of trace impurities and binder selection is integral to managing whisker-driven behaviour [92]. Dong et al. then close the loop by demonstrating that pellet microstructures can be intentionally engineered (through the addition and fine grinding of blast-furnace return ore) to produce a more homogeneous ferrite/liquid skeleton that suppresses ferric whiskers and substantially lowers RSI in both laboratory and industrial settings [94].

Within this framework, the influence of operating conditions and material characteristics can be clearly articulated. The materials examined in the classical studies span chemically pure Fe_2O_3 pellets, industrial pellets derived from specific Indian ores, and binder-bonded pellets formulated with different binders and gangue levels [88], [89], [90], [91], [92]. In Dong's work, low-Si fluxed pellets modified with fine blast-furnace return ore represent a contemporary industrial product [92]. Methodologies range from isothermal reduction in controlled gas mixtures, through non-isothermal (ramp) reductions, to standardised RSI tests, all complemented by microscopic characterisation of both reduced and fired microstructures. The operating variables systematically explored include reduction temperature (typically 700-1000 °C), gas composition and partial pressure (CO-CO_2, H_2/CO mixtures, COS additions), gas flow rate, heating rate, firing temperature and time, porosity, and additive content. Across this experimental space, the results consistently show that high porosity, high reduction rates, strong reducing atmospheres, and unfavourable binder or impurity chemistries produce larger swelling indices and more extensive whisker formation. Conversely, controlled porosity, sufficient gangue and flux to form bonding phases, carefully selected binders, and low sulfur activity all act to mitigate whisker growth and its damaging consequences.

From a technological standpoint, the implication is that whiskers are not an incidental curiosity but a critical failure mechanism that can and should be explicitly targeted. The evidence points toward pellet-design strategies that balance reducibility against the risk of whisker-driven swelling: porosity must be optimised rather than maximised; slag and ferrite phases must be engineered to occupy and strengthen the pore network; and both sulfur levels and binder chemistry must be controlled to avoid creating local environments favourable to fibrous-iron growth. On the process side, reduction profiles in blast and shaft furnaces should be tuned so that pellets do not remain for extended periods within the specific temperature–gas–rate window in which the reduction rate becomes critical for whisker formation. In this sense, the collective work of Sharma, Hayashi and Iguchi, and Dong et al. transforms whiskers from a descriptive feature of micrographs into a design parameter situated at the intersection of materials science and process engineering.

II.3.3. Blast furnace: pellet behaviour from top to hearth

At the top of the blast furnace and through the upper shaft, pellets enter the process in their cold, unreduced state. As they descend, they encounter progressively hotter gases and begin to undergo preheating and the earliest stages of indirect reduction. This region is characterised not by softening or cohesive behaviour, but by the phenomena collectively known as low-temperature degradation: reduction–disintegration, pulverisation, and the onset of swelling. The mechanical stability of pellets in this zone is therefore governed by the interplay between their initial microstructure and the kinetics of early reduction, long before the burden reaches temperatures where melting or plastic deformation become relevant.

The classical work of Sharma and co-workers provides the mechanistic foundation for understanding pellet behaviour in this part of the furnace, even though their experiments were not conducted in a blast-furnace simulator. Across their works [88], [89], [90], [91] reduced industrial and synthetic Fe_2O_3 pellets (as well as briquettes and lump ore) in CO or H_2/CO atmospheres at 800-1000 °C, systematically varying temperature, gas partial pressure, flow rate, and porosity. Swelling indices and disintegration were measured after reduction, and microstructures were examined to identify the underlying causes of degradation. Their results showed that high porosity and strong reducing conditions at high pCO or pH_2, elevated flow rates, and rapid heating, producing large swelling indices, whereas increased gangue content and basic additives suppress swelling. Crucially, was argued that macroscopic swelling and disintegration is originated from the formation of iron whiskers during the conversion from wustite to metalic iron transition, and that a critical reduction rate exists at which swelling is maximised.

Although these experiments were not explicitly designed to replicate blast-furnace conditions, the thermal and chemical environments they

explored correspond closely to those experienced by pellets in the upper and middle shaft, where indirect reduction is active but softening has not yet begun.

Complementing these generic studies, several investigations explicitly employ blast-furnace shaft simulators and standardised indices to characterise pellet behaviour in this region. Mikko Iljana at al., as shown, examined the dynamic and isothermal swelling behaviour of acid and olivine pellets under simulated BF-shaft conditions using a tube furnace equipped with video monitoring [95]. Pellets containing different proportions of magnetite cores and olivine gangue were exposed to CO-CO_2-N_2 atmospheres following a realistic shaft-temperature profile up to ~1100 °C. Their key observation is that gradual, dynamic heating produces markedly lower swelling (lower than 17 vol%) than sudden isothermal exposure (up to 51 vol%), and that pellets with large magnetite nuclei develop cracks at the magnetite–hematite interface and exhibit poor low-temperature disintegration (LTD) values. This directly captures pellet behaviour in the BF upper shaft and thermal reserve zone, where heating and reduction proceed progressively: swelling remains significant but is less extreme than standard isothermal RSI tests imply, and internal zonal structures, particularly magnetite cores, play a decisive role in crack formation and LTD performance.

A broader picture of upper-shaft degradation emerges form the work of Yi et al. presented above [96], where investigation of pellet disintegration mechanisms under simulated shaft-furnace conditions were addressed. Although formally framed for direct-reduction reactors, their results are highly relevant for the early stages of reduction because the temperature and gas profile mirror those encountered by pellets in the blast-furnace upper shaft. As commercial pellets were reduced through a gradually increasing temperature schedule, the authors recorded the progressive development of fragmentation, chipping, and surface spalling. Their observations help fill in the qualitative sequence of damage that accumulates as pellets traverse the top of a shaft-type reactor: even before substantial swelling occurs, surface cracking and edge breakage begin to weaken the pellet structure.

Low-temperature pulverisation at the furnace top is addressed more explicitly by Wang et al. [97], who used a KSZ-03 ore-property tester and drum devices to quantify the pulverisation resistance of pellets under low-temperature reducing conditions. Their study shows that, under otherwise fixed gas compositions, increasing the reduction-gas flow rate intensifies pulverisation, and that the phenomenon is most severe around 500 °C, diminishing at both higher and lower temperatures. Because pellets encounter this 400-600 °C interval early in their descent, these results indicate that fines generation begins well before the classical swelling regime is reached. Gas-flow-driven reduction, thermal shock, and the onset of microcracking can therefore produce measurable degradation in the upper shaft, even in the absence of the high-temperature mechanisms that dominate deeper in the furnace.

A final group of studies, although not explicitly resolved by blast-furnace zone, directly targets the material properties that govern pellet in the upper shaft. Dwarapudi and Ranjan [86] linked the fragementation of commercial pellets to the amount and spatial distribution of silicate-melt bonding and to overall porosity, showing that weak or discontinuous bonding phases leave pellets vulnerable to early cracking. Guo et al. [98] demonstrated that increasing SiO_2 content promotes the formation of $2FeO{\cdot}SiO_2$, which in turn lowers cold-compression strength (CCS) and reducibility, thereby compromising pellet integrity during the initial descent. Chai et al. [99] showed that modest CaO additions to medium-silica pellets reduce fragmentation while simultaneously improving reducibility, highlighting the stabilising effect of controlled basicity on early-stage degradation. Similarly, Prasad et al. [100] and Dishwar et al. [101] optimised firing conditions and fineness distributions to achieve favourable CCS values and fragmentation. Although these works do not simulate the blast-furnace shaft directly, they converge on a common objective: designing pellets that resist cracking, disintegration, and fines generation as they pass through the upper and middle shaft, where thermal shock, indirect reduction, and early microcracking dominate the degradation landscape.

As pellets descend into the middle and lower shaft, the thermal and chemical environment changes markedly. Temperatures rise, the degree of reduction increases, and wüstite becomes the dominant intermediate phase. Yet the burden still behaves as a granular bed: pellets retain their discrete form, and although softening has not fully begun, the mechanisms governing swelling, cracking, and early strength loss evolve as the system approaches the onset of cohesive behaviour. This transitional region is where the interplay between advanced reduction, emerging liquid phases, and circulating impurities becomes especially consequential.

Iljana's dynamic shaft experiments with circulating elements are particularly instructive for this part of the furnace [102]. Using CO-CO_2-N_2 atmospheres up to ~1100 °C and controlled additions of sulfur (S_2) and potassium, Iljana et al. tracked swelling, cracking, and contraction in acid and olivine pellets under a realistic shaft-temperature profile. They found that sulfur in the reducing gas promotes the formation of an FeO-FeS liquid phase, which leads to pellet contraction and, at sufficiently high sulfur partial pressures, even hinders the wustite to iron reduction step. Potassium, by contrast, induced swelling and cracking in olivine pellets, though still within the range of normal swelling behaviour. This work effectively can be used to describe pellet behaviour in a high-temperature shaft environment contaminated by circulating S and K, just above the cohesive zone. In this region, reduction is already advanced, wustite is present, and the first liquid phases begin to appear. Depending on local chemistry, swelling can transition into contraction, and the mechanical response of pellets becomes increasingly sensitive to trace elements carried by the gas stream. Iljana's findings therefore bridge the gap between classical

low-temperature swelling mechanisms and the complex thermo-chemical interactions that precede softening deeper in the furnace.

Yur'ev and Dudko's investigation of fluxed Kachkanar pellets adds another layer to our understanding of pellet integrity in the mid-shaft region [102]. Working with industrially fired pellets subjected to realistic heating and reduction sequences, and using a sinter pot for thermal treatment and laboratory reduction tests for mechanical evaluation, they examined how internal structure and oxidation state influence strength. Their key finding is that roasted pellets which remain partially oxidised and retain pronounced zonal structures fail to meet the strength requirements needed for blast-furnace operation. To address this, they developed a process in which hematite dissociation occurs in the presence of a calcium ferrosilicate melt, producing pellets that begin to reduce only above 700 °C and thereby avoid premature structural collapse. These insights are particularly relevant to the middle shaft, where pellets encounter temperatures high enough to initiate wustite formation but not yet high enough to induce softening. In this transitional zone, any residual zonal structure or incomplete oxidation can become a liability: if such pellets meet strong reducing conditions too early, they are prone to cracking and breakage. Yur'ev and Dudko's work therefore highlights the importance of ensuring structural homogeneity and controlled reduction onset, reinforcing the broader theme that pellet microstructure must be engineered with the entire shaft profile.

Across all of these works, the burden remains non-cohesive, gas percolation is relatively unimpeded, and the dominant phenomena are swelling, contraction, cracking, and strength evolution under increasingly severe reduction conditions. These studies collectively set the stage for the transition into the cohesive zone, where the granular bed begins to lose permeability and the mechanical behaviour of pellets changes fundamentally.

At the cohesive zone, pellets enter a fundamentally different regime: temperatures are high enough for softening, coalescence, and partial melting to occur, causing the granular bed to shrink, voids to close, and gas permeability to deteriorate sharply. This transition marks the point where the mechanical behaviour of the burden shifts from limited interactions among pellets to semi-molten deformation, and where the interplay between reduction degree, load, and liquid-phase formation becomes decisive.

A number of experimental studies explicitly simulate this environment under load and realistic blast-furnace gas and temperature profiles. Kemppainen et al. [103] provide one of the clearest comparisons of pellet softening behaviour under cohesive-zone conditions. Using a high-temperature furnace equipped with a load and BF-like reducing gas, they measured the onset temperature of softening, the progression of bed displacement, and the point at which gas permeability collapses. Their results reveal distinct softening intervals for acid versus olivine-fluxed pellets, with olivine fluxing improving resistance to softening but still falling short of sinter performance at high

reduction degrees. These observations correspond directly to the upper cohesive zone, where pellets are already significantly reduced (reduction degree higher than 50 %) and begin to deform under the burden load. In this region, the emergence of liquid phases and the weakening of intergranular bonding dictate how quickly the bed compacts and how rapidly permeability is lost—key determinants of furnace stability.

Iljana et al. expanded the understanding of cohesive-zone behaviour through their ARUL (Advanced Reduction Under Load) experiments [104]. In these tests, acid and olivine pellets, along with basic sinter, were subjected to simulated blast-furnace gas compositions, temperature ramps, and mechanical loads while bed shrinkage, reduction degree, and pressure drop were continuously monitored. Their results reveal a clear hierarchy in permeability retention: basic sinter maintained gas flow up to roughly 1329 °C at a reduction degree of about 90 %, whereas acid pellets lost permeability much earlier, around 1160 °C at 49 % of reduction degree, with olivine pellets occupying an intermediate position. ARUL therefore captures the full evolution of the cohesive zone for different burden components and identifies pellets, particularly acid pellets, as the earliest contributors to permeability loss under cohesive-zone conditions.

Sternel and Lahiri [105] further refined this picture by examining the contraction and meltdown behaviour of olivine pellets under simulated blast-furnace conditions. Subjecting both acid and olivine pellets to a controlled temperature ramp in BF-like gas under load, tracking the onset of contraction, the rate of bed shrinkage, and the transition into meltdown and dripping. Their results map the progressive transformation from a granular bed to a semi-coherent mass and ultimately to a semi-liquid structure in the middle and lower cohesive zone for pellet-only burdens. This work highlights how pellet chemistry and fluxing determine not only softening resistance but also the temperature window in which structural collapse and dripping begin, that can be considered as critical parameters for cohesive-zone stability.

Broader softening-melting investigations, such as those by Shatokha and Velychko [106] and Nishimura et al. [107], extend this picture by examining the full thermal window in which pellets transition from load-bearing solids to partially molten aggregates. Using softening–melting tests under load, these studies evaluated the temperature at which permeability is lost (T_1), the temperature of maximum dripping (T_2), the evolution of pressure drop, and the formation of liquid slag and metal phases in both sinter and pellets. Shatokha and Velychko showed that increasing basicity raises T_1 and modifies T_2 by shifting the slag liquidus temperature, thereby influencing both the thickness of the cohesive zone and the efficiency of melt evacuation [106]. Nishimura et al. complemented this by introducing a softening-viscosity model that links shrinkage below 1300 °C to bed porosity, void ratio, and liquid fraction, and by contrasting how sinter, lump ore, and pellets evolve through the melting-reduction stage [107]. Together, these studies delineate

the full softening-melting interval in which pellets lose structural integrity, coalesce, and begin to drip; capturing the critical transformation that governs gas flow, burden descent, and cohesive-zone stability.

Gavel et al. [108] extend these pellet-focused insights to the behaviour of mixed burdens, showing how pellets and sinter interact during the softening-melting sequence. In smelting and quenching experiments on beds composed of pellets, sinter, and a 60:40 pellet–sinter blend, they imposed a blast-furnace-like temperature and gas profile under load up to 1500 °C, tracking bed shrinkage and permeability as functions of temperature. Across all burden types, they identified three distinct shrinkage stages: indirect reduction, softening, and melting; wherefore the relative contribution of each material shifted depending on the mixture. Crucially, in the mixed bed, pellets governed the first shrinkage stage, determining the onset of cohesive-zone compaction and the initial loss of permeability, while sinter dominated the final melting stage; the intermediate stage transitioned from pellet-like to sinter-like behaviour as liquid phases accumulated.

This result underscores a central point for cohesive-zone engineering: even in realistic mixed burdens, pellets largely dictate when and where the cohesive zone begins to form. Their softening and early deformation behaviour set the timing of permeability loss in the upper cohesive zone, making pellet design and quality control decisive for furnace stability.

Cohesive-zone performance is also strongly shaped by the chemistry and evolution of slag phases, a factor highlighted in several pellet-design studies. Guo et al. [45] examined how varying SiO_2 content influences compressive strength, reduction behaviour, and melting–dripping properties. They found that higher SiO_2 promotes the formation of $2FeO{\cdot}SiO_2$, which lowers CCS, reduces the attainable reduction degree, and degrades melting-dripping performance. Cai et al. [98] focused on medium-silica pellets with controlled CaO additions, showing that moderate basicity (~0.6) improves reducibility and reduces RSI and fine formation, but that further increases in basicity decrease the maximum pressure drop while widening the softening–melting interval due to the formation of more fluid CaO-rich slags. Fan et al. [109] added a microstructural perspective by analysing both pellet and sinter interfaces under non-load conditions, mapping the development of FeO-CaO-SiO_2-(MgO,Al_2O_3) slags and network iron at contact points, and linking these interfacial reactions to softening-melting behaviour and pressure-drop evolution. Taken together, these studies show that pellet behaviour in the cohesive zone is governed not only by reduction degree and temperature but also by the dynamic formation and flow of slag phases, as well as by cohesion among solids. Slag chemistry therefore becomes a decisive variable in determining permeability loss, cohesive-zone thickness, and the overall stability of the burden as it transitions from solid to semi-molten states.

Below the cohesive zone, in the dripping zone and hearth, the identity of individual pellets is effectively lost. Temperatures are high enough that the

semi-molten burden collapses into a mixture of slag and metallic iron, and the relevant questions shift from pellet mechanics to melt flow, slag-metal separation, and hearth drainage. The studies that address this region [98], [105], [106], [107], [110] therefore focus on meltdown temperatures, dripping rates, and the proportions of slag and metal that are evacuated versus retained. Shatokha and Velychko [106] observed that both slag and metal phases are only partially flows from crucibles during softening-melting tests, and that increasing gangue content raises the meltdown temperature, delaying the onset of dripping. Nishimura et al. [107] added that sinter tends to form a solid FeO-gangue framework that hinders melt reduction, whereas pellets do not exhibit this behaviour, leading to different melt-flow characteristics in the lower furnace. In this region, the burden no longer behaves as a granular assembly; instead, pellet-derived slag and metal contribute to the rheology, permeability, and drainage behaviour of the hearth. As a result, the direct mechanical of pellet behaviour, in terms of swelling, cracking, softening, effectively concludes at the lower cohesive zone, giving way to a melt-centric description governed by slag chemistry, liquid flow, and tapping dynamics.

II.3.4. Shaft furnaces: pellet behaviour from top to discharge

Gas-based shaft furnaces such as MIDREX and HyL can be divided into a top charging and preheating zone, a main reduction and metallisation zone, and a lower cooling and discharge zone. At the shaft top, pellets enter relatively cold and encounter upward-flowing preheating gases before reaching the active reduction front. Early reduction and swelling in this region follow the same mechanistic principles identified for the blast-furnace upper shaft, but with gas compositions dominated by H_2 and CO, which accelerate reduction and shift swelling behaviour toward higher temperatures and faster kinetics.

Kovtun et al. [111] provide one of the clearest mappings of this early behaviour under hydrogen-rich conditions. Studying pellet swelling in pure H_2 and N_2/H_2 atmospheres between 700 and 1000 °C, temperatures representative of the upper and middle sections of a gas-based shaft. They used standard RSI measurements and microstructural analysis to quantify swelling intensity and timing, founding that RSI increases with temperature in both atmospheres and exceeds 20 % above 900 °C. Moreover, peak swelling occurs extremely rapidly in pure H_2 (within about 5 minutes), whereas in N_2/H_2 mixtures it is delayed to 25–45 minutes depending on temperature. These results effectively chart the thermal and temporal window in which pellets are most vulnerable to swelling as they descend from the preheating zone into the active reduction zone of a hydrogen-rich shaft furnace.

Wang et al. [112], although working in the context of hydrogen-enriched blast-furnace operation, produced results that can be translated directly to gas-based shaft furnaces. Reducing pellets at 900 °C in a series of H_2-rich gas mixtures, they measured both RSI and compressive strength before and after

reduction. Their key observation, that post-reduction CCS increases with increasing H_2 fraction, is highly relevant for DR shafts, because it implies that pellets emerging from the upper reduction zone may be mechanically stronger, even if somewhat more swollen, when reduced predominantly by hydrogen. This dual effect, enhanced strength but accelerated swelling, helps define the mechanical state of pellets as they enter the main metallisation zone.

Huang et al. [86], [113] added another dimension by examining how thermal charging influences reduction kinetics and mechanical robustness in gas-based processes. By varying preheating regimes before exposing pellets to reducing gases, they altered the temperature history with which pellets entered the main reduction zone. Their results show that both reduction rate and compressive strength are sensitive to these preheating histories, demonstrating that the early thermal profile near the shaft top mechanically pre-conditions pellets for subsequent stages of reduction. In other words, the way pellets are heated before active reduction begins can either stabilise or weaken them for the high-temperature, high-conversion environment deeper in the shaft.

Finally, as presented in Section II.3.2, microstructural RDI-oriented studies such as those by Dwarapudi S. and Ranjan M. [86] and subsequently by Dishwar et al. [100] analyse directly pellet behaviour in the upper regions of DR shafts, where low-temperature degradation is most critical. By characterising commercial and highly fluxed DR pellets in terms of RDI, CCS, porosity, and bonding phases, these works identify microstructural configurations that minimise fines generation when pellets encounter strong reducing gases. They define the structural prerequisites for pellets to survive the transition from preheating into active reduction without excessive degradation, emphasizing that the processes used to manufacture lamps in order to obtain pellets also play a major role in the behavior of the solid phase during processing.

In the main reduction zone, pellets encounter high-temperature H_2/CO-rich gases and undergo the bulk of their metallisation. This is the region where internal cracking, swelling, and the evolution of mechanical strength become most consequential, as reduction proceeds rapidly and the pellet microstructure transforms from oxide to metallic iron. The study of Yi et al.'s, pellet disintegration under simulated shaft-furnace conditions, has already been presented [96] and it directly targets this part of the process. Using a vertical furnace with a temperature and gas profile approximating a MIDREX-type shaft, they reduced industrial pellets and examined the mechanisms by which they degrade as metallisation advanced, through surface chipping, spalling, or internal fracture. Although the abstract provides limited detail on specific materials and operating parameters, the study clearly captures the mechanical response of pellets as they progress through the active reduction zone. It therefore offers insight into how reduction-driven stresses, evolving porosity, and phase transformations interact to determine pellet integrity during the most intense stage of furnaces operation.

In the main reduction zone, pellets experience the highest reduction rates and undergo most of their metallisation under H_2/CO-rich gases. This is where the interplay between swelling, internal cracking, and evolving mechanical strength becomes most pronounced, as the oxide lattice collapses and metallic iron begins to form and sinter. Huang et al. [87] provide a mechanistic foundation for understanding strength evolution in this region. By reducing oxide pellets under controlled conditions and measuring compressive strength at different reduction degrees, they identified the microstructural origins of the initial strength drop: microcracks generated during the hematite to magnetite transition, decohesion at oxide/slag interfaces, and the development of new porosity. Strength recovers only later, once wustite begins to transform into metallic iron and sintering consolidates the structure. This non-monotonic strength trajectory is central to the mid-shaft, where pellets are neither fully oxidised nor fully metallised and are therefore most vulnerable to mechanical damage.

Gupta R. and Gautam J. [114] extended the picture into the fully metallised regime, studying the strength of directly reduced pellets as a function of reduction temperature (up to 1250 °C), sintering time, additive content, and solid reductant type. They reported that cold-crushing strength can vary dramatically, from as low as 5 kg to as high as 200 kg, depending on processing conditions, and that higher temperatures and longer sintering times promote metallic bonding and ductile behaviour. Although their experiments were not tied to a specific reactor geometry, the conditions correspond closely to the lower part of the main reduction zone, where metallisation approaches completion and the metallic skeleton begins to densify.

These studies [87], [114] outline the mechanical evolution of pellets across the active reduction zone: an initial weakening driven by phase transitions and microcracking, followed by progressive strengthening as metallic iron forms and sinters. This trajectory determines how pellets withstand the stresses of descent and gas flow before entering the cooling and discharge zone.

Zhu et al. [115] reinforce this observations by showing that preheated pellets, initially weak due to their high porosity, develop into strong, intact metallised pellets by the end of reduction as a continuous iron network forms. Their results align closely with the observations of Kovtun [93] and Wang [97] in hydrogen-rich atmospheres, illustrating a general pattern across DR processes: pellets pass through a window of maximum mechanical vulnerability during the early reduction stages, when phase transformations, swelling, and microcracking dominate, before progressively strengthening as metallic iron nucleates, grows, and sinters into a coherent load-bearing skeleton.

In the lower shaft and discharge region, reduction is essentially complete and pellets have transitioned into direct-reduced iron (DRI). At this stage, chemical transformations no longer govern behaviour; instead, mechanical degradation driven by movement, collisions, and handling becomes the dominant concern. Pellets may chip, abrade, or fracture as they descend and

are discharged, and the fines generated in this region can have disproportionate operational consequences.

As presented, Boechat et al. [116] addressed this issue directly by quantifying the susceptibility of industrial DRI pellets to mechanical degradation. Subjecting reduced pellets to controlled impact tests, they distinguished between surface chipping and full body breakage and related fines generation to both impact energy and intrinsic pellet strength. Their key conclusion is that fines produced inside the DR furnace, through impact-induced breakage rather than feed contamination, are particularly harmful for the process effiicency, promoting cluster formation and reducing gas permeability even when the feed has been carefully screened. This work therefore characterises pellet behaviour in the lower shaft and discharge zone, where mechanical forces dominate and the structural integrity of fully metallised pellets becomes critical for maintaining smooth furnace operation.

A more detailed description of how this information was used to develop DEM-CFD models capable of predicting the behavior of the solid phase is presented in Section II.3.5. The DEM models, calibrated with data from literature and targeted experiments, were developed to calculate the collision energies experienced by pellets during their fall, describing their mechanical degradation.

When these studies are aligned along the vertical axes of blast and shaft furnaces, a coherent progression of pellet behaviour emerges. In the upper regions, pellets are largely unreduced, and their response is governed by early reduction, swelling, and low-temperature degradation. In the middle and lower shafts, where wustite and metallic iron form, pellets encounter their window of maximum mechanical vulnerability: swelling peaks, strength reaches its minimum, and behaviour becomes highly sensitive to gas composition (CO/H_2), reduction rate, circulating elements, and pellet microstructure. Finally, in the lower DR shaft, pellet identity persists even though susceptible to impact-induced fragmentation, where DEM-based studies capturs this last stage of mechanical degradation.

II.3.5. Modelling of Direct-Reduction Shaft Furnaces

Great progress has been made in simulating the behaviour of complex systems such as the direct reduction of iron oxides, thanks especially to the increasing use of DEM, CFD, and multi-physics modelling tools [118], [119]. These approaches have enabled researchers to analyse not only the chemical conversion of iron oxides but also the hydrodynamics, heat transfer, and mechanical stability of pellets inside MIDREX-type shaft furnaces [117], [118], [119]. A series of recent studies has significantly advanced the understanding of gas–solid interactions, pellet behaviour, and operational performance in these reactors.

Shams A. and Moazeni F. [117] developed a comprehensive mathematical model of the MIDREX shaft furnace, explicitly resolving the reduction, transition, and cooling zones. Their formulation couples mass and energy balances for both phases, applies the unreacted shrinking-core model to pellet reduction, and incorporates equilibrium chemistry in the lower zones. The model is parameterised using industrial operating conditions from the Gilmore MIDREX plant: reducing gas at 930 °C, 1.4 bar, and 53,863 Nm^3/h, hematite pellets of ~10 mm fed at 26.4 t/h, and cooling gas at 43 °C and 11,800 Nm^3/h. By solving the resulting system of differential and algebraic equations, the model predicts temperature, composition, pressure, and metallization profiles along the furnace height. Validation against industrial data showed strong agreement, enabling the authors to explore operational sensitivities such as reactor length, cooling-gas flow, and natural-gas addition. This work demonstrates how the thermal and chemical balance of the furnace governs metallization efficiency and energy consumption, offering a predictive tool for process optimisation across the entire furnace.

On the other hand, building on the need to understand pellet behaviour under realistic furnace conditions, Zare Ghadi et al. [118] introduced a two-dimensional CFD model of the MIDREX reduction zone, treating the furnace as a counter-current moving bed with detailed gas-solid heat and mass transfer. Their work focused on the effect of gas-injection configuration, comparing single and dual hydrogen-inlet systems under conditions representative of the Mobarakeh Steel plant (gas at 1174 K, 177,180 Nm^3/h, pellets of 11 mm, bed porosity 0.562, reactor radius 2.75 m). By solving continuity, momentum, species, and energy equations for both phases, again coupled with a shrinking-core reaction model, the study revealed that dual injection improves radial gas distribution, enhances reduction uniformity, and reduces overall energy demand. This contribution shows that furnace hydrodynamics and injection design directly influence reduction kinetics, gas utilisation, and thermal efficiency. In practice, this means that modifying the gas-injection strategy can mitigate maldistribution, reduce dead zones, and improve productivity without altering the furnace geometry.

A complementary perspective is offered by Petit et al. [120], who examined the mechanical degradation of iron ore pellets and its consequences for gas flow inside a MIDREX furnace. Using a hybrid simulation framework that integrates DEM, continuum damage mechanics, and CFD–KTGF, the authors quantified how pellet–pellet collisions generate fines during descent and how these fragments alter gas velocity fields and pressure drop. Their simulations, based on MINIMOD MIDREX conditions (pellets ~12 mm, gas at 1100 K, 1.4 bar, 53,863 Nm^3/h, solids at 26.4 t/h), showed that even small amounts of degradation, on the order of 2–4% fines that is a quantity typically observed during the pellets transport, can significantly reduce bed permeability, promote gas maldistribution, and increase the risk of clustering. Therefore, this paper addresses more closely the effects of fragmentation underlining a

critical operational issue: fines not only reduce the permeability of the bed, lowering gas-solid contact efficiency, but also act as adhesive particles that promote sticking and agglomeration, potentially leading to channeling, unstable pressure drop, and reduced metallization. By linking mechanical stressing events to fines generation and then to gas-flow perturbations, the study provides a mechanistic explanation for several operational instabilities observed in industrial DR furnaces.

Overall, these contributions demonstrate that modern multiphysics modelling, whether focused on reactor-scale transport phenomena, gas-injection strategies, or pellet-scale mechanical degradation, are able to provide essential insight into the coupled chemical, thermal, and mechanical processes governing the performance of MIDREX-type furnaces. For the purposes of this thesis, these studies collectively highlight the need to treat pellet behaviour not as a static material property but as an evolving response to reduction conditions, gas flow, and mechanical loading. Understanding how pellets transform, weaken, fragment, and interact with the surrounding gas phase is therefore fundamental for predicting reactor performance, diagnosing operational instabilities, and ultimately improving the reliability and efficiency of direct-reduction processes.

III. Design and Construction of the Innovative Prototype

III.1. Operative Conditions of the Shaft Furnace

The design of a custom-built prototype is driven by the need to replicate, at laboratory scale, the critical operating conditions that govern particulate flow behaviour in industrial processes. These conditions include temperature, compressive stress, and the composition of the reacting atmosphere: each exerting a distinct influence on the mechanical and chemical evolution of the solid phase.

Compressive stress arises from the mechanical load imposed by overlying layers of material as the bed descends within the furnace. This stress affects particle rearrangement, densification, cohesion, and surface integrity, often leading to deformation or fragmentation of pellets. Accurate control of this parameter is essential to simulate realistic flow dynamics and structural transformations. Temperature plays a central role in activating reduction reactions, promoting sintering, and inducing surface and phase changes, including partial melting. Meanwhile, the gas atmosphere, particularly its hydrogen content, shapes the reduction pathways and efficiency. High hydrogen concentrations can lead to disruptions in the crystal lattice, increased porosity, and enhanced fragility of the solid matrix. Together, these factors define a complex and interdependent environment in which iron-bearing materials undergo deformation, chemical transformation, and flow. Capturing this behaviour with precision requires a tailored experimental setup capable of reproducing severe process conditions, beyond the capabilities of standard commercial equipment.

As discussed in Section I.2, direct reduction (DR) processes involving iron ore pellets typically reach temperatures up to 1050 °C, particularly in hydrogen-rich environments. In conventional DR setups, pellets are exposed to a gaseous mixture containing approximately 60% hydrogen, a condition already implemented in plants. However, despite the operational feasibility of

these conditions, the mechanical behaviour of the solid phase under such thermal and chemical loads remains poorly understood. In line with the objectives of the MaxH2DR project, it is essential to investigate the flow behaviour of the solid under atmospheres with significantly higher hydrogen concentrations, which may induce different reduction kinetics and cohesion dynamics.

In contrast to temperature and gas composition, compressive stress remains an underexplored parameter. The literature offers no direct measurements of the mechanical loads experienced by pellets during reduction, and furnace designs are often based on empirical knowledge rather than quantitative stress analysis. Although this has led to a marginal role for stress estimation in furnace construction, it is nonetheless a critical factor in determining the deformation, densification, and flowability of the solid phase.

To estimate the compressive stress acting on the solid phase during reduction, a geometric analogy was drawn between the operating conditions inside a reduction furnace and those observed in silos used to store granular materials. By considering a silo equipped with a conical hopper at its base and analysing its behaviour during discharge operation, it becomes evident that the solid undergoes a flow regime characterized by a non-uniform stress distribution. This distribution varies with depth and radial position, closely resembling the mechanical environment encountered in furnaces during the conversion of iron oxides.

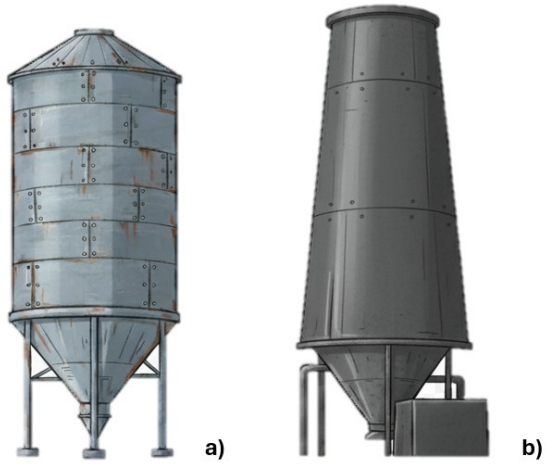

Figure III.1 Schematic representation of (a) a silo for storage and feeding of granular solid materials, and (b) a shaft furnace.

Given this similarity, established models used in silo design were adopted to approximate the stress components within the furnace. These models allow for the estimation of vertical and horizontal stresses as a function of depth and material properties. In particular, the mathematical framework developed by

Janssen (Sperl, 2006)[34](Sperl, 2006) for cylindrical systems was applied. This approach accounts for the effects of wall friction and stress saturation, providing a realistic estimate of the maximum compressive stress that can be exerted on the solid phase in an industrial-scale furnace.

$$\sigma_{yy} = \frac{\rho_b g D}{4 K \mu_w}\left[1 - exp\left(-\frac{4 K \mu_w z}{D}\right)\right] \tag{50}$$

Eq. (50) corresponds to the classical Janssen formulation, which enables the estimation of the vertical component of the normal stress acting on a horizontal cross-section within a cylindrical container. This stress arises from the weight of the overlying granular material and is influenced by several key parameters: the bulk density of the solid ρ_b, the gravitational acceleration g, the depth from the free surface z, and the diameter of the cylindrical section D. A central element of the model is the lateral stress ratio K, which defines the proportion between horizontal and vertical stresses and reflects the internal friction characteristics of the material. The equation also incorporates the wall friction coefficient μ_w, which accounts for the interaction between the solid and the container walls. The combined influence of these parameters governs the rate at which vertical stress saturates with depth, primarily due to the redistribution of load toward the container walls. At sufficient depths, the Janssen equation (eq. (50)) can be simplified.

$$\sigma_{yy}\big|_{y>10D} \cong \sigma_{yy}\big|_{y\to\infty} \propto \rho_b g D \tag{51}$$

As shown in eq. (51), the vertical stress component approaches a constant value, which is proportional to the product of the solid's bulk density, gravitational acceleration, and the diameter of the cylindrical section under consideration.

Assuming a conservative estimate for the bulk density of the solid phase at 2500 kg/m³, and a furnace diameter of approximately 7 m, the resulting vertical normal stress reaches 300 kPa. This value represents the upper bound of compressive stress that the solid phase may experience under realistic process conditions during the direct reduction.

Nevertheless, the operating window was intentionally expanded to allow the equipment to investigate more demanding mechanical conditions and to enhance its versatility. In particular, the stress range was extended up to 800 kPa, a value representative of the compressive loads typically encountered in traditional blast-furnace processes. On this basis, the design phase incorporated both the realistic operating stress of 300 kPa and the higher limit of 800 kPa, ensuring that the system could accommodate and analyse the full spectrum of conditions relevant to industrial reduction technologies.

Therefore, the following operating conditions for the analyses were considered during the design phase.

- High temperatures, reaching up to 1000 °C.

- Elevated hydrogen concentrations, ranging from 55 percent to 100 percent by weight.
- Maximum compressive stress, approaching 800 kPa.

As outlined in Section II.3, these conditions cannot be simultaneously reproduced using commercially available equipment. It is therefore essential to design and construct a robust experimental unit capable of operating under such extreme conditions, while ensuring safe and controlled testing procedures.

Another aspect to be addressed later in this work concerns the scale and nature of the solid materials involved. Existing mathematical models and experimental protocols are typically developed for granular solids with particle sizes below a few millimetres. Consequently, the characterization of larger or more complex particulate systems will require the integration of Discrete Element Method (DEM) modelling. This component of the MaxH2DR project is being developed by project partners and, while it is not the central focus of this thesis, it will be discussed in relation to the validation of experimental procedures. The combined use of experimental data and DEM simulations will extend the applicability of the developed apparatus, enabling both the characterization of fine particulate materials and the calibration of numerical models for predicting the flow behaviour of granular solids, such as iron oxide pellets.

III.2. Design implications of hydrogen-rich atmospheres

Although hydrogen is widely recognized as a cornerstone of the clean energy transition, its application under extreme conditions, such as those encountered in green steel production, ammonia synthesis, and methanol reforming, presents significant engineering challenges. The primary difficulty lies in hydrogen's high chemical reactivity at elevated temperatures, which can severely compromise the integrity of structural materials.

Many commonly used industrial alloys, including ferritic steels, cast irons, nickel-based alloys, and titanium alloys, exhibit poor resistance to hydrogen-induced degradation under such conditions [122]. These materials are often unsuitable for constructing experimental units or process equipment exposed to high temperatures, compressive loads, and torsional stress. While steels, iron-carbon alloys, are widely employed due to their mechanical robustness and versatility, they are not immune to hydrogen-related damage. Two major degradation mechanisms must be considered: High-Temperature Hydrogen Attack (HTHA) and Hydrogen Embrittlement (HE).

HTHA occurs when molecular hydrogen dissociates into atomic hydrogen at elevated temperatures. The atomic hydrogen diffuses into the steel's crystal lattice and reacts with carbon atoms in iron carbides (cementite, Fe_3C), forming methane gas (CH_4) [123]. This gas poses two critical problems. First, methane molecules are too large to diffuse out of the steel and become trapped

at microstructural features such as grain boundaries. The accumulation of methane generates internal pressure, leading to the formation of micro-cracks, fissures, and blisters that compromise structural integrity. Second, the reaction depletes the steel's carbon content, a process known as decarburization, which weakens the matrix by removing the primary source of strength. The combined effect is a severe reduction in both strength and ductility. Notably, HTHA can begin at temperatures as low as 200 °C, especially under high hydrogen partial pressures.

At lower temperatures, Hydrogen Embrittlement (HE) becomes the dominant concern. Unlike HTHA, HE does not involve methane formation. Instead, atomic hydrogen enters the metal through processes such as welding, electroplating, or corrosion, and diffuses into regions of high stress, such as crack tips or grain boundaries. Even at concentrations as low as parts per million, this hydrogen can initiate failure through mechanisms that remain under active investigation [124]. Two prevailing theories are:

- Hydrogen-Enhanced Decohesion (HEDE): Hydrogen atoms weaken the metallic bonds between iron atoms, reducing cohesion and facilitating crack propagation.
- Hydrogen-Enhanced Localized Plasticity (HELP): Hydrogen increases local plasticity at the crack tip, promoting intense deformation that rapidly exhausts the material's ability to accommodate strain, resulting in brittle failure [125].

Both phenomena underscore the need for careful material selection and environmental control when designing systems for hydrogen-rich, high-temperature applications, but a choice can be made based on the composition of the steel.

Steel classification is primarily based on microstructure, the specific arrangement of atoms within the crystal lattice. This internal structure, shaped by chemical composition and thermal treatment, governs the mechanical and physical properties of the alloy and determines its suitability for various applications.

Among the main categories:

- Ferritic steels contain chromium as the principal alloying element, with little or no nickel. They exhibit a ferritic microstructure, are magnetic, and offer moderate corrosion resistance in less aggressive environments. Although they are less ductile and weldable than austenitic grades, their lower cost makes them suitable for applications such as household appliances, exhaust systems, and heat exchangers.
- Martensitic steels are defined by a moderate chromium content and sufficient carbon to enable hardening through tempering. Following heat treatment, they develop a martensitic structure that provides high hardness and wear resistance. However, they are more brittle and less corrosion-resistant than other steel families. These steels are

commonly used in cutting tools, mechanical components, and structural parts requiring high surface durability.

- Austenitic steels are the most widely used stainless steels. Their high chromium and nickel content ensures excellent corrosion resistance, good formability, and stable austenitic structure at room temperature. They are generally non-magnetic and are employed in sectors such as food processing, pharmaceuticals, and chemical manufacturing. Common examples include AISI 304 and AISI 316.

For high-temperature applications, material selection must consider hot strength, thermal stability, and oxidation resistance. The long-term mechanical performance of steels at elevated temperatures depends on their ability to resist deformation, maintain structural integrity, and withstand chemical attack. Chromium plays a central role in oxidation resistance. To ensure stability at temperatures approaching 1093 °C, a chromium concentration of at least 25 percent is required. However, repeated thermal cycling can lead to expansion and contraction, causing cracking and cleavage that increase susceptibility to corrosion and hydrogen attack.

Nickel contributes to structural resilience by reducing cleavage tendency and minimizing thermal mismatch between the metal and its oxide layer. This behaviour reduces interfacial stress during cooling and enhances durability. For hydrogen-rich environments, alloys must contain 18 to 20 percent chromium and 8 to 20 percent nickel, along with extremely low carbon content to mitigate hydrogen-induced degradation. These compositional constraints significantly narrow the range of suitable materials.

While AISI 304 and 316 offer acceptable performance under moderate conditions, components exposed to the highest mechanical and thermal loads were manufactured using AISI 310 [126], [127], a less common austenitic stainless steel. Its elevated chromium and nickel content, combined with minimal carbon, provides superior resistance to high-temperature hydrogen environments and better retention of mechanical properties under severe operating conditions. The detailed composition of AISI 310 is presented in Table III.1.

Table III.1 Chemical composition of AISI 310.

AISI 310

C	Mn	P	S	Si	Cr	Ni
0.25	2.00	0.015	0.030	1.5	24.00÷26.00	19.00÷22.00

The mechanical properties relevant to short-term loading and elastic behaviour are summarized in Table III.2, which focuses on the temperature range between 800 and 1000 °C. Although elastic properties become less significant at elevated temperatures, where material behaviour is increasingly

governed by creep and time-dependent plastic deformation, they remain essential for the preliminary design and dimensional definition of structural components.
Due to the limited relevance of elasticity at high temperatures, such parameters are often omitted from supplier datasheets and are scarcely documented in the literature .
An illustrative example is provided by the work of Amirkhiz et al.[128], [129], [130], who investigated the high-temperature creep behaviour of a commercial AISI 310S stainless steel containing fine titanium-based precipitates. Cylindrical specimens machined along the rolling direction were subjected to uniaxial creep at 1073 K and 1123 K across a broad range of applied stresses, with additional interrupted tests at 20 MPa to capture microstructural states representative of primary and secondary creep. At 1073 K the material exhibited rupture lives decreasing from 58.6 h at 80 MPa to more than 18 000 h at 20 MPa, providing a clear framework for interpreting the stress–temperature dependence of creep resistance in this alloy.
Nevertheless, for the purpose of mechanical modelling and component size design, it was necessary to estimate these values. Starting from available data at lower temperatures, the elastic parameters were extrapolated using a regression model that best fits the material's behaviour across the full temperature range from 25 to 1000 °C (Figure III.2 III.2). This approach ensures continuity in the mechanical characterization and supports the accurate definition of stress distributions and deformation limits within the experimental apparatus.

Table III.2 mechanical properties of AISI 310 at different temperatures.

Temperature [°C]	800	900	1000
Short-term [MPa]			
Ultimate Tensile Strength	~215	~135	~85
0.2% Offset Yield Strength	~110	~90	~58 (ext.)
Elastic properties [GPa]			
Young's Modulus	~49	~45 (ext.)	~43 (ext.)
Shear Modulus	~134	~126 (ext.)	~118 (ext.)
Thermal properties			

Mean Coefficient of Linear Thermal expansion*10^{-6}/K	19.1	19.8 (ext.)	20.9 (ext.)
Thermal Conductivity [W/(m*K)]	24.5	26	27.7

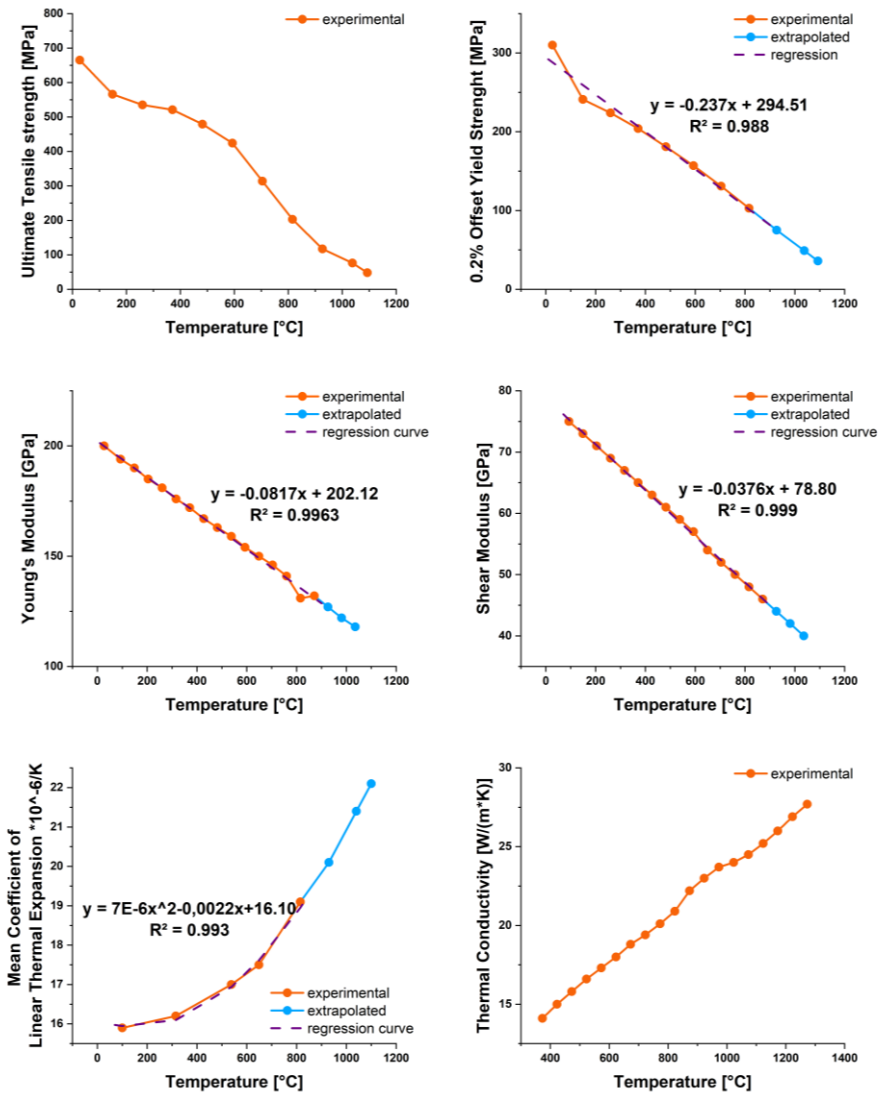

Figure III.2 Temperature-dependent properties of Iron AISI 310. Experimental values from literature are shown in blue, extrapolated values in orange, and regression curves in purple, including the curve fitted to the experimental data.

Achieving high operating temperatures requires placing the test material in direct contact with the heating environment, typically within a furnace. When the reacting atmosphere contains hydrogen, the selection of suitable materials

becomes significantly constrained not only for structural components and test fixtures, but also for the thermal insulation surrounding the hot zone.

Hydrogen's chemical aggressiveness at elevated temperatures severely limits the use of conventional refractory materials. In particular, materials containing silica oxide (SiO_2) must be categorically excluded. These materials include most commercially available and cost-effective refractories, such as fireclays, castables, and aluminosilicates like mullite, which rely on a silica or silicate glass phase for structural cohesion.

At temperatures around 1000 °C, hydrogen reacts with solid silica to form volatile silicon monoxide (SiO) and water vapor. This reaction initiates rapid embrittlement of the refractory, leading to progressive degradation through crumbling and gasification. The hydrogen selectively leaches the SiO_2 component from the material's chemical matrix, leaving behind a weakened and porous residue that cannot maintain mechanical integrity. This process results in premature structural failure, making silica-based refractories unsuitable for hydrogen-rich, high-temperature environments.

As a result, the furnace design of the furnace and its insulation system must include alternative materials capable of withstanding both elevated temperatures and chemical reactivity. Among the most suitable options are alumina (Al_2O_3) and magnesia (MgO) [131], which exhibit excellent thermal stability and resistance to hydrogen-induced degradation. These oxides maintain their structural integrity at temperatures exceeding 1000 °C and do not participate in the volatile reactions that compromise silica-containing materials.

The use of such chemically inert and thermally robust refractories is essential to ensure the long-term durability and operational safety of experimental setups intended to replicate the severe conditions of hydrogen-based reduction processes.

III.3. Prototype design

Following the evaluation of the advantages outlined in Section II.1.5, the rotational shear cell was selected as the core measurement principle for the experimental prototype. This choice defines the design of the surrounding mechanical components, which were developed to ensure compatibility with the shear cell's geometry and operating requirements. The entire assembly was modelled and integrated in SolidWorks, enabling detailed verification of spatial constraints, mechanical alignment, and functional coherence across all subsystems. This section presents only the three-dimensional representations of the main components. For a comprehensive description, including the corresponding orthogonal projections, Appendix A should be referred to.

III.3.1. Maximum distortion energy: Von Mises' criterion

The von Mises maximum distortion energy criterion [132] was widely employed to evaluate the structural integrity of components subjected to complex stress states; particularly effective for ductile materials such as steel, which exhibit similar behaviour under tensile and compressive loading. It provides a scalar measure of the stress state, the von Mises equivalent stress, which can be directly compared to the material's yield strength.

To formalize the criterion, the stress tensor S is decomposed into a hydrostatic part, representing the mean normal stress, and a deviatoric part, representing the shear-induced distortions.

$$[S] = \begin{bmatrix} \sigma_{xx} & \tau_{yx} & \tau_{zx} \\ \tau_{xy} & \sigma_{yy} & \tau_{zy} \\ \tau_{xz} & \tau_{yz} & \sigma_{zz} \end{bmatrix} = \\ = \begin{bmatrix} \sigma_p & 0 & 0 \\ 0 & \sigma_p & 0 \\ 0 & 0 & \sigma_p \end{bmatrix} + \begin{bmatrix} \sigma_{xx} - \sigma_p & \tau_{yx} & \tau_{zx} \\ \tau_{xy} & \sigma_{yy} - \sigma_p & \tau_{zy} \\ \tau_{xz} & \tau_{yz} & \sigma_{zz} - \sigma_p \end{bmatrix} \tag{52}$$

The hydrostatic stress state is characterized by principal stresses σ_p, equal to each other:

$$\sigma_p = \frac{\sigma_{xx} + \sigma_{yy} + \sigma_{zz}}{3} \tag{53}$$

The deviatoric stress tensor captures the differential stresses responsible for plastic deformation. The criterion is grounded in the concept of strain energy decomposition, where the total elastic strain energy U_T is separated into two components: volumetric energy (associated with uniform dilation or compression) U_V, and distortion energy (associated with shape change) U_D. Since yielding in ductile materials is primarily governed by distortional effects rather than volumetric changes, the von Mises approach focuses exclusively on the deviatoric component of the stress tensor. The general definition of U_T is:

$$U_T = \frac{1}{2}(\sigma_{xx}\epsilon_x + \sigma_{yy}\epsilon_y + \sigma_{zz}\epsilon_z) \tag{54}$$

where ϵ_i is the strain in the i direction. The total elastic strain energy, U_T,can be expressed using Hooke's law:

$$U_T = \frac{1}{2E}[\sigma_{xx}^2 + \sigma_{xx}^2 + \sigma_{xx}^2 - 2\nu(\sigma_{xx}\sigma_{yy} + \sigma_{yy}\sigma_{zz} + \sigma_{zz}\sigma_{xx})] \tag{55}$$

and the distortion energy U_d can be estimated, by definition, between the difference of U_t and U_v:

$$U_V = \frac{1-2\nu}{6E}\left(\sigma_{xx}+\sigma_{yy}+\sigma_{zz}\right)^2 \tag{56}$$

$$U_D = \frac{1+\nu}{6E}\left[\left(\sigma_{xx}-\sigma_{yy}\right)^2+\left(\sigma_{yy}-\sigma_{zz}\right)^2+(\sigma_{zz}-\sigma_{xx})^2\right] \tag{57}$$

The von Mises criterion states that yielding occurs when the distortion energy exceeds a critical threshold:

$$U_D \geq U_{D_l} = \frac{1+\nu}{3E}\cdot\sigma_{amm} \tag{58}$$

Where U_{D_l} represents the limit distortion energy, ν is the Poisson's ratio, E is the Young's modulus, and σ_{amm} is the yield stress, which indicates the transition between elastic and plastic deformation of the material.
Substituting eq. (57) into eq. (58) and simplifying, we obtain the final expression for the distortion energy in terms of the stress components and elastic constants.

$$\frac{1}{\sqrt{2}}\sqrt{\left[\left(\sigma_{xx}-\sigma_{yy}\right)^2+\left(\sigma_{yy}-\sigma_{zz}\right)^2+(\sigma_{zz}-\sigma_{xx})^2\right]} \geq \sigma_{amm} \tag{59}$$

This formulation allows the direct evaluation of the von Mises equivalent stress $\sigma_{eq,vM}$, on the right side of the inequation, which can then be compared to the material's yield strength to assess the onset of plastic deformation and in practical applications, the $\sigma_{eq,vM}$ must be evaluated at the location experiencing the highest combined loading. For components subject to biaxial or triaxial stress states, the uniaxial formulation is extended using the general expression for von Mises stress, which incorporates both normal stresses σ and shear stresses τ.

$$\sigma_{eq_{vM}} = \sqrt{\sigma_{xx}^2+\sigma_{yy}^2-\sigma_{xx}\sigma_{yy}+3\tau_{xy}^2} = \sqrt{\sigma^2+3\tau^2} \tag{60}$$

$$\sigma = \frac{N}{A} \tag{61}$$

$$\tau = \frac{M_e \cdot y}{I_P} \tag{62}$$

Where N it is the total normal force applied, A is the cross section, M_e is the applied moment, y is the distance from the neutral axis, and I_p is the polar moment of the cross-section.

Shear stress contributions are often calculated from bending M_b and torsional M_t moments using the relation:

$$M_e = \sqrt{M_b^2 + \frac{3}{4}M_t^2} \tag{63}$$

To ensure structural safety and prevent permanent deformation, the design must satisfy the inequality:

$$\sigma_{eq,vM} < \sigma_{adm} \tag{64}$$

From this condition, the minimum allowable cross-sectional dimensions can be determined, ensuring that the material remains within the elastic regime under the expected loading conditions.

III.3.2. Shear cell

Figure III.3 shows the shear cell in cross-section (a), which provides information on the specific position of the two components during the experimental test. It is composed of two fundamental parts: the lid (b) and the trough (c). The construction material is AISI310 steel.

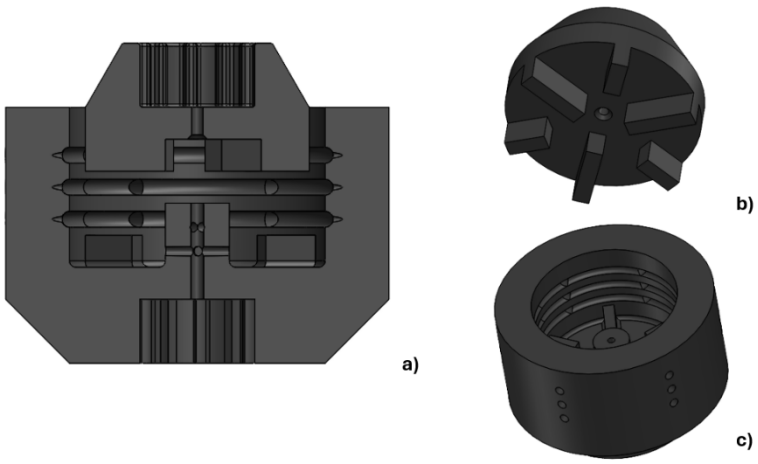

Figure III.3 Shear cell designed in SolidWorks: (a) sectional view, (b) lid, and (c) trough.

The geometry adopted for the designed shear cell follows the general layout of commercial devices but introduces several modifications aimed at overcoming their inherent limitations. The wall and lid thicknesses were increased to guarantee adequate mechanical strength even under the most severe operating conditions considered in this work. A further improvement concerns the volume available to the sample: commercial shear cells typically

accommodate only shallow beds of material, which is unsuitable for the characterization of coarse granular systems. In the present case, the need to investigate an unconventional solid phase with particle sizes exceeding 10 mm required a substantially larger trough, capable of hosting multiple layers of pellets and ensuring a representative number of interacting particles. This configuration minimizes wall effects and allows the sample to consist of at least thirty pellets, a number far greater than what can be achieved with standard equipment. Such a departure from traditional geometries, however, introduces features that must be analysed through DEM modelling to fully capture their mechanical implications. Although even larger volumes could have been considered, an excessive increase would have significantly prolonged the time required to achieve thermal uniformity within the solid and would have led to higher internal stress gradients. The final design therefore represents a compromise between mechanical robustness, thermal manageability, and the need for a sufficiently large representative volume of material.

The lid, Figure III.3.b, has a cylindrical cross-section with a diameter of 70 mm and a height of 40 mm and will be kept stationary during the test. The surface of the lid in contact with the sample is equipped with six radially arranged vanes, each with a rectangular cross-section. Two diverse types of vanes were manufactured and alternated, each offset by 60 degrees to improve performance. The shortest vanes measure 6(t) x 10(h) x 15(w), while the longest are 6(t) x 10(h) x 25(w). Compared to conventional devices, which also feature fins, the thickness of the fins on the lid features an unconventional geometry. This geometry was chosen to ensure the blades' mechanical strength at elevated temperatures and under normal stress conditions, thanks to their high thickness. The use of two types of blades also extends the prototype's versatility, particularly when working with coarse particulate materials. On the side opposite the material, there is an toothed insert that allows for a perfect fit between the lid and the rod that connects it to the remaining components of the structure. In this case too, the geometry and contact surface between the two elements were defined to ensure proper operation and prevent deformation under high stresses, even at elevated temperatures.

The ability to withstand stress was verified using the SolidWorks tool to determine deformations, using the material properties under limiting conditions.

The simulations were conducted using the Static Analysis module in SolidWorks. This tool requires several inputs: the geometry under investigation, the material properties of the solid, and the definition of constraints and external loads, selected according to the type of analysis.

Figure III.4 illustrates the case study of the lid.

- Figure III.4.a depicts the insert with a defined tooth profile. The side surfaces of the tooth, oriented opposite to the motion, were constrained (indicated by green arrows). This condition reflects the

physical coupling of the lid with the upper rod, which prevents the lid rotation.

- Figure III.4.b shows the torsional load applied to the lower surfaces of the fins, the region in contact with the rotating solid. The applied torque was set to 100 Nm, the estimated maximum, with clockwise rotation aligned to the lid's axis of symmetry.
- Figure III.4.c highlights the lid surface in contact with the solid. Although the load originates from the opposite direction, the reaction force exerted by the solid was included to ensure accurate simulation. Here, the maximum load considered was 5000 N.

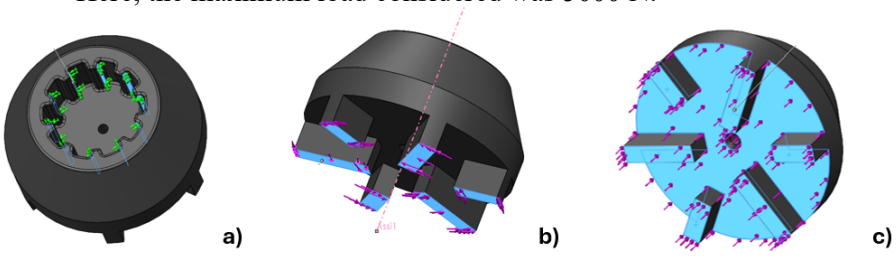

Figure III.4 3D view of the lid modelled in SolidWorks. Surfaces subjected to forces are highlighted in blue; constraints are indicated by green arrows, while external stresses are represented by pink arrows. a) Fixed constraint applied to the cavity teeth, b) torsional loading of the lid, c) reaction of the solid under normal stress.

The SolidWorks simulation provides key outputs, including the von Mises equivalent stress and the ESTRN (Equivalent Strain), as shown in Figure III.5.

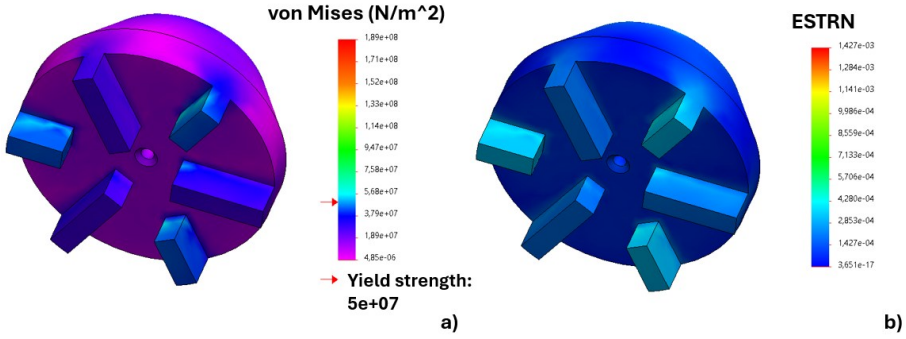

Figure III.5 Simulation results obtained using SolidWorks. a) von Mises equivalent stress, b) equivalent strain (ESTRN).

Figure III.5.a presents the stress distribution across the lid, visualized through a colour gradient. The colour scale on the right is used to show the intensity of $\sigma_{eq,vM}$ and the material's yield strength, calculated based on its properties at 1000 °C is indicated by a red arrow. The analysis reveals that the vanes are the most stressed components, particularly those with the lowest width, which exhibit the highest stress concentrations. Light blue regions correspond to

stress levels near the yield strength (5×10^7 N/m²), but these are confined to small areas and do not compromise the structural integrity of the lid during operation.

Figure III.5.b illustrates the ESTRN distribution. Once the material reaches its yield strength, stress no longer increases linearly, but plastic deformation continues. In such cases, ESTRN becomes the most reliable indicator of permanent deformation. The strain deformation is computed using eq. (65), which derives a dimensionless scalar representative of the equivalent deformation, ϵ_{eq}, that comes from the distortion energy acting in three directions that leads the solid corresponding solid deformation, ϵ_i.

$$\epsilon_{eq} = \frac{\sqrt{2}}{3}\sqrt{\left(\epsilon_x - \epsilon_y\right)^2 + \left(\epsilon_y - \epsilon_z\right)^2 + (\epsilon_z - \epsilon_x)^2} \tag{65}$$

The maximum strain observed in the most stressed regions is approximately 4×10^{-4} mm/mm, a negligible value considering the vane thickness.

Although increasing the vane thickness could further reduce stress intensities, it would significantly narrow the vane spacing, limiting the volume available for material accumulation. Therefore, the current geometry is considered optimized for both mechanical performance and functional efficiency.

The rotating trough, Figure III.3.c, houses the sample during testing and features an internal diameter of 80 mm, a height of 50 mm, and an internal volume of about 250 ml. Centrally positioned within the trough is a gas distributor, measuring 20 mm in both diameter and height, designed to deliver the process gases through 4 mm perforations. To enhance gas percolation and ensure uniform flow throughout the particulate bed, the inner wall of the trough has been machined with hemicylindrical cavities. Each cavity is fitted with 5 mm exhaust holes drilled perpendicularly through the 20 mm-thick wall, enabling the injected gas to diffuse efficiently into the surrounding volume and ensuring uniform distribution throughout the cell. Similar to the lid, the trough features a recess on the surface opposite to the one in contact with the particulate material. This recess has a similar geometry to that of the lid and is designed to accommodate the connecting rod, enabling secure coupling and effective transmission of rotational motion.

As previously described, the lid and the trough together constitute the core of the shear cell. Once these geometries were defined, the next step was to specify the two components required to conduct the experimental tests. In analogy with the Schulze-type rotational shear cell, the trough is designed to rotate alternately in both directions, while the lid has the main function to apply a compressive load on the sample. The lid must remain vertically mobile to accommodate volumetric changes in the particulate bed, yet be constrained against rotation.

To achieve this, the lid must be guaranteed to move in the vertical direction, while all rotational degrees of freedom are mechanically restricted.

Additionally, the force required to maintain this constraint must be estimated to ensure that the lid remains stationary under the applied torque. These conditions are to be verified and maintained under ambient temperature.
With the operational procedure defined, the remaining components required to complete the prototype can be identified. These include: a compression system to apply and control the normal load, a mechanical constraint to prevent lid rotation while allowing vertical displacement; a force sensor to monitor the applied load; a rotary motor to drive the trough; and a furnace to enable high-temperature operation during future test campaigns. In addition, appropriate thermal insulation must be applied to all metallic components exposed to the furnace environment in order to minimize heat loss and reduce overall energy consumption. Equally important is the integration of a cooling system for components that extend beyond the furnace chamber, particularly those connected to electrical or mechanical subsystems, whose functionality could be compromised by excessive heat. These measures are essential not only to ensure the reliability and accuracy of the experimental tests, but also to guarantee the safety of the operator and the long-term durability of the apparatus.

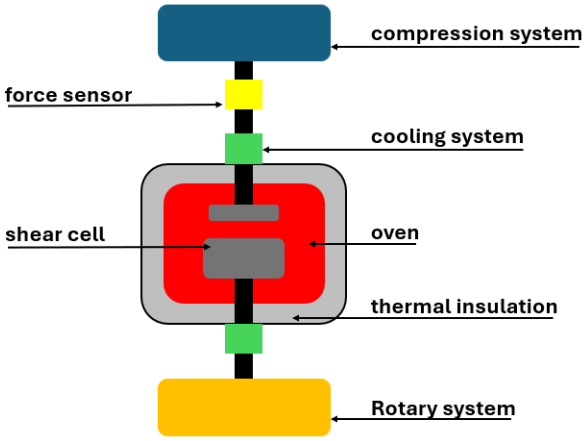

Figure III.6 Schematic representation of the components required to perform a shear test under high-temperature and controlled environmental conditions.

III.3.3. Rods

The components of the shear cell are mechanically interfaced with external systems via connecting rods, which serve to transmit both axial and torsional loads to the sample. These rods, manufactured from AISI 310 stainless steel, were dimensioned to ensure adequate mechanical strength under the expected operating conditions, particularly at elevated temperatures.

During the design phase, it was assumed that the two rods, although connected to the two distinct parts of the cell, would be subjected to comparable stress states. The upper rods, responsible for applying the normal load, are connected to a compression unit capable of delivering the required pressure. Given the axial alignment of the cell components, the compressive force exerted on the upper rod is transmitted through the sample and absorbed by the lower rod.
Conversely, the trough is coupled to a rotary drive system that applies a controlled torque to induce shear. This torque is also transmitted through the sample and partially resisted by the upper rod, which must remain rotationally constrained. As a result, both rods experience similar combinations of axial and torsional loads, and their mechanical sizing was unified accordingly.
For safe and reliable operation, the rods were conservatively dimensioned based on the maximum expected stress values derived from the experimental design envelope, ensuring that all components remain within the elastic regime under worst-case loading scenarios.
For the mechanical sizing of the rod, a compressive stress of 10 MPa applied to the sample was considered. Based on the 70 mm diameter of the lid, the corresponding axial force transmitted through the rod is known. The objective is to verify structural integrity using the von Mises criterion, which requires both axial and shear stress components.
Since the torque applied by the rotational system is not directly measurable, it was estimated by approximating the behaviour of the sample to that of a low-flowability material. Under this assumption, the shear stress τ in the material can be related to the normal stress σ describing the material using the Colburn equation, but considering a slope, α, of 30°.

$$\tau = \tan(\alpha) * \sigma \tag{66}$$

This relation allows the estimation of shear stress in the sample, which is then transmitted to the rod through the contact interface.
Although the axial force depends on the rod's cross-sectional area, which is initially unknown, the moment balance remains valid and conserved. Therefore, the von Mises equivalent stress can be expressed as a function of the rod's cross-section and compared to the yield strength of AISI 310 stainless steel at 1000 °C. As shown in eq. (67), the rod's cross-sectional area is the only unknown in the inequality.

$$\sigma_{eq,vM} = \sqrt{\left(\frac{F_n}{A_{rod}}\right)^2 + 3\tau^2} \leq \sigma_{amm} \tag{67}$$

Based on this analysis, the critical cross-section required to avoid plastic deformation was estimated to be 6.41 cm². For safe operation and compliance with industrial standards, the next available size was selected from ISO catalogues, resulting in a final design diameter of 36.0 mm.

Table III.3 Stress conditions applied to the rods for the estimation of the critical diameter.

σ [kPa]	F_n [N]	τ [Nm]	A_{rod} [cm^2]	D_{rod}(est) [mm]	D_{rod}(ISO) [mm]
10000	~5000	~78	6.4	28.6	36.0

Once the rod's cross-section was determined, it was essential to ensure that it would not undergo flexural deformation during the measurement phases. To this end, the empirical criterion for flexural stability was applied, which states that the length-to-diameter ratio must satisfy the condition:

$$L_{rod} \leq 10 D_{rod} \tag{68}$$

This relationship, commonly adopted in mechanical design to prevent buckling and bending under axial loads, was used to define the maximum allowable length of the rod. Given that the rod had already been oversized to withstand the expected stresses, and that several components needed to be mounted along its length, a maximum length of 360 mm was selected. However, while larger cross-sections would undoubtedly offer increased mechanical safety, they also introduce thermal drawbacks. The rods are the only mechanical components protruding from the furnace, and an oversized cross-section would significantly increase heat conduction outward. This would lead to higher thermal losses, increased furnace power demand, and longer heating times for the system. Therefore, the selected cross-section represents a compromise between mechanical robustness and thermal efficiency, ensuring both structural integrity and energy-conscious operation.
As previously discussed, the rods are responsible for transmitting both axial and torsional loads to and from the shear cell. It is therefore essential to ensure proper mechanical coupling between the rods and the components to which they are connected. To this end, both rods are equipped at one end with eight evenly spaced, rounded teeth distributed along the circumference. As illustrated in Figure III.7.c, these teeth engage with complementary cavities machined into the lid and the trough, ensuring precise alignment and reliable torque transmission. The resulting contact surface area of approximately 420 mm² is sufficient to prevent torsional deformation under the expected loading conditions.
At the opposite end, each rod terminates in a perforated flange, designed to allow secure attachment via screws to the adjacent mechanical units. Specifically, the upper rod is connected to a flanged torque transducer, while the lower rod interfaces with a gearbox that drives the trough's rotation. This configuration ensures both mechanical integrity and functional continuity across the system's transmission chain.

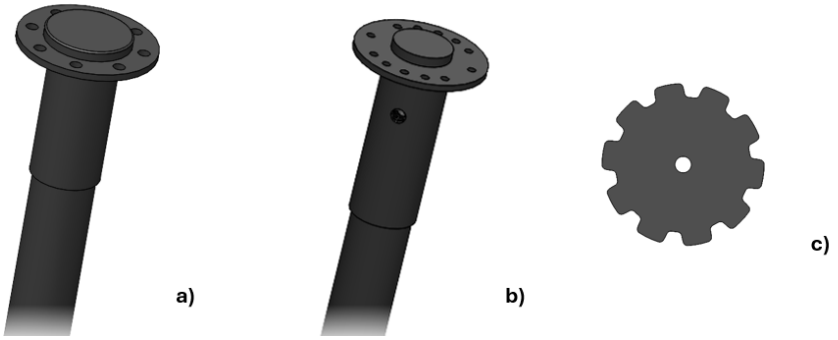

Figure III.7 Representation of the rods modelled in SolidWorks: (a) upper piston, (b) lower piston, and (c) tooth geometry (bottom view of rods) for connection with the corresponding components of the shear cell.

As shown in Figure III.7, the configuration of holes and mechanical joints differs between the two rods. Notably, the lower rod, Figure III.7.b, features a lateral inlet that initiates a 90° elbow channel, extending longitudinally through the rod and terminating at the opposite end. This internal passage spans 310 mm and has a 4 mm diameter, a value selected to balance sufficient gas flow with minimal structural weakening. Larger diameters were excluded to preserve the rod's mechanical integrity under torsional and axial loads.
This channel was designed to deliver process gases directly to the distributor embedded in the trough, allowing the gas to be preheated as it travels through the rod, improving thermal stability and consistency during testing.

III.3.4. Reaction chamber

The shear cell is enclosed in the reaction chamber and consists of two hollow cylindrical sections joined by a pair of flanges, creating an internal cavity 360 mm in diameter and 360 mm high. The chamber is made of AISI 310 stainless steel and serves to confine the gases flowing through the sample during the test. It was designed to address two issues related to measurement under harsh conditions: limit friction on moving elements; isolate the measurement environment from air. For this reason, two coaxial cylindrical channels, each with an internal diameter of 39 mm, are connected to the upper and lower plates of the reaction chamber. These channels allow the two rods, connected at the top to the shear cell lid and at the bottom to the trough, to move. Two gas inlets with an internal diameter of 4 mm are positioned along these channels to introduce fresh inert gases such as nitrogen to establish a net flow of gas towards the reaction chamber and prevent the internal gaseous atmosphere from escaping into the environment. The free ends of the cylinders surrounding the pistons have been designed to accommodate sealing elements and cooling units. The upper section of the reaction chamber features two additional openings: one designed to accommodate a thermocouple for

monitoring the temperature of the measurement environment, mounted near the shear cell, while the other serves as a gas outlet line for the collection and analysis of exhaust gases. The chamber is completely immersed in an oven.

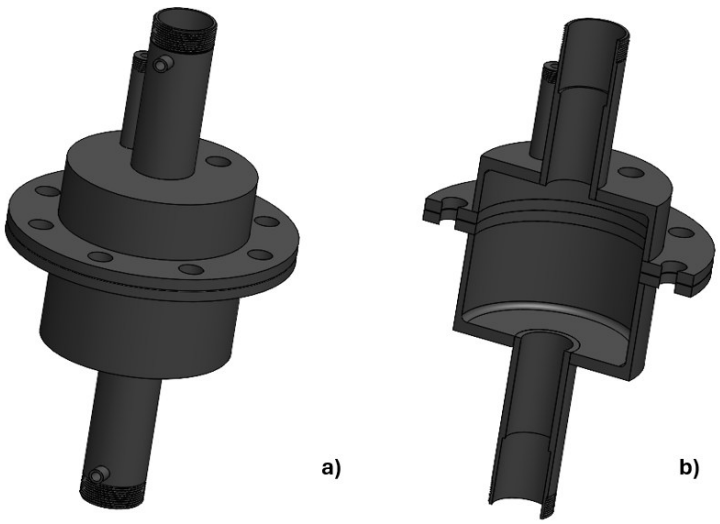

Figure III.8 Representations of the reactive chamber modelled in SolidWorks: (a) complete view of the two components forming the containment region of the cell, and (b) cross-sectional view of the reactive chamber.

III.3.5. Cooling and sealing system

Among the various engineering challenges encountered, sealing and cooling emerged as the most critical aspects of the system's design.

Sealing plays a fundamental role in ensuring both process fidelity and operational safety. Establishing a controlled environment around the solid phase is essential not only for replicating the intended reaction conditions but also for maintaining precise control over the gas-solid interactions. The ingress of external reactive species, such as oxygen, which is particularly detrimental in handling reduced pellets, can alter reaction pathways or disrupt the pressure balance within the chamber. Conversely, gas leakage from the system poses serious safety risks, especially when operating with highly reactive gases like hydrogen at elevated temperatures. The sealing strategy must therefore prevent both inward contamination and outward escape, ensuring the integrity of the reactive atmosphere and the safety of the operator. The sealing system must also be designed to minimize friction on the rods. Excessive friction at the sealing interfaces can introduce significant mechanical resistance, affecting the measured values and compromising test accuracy. In extreme cases, the additional forces generated by friction may

exceed the actual stress being evaluated, thereby masking the true mechanical response of the material and obscuring its flow behaviour.

Cooling, on the other hand, is essential for preserving the mechanical and electronic integrity of the prototype. While the structural components are fabricated from temperature-resistant materials, prolonged exposure to thermal gradients can cause geometric distortion, compromising the measurement accuracy and repeatability. Moreover, the electronic instrumentation, including sensors positioned near the rods protruding from the furnace, has limited thermal tolerance, typically up to 40 °C, with optimal performance at ambient temperature. This limit necessitates the implementation of rapid cooling systems for the rods and effective thermal insulation for the furnace, which operates at temperatures approaching 1000 °C.

These constraints have driven the iterative development of specialized components and design solutions, each tailored to address emerging issues that were not fully predictable during the initial design phase. The result is a progressively refined system architecture capable of maintaining both experimental reliability and operator safety under demanding conditions.

III.3.5.1. Cooling and sealing system: integrated solution

The first configuration developed offered an integrated approach to simultaneously address sealing and cooling challenges. This solution included an annular cooling chamber, mounted around the rod at the terminal cylinders of the reactive chamber. The chamber consisted of three modular components: a central body with a cooling cavity, and two anchoring and closure elements. The central section, with an internal diameter exceeding 42 mm, houses the cooling fluid channel, allowing direct thermal exchange with the rod surface. The two end components were machined to form seating cavities at their interface with the central body, specifically shaped to accommodate O-rings made from high-performance sealing materials. Upon assembly, the tightening of the three elements caused the O-rings to deform slightly and adhere to a localized region of the rod, ensuring effective sealing while maintaining low friction. This configuration permitted, in principle both rotational and translational motion of the rod, while enabling efficient cooling through direct contact with the circulating fluid.

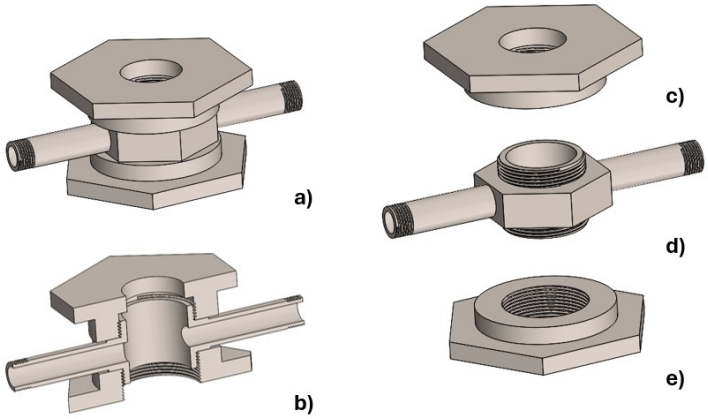

Figure III.9 Representation of the cooling chamber and its components modelled in SolidWorks: (a) fully assembled cooling chamber, (b) sectional view, (c–e) perforated hexagonal head elements, and (d) central body of the jacket.

Figure III.9 illustrates the complete assembly of the cooling chamber (a), its cross-sectional view (b), and the individual components. As shown in Figures III.9.c and III.9.e, the end elements feature internal threading and a 120 mm hexagonal head, facilitating manual opening and closure. The base element included a fully threaded body, partially engaged with the reactive chamber, with an additional O-ring positioned to seal the interface. The central body was equipped with two male threaded connectors, serving as junctions for the end components, and includes inlet and outlet channels for the cooling fluid. A final O-ring was seated at the upper interface of the central body and compressed by the upper closure element, completing the sealing system.

The operation of the equipment and the corresponding design dimensions were validated by solving the energy and momentum balances across the system, including the cooling chamber, rods, and the hollow walls of the reactive chamber that surround the pistons. For the mathematical description, it was essential to analyse the physical phenomena occurring in each region of the system. For simplicity, the system was divided into two main zones: the cooling chamber and the region below it. In the region below the chamber (Figure III.10.b), three distinct volumetric regions can be identified: the central solid body (the rod), the gas that fills the volume between the piston and the reaction chamber, and the outer wall of the reactive chamber, which is exposed to ambient air.

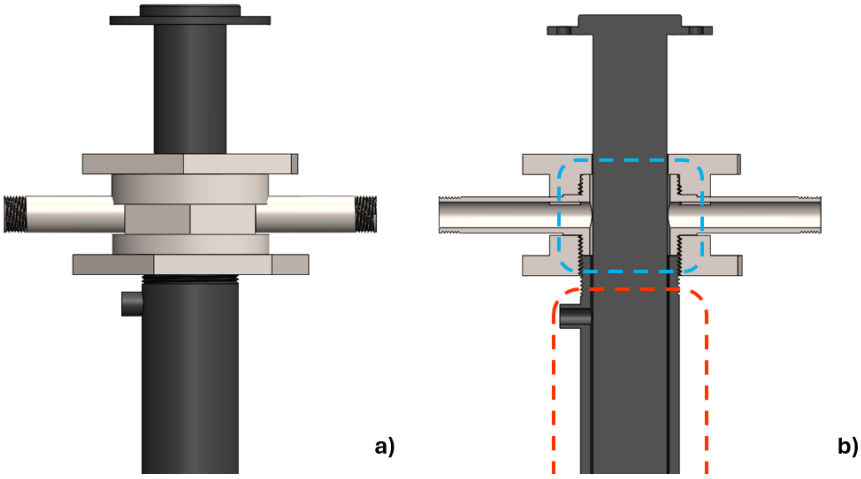

Figure III.10 SolidWorks model of the rod, cooling chamber, and reaction chamber: (a) overall view; (b) sectional view in which the two boxes indicate the two volumes described with the balances.

Each component was subject to different heat-transfer mechanisms. The rod conducts heat upwards and exchanges energy with the downward-flowing gas through forced convection. The reaction chamber, in turn, exchanged heat with the internal gas via forced convection, while simultaneously exchanging heat by conduction within its solid body and by natural convection with the surrounding air.

Once these phenomena were defined, the analysis proceeded by considering the properties of the three relevant phases: solid, liquid, and gaseous. The gaseous phase consists of nitrogen: introduced specifically as an auxiliary sealing element. The liquid phase is the coolant: water was selected for its low cost, wide availability, and thermophysical properties well-suited to the cooling system's operation. The solid phase, the conductive body, in contrast, is composed exclusively of AISI 310 stainless steel.

This section presents the rationale and numerical results used to verify the performance of the integrated cooling and sealing system. The full set of governing equations and the corresponding mathematical derivations are reported in Appendix C.

A numerical solution of energy balance for the entire region was obtained using the SolidWorks module for heat transfer modelling to perform the simulations, and Figure III.11 presents the resulting temperature distribution in the region below the cooling chamber.

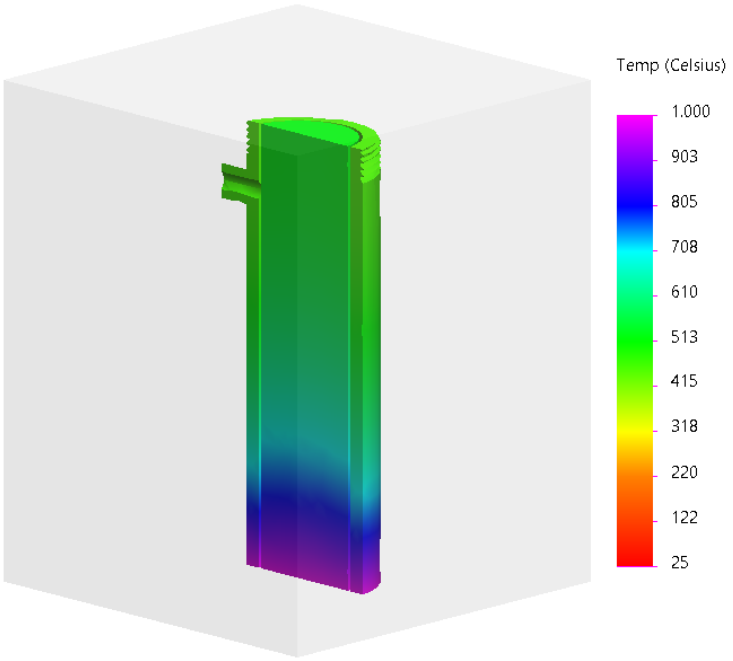

Figure III.11 Cross-sectional view of the prototype section located beneath the cooling chamber, including the rod and the corresponding region of the reactive chamber. The simulated air volume is displayed in transparency.

Figure III.11 illustrates exclusively the behaviour of the solid phase, in order to facilitate interpretation. Owing to the significant temperature difference between the hottest regions of the solid, a sharp decrease in temperature is observed in the zones of maximum heating, followed by a more gradual decline toward rod temperatures of approximately 510 °C at the upper boundary of the figure. Between the rod and the outer wall, corresponding to the reactive chamber, a temperature difference of about 150 °C is evident, in agreement with the combined effects of radiation and natural convection with the external environment; phenomena that characterise the portion of the reaction chamber that exits the furnace.

Accordingly, the rod enters the cooling chamber at a temperature of roughly 510 °C, while the reactive chamber wall reaches about 380 °C. It must be noted, however, that these values are significantly overestimated, since the presence of the cooling chamber will strongly reduce the temperature of the rod. Heat exchange with the circulating water can induce a pronounced decrease in temperature along the rod, resulting in a steeper thermal gradient than shown. Nevertheless, the overestimated values remain acceptable for the purposes of this analysis, which aims to define the appropriate water flow rate to ensure effective cooling of the rod end in contact with the electrical and mechanical components.

As shown in Figura II.10.b, in the cooling chamber, water enters perpendicularly to the rod, generating an impact jet at the inlet region. After the jet dissipates, the flow is redirected into the chamber, which is coaxially aligned with the rod and defines an annular region for heat exchange. This annulus has an internal diameter of 36 mm, an external diameter of 39 mm, and a height of 50 mm, thereby establishing the effective cooling surface in contact with the solid.

To determine the water flow rate required for piston cooling, the heat transfer within the cooling chamber was evaluated by imposing the temperatures at the two ends of the rod located inside the reaction chamber. The conductive heat flow q through the solid was first calculated based on the temperature difference between the ends and the material's thermal conductivity k_s, assuming perfect insulation along the height corresponding to the cooling chamber. Fourier's law (eq. (69)) was applied using the thermophysical properties of the solid phase reported in Section III.2 and defined by eq. (70).

$$q = -k_s \frac{dT}{dx} \tag{69}$$

$$k_s = 0.015T + 8.75 \tag{70}$$

Fixing the temperature at the piston head is equivalent to prescribing the conductive heat flow within the solid, which represents the thermal load that the cooling water must remove to maintain the target temperature. Under steady-state conditions and considering the absence of further dissipations, an overall energy balance requires the thermal power transferred through the solid to equal the thermal power extracted by the water.

Therefore, by multiplying Fourier's law by the rod's cross-sectional area, the thermal power $\dot{Q}$ is obtained. Integrating eq. (69) and multiplying the result by the cross-sectional area yields:

$$\dot{Q} = -\frac{0.015T^2 + 8.75T}{L}\frac{\pi D_1^2}{4}\Bigg|_{T_{bottom}}^{T_{top}} \tag{71}$$

where L is the height of the cooling chamber, T_{top} is the temperature at the upper rod boundary, and T_{bottom} is the temperature at the lower rod boundary, and D_1 is the rod diameter .

Once this value is known, the required water volumetric flow rate $\dot{V}$ is calculated using eq. (72). The maximum allowable temperature rise of the cooling water was set to 10 °C, with an inlet temperature of 20 °C. Consequently, the water properties, such as the density of the liquid ρ_w and the specific heat at constant pressure Cp_w, were evaluated at the intermediate temperature of 25 °C.

$$\dot{Q} = \rho_w \dot{V} Cp_w \Delta T \tag{72}$$

Table III.4 reports the numerical results obtained using the bottom temperature estimated from the energy balance in the region below the reaction chamber (510 °C), together with the results calculated assuming the maximum operating temperature of 1000 °C, included to assess the upper-bound flow rate required for safety.

Table III.4 Calculated water flow rates required for piston cooling under nominal (510 °C) and maximum operating (1000 °C) temperatures.

T_{bottom} [K]	$\dot{Q}$ [W]	$\dot{V}$ [l s^{-1}]
783	245.6	0.006
1273	635.9	0.015

As expected, the highest demand occurs at 1000 °C, corresponding to a volumetric flow rate of 0.015 L/s: an order of magnitude lower than the typical supply capacity of the national water network (approximately 0.15 L/s).
These results confirm that the cooling chamber operates effectively even under conservative thermal conditions and requires only a modest water flow rate, ensuring reliable performance without imposing significant demands on the water supply system.

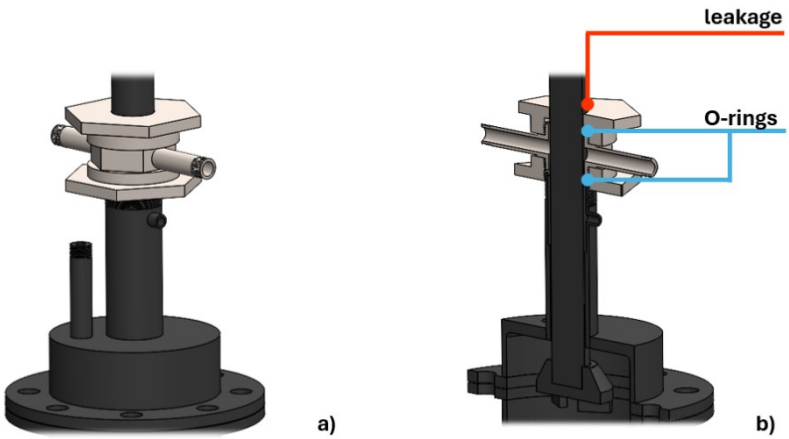

Figure III.12 Representation of the integration between the reaction jacket, the piston, and the upper section of the reactive chamber: (a) 3D view, and (b) sectional view showing the cavities for O-ring placement and the areas where water leakage was detected.

Figure III.12 illustrates the assembly of the cooling chamber mounted on the reactive chamber including the rod, in pane (a), along with its cross-sectional view in pane (b).

During experimental trials, however, it was observed that liquid droplets emerged from the upper region of the jacket, specifically at the O-ring interface and along the rod surface. Despite preliminary validation tests, this behaviour proved highly undesirable. On the one hand, it introduces coolant leakage, compromising the thermal management system's efficiency; on the other, it raises concerns about undetected ingress into the reactive chamber itself.

The presence of water within the reactive volume is particularly problematic, as it may interfere with the reduction reaction by altering the gas-phase composition, especially when water is a reaction product, as in the reduction of iron ores. Such contamination undermines the control of the reacting atmosphere and introduces uncertainty into the experimental conditions.

To preserve the integrity of the prototype and ensure precise control over both thermal and chemical environments, a revised configuration was adopted in which sealing and cooling are treated as independent systems, each optimized to address its respective functional requirements without mutual interference.

III.3.5.2. Cooling and sealing system: split solution

The revised configuration introduced dedicated solutions for sealing and cooling, each independently optimized to meet the system's specific functional requirements.

For sealing, a Swagelok connector with an internal diameter of 38 mm was selected and welded to the free ends of the reactive chamber to ensure a secure and gas-tight closure. Internally, the connector houses a metal back ferrule and a PTFE (Teflon) front ferrule, which together provide a reliable seal. The use of Teflon in the ferrule is critical to enabling non-permanent deformation during tightening. This property allows the Swagelok connector to be repeatedly opened and closed without compromising the sealing performance or damaging the contact surfaces, ensuring long-term operational flexibility across multiple test cycles. However, this new sealing strategy introduces a significant change to the measurement protocol. Unlike the previous configuration, where measurements could potentially be acquired during the reaction phase, the deformation of the Teflon ferrule during tightening introduces substantial friction at the rod-ferrule interface. This friction is incompatible with accurate shear measurements.

As a result, the experimental procedure has been restructured into two distinct phases, which are alternated as needed: reaction and shear. This separation ensures that the sealing integrity required during the reaction phase does not interfere with the mechanical sensitivity needed during shear testing.

Given that Teflon remains stable up to approximately 460 °C, it is essential to keep the sealing region temperature well below this threshold. To achieve this, the cooling system was also re-engineered, now divided into two independent stages, each targeting a specific thermal zone to ensure both the thermal

protection of the sealing elements and the preservation of measurement accuracy.
The initial cooling modifications were implemented directly on the rods, targeting the exposed flange region. In this configuration, two openings machined into the free portion of the flange serve as the inlet and outlet for water, which circulates through a semicircular channel carved along the outer wall of the rod. This channel, with a diameter of 8 mm, ensures effective thermal exchange without compromising the rod's mechanical integrity. Due to the continuous presence of water, this portion of the rod operates at temperatures significantly lower than those of the surrounding furnace, enabling rapid cooling and preserving the mechanical properties of the material under load.
To contain the flow and prevent leakage, the cooling path is enclosed by a hollow cylindrical sleeve with a wall thickness of 1 mm, designed solely to seal the system and maintain pressure. Figure III.13 illustrates the cooling channel geometry along the rod and the current configuration of the assembled system.

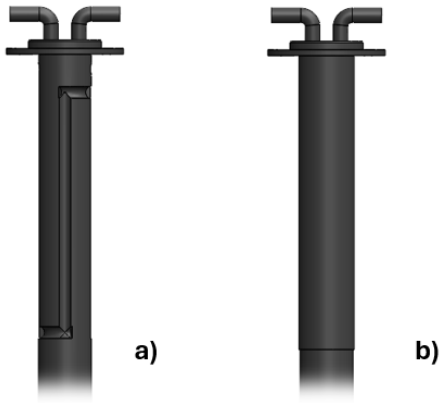

Figure III.13 Modified upper piston: (a) configuration with exposed cooling channels, and (b) fully assembled version.

As previously discussed, the Swagelok connector must operate at temperatures well below the critical thresholds of its constituent materials to ensure long-term sealing performance. To meet this requirement, a secondary cooling chamber was integrated directly onto the free end of the reactive chamber, in direct contact with the base of the Swagelok.
This unit consists of a hollow cylindrical cavity, with an internal diameter of 49 mm, an external diameter of 62 mm, and a height of 12 mm. Within this cavity, cooling water circulates along two semicircular paths, providing efficient thermal exchange and enabling rapid heat removal from the Swagelok body. This configuration ensures that the sealing region remains

within the safe operating range of the PTFE ferrule, even during prolonged exposure to elevated furnace temperatures.

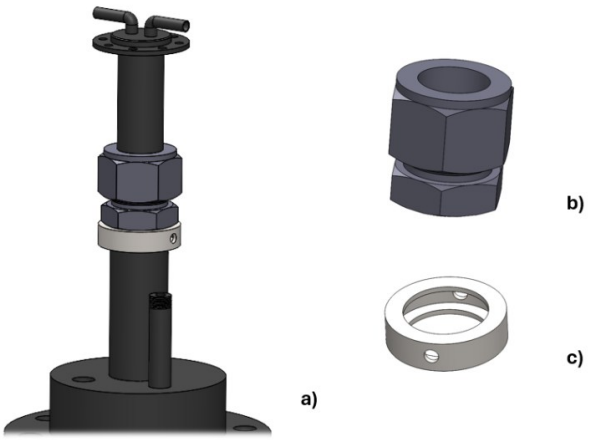

Figure III.14 Integration of the new cooling system: (a) top view showing the reactive chamber, piston, and updated sealing and cooling configuration; (b) Swagelok connector; and (c) redesigned cooling chamber.

The complete sealing and cooling assembly is illustrated in Figure III.14.a, showing both the structural integration and the fluidic layout of the system.
The central body of the assembly is designed to be symmetrical about the horizontal axis, as illustrated in Figure III.15. This symmetry facilitates balanced flow distribution and simplifies both installation and maintenance. In the figure, the inlet and outlet channels are clearly marked, distinguishing between the two fluid systems involved. The process gases, such as nitrogen, are represented in green, while the service fluids used for cooling are shown in blue, visually emphasizing the separation between the reactive and thermal control circuits.

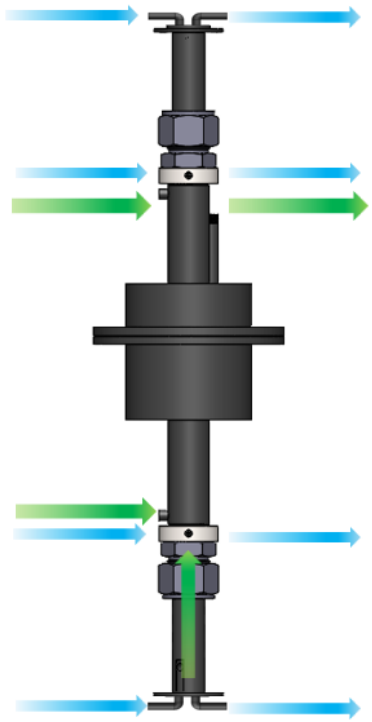

Figure III.15 Representation of the prototype's central body, comprising pistons, Swagelok connectors, cooling chambers, and the reactive chamber. Blue arrows indicate the water inlet and outlet paths, while green arrows highlight the gas flow routes.

III.3.6. Actuators

Once the materials and geometries involved in the shear cell have been defined, a fundamental aspect of the experimental setup is the distribution and application of forces required to conduct the tests.

As previously described, the lid serves to apply compressive force to the sample, while the trough is maintained in continuous rotation to induce shear. For the compression phase, a linear actuator.

r was selected to deliver controlled axial force through the lid. This actuator ensures precise displacement and load application, allowing the sample to be compacted under well-defined conditions.

For the shear phase, a more complex actuation system was implemented. It consists of a rotary engine coupled with a planetary gearbox, designed to operate at a constant angular velocity. In this configuration, the torque output of the engine dynamically adjusts in response to the resistance offered by the sample. This dual-actuation approach enables independent control of normal

stress and shear stress, providing the flexibility needed to simulate complex mechanical environments.

The compression system integrates a linear actuator with a precise force regulation mechanism, enabling controlled application of normal stress during testing. The actuator selected is the DSBC-125-100-PPVA-N3 (Figure III.16.b), a double-acting compliant pneumatic cylinder designed to convert the energy of compressed air into linear motion. Air was chosen as the operating medium due to its compressibility, which allows the piston to respond dynamically to variations in sample behaviour. For instance, if the sample undergoes expansion during the test, the piston can move upward even under a fixed chamber pressure, accommodating the change without compromising the system's integrity.

The pressure within the cylinder is regulated by a proportional electro-pneumatic valve (Figure III.16.a), which translates a variable electrical reference signal (0-10 V) into a modulated output pressure. This regulator does not directly control the piston's movement; rather, it governs the pneumatic pressure supplied to the cylinder ports. The cylinder then converts this pressure into a linear force, following the relationship $F = PA$, where P is the regulated pressure and A is the cross-sectional area of cylinder.

The system is configured in a sequential integration, with the regulator supplying air directly to the DSBC cylinder ports. This setup enables active force control, allowing the applied compressive load to be finely tuned in real time based on experimental requirements.

System limits are defined by the mechanical and performance characteristics of the components. The fixed stroke length of the DSBC cylinder is 100 mm, representing the maximum allowable vertical displacement. The bore diameter of 125 mm defines the upper bound of the applicable force, which can be calculated based on the maximum pressure supplied by the regulator.

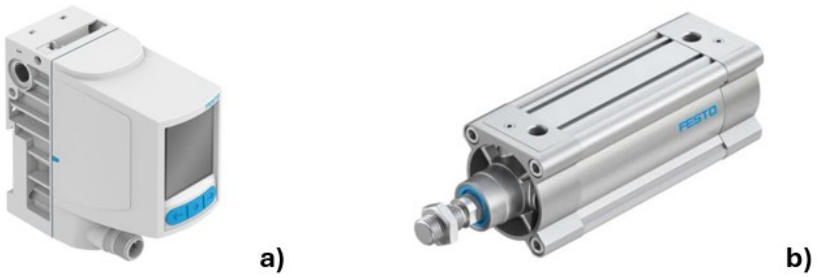

Figure III.16 Elements of the compression system: (a) proportional electro-pneumatic valve, and (b) linear actuator.

To ensure precise control of the channel movement, a critical and sensitive aspect of the measurement process, a high-performance mechatronic system supplied by Bianchi S.r.l. was selected. This system integrates three core components: a servo drive, a rotary engine, and a planetary gearbox, each contributing distinct functionalities to the overall motion architecture.
At the heart of the control system is the servo drive CMMT-AS-C3-11A-P3-MP-S1, that functions as a regulated power amplifier. It governs the system's position, velocity, and torque with high precision, translating control signals into finely tuned electrical outputs (Figure III.17.a).
This drive interfaces directly with a high-speed rotary engine of series EMMT-AS-80-S-HS-RMB , designed for dynamic and accurate rotary motion (Figure III.17.b). The engine converts the drive's electrical output into mechanical rotation, delivering a nominal torque of approximately 1.3 Nm, with peak torque up to 4.1 Nm, and achieving maximum speeds between 7,440 and 8,950 rpm, depending on the internal configuration and load conditions. Its low rotational inertia and high responsiveness ensure precise control over angular displacement and torque delivery.
To adapt the engine's high angular velocity to the mechanical requirements of the system, the output shaft is coupled to a Neugart flanged planetary gearbox (Figure III.17.c). This gearbox employs a planetary gear train with a reduction ratio of 100:1, allowing the system to:

- Reduce the engine's angular velocity to a usable output speed.
- Multiply the available torque at the output shaft.
- Maintain low backlash and high torsional stiffness, essential for accurate torque transmission during shear testing.

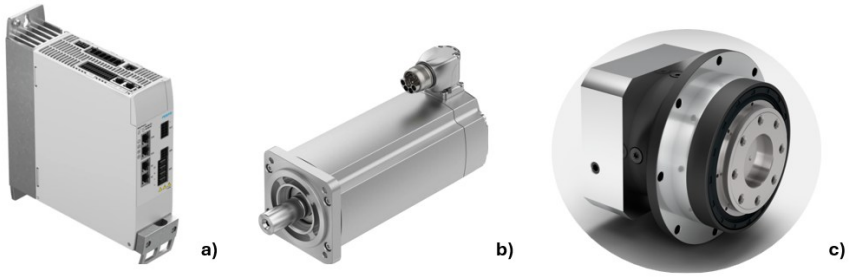

Figure III.17 Mechatronic system for trough rotation. a) servo drive; b) rotary engine; c) gearbox.

With the current configuration, it is possible to apply the torque required to rotate the trough, estimated at approximately 70 Nm, while maintaining an extremely low angular velocity of around 0.015 rpm, in accordance with standard testing protocols. These parameters are transmitted directly to the

lower arm via the planetary gearbox, which serves as the mechanical interface between the rotary engine and the shear cell.
The rotary engine selected for this task has a maximum rotational speed of 15.92 rpm and an output torque of 0.80 Nm. This input is processed by the Neugart planetary gearbox, which features a reduction ratio of 100:1. As a result, the gearbox delivers an output speed of approximately 0.016 rpm and a maximum torque of 74 Nm, accounting for its mechanical efficiency of 93%.
This configuration ensures that the system can maintain a constant angular velocity, while the delivered torque dynamically adjusts in response to the mechanical resistance of the sample.
In summary, each component plays a distinct role:

- The servo actuator provides the intelligent control and regulated power delivery.
- The rotary engine ensures responsive and accurate motion.
- The Neugart gearbox delivers mechanical adaptation and torque amplification.

Together, they form a robust and responsive actuation system capable of maintaining precise control over the channel's movement, even under demanding thermal and mechanical conditions.

III.3.7. Skeleton

Once the sequence of components required for testing had been defined and aligned along the shear cell axis, it became necessary to design a supporting skeleton capable of maintaining their relative positions and withstanding the mechanical loads generated during operation. The structural skeleton was developed as a vertically oriented frame, consistent with the functional layout of the components, and constructed using Bosch modular profiles.
Although the inter-component spacing was largely determined by the mechanical and functional constraints of the system, the profiles' cross-sectional geometry required careful selection. This choice was guided by the mechanical equations and design parameters provided by the manufacturer, which were used to evaluate the deformation response of the profiles under load.

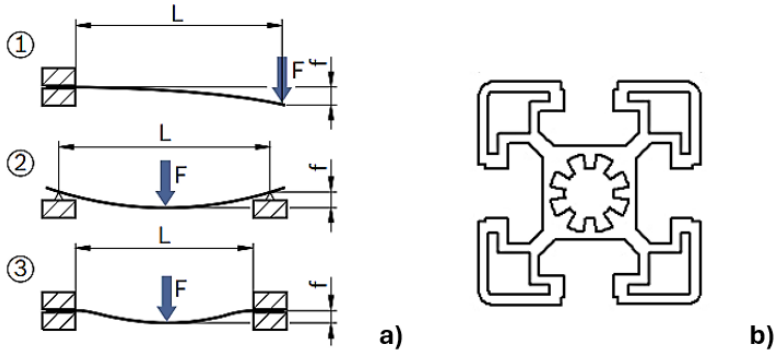

Figure III.18 (a) Illustration of the possible stress conditions acting on Bosch profiles, and (b) sectional view of the selected profile.

Three distinct constraint scenarios were considered, as illustrated in Figure III.18, each corresponding to a different boundary condition and loading configuration. The relevant equations, reported in the manufacturer's technical documentation and referenced as eqs. (73) to (75), were used to calculate the deflection f_i of the profile under an applied force F. These equations incorporate the profile length L, estimated via SolidWorks modelling, the elastic modulus E of the material, and the moment of inertia I, which depends on the internal geometry.

$$f_1 = \frac{F \cdot L^3}{3E \cdot I \cdot 10^4} \tag{73}$$

$$f_2 = \frac{F \cdot L^3}{48E \cdot I \cdot 10^4} \tag{74}$$

$$f_3 = \frac{F \cdot L^3}{192E \cdot I \cdot 10^4} \tag{75}$$

The maximum forces expected during operation were determined to be approximately 5000 N for the compressive load and 1500 N for the moment-induced force couple. Given the dominance of the compressive load, the selection of the internal geometry and cross-sectional profile was based on a conservative assumption: that the entire compressive force would be transferred through a single profile, aligned with the direction of the applied load in each of the three constraint scenarios. Table III.5 summarizes the numerical values provided by the supplier, including the geometric and mechanical parameters for the profile reported in Figure III.18.b considering different square sections, along with the estimated deflection results calculated for each constraint scenario.

Table III.5 Stress distribution and resulting estimated deformations in Bosch profiles with identical geometry but varying cross-sectional dimensions.

F [N]	Square section [cm2]	I [cm4]	L [mm]	f_1 [mm]	f_2 [mm]	f_3 [mm]
5000	45x45	13.8	420	12.78	0.79	0.19
			160	0.22	0.014	0.0034
	50x50	21.2	420	8.32	0.52	0.13
			160	0.14	0.0091	0.0023
	60x60	52.2	420	3.38	0.21	0.053
			160	0.059	0.0037	0.00092
	90x90	299.8	420	0.59	0.037	0.0092
			160	0.010	0.00064	0.00016

As shown in Table III.5, the only profile geometry that yields minimal deflection across both estimated lengths is the 90×90 mm square section. This configuration demonstrated superior mechanical stability under the applied loads, making it the most suitable choice for the construction of the supporting skeleton. Accordingly, each segment of the profile was constrained at both ends, following the boundary condition defined as typology 3 in Figure III.18, which corresponds to a fixed-fixed constraint scenario. This arrangement was adopted specifically to minimize structural deformation, ensuring reliable alignment and load-bearing capacity throughout the testing sequence.

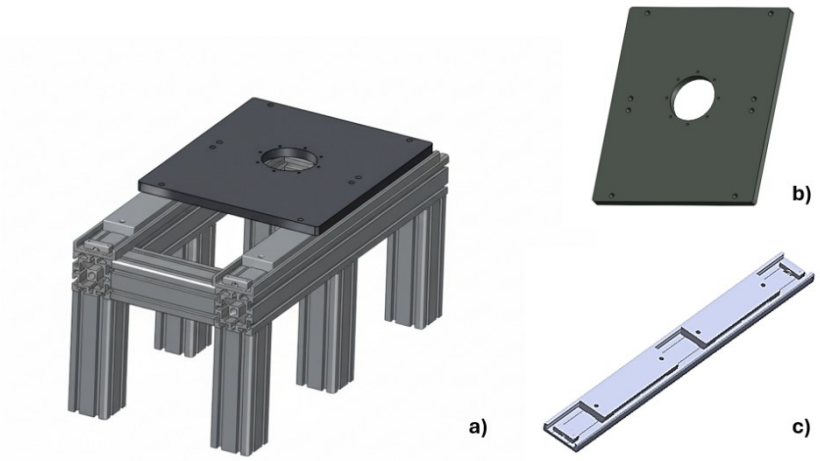

Figure III.19 Representation of the sliding horizontal platform and its support structure: (a) overall assembly, (b) steel platform, and (c) linear ball bearings.

An additional feature of the structural skeleton is a sliding horizontal platform, designed to facilitate loading and unloading of material from the trough. This platform is constructed using Borsh modular profiles, forming a flat rectangular surface that integrates seamlessly with the upper base of the frame. To ensure mechanical stability under load, two Chambrelan E98 series linear ball bearings with G12 slides were installed along the depth axis of the upper base. These guides were selected for their high load capacity and precision movement, as they represent the only interface through which the normal force applied by the linear actuator is transmitted during testing. Each slide is rated to support up to 600 kg, and the use of rotating ball bearings ensures smooth, controlled motion with minimal friction and deformation.

Mounted above the slides is a steel platform measuring 42 cm in width, 50 cm in depth, and 2 cm in thickness. The platform is machined with attachment holes for secure fastening to the slides, and features a central opening designed to accommodate the gearbox. This configuration allows the applied weight to be first transferred to the gearbox, engineered to withstand internal pressures exceeding 10 bar, and then progressively distributed across the platform, the linear guides, and the supporting skeleton.

This integrated design ensures that the mechanical loads are efficiently managed, preserving the structural integrity of the system and enabling reliable operation throughout the loading, testing, and unloading phases.

Figure III.20 presents the complete prototype, illustrating the integration of structural, mechanical, and functional elements. In Figure III.20.a, the Borsh profile skeleton is shown in its assembled form, with the various shelves and lateral supports positioned according to the spatial requirements of the

mechanical and electrical subsystems. This view highlights the modular architecture and the vertical alignment of the components.
Figure III.20.b depicts the system in its operational configuration, with all core elements (motors, actuators, sensors, and the furnace) installed and connected. The furnace is shown in its closed state, corresponding to the measurement phase, during which the sample is subjected to controlled thermal and mechanical conditions.
Figure III.20.c illustrates the open configuration, required for the loading and unloading of material. This state allows unobstructed access to the trough and facilitates the placement or removal of the sample, ensuring safe and efficient handling between test cycles.

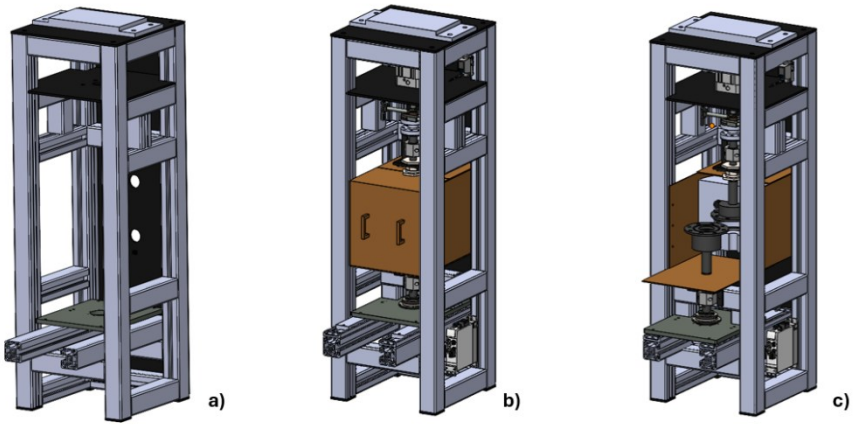

Figure III.20 3D representation of the complete prototype: (a) structural frame composed of Bosch profiles and shelves, (b) fully assembled configuration under experimental test conditions, and (c) open configuration of the prototype.

III.3.8. Water recovery unit

Given the potential reactivity of the system, a dedicated condensate recovery unit was developed to quantify the degree of iron oxide reduction using hydrogen. The focus was placed on recovering water, the only reaction product capable of condensing under ambient pressure and temperature conditions. Based on the geometry of the new trough, the bulk density, and the average particle size, the mass of pellets loaded for each test was estimated to be approximately 530 g.
To determine the maximum amount of water potentially produced, a conservative assumption was made: the solid phase was considered to consist entirely of Fe_2O_3, maximizing the stoichiometric yield of H_2O. Monitoring the

recoverable water from the outlet stream of the reaction chamber thus provides a direct indication of the conversion degree of the pellets.

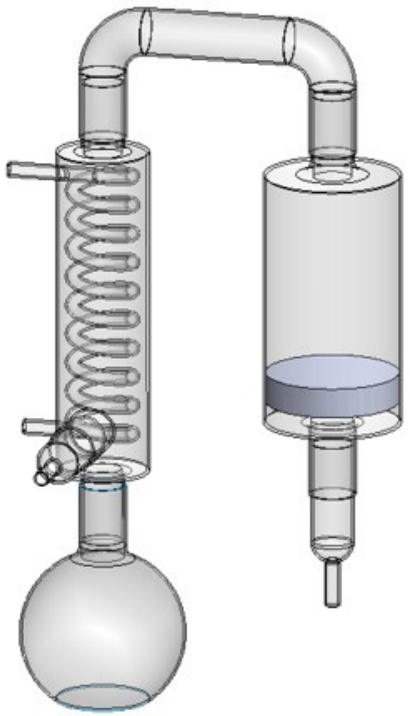

Figure III.21 Illustration of the assembled glass condensate recovery unit for water reclamation.

The final design of the recovery unit, illustrated in Figure III.21, consists of two sequential stages engineered to maximize the condensation and capture of water produced during the reduction of iron oxides. The first stage involves a single-pass tube-to-shell heat exchanger, where liquid cooling water circulates through an internal coil while the reaction gases flow through the surrounding shell. This configuration promotes efficient thermal exchange, causing the water vapor in the gas stream to condense. The resulting condensate precipitates into a burette, with a volume of 300 ml, positioned below the exchanger, enabling direct volumetric measurement of the recovered liquid.

To capture residual moisture, the gas stream is subsequently directed through a bed of zeolites mounted on a porous junction. The porous crystalline structure of the zeolite acts as a molecular sieve, selectively adsorbing water molecules from the gas phase. The unabsorbed gases exit through an opening located beneath the junction and are routed to a Bunsen burner, where any remaining reactive species are safely combusted. Based on the adsorption capacity of the selected zeolite, a mass of approximately 700 g was determined

to be sufficient to reduce the dew point of the gas stream to -70 °C, thereby ensuring near-total water recovery [133].
All components of the unit are fabricated from tempered glass, chosen for its chemical resistance, thermal stability, and visual transparency, which facilitates monitoring during operation.
To quantify the amount of water produced, a bench balance was selected as a compromise between market availability and essential performance requirements such as sensitivity, precision, accuracy, and plate size. The structure to be weighed has a dead weight of approximately 6.5 kg, which includes the glass components, the cooling water, and the zeolites required for complete recovery of moisture from the outlet air stream. This mass, together with the physical weighing platform, necessitates careful consideration of the scale's capacity and dimensions.
In selecting the instrument, economic optimization was a key parameter, balancing market availability with the required measurement range. It is well established that the accuracy of a measuring device is highest when operating between 30% and 80% of its full scale. Ideally, therefore, a maximum load of about 10 kg would ensure that the system operates within this optimal accuracy window. However, extending the measuring range inevitably reduces sensitivity, and excessive extension would compromise the ability to measure small quantities with the required resolution. In practice, smaller load ranges are also associated with smaller weighing plates, which can limit the usable weighing platform.

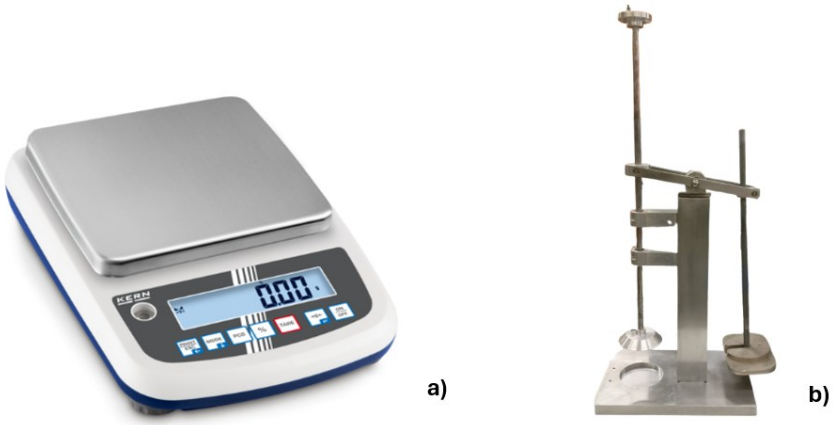

Figure III.22 Photograph image of: a) KERN FKB 6K0.02 balance; b) counterweight system.

The instrument selected is the KERN FKB 6K0.02 (Figure III.22.a), a high-precision balance designed for laboratory and production environments. It operates using a strain-gauge load cell mechanism, in which the deformation of a metallic element alters electrical resistance; this signal is processed by an internal microprocessor to provide accurate digital weight values.

The metrological specifications define the operational limits of the scale: a maximum capacity of 6,0 kg, a minimum readable increment of 0.02 g, and linearity maintained within ± 0.1 g across the entire range. The weighing platform dimensions is of 340 × 240 mm. and data integration is achieved through standard interfaces, with USB adopted as the sole protocol to ensure reliable connectivity.

To overcome the limitation of the measurement range while preserving sensitivity, a counterweight system was developed (Figure III.22.b). This system consists of a robust vertical upright with a square cross-section, anchored at the centre of a reinforced base. At its upper end, a first-class lever generates the counterweight required to offset the combined mass of the glass, water, and zeolite components. These components are mounted on a vertical rod opposite the one carrying the counterweight loads. The base of the counterweight system is positioned directly beneath the weighing platform, while the glass components are placed on the weighing platform. In this configuration, the effective load applied to the scale is partially offset by the counterweight, allowing the measured weight to remain within the instrument's operating limits.

III.4. Monitoring and control

Once the procedures and mechanical configuration of the system were defined, it became essential to identify the key parameters to be monitored over time in order to conduct the experimental tests with consistency and reliability.

During each test, the pressure applied by the linear actuator must be carefully controlled. This pressure governs the normal force exerted on the sample, both during the preshear phase, where the material is consolidated, and during the shear phase, where the load is maintained to simulate operational stress conditions.

Another critical parameter is the torque required to prevent lid rotation. As the trough rotates, the transmission of motion through the granular medium tends to induce rotation in the lid. Measuring the torque necessary to counteract this movement provides a direct indication of the shear resistance of the material. Additionally, the lid is free to move vertically, allowing it to respond to density changes in the sample caused by deformation, which must be accounted for during data interpretation.

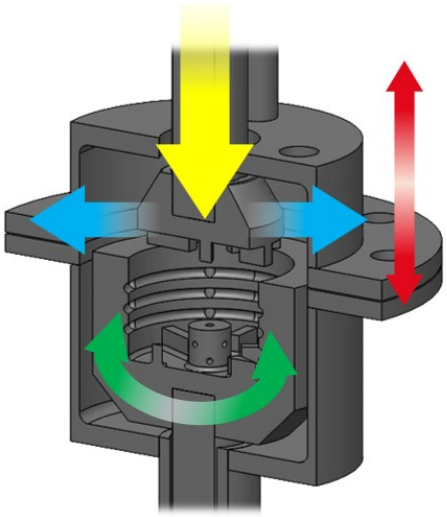

Figure III.23 Cross-sectional view of the measurement environment, including the shear cell and reactive chamber. The yellow arrow indicates the applied compressive stress, the blue arrow represents the torque, the red arrow shows the lid displacement, and the green shows the directions of rotation of the trough.

The power required to maintain a constant rotational speed, despite variations in torque, is also a key operational metric. It reflects the energy demand of the system and offers insight into the mechanical behaviour of the sample under dynamic conditions.

The temperature of the reaction chamber must be continuously monitored. This parameter is essential for correlating the measured torque and normal stress values with the thermal state of the system, particularly in tests involving reactive or temperature-sensitive materials. Accurate temperature tracking ensures that the mechanical data are interpreted within the correct thermodynamic context, enabling meaningful conclusions about material behaviour under coupled thermal-mechanical loading.

In addition to mechanical and thermal parameters, gas flow rate emerges as a critical variable in the control of the reactive chamber, particularly in tests involving chemical reduction. As previously discussed, the system accommodates multiple gas inputs, each serving a distinct function: hydrogen (H_2) as the reactive agent, and nitrogen (N_2) as the inert carrier or purge gas. The ability to precisely define, regulate, and maintain the flow rate of each gas stream is essential for ensuring both process safety and experimental reproducibility.

III.4.1. Transducers

With the control parameters clearly defined, the next step involves selecting the appropriate sensor systems and control units to ensure reliable operation and accurate data acquisition throughout the experimental procedure.

As previously described, the pressure applied to the linear actuator is a critical variable, directly influencing the normal stress exerted on the sample. This parameter is regulated via an electro-pneumatic proportional valve, detailed in Section 3.3.6, which not only modulates the pressure with high precision but also provides a feedback signal for real-time verification of the applied force. This feedback loop is essential for maintaining consistent consolidation and shear conditions during testing.

The rotational motion of the trough is governed by a servo motor, controlled through a dedicated servo drive (also discussed in Section 3.3.6). This unit defines the angular velocity of the motor and simultaneously monitors the torque output transmitted through the gearbox, offering a direct measure of the shear stress required to maintain lid stability during rotation.

To complete the control architecture, it is necessary to define the communication interface between the hardware and the user, as well as the data logging strategy which will be the subject of Section 3.5.

It remains necessary to define the characteristics of the transducers required to monitor the remaining variables: namely, the variation in lid position, the torque applied to maintain lid stability, and the temperature within the reactive chamber. The selection of suitable sensors depends not only on cost but also on a set of performance criteria that determine their reliability and precision under experimental conditions.

Sensitivity refers to the sensor's ability to detect small variations in the measured physical quantity; higher sensitivity enables the detection of minimal changes, which is particularly important in low-load regimes. Linearity describes the proportionality between the input physical quantity and the output signal; a sensor with good linearity ensures a predictable and consistent response across its operating range. Accuracy defines how closely the sensor's readings match the true value of the measured quantity, minimizing systematic errors and improving the validity of the data.

Repeatability is the sensor's capacity to produce consistent results under identical conditions, which is essential for ensuring reproducibility across multiple test cycles. Resolution indicates the smallest detectable change in the measured quantity; higher resolution allows for finer distinctions and more detailed analysis. Response time measures how quickly the sensor reacts to changes in the physical quantity, a critical factor in dynamic systems where transient behaviour must be captured.

Stability reflects the sensor's ability to maintain its performance over time, even in the presence of environmental fluctuations or aging effects. Finally, hysteresis quantifies the difference in sensor output when the measured quantity increases versus when it decreases; low hysteresis is desirable to

ensure that the sensor's response remains accurate and consistent regardless of the direction of change.
These parameters collectively guide the selection of transducers that are not only compatible with the mechanical and thermal demands of the system, but also capable of delivering high-fidelity data throughout the experimental campaign.

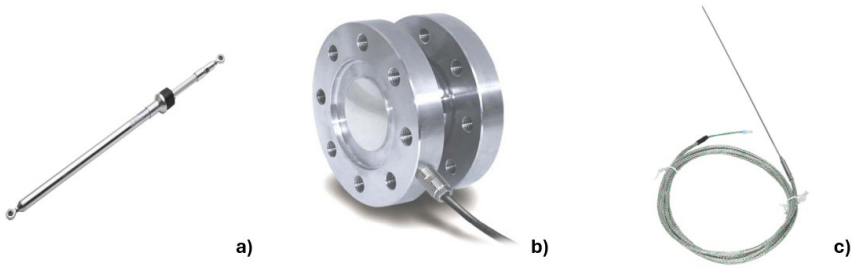

Figure III.24 Photographic images of the transducers used in the experimental setup: (a) position transducer, (b) torque transducer, and (c) temperature transducer.

To monitor the vertical displacement of the lid during testing, a Gefran PMA12-F0100 series position sensor was selected, as shown in Figure III.24.a. This device belongs to a class of high-performance linear position transducers and operates on a potentiometric principle, where a resistive element functions as a voltage divider, producing an analog output signal directly proportional to the position of a moving component.
One of the defining features of this sensor is its contactless design, achieved through magnetic coupling. The fixed body of the transducer is mechanically isolated from the moving cursor, which consists of a magnetic element that travels along the exterior of the sensor's anodized aluminium housing. This configuration eliminates mechanical friction, wear, and side loading effects, significantly extending the sensor's operational lifespan, and ensuring consistent performance over time.
The designation "F0100" indicates a useful electrical travel of 100 mm, suitable for capturing the full range of lid motion during compression and deformation phases. The sensor offers infinite resolution, enabling the detection of infinitesimal position changes, and boasts a repeatability of 0.08 mm, with minimal hysteresis, ensuring precise and reproducible measurements.
Engineered for harsh industrial environments, the sensor carries an IP67 rating, which guarantees complete protection against dust ingress and resistance to temporary immersion in water. This makes it particularly well-suited for operation in humid, wet, or contaminated conditions. Furthermore, its wide operating temperature range, from −30 °C to +100 °C, ensures compatibility with the thermal conditions expected during reactive testing.

To measure the torque required to maintain lid stationary during shear testing, a MTRX100NM01 flanged torque transducer was selected, as shown in Figure III.24.b. This sensor is engineered for high-precision torque measurement in static or reaction configurations, where the torque is exerted against a fixed structure rather than transmitted through a rotating shaft.
Its flanged architecture allows for rigid mounting between structural components, such as between the upper rod and the support frame, ensuring stable alignment and minimizing parasitic forces.

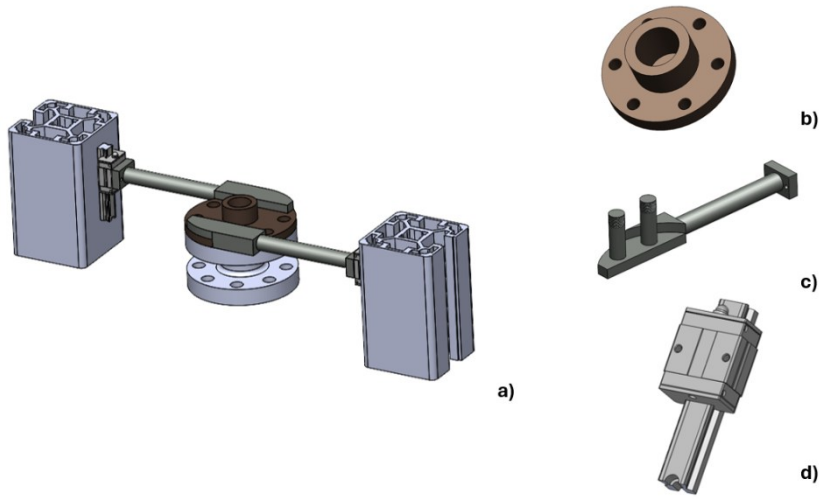

Figure III.25 Torque meter anchoring system: (a) complete assembly view, (b) steel adapter, (c) support branches, and (d) linear guide.

To ensure correct alignment of the torque transducer along the axis of normal force application, the flange geometry was carefully considered. The transducer features a flange with an external diameter of 80 mm, equipped with six DM 6 mounting holes spaced 64 mm apart, allowing for seamless integration with adjacent mechanical components. This configuration was mirrored in the design of the upper piston, which includes a corresponding flange at the end opposite the lid, facilitating direct coupling.
To connect the rod-piston-lid assembly to the linear actuator, and to secure one of the transducer's flanges to the fixed structure, thus preventing rotational motion, a custom steel adapter was developed, as illustrated in Figure III.25.b. This adapter serves a dual function: it transmits the compressive force from the actuator to the lid while simultaneously anchoring the transducer to the frame.
To achieve rotational constraint without impeding vertical motion, two branches with tailored geometry were fabricated and mounted on linear guides, also shown in Figure III.25.c. These guides are oriented orthogonally to the arms and are designed to withstand forces exceeding those generated during testing. Their low-friction design permits vertical displacement of the

rod and piston, while the arms effectively block any rotational movement, ensuring that torque measurements reflect only the shear-induced resistance.
The complete assembly (including the torque transducer, adapter, anti-rotation arms, linear bearings, and the Bosch profile frame to which they are anchored) is depicted in Figure III.25.a, which presents the SolidWorks reconstruction of the integrated system.
While primarily designed for static applications, the sensor's mechanical robustness and strain gauge configuration also make it suitable for low-speed dynamic torque measurements, provided the rotational motion remains within the sensor's bandwidth and mechanical tolerances.
Internally, the transducer operates on the strain gauge principle, with a deformable sensing element instrumented with foil strain gauges arranged in a Wheatstone bridge. When torque is applied, the element undergoes controlled elastic deformation, altering the resistance of the strain gauges and producing a ratiometric analog signal proportional to the applied torque. This output, typically expressed in millivolts per volt (mV/V), requires a stable excitation voltage and a high-resolution amplifier for accurate signal conditioning and data acquisition.
The sensor's solid-state construction ensures high mechanical rigidity, excellent repeatability, and low hysteresis, with integrated protection against overload and side loading. It is rated for compressive loads up to 19000 N and can operate reliably at temperatures up to 80 °C, making it well-suited for industrial environments and research applications where precision and durability are essential.
To monitor the temperature within the furnace and reactive chamber, Type S thermocouples, Figure III.24.c, were selected due to their proven reliability in high-temperature environments. This thermocouple consists of two electrodes: the positive terminal is composed of an alloy containing 90% platinum and 10% rhodium, while the negative terminal is made of pure platinum. The exclusive use of platinum group metals is central to the sensor's thermal stability, chemical inertness, and long-term accuracy under extreme conditions.
Type S thermocouples are specifically designed for continuous operation in oxidizing or inert atmospheres, with a functional temperature range extending from 0 °C to approximately 1600 °C.
Despite their robustness, Type S thermocouples present several limitations. The most notable is their cost, driven by the use of precious metals such as platinum and rhodium. Additionally, they exhibit low thermoelectric sensitivity, generating only 6–12 μV/°C, which necessitates the use of high-impedance, low-noise amplification systems to ensure accurate signal acquisition.
Another critical concern is their susceptibility to contamination, commonly referred to as platinum poisoning. In hydrogen-rich atmospheres electrode can

undergo chemical interactions that lead to embrittlement, structural degradation, and irreversible calibration drift [134].
To enhance the sensor's durability, the application of a titanium nitride (TiN) coating has been considered. TiN acts as a diffusion barrier, limiting the interaction between hydrogen molecules and the platinum surface. Although the formation of metal–hydrogen complexes may be transient and reversible, repeated exposure can lead to subtle structural changes and progressive loss of measurement accuracy. The TiN coating reduces hydrogen permeability, minimizes catalytic surface reactions, and extends the operational lifespan of the thermocouple under demanding thermal–chemical conditions.
These elements ensure that all monitored parameters (pressure, torque, speed, and temperature) are not only accessible in real time but also stored for post-processing and analysis, thereby supporting reproducibility and traceability of the experimental results.
Further technical specifications and reference datasheets for the transducers discussed in this section are provided in Appendix B, where each sensor is documented with its model designation, operating principles, performance parameters, and integration notes.

III.4.2. Signal conditioning modules and DAQ

The intrinsic limitations of transducers, such as low signal amplitude, nonlinearity, and susceptibility to noise, necessitate the integration of signal conditioning circuits to ensure accurate, stable, and interpretable measurements. This section outlines the adopted strategy for coupling each transducer with its corresponding conditioning module and describes how the resulting signals are acquired and processed.
Signal conditioning circuits, also referred to as transmitters or converters, serve as the interface between the raw sensor output and the data acquisition or control system. In most cases, the native signal generated by a transducer, such as the millivolt output of a thermocouple or the resistance variation of a strain gauge, is not directly compatible with standard acquisition hardware. These signals are often too weak, nonlinear, or prone to electrical interference. The role of the conditioning circuit is to transform this raw signal into a clean, stable, and standardized output, suitable for reliable acquisition and interpretation.
These circuits typically perform several essential functions. Conversion involves translating the physical signal into a standardized electrical format, such as a 4-20 mA current loop or a 0-10 V voltage signal, which are widely used in industrial environments. Amplification boosts low-level signals to improve robustness against noise and transmission losses. Electrical isolation protects both the sensor and the acquisition system by preventing ground loops and shielding sensitive electronics from voltage spikes. Linearization compensates for the inherent nonlinearity of many sensors, such as

thermocouples, ensuring a proportional relationship between the measured quantity and the output signal. Excitation is provided for passive sensors like strain gauges, supplying a stable voltage or current necessary for their operation. Finally, filtering removes high-frequency noise and electromagnetic interference, improving signal clarity and measurement stability.

In this system, signal conditioning is entrusted to modules from the DATEXEL DAT series, selected for their versatility, modularity, and broad compatibility with various sensor types. Although each module is optimized for a specific class of transducers (e.g., thermocouples, RTDs, strain gauges), they can be easily reconfigured to accommodate different sensor variants. Configuration is achieved either digitally via software or manually through internal DIP switches, allowing the user to define the measurement range, sensor type, and input/output signal format. This flexibility ensures seamless integration across the entire instrumentation chain and supports future modifications or expansions of the experimental setup.

For temperature measurement, the Type S thermocouple offers excellent stability and durability at high temperatures, but it generates a low-level, nonlinear voltage signal in the microvolt range, which depends on the temperature gradient between the measuring junction and the cold junction. To address these limitations, the DAT-4531/A universal temperature transmitter is employed. This module performs multiple critical functions: it supplies the thermocouple with the necessary connection power, applies cold junction compensation (CJC) to correct for ambient terminal temperature, linearizes the thermoelectric response specific to the thermocouple type, and amplifies the weak signal. The conditioned output is a standardized 0-10 V analog signal, directly proportional to the measured temperature and suitable for processing by control systems or data loggers.

In the case of torque measurement, the MTRX100NM01, this bridge configuration does not generate a usable signal autonomously; it requires a precise and stable excitation voltage, and its output is a low-level differential signal expressed in mV/V. The DAT-5025 module serves as a dedicated strain gauge amplifier, providing the required excitation and amplifying the return signal. The resulting output is a robust 0-10 V analog signal, linearly proportional to the applied torque, ensuring compatibility with standard acquisition systems and enabling high-resolution monitoring of mechanical response.

The proportional valve, unlike sensors, requires an active control signal in the form of a regulated current to drive its internal solenoid which acts on the air flow. The DAT-4532D module functions as a valve driver, converting a low-power setpoint signal (0-10 V) into a precise current output suitable for the valve. Operating in closed-loop mode, it also accepts a feedback signal from the valve, allowing it to monitor the actual position and adjust the output

accordingly. This ensures accurate regulation of the delivered pressure and maintains the desired process conditions with high precision.
Analog position measurement using a potentiometric sensor coupled with a dedicated transmitter represents a well-established configuration in industrial systems. The sensor itself is a passive element, functioning as a variable resistor whose produces a voltage proportional to the position of a moving component relative to a fixed excitation reference.
However, the raw signal generated by the potentiometer is inherently high impedance, making it vulnerable to electrical noise, voltage drop, and signal degradation over long transmission distances. These limitations render the signal unsuitable for direct acquisition by control systems or data loggers.
To overcome these issues, a signal conditioning circuit GRAFEN PCIR 101 is employed. Its first function is to supply the potentiometer with a precise and stable excitation voltage, ensuring consistent reference conditions for ratiometric measurement. The circuit then reads the variable voltage output, applies buffering and amplification, and converts it into a robust 0-10 V analog signal.

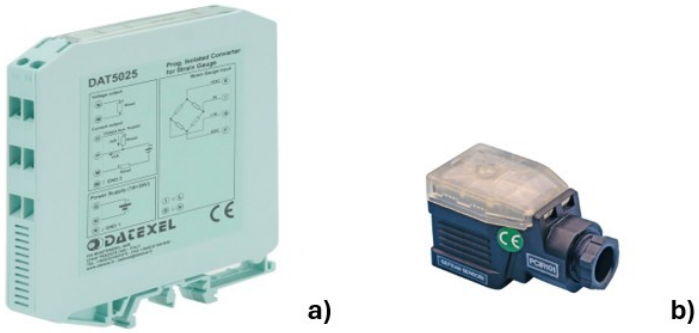

Figure III.26 Photographic images of the DATEXEL and GRAFEN PCIR 101 modules used in the instrumentation setup.

For the acquisition of conditioned signals and the generation of control setpoints, the system employs the NI USB-6341, a portable multifunction data acquisition (DAQ) device developed by National Instruments. This unit is part of the X Series family, recognized for its advanced timing architecture, high-performance analog and digital I/O, and seamless integration via a high-speed USB interface, making it suitable for both laboratory and industrial environments.

Figure III.27 Photographic images of NI USB-6341.

The device features 16 analog input (AI) channels, each capable of measuring voltages in the 0-10 V range. These channels are used to acquire the output signals from the various signal conditioning modules, capturing physical quantities such as temperature, torque, and position with high resolution and fast sampling rates, ensuring accurate temporal tracking of dynamic phenomena.
In addition to acquisition, the NI USB-6341 provides two analog output (AO) channels which are used to generate precise control signals, typically in the 0-10 V range, to drive actuators or set operating points for conditioning modules such as proportional valve controllers.
The device also includes 24 digital input/output (DIO) lines, which support binary logic operations, status monitoring, and simple control tasks such as triggering, flagging, or interfacing with auxiliary systems. All I/O functions are managed through NI LabVIEW, a graphical programming environment that enables real-time control, data logging, and flexible integration with custom experimental protocols.

III.5. LabVIEW

To enable on-screen visualization, parameter recording, and user interaction with the prototype, a control and command interface was developed in LabVIEW. The interface is structured within a Tab control, a LabVIEW element that functions as a set of subfolders, allowing the creation of user-selectable views.
Once the sample has been prepared, weighed, and positioned on the lower rod, the dedicated interface for testing - named “Shear Testing” - can be chosen. This interface is organized into several sections. Starting from the left size, the user may enter optional information such as material type, sample mass, and additional notes.

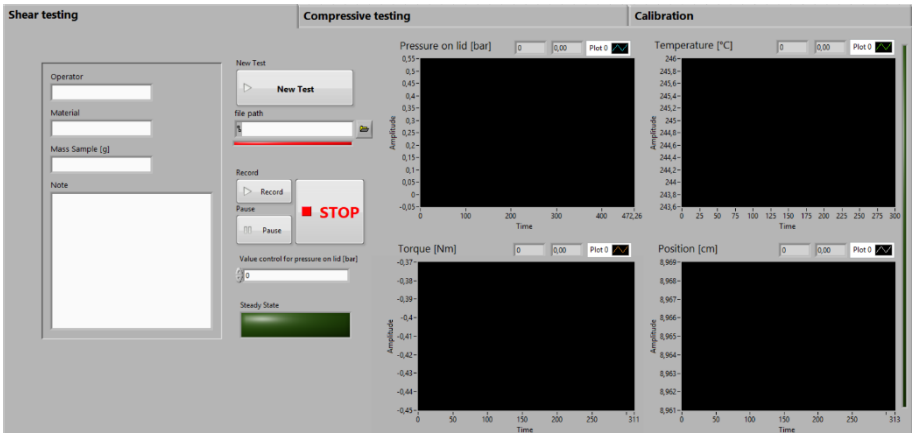

Figure III.28 Shear testing interface. The layout presents the area dedicated to optional information on the left, the central section with buttons for initiating data acquisition and control, and the right side, displaying real-time graphs of the prototype data.

The next step is to define the file path that specifies the memory location where the recorded data will be stored. Confirmation of this operation is provided by an LED indicator located below the input box, which switches from red to green once the path has been successfully validated.

After the file path has been set, the test can be initiated by pressing the "New Test" button. At this stage, a message prompts the user to verify that the file has been correctly created, thereby minimizing the risk of data loss during acquisition.

During the test, three control buttons are available: Record, Pause, and Stop. These allow the user to decide when to begin data acquisition, when to temporarily suspend recording while continuing to display sensor outputs on screen, and when to terminate the test permanently.

In accordance with standard procedures, the only adjustable parameter during room-temperature testing is the pressure applied to the sample by the lid. This value is entered in the input box labelled "Value control for pressure on lid (bar)". To ensure reliability, input values are constrained between 0 and 8; any number outside this range is automatically converted to the nearest valid limit.

A second LED is positioned below the input box and linked to the steady-state condition of the measured shear stress value. Its function is to provide an additional visual indication to the operator regarding the current status of the system.

The interface includes four real-time graphs that display the pressure applied to the lid, the torque, the temperature inside the reactive chamber, and the lid position. Together, these elements enable the user to acquire, monitor, and store data while maintaining full control of the prototype.

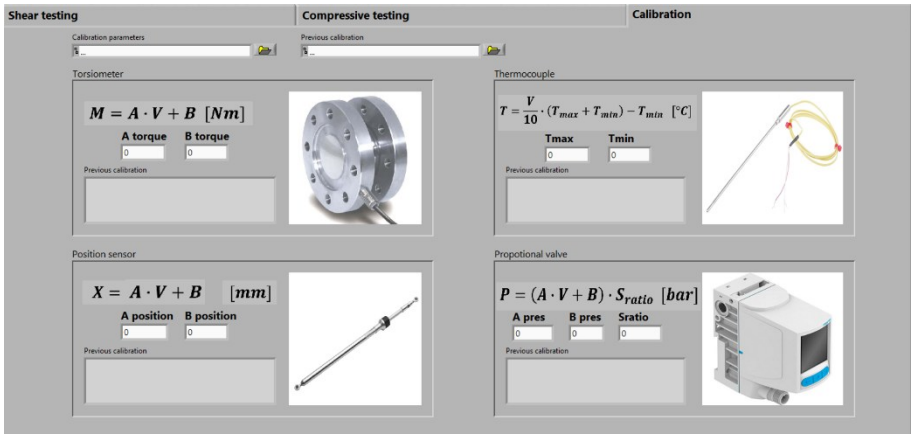

Figure III.29 Calibration interface.

The second interface available to the user is "Calibration", which contains all the conversion parameters for signals generated by the various reading and control elements. The signals output from the conditioning circuits, as described in Section III.4.2, are adapted to the format required by the DAQ acquisition unit (0-10 V). Each input value is then translated into the monitored physical quantity through calibration equations.

The interface provides a dedicated box for each input signal. Alongside the image of the corresponding electronic component, the box displays the conversion equation in use, the date and parameters of the previous calibration, and two input fields for modifying the coefficients of the equation. All equations adopt a linear relationship between the monitored quantity and voltage, which represents one of the main advantages of employing conditioning circuits.

In terms of operation, when the software is launched the code automatically retrieves the coefficient data stored in memory. The source location is specified by the "Previous calibration" file path. At the beginning of each test, the operator may choose to define a new calibration file by entering the destination address in the "Calibration parameters" file path. If new coefficients are introduced in the input fields, a new calibration file is generated to replace the previous one. Otherwise, the coefficients are automatically loaded from the existing file and applied throughout the test.

III.5.1. Calibration

Calibration was conducted in accordance with standard protocols. As an example, the procedure applied to the position sensor involved progressively increasing its extension across the entire measurement range, following a positive step function. During this ascent phase, the corresponding voltage was monitored continuously. The same procedure was then repeated in reverse: the extension was reduced step by step according to a negative

function, and the voltage was again recorded. As illustrated in Figure III.30.a, the measured signal remained within the expected 0-10 V range and demonstrated excellent stability. In the plot, the ascent phase is represented in blue, with each step corresponding to a one-centimetre increase in extension, while the descent phase is shown in orange, with each step representing a similar reduction.
To obtain the calibration curve, the signal was acquired over a defined period. For each extension step, the last 50 recorded voltage values were averaged using an arithmetic mean, thereby establishing the extension-voltage relationship for both the rise and fall phases.

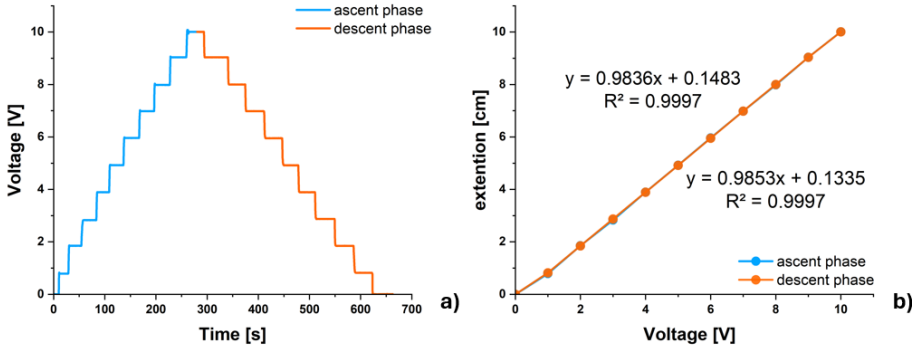

Figure III.30 (a) Raw voltage data acquired during the calibration procedure. (b) Averaged values for the ascent and descent phases, showing the extension-voltage relationship.

Figure III.30.b presents the resulting regression curves. The near-perfect overlap between the ascent and descent data confirms the absence of hysteresis, validating the reliability of the sensor response. Consequently, the derived linear equation was implemented in the software to convert the signal from the conditioning circuit into the corresponding position measurement.
The calibration procedure for the torque meter differs from that of the other sensors, as it follows the protocol specified in the DAT5025 manual. The output signal range (0-10 V) must be distributed across the entire measurement span in both directions of rotation.

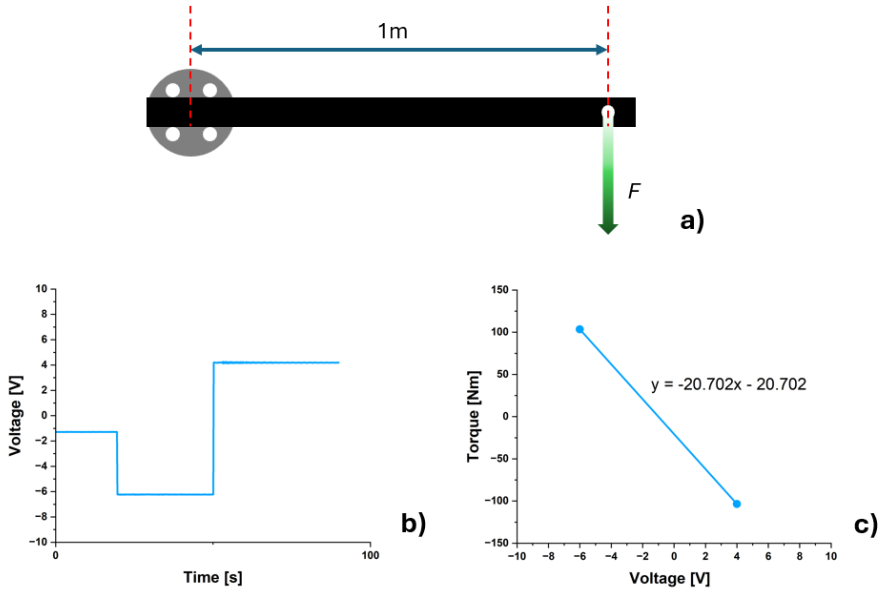

Figure III.31 (a) Schematic representation of the calibration setup. (b) Raw data acquired during the calibration phase, highlighting the two-step procedure. (c) Calibration curve with regression line, showing the relationship between applied torque and the average of the last 50 voltage points recorded at each step.

The configuration illustrated in Figure III.31.a was adopted for calibration. One flange of the torque meter was fixed to a vertical wall to secure the body, while the opposite flange was subjected to a force *F* applied at a distance of 1 m using a perforated rod. The applied load was carefully selected to account for all implicit contributions to the system, including the weight of the rod itself. In accordance with the manual, the maximum load was applied in the counterclockwise direction to establish the zero-reference value on the conditioning circuit. Subsequently, the same maximum load was applied in the clockwise direction to define the span value.

The calibration results are presented in Figure III.31.b, showing the relationship between torque and voltage. The data confirm a linear correlation, which was implemented in the software to ensure accurate conversion of the torque meter signal.

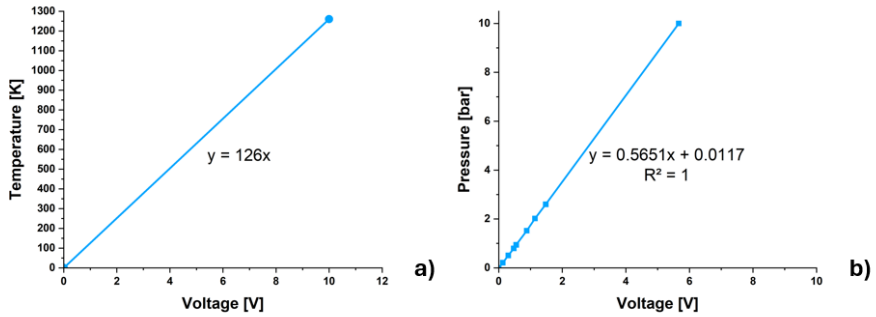

Figure III.32 a) Graph showing the temperature–voltage relationship derived from thermocouple calibration. b) Graph showing the air pressure–voltage relationship obtained for the proportional control valve.

For temperature calibration, the supplier tables were used to establish the relationship between thermocouple output voltage and temperature. As thermocouples are widely standardized sensors, these tabulated values can be considered representative of the transducer implemented. Once the conditioning circuit was configured to accept millivolt input and provide a 0-10 V output, the tabulated values were expressed through a linear law and scaled accordingly to match the new output range. The resulting regression line is shown in Figure III.32.a.

For the proportional control valve, calibration was performed by imposing a defined input voltage and directly reading the corresponding pressure value on the valve's display. In this way, the voltage-pressure relationship of the linear actuator chamber was determined. The output signal was acquired via LabVIEW, averaged, and associated with the set-point value displayed on the valve. The regression line obtained is presented in Figure III.32.b.

The implemented equation does not explicitly account for the ratio between the surface area of the actuator's internal rod and that of the lid, even though this ratio influences the pressure applied to the material. Instead, this correction factor is incorporated directly into the code. As a result, the value entered by the operator in the input box corresponds to the actual pressure applied to the material.

The evaluation of the extended uncertainty associated with each sensor is reported in Appendix D, where the complete methodology and numerical results are presented.

III.5.2. LabVIEW Code

The code underlying the user interfaces is presented in Figures III.33-35. Within these figures, specific portions of the LabVIEW code are highlighted in dedicated boxes. These segments correspond to distinct tasks performed by the system and will be examined in detail in the following discussion,

illustrating how each block contributes to data acquisition, control, and data storage.

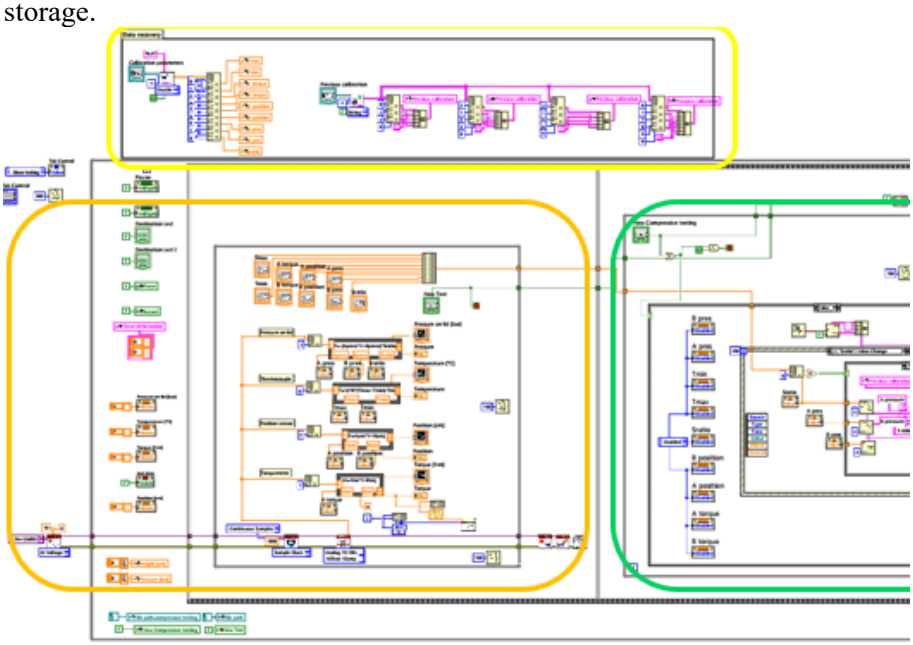

Figure III.33 LabVIEW code: Part I.

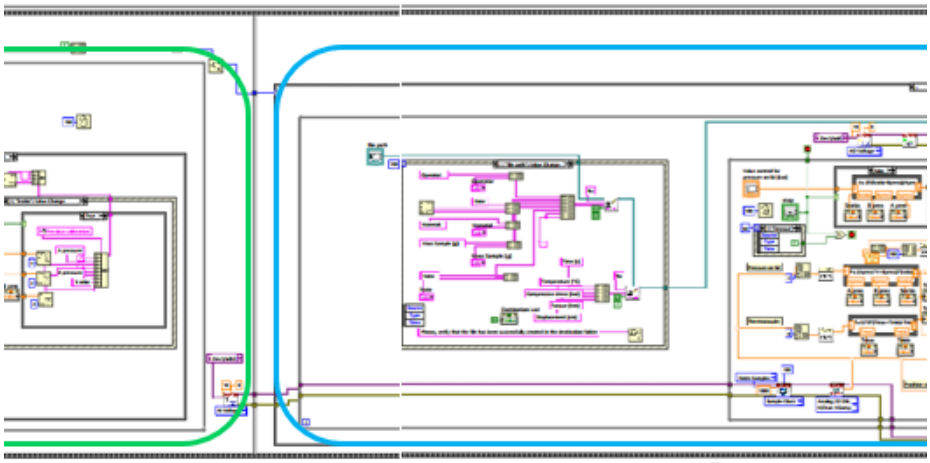

Figure III.34 LabVIEW code: Part II.

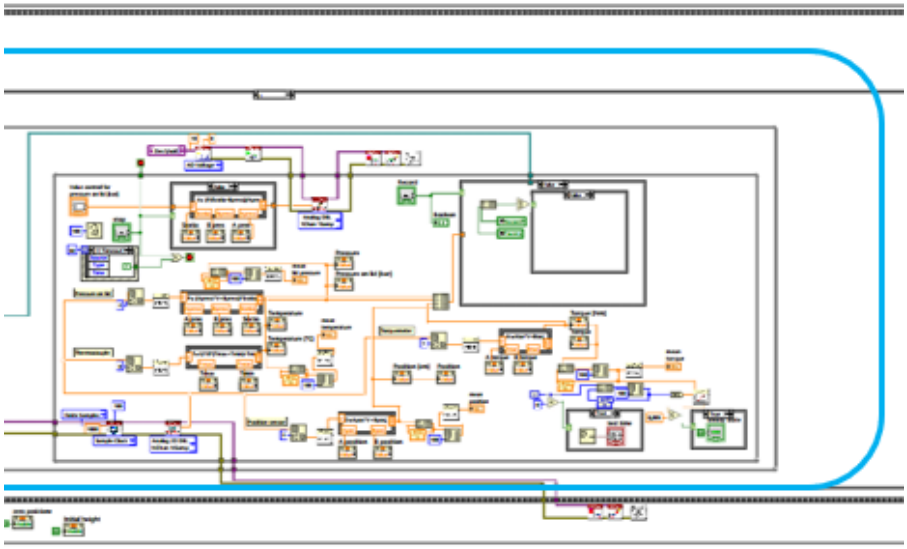

Figure III.35 LabVIEW code: Part III.

The first operation executed when the code starts is contained in the yellow box shown in Figure III.36, which retrieves the calibration parameters displayed in the Calibration interface (Section III.5). The sequence of blocks *File Path* and *Read Delimited Spreadsheet.vi* forms the core of this process, enabling access to calibration parameters stored in .txt format. The Read Delimited Spreadsheet.vi block requires several input specifications, including the number of lines to be read (with –1 indicating that the entire file should be processed) and the number of significant digits in the data (%.4f, a floating-point format with four decimal places).

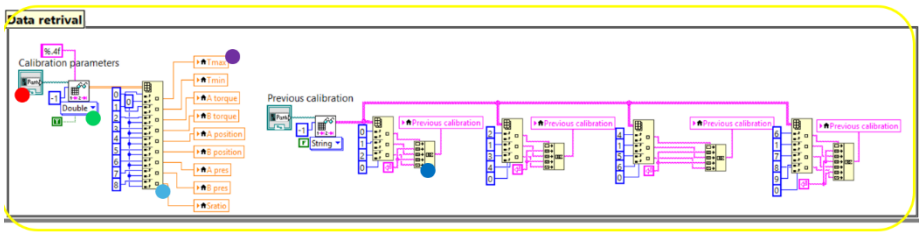

Figure III.36 LabVIEW code: data retrieval. The circles indicate the main functional blocks: red, File Path; green, Read Delimited Spreadsheet.vi; light blue, Index Array; purple, property node Value (used to print the value inside the input box); and blue, Concatenate String.

The output generated is a two-dimensional array, i.e., a matrix of elements that must be decomposed to extract the required values. Individual parameters, subsequently displayed on screen through the corresponding input blocks, are retrieved using the *Index Array* block, which requires the row-column coordinates of the desired element as input.

A second sequence of elements, beginning with the same File Path and Read Delimited Spreadsheet.vi configuration, is used to display in dialog boxes the information relating to the calibration execution date (specific to each electronic component) and the parameters stored in the file. In this case, the output signal from Read Delimited Spreadsheet.vi is a string, which is reconstructed using the *Concatenate String* block to ensure correct display to the operator.

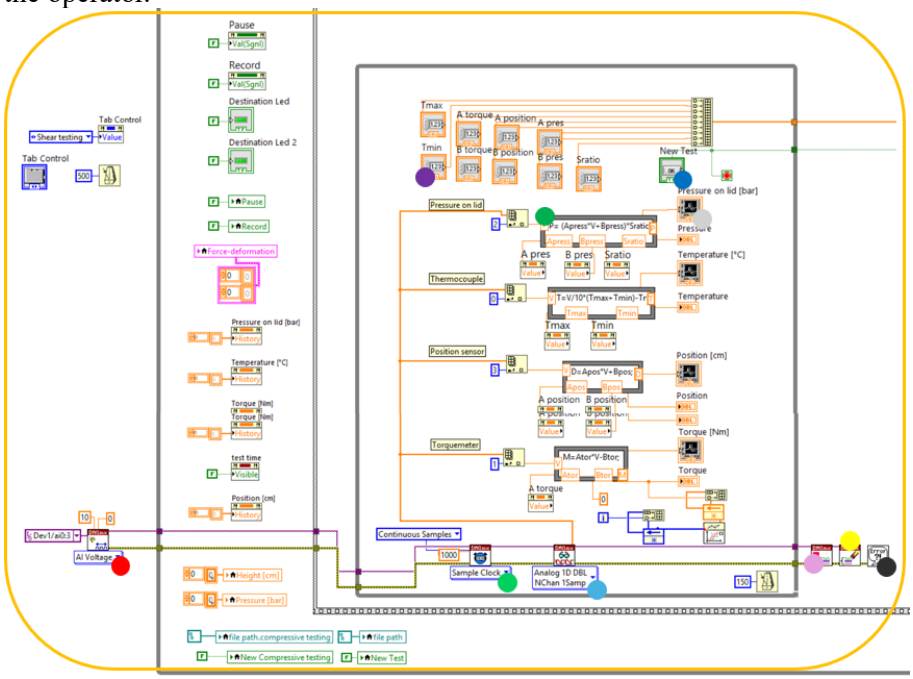

Figure III.37 LabVIEW code: data input. The circles indicate the main functional blocks: red, DAQmx Create Channel*; light green,* DAQmx Timing.vi*; light blue,* DAQmx Read *block; purple, input box value; dark green,* Formula Node*; blue, new Test button; grey,* Waveform charts; *light purple, DAQmx Stop Task.vi; yellow, DAQmx Clear Task; black, Simple Error Handling.vi.*

The remaining portion of the code is contained within a flat sequence, a logical structure that ensures a defined execution order from left to right. Beginning from the left, the content shown in Figure III.37 can be examined.
At the bottom of the figure, a logical path is highlighted in purple and yellow. This sequence defines the communication channel with the acquisition board in a clear and readable form. The chain begins with the *DAQmx Create Channel* block, which specifies the board channels from which input signals are read in terms of voltage; in this case: Dev0/3. This block requires the definition of the signal type (here, analog voltage: AI Voltage) and the permissible range of values, set between 0 and 10 V. Following this, the *DAQmx Timing.vi* block defines the acquisition mode and sampling frequency, thereby establishing the temporal structure of the data acquisition process.

The next element in the sequence is the *DAQmx Read* block, which defines the task to be performed and specifies the type of reading. In this case, the configuration involves one analog input, represented as a one-dimensional double array, with each channel providing a unique reading value. Since these operations must be repeated an indefinite number of times, the blocks are enclosed within a *While* loop, which continues execution until a defined event occurs: the start of the test using the *New Test* button.

The output signal from the DAQmx Read block, a 1D array, is subsequently decomposed and reprocessed according to its source. Several *Formula Node* blocks are employed to convert the raw signal into voltage values of the desired magnitude. The equations described in Section III.5.1 are embedded within these structures, incorporating the calibration parameters. The input boxes from the Calibration interface, in reading mode, are also integrated into the While loop. As a result, any updates made to the calibration parameters within the interface are automatically applied, ensuring that the displayed values are corrected and adapted in real time.

The converted voltage values are then presented to the user through *Waveform charts*. Each instantaneous value is displayed both graphically and numerically, providing a clear and immediate representation of the system's behaviour during the test.

Once the test is initiated, the While loop is terminated and the logical communication path with the acquisition board is closed through three specific blocks. The *DAQmx Stop Task.vi* block instructs the board to halt data acquisition, while the *DAQmx Clear Task* block cancels the task and releases the associated resources. Finally, any errors generated during execution are managed by the *Simple Error Handling.vi* block, ensuring proper closure of the process and maintaining system stability.

The purpose of this portion of code is to guide the operator through the pre-test procedures, enabling both visual and numerical verification of the system's correct functioning. In addition, it provides sufficient time for the operator to enter optional information, such as the destination folder and the name of the file to be generated.

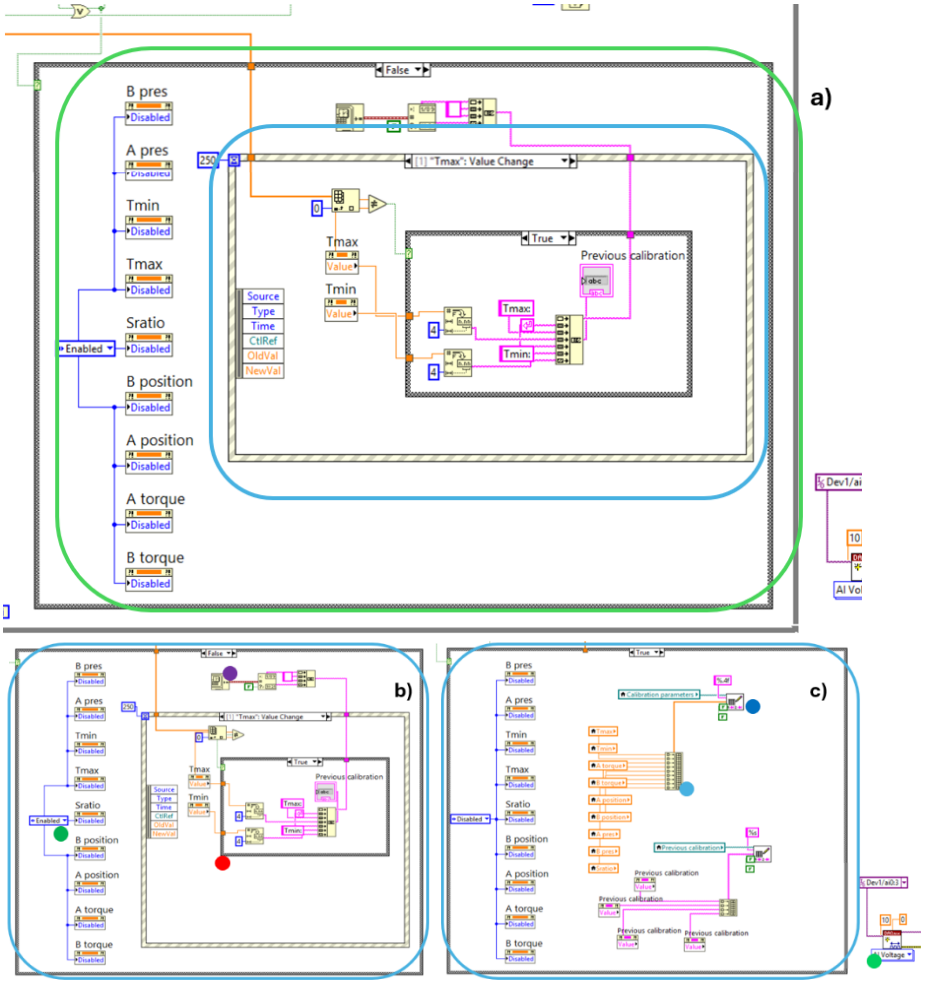

Figure III.38 LabVIEW code: calibration parameter management. The circles highlight the main functional blocks: (a) Second portion of the Flat Sequence. (b) False case of the Case Structure: in green, enabling changes to the input boxes for the coefficients (Writing mode); in purple, the Get Date block; in red, a second Case Structure for updating the coefficients in memory. (c) True case of the Case Structure: in light blue, the Build Array block; in blue, Write Delimited Spreadsheet.vi; in green, DAQmx Create Channel.vi.

The second section of the Flat Sequence is dedicated to saving the calibration parameters (Figure III.38.a). It contains a *Case Structure*, which enables the execution of specific portions of code depending on the input condition; in this case a true/false state.

As long as the New Test button has not been pressed (false state), the input boxes associated with the calibration coefficients remain enabled in Writing mode (Figure III.38.b). Any modifications made by the user are saved, and the calibration file is updated accordingly. This update incorporates both the new

parameter and the date of modification, retrieved via the *Get Date* block, which is linked exclusively to the component being altered.
When the New Test button is pressed (true state, Figure III.5.c), the input boxes switch to Read-Only mode, preventing further changes during the test. All the data required for the conversions are collected into a single one-dimensional array using the *Build Array* block. The file is then written in .txt format through the *Write Delimited Spreadsheet.vi* block, which, in addition to specifying the data type, also allows the user to define the number of digits associated with each value. Therefore, at this stage, the calibration files are updated to reflect the locked parameters, ensuring consistency and reliability throughout the test execution.
After the data have been saved, a new acquisition cycle is initiated by defining a new communication path with the board through a DAQmx Create Channel.vi block, and then the process moves on to the third and final section of the Flat Sequence.

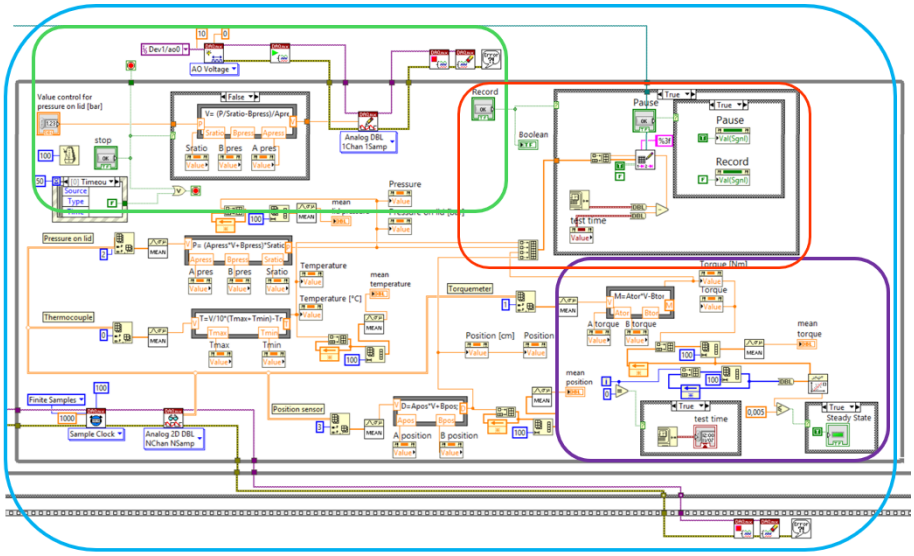

Figure III.39 LabVIEW code: shear testing.

The logical operating principle of this portion of the code is closely aligned with that of the first segment of the Flat Sequence. In the lower part of Figure III.39, the sequence of reading blocks can be identified: DAQmx Timing.vi followed by the DAQmx Read block. Unlike the previous case, the output of the DAQmx Read block generates a two-dimensional signal (matrix). This difference arises from the configuration of the timing block, which specifies that 100 units must be acquired at the indicated frequency. The resulting 2D output signal is then decomposed, and the individual vectors containing the 100 samples are averaged (arithmetic mean). These averaged values are subsequently converted via Formula Nodes into the physical quantities displayed to the user.

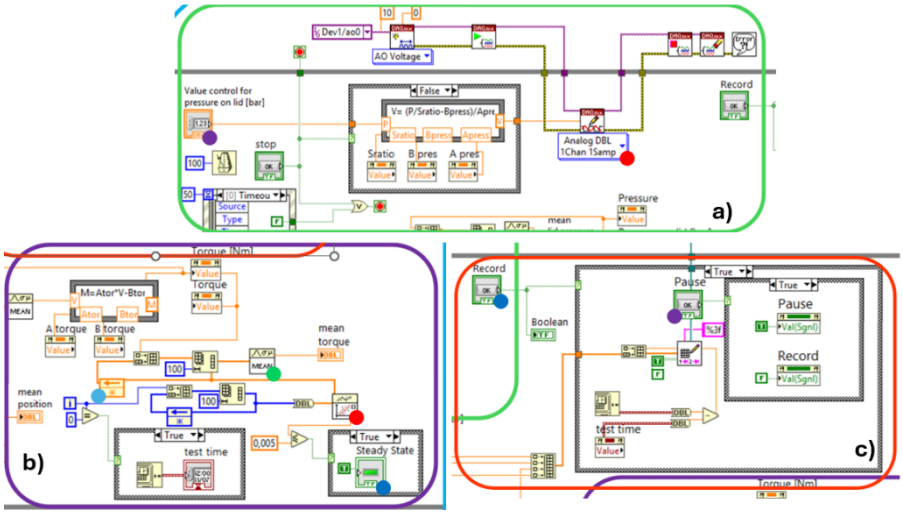

Figure III.40 Functional blocks within the Flat Sequence. The circles highlight the main functional elements: (a) Input box for pressure control in purple, and DAQmx Write.vi in red. (b) Feedback Node in light blue, Mean.vi in green, Linear Fit.vi in red, and LED indicator in blue. (c) Record button in blue; and Pause button in purple.

In this code window, three additional portions of code are introduced. The first, shown in Figure III.40.b, represents the portion of code required to determine the steady-state condition of the measured torque value. A finite-size vector (100 elements) is created after the conversion of the averaged points, corresponding to approximately 10^3 samplings. The ability to store values between successive cycles is provided by the *Feedback Node*, which fulfils this function. The arithmetic mean of this numerical sequence is calculated using *Mean.vi* and displayed on the screen, while the slope is determined via the *Linear Fit.vi* block. If the slope value remains close to zero, within an error margin of 0.005, the LED positioned on the Shear Testing interface is activated, providing a clear visual indication of the steady-state condition.

The second portion of the Flat Sequence (Figure III.40.a) concerns the control of the pressure applied to the sample. The value entered by the operator is converted via a Formula Node and transmitted to the acquisition card. To interface with the DAQ, a new channel must be opened, specifying only the analog output ports of the hardware through a DAQmx Create Channel.vi block. The task is then initialized using the DAQmx Start Task.vi block. Since both reading and writing operations must be executed throughout the entire experimental cycle, the writing block (*DAQmx Write.vi*) is also included within the While loop. Outside the loop, the task-closing blocks are positioned: Stop Task.vi, Clear Task.vi, and Simple Error Handler.vi; the same sequence employed for the reading operations.

Finally, the last sequence of blocks (Figure III.40.c) manages the writing phases of the .txt file associated with the test. Depending on the operator's

actions, specific portions of the acquired data are stored when the Record button is pressed. If the Pause button is pressed, writing is suspended; however, the processing, conversion, and representation phases continue to operate, as they are handled by distinct portions of the code.

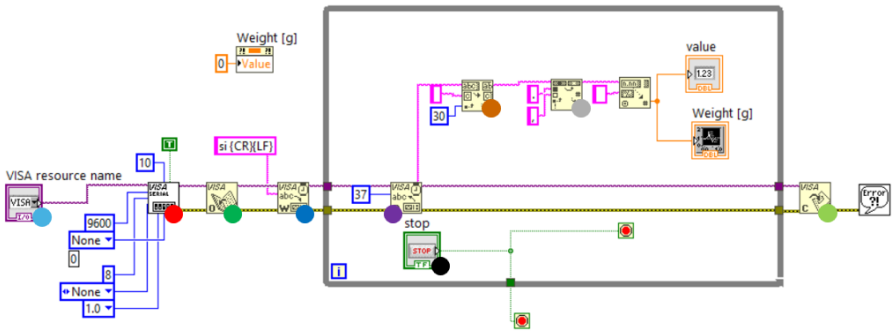

Figure III.41 LabVIEW code: balance. The circles highlight the main functional elements: VISA Resource Name in light blue, VISA Configure Serial Port in red, VISA Open in green, VISA Write in blue, VISA Read in purple, Search/Split String sequence in brown, Search and Replace String in grey, Stop button in black, and VISA Close in light green.

The balance is the only transducer that uses USB as its communication protocol; consequently, some variations in the blocks are required (Figure III.41), although the logical sequence remains unchanged.
The main block is *VISA Configure Serial Port*, which initializes the serial port specified by the *VISA Resource Name* block. To configure the serial port, the parameters must be adapted to match the signal generated by the transducer. Accordingly, the baud rate, number of bits, parity, and type of flow control are set in accordance with the scale's manual. The next block, *VISA Open*, establishes the selected channel. With the *VISA Write* block, the command string is sent to the transducer, instructing it to transmit the measured value. This requires implementing a code string consistent with the language recognized by the device. Once the task has been defined, continuous reading is necessary; therefore, the subsequent elements are placed inside a While loop.
The *VISA Read* block acquires the input information, with the required length specified. The input is not a numerical value but a string that follows the syntax defined by the hardware. To represent the data on a waveform chart, the string must be converted into a numerical value. Since the code string contains non-numeric characters and uses a comma as a separator, preprocessing is required. This is achieved through the *Search/Split String sequence*, which isolates the portion of the string containing the numerical values, and the *Search and Replace String* block, which replaces the separator to make the data suitable for numerical representation.

When acquisition is stopped via the Stop button, the *VISA Close* block terminates the communication channel, and any errors are managed by the Simple Error Handler.vi block, ensuring proper closure of the process.

III.5.3. Festo Automation Suite

The only elements that cannot be managed directly through LabVIEW are the furnace temperature and the rotational speed of the rotary motor.
For the furnace, a Pixys ART 264 temperature controller is installed at the power supply. This device is based on PID logic for temperature regulation.
The situation is different for the rotary engine, which is controlled using the proprietary software Festo Automation Suite. Since this software was not developed internally, only the key interfaces required for the correct use of the prototype are presented. The Festo software operates by Projects: for each project, it is necessary to define the sequence of elements that are directly or indirectly connected to the servo drive.

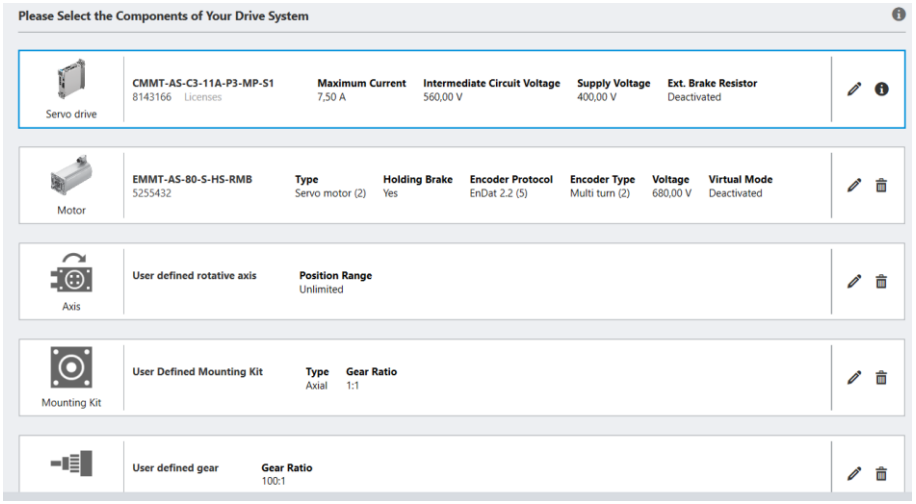

Figure III.42 Festo Automation Suite: Parametrization interface

In the Parametrization section, the properties of the various components must be specified, as shown in Figure III.42.

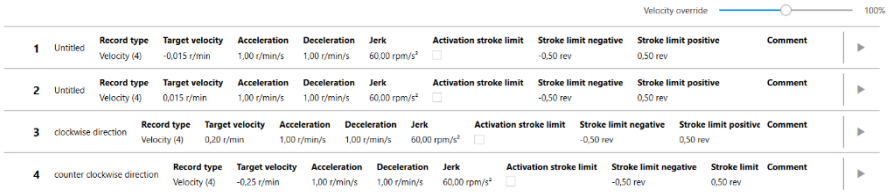

Figure III.43 Festo Automation Suite: Record table interface.

For control purposes, the software uses the Record Table interface (Figure III.43), which allows the definition of target conditions. In the case under examination, the control objective is the rotational speed. From the figure, it can be observed that the elements identified as 1 and 2 are characterized by extremely low rotational speeds, similar to standard procedures, but opposite in direction. The remaining elements, 3 and 4, exhibit higher speeds. In this way, the operator can easily manage the rotating portions of the prototype both during the execution of the test and in the system preparation phase.

III.6. Prototype validation

A fundamental step in the development process was the verification of the prototype's functionality. However, a direct comparison with commercial equipment proved challenging due to the extended measurement range of the prototype, which was specifically designed to operate under higher temperatures and compressive loads than those typically supported by standard shear testing devices.

As discussed in Section 2.3, the Schulze RST-01 rotational shear cell represents the most robust commercial solution currently available for high-load applications. To enable a meaningful comparison within the load constraints of this equipment, the decision was made to operate with the S-cell, the smallest cell in the Schulze system. This choice was motivated by the fact that, for a given applied force, a smaller lid cross-section results in a higher compressive stress, thereby allowing the test conditions to approach the upper operating limits of the prototype.

The S-cell is equipped with a lid of annular geometry, featuring an inner diameter of 31 mm and an outer diameter of 59 mm. The lid surface in contact with the sample is fitted with twenty radially aligned parallelepiped vanes, each measuring 1 mm of thickness, 4 mm height and 28 mm width. The corresponding trough has a toroidal geometry, with an inner diameter of 30 mm, an outer diameter of 60 mm, and a height of 24 mm.

This configuration enables the S-cell to generate shear and compressive stresses comparable to those applied by the prototype, particularly in the upper range of its operating envelope, thereby providing a qualitative benchmark for evaluating the prototype's performance.

A critical aspect of the experimental setup was the selection of a granular material capable of withstanding high compressive loads without undergoing deformation. It was observed that the flow properties of granular media are strongly dependent on particle size; therefore, any comminution would alter the particle size distribution, compromising the comparability of the experimental data. To avoid this, quartz sand with an average particle diameter of approximately 250 μm was selected as the reference material, due to its mechanical stability and inert behaviour under test conditions.

For both shear cells, sample preparation followed the standard test methods for bulk solids. The sand was gently introduced into the troughs using a spoon, in order to minimize undesired consolidation and ensure the absence of internal voids. Once filled, the excess material was carefully removed with a spatula, avoiding any vertical pressure on the free surface, until a uniform level was achieved at the top edge of the trough. The filled trough was then weighed to estimate the initial bulk density and subsequently connected to the corresponding rotary engine to initiate the test sequence.
Regarding the operating conditions, the temperature was constrained by the specifications of the Schulze RST-01 shear cell, which limits testing to ambient conditions. Consequently, all tests were conducted at room temperature. The applied loads, however, were selected based on the measurement ranges of the two devices, and the corresponding values are reported in Table III.6.

Table III.6 Investigated conditions in terms of normal stresses applied to the sample, and the corresponding plateau value of shear stress recorded in the prototype and in the Schulze ring shear tester equipped with an S-cell.

Prototype		Schulze RST-01 + S-cell	
Normal stress [kPa]	Shear stress [kPa]	Normal stress [kPa]	Shear stress [kPa]
805.5	550.4	12.5	7.0
604.3	369.2	10	5.9
402.6	284.3	7.5	4.3
303.5	190.3	5.0	2.9
202	99	2.5	1.5
102.2	48.1	0	0.2
52.2	26.8		
11.9	6.5		

The validation procedure did not adhere to the standardized protocol for determining a flow function, which typically involves alternating consolidation and shear phases. Instead, a simplified approach was adopted to evaluate the behaviour of powder samples under varying normal stresses. Each sample was initially subjected to the maximum normal load permitted by the apparatus, and the load was then progressively reduced in discrete steps, following a negative step function, until the full measurement range was covered.
At each level of applied normal stress, the torque and the corresponding shear stress required to maintain the lid in a stationary position were recorded, while

the trough rotated clockwise at a constant angular velocity of 0.0015 rpm. The resulting data, including the applied normal stress and the measured shear stress for both devices, are presented in Figure III.44, providing a comparative overview of the mechanical response under controlled conditions.

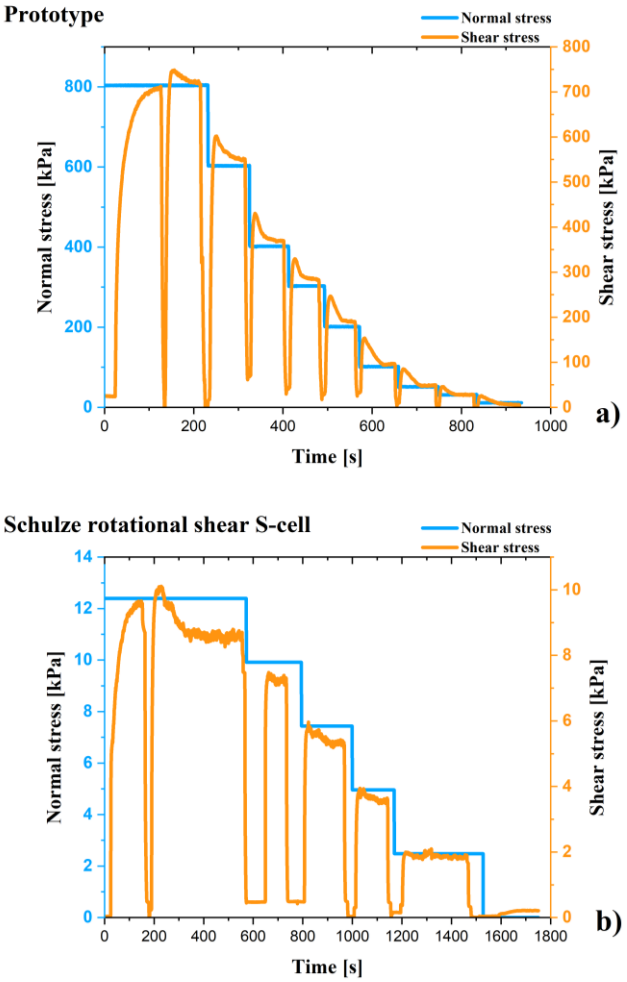

Figure III.44 Recorded raw data during the prototype validation test: a) from the prototype; b) from the Shulze ring shear tester RST 0.1 equipped with cell S type. Blue lines for the normal stress, yellow lines for the shear stress.

To compare the performance of the two devices, the failure point was not derived from the normal stress–shear stress curves, as is typically done in the determination of a flow function. Instead, the analysis focused on the steady-state conditions reached under a given compressive load. In this regime, the shear stress, τ, is no longer influenced by the pre-consolidation history, but rather becomes a material-specific parameter, dependent solely on the applied

normal stress and the intrinsic properties of the granular medium (Tomas, 2004)(Tomas, 2004).

Given that a direct comparison of failure conditions was not feasible, the study shifted toward quantifying the material's behaviour across a range of normal stresses, observing how the corresponding steady-state shear stress evolved. The data points representing these steady-state conditions for both devices are presented in Figure III.45.a. Due to the difference in scale between the prototype and the Schulze S-cell, a direct overlay is not possible; however, the experimental data from the prototype reveal a linear trend in the sand's behaviour at low compressive loads, with a noticeable deviation from linearity observed for normal stresses exceeding 200 kPa.

A more detailed comparison is provided in Figure III.45.b, which zooms in on the region characterized by low compressive loads. A logarithmic scale was employed to enhance the visibility of the trends in this region. A linear model was fitted to the data obtained from the Schulze S-cell, and the same approach was applied to the four low-load data points from the prototype, which also exhibited linear behaviour consistent with the commercial equipment.

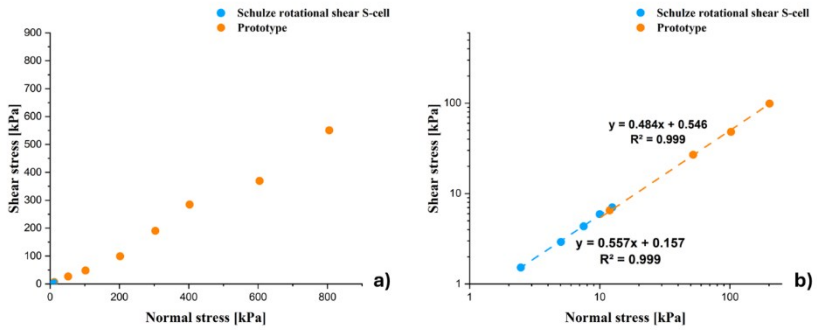

Figure III.45 Measured steady-state shear stresses as a function of applied normal stresses; blue symbols correspond to the Schulze rotational shear S-cell, orange to rhe prototype (a) full experimental data range, and (b) magnified view on a logarithmic scale, highlighting shear stress values between 1 and 100 kPa.

The confirmation of linear behaviour in both systems, supported by coefficient of determination (R^2) values approaching unity and numerical constants of comparable magnitude, offers compelling evidence of the prototype's validity, even in the absence of a direct comparison under identical operating conditions. These findings demonstrate that, under low compressive loads, the prototype successfully replicates the mechanical response observed in the commercial device, thereby confirming its suitability for controlled shear testing of granular materials. Moreover, the extended operational range of the prototype enables testing under more severe conditions, effectively broadening the spectrum of accessible experimental parameters and enhancing its utility for advanced material characterization.

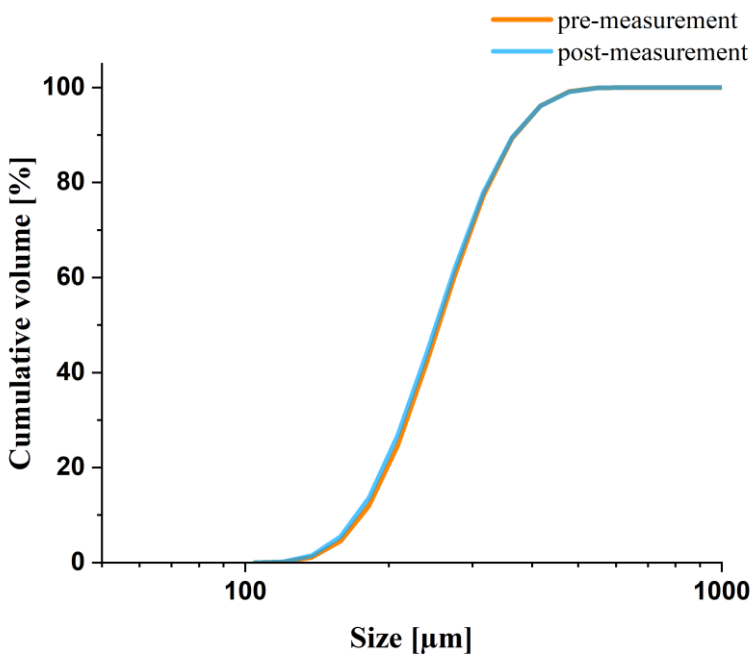

Figure III.46 Particle size distributions of the quartz sand used in the experiments, measured before and after testing under ambient and high-temperature conditions.

To further confirm the mechanical stability of the quartz sand under test conditions, Particle Size Distribution (PSD) measurements were conducted before and after the experimental treatments using a Mastersizer 2000 laser diffraction system. The resulting cumulative PSD curves for the pre- and post-treatment samples are presented in Figure III.46, plotted on a semilogarithmic scale to enhance resolution across the particle size range.

Based on the distribution function, the mean particle diameter of the pre-treatment sample was calculated to be 254.8 µm, with the 10th percentile (D_{10}) at 176.8 µm and the 90th percentile (D_{90}) at 366.9 µm. In the post-treatment sample, the measured values remained fully consistent with those of the initial sample, indicating that the quartz sand retained its structural integrity throughout the compression and thermal exposure phases of the experiment. This result confirms that the selected granular material is resistant to mechanical degradation, and that the experimental procedure did not induce significant comminution or fragmentation, thereby preserving the granulometric consistency required for reliable and reproducible shear testing.

IV. Materials and Experimental methods

The definition of the prototype's functional and structural properties was guided by a series of preliminary studies aimed at both predicting the mechanical behaviour of the granular solid and assessing the feasibility of the proposed experimental approach. As outlined in Section 2.1.1, two principal methodologies are currently employed to investigate the frictional behaviour of granular materials: Discrete Element Method (DEM) modelling and continuum mechanics.

In the present context, the materials of interest, primarily iron oxide pellets, exhibit non-conventional characteristics due to their size distribution, morphology, and the nature of interparticle interactions. These features render traditional rotational measurement systems and classical shear cell configurations inadequate. The interstitial spacing between pellets, combined with the emergence of force chains, introduces a level of heterogeneity and anisotropy that cannot be captured by continuum-based models. Under these conditions, DEM modelling emerges as the only viable framework for simulating and interpreting the mechanical response of the system.

To evaluate the compatibility between DEM simulations and experimental testing, a series of preliminary trials were conducted using idealized particles, with controlled geometries and interaction parameters. The system's complexity was then incrementally increased to assess the influence of various physical and operational variables, including particle shape, contact mechanics, and boundary conditions.

Although DEM modelling is not developed within the scope of this thesis, it remains an integral component of the broader research framework, particularly in the context of the European project consortium. The Particle Technology group at the University of Salerno (Unisa) contributed to the generation of experimental datasets, which were subsequently used by other consortium partners, most notably the research team at the University of Bochum, to validate and refine DEM simulations. For this reason, a brief

reference to DEM modelling is included, and the simulation data discussed herein are derived from collaborative efforts with external institutions.

IV.1. Procedure validation

The experimental campaign was initiated with the objective of characterizing the flow properties of an unconventional granular material using a commercial shear testing device. The solid phase was represented by wooden spheres, selected in two distinct monodisperse size classes: 6 mm and 10 mm in diameter. Wood was selected as the material for the spheres due to its favourable mechanical properties, moderate density, and ease of machining. Its structural integrity ensures consistent behaviour under compressive and shear loads, while its relatively low density (approximately 700 kg/m³) facilitates handling and operability at low loads. Moreover, wood's workability allows for precise shaping and surface finishing, enabling the production of monodisperse spheres with uniform sphericity and smooth surfaces, which are essential for controlled experimental conditions.

Figure IV.1 Photograph image of wooden spheres.

For instrumentation, the Schulze RST-01 rotational shear cell was employed, specifically configured with the M cell, which corresponds to the medium-sized trough available in the system (Figure IV.2). The trough dimensions are as follows: inner diameter 100 mm, outer diameter 200 mm, and height 40 mm. The lid, designed to engage with the sample during rotation, has an inner diameter of 102 mm and an outer diameter of 198 mm, and is equipped with 20 radial vanes, each measuring 1 mm of thickness, 10 mm height and 48 mm width, arranged equidistantly around the circumference.

Based on these dimensions, the internal volume of the trough is calculated to be 940.23 cm^3, while the total volume occupied by the vanes amounts to 11.54 cm^3.

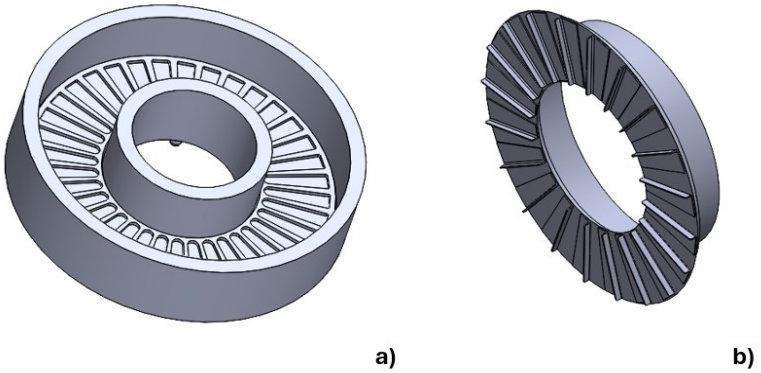

Figure IV.2 Rotational Shulze shear tester RST-01 M size. a) the trough, b) the lid.

The experimental procedure followed the ASTM D6773-16 ("Test Method for Bulk Solids Using Schulze Ring Shear Tester," 2016)("Test Method for Bulk Solids Using Schulze Ring Shear Tester," 2016) standard for the characterization of bulk solids using the Schulze RST-01 shear tester, applying a conventional testing protocol to a non-conventional granular system. Although the apparatus and methodology are standardized, the use of spherical wooden particles required specific adaptations, particularly during sample preparation.

The trough was filled manually with the spheres, ensuring a uniform distribution without inducing compaction. Unlike fine powders, which can be levelled using a spatula with minimal disturbance, the size and rigidity of the spheres made this approach impractical. Instead, excess material was removed by hand, taking care to produce a flat, flush surface aligned with the upper edge of the trough. The filled trough was then weighed, and the mass of the empty container subtracted to determine the net sample mass. Generally, the sample weight was about 415g and once positioned on the rotary drive unit, the system was ready for testing.

The characterization protocol adopted the two-step procedure described in Section 2.1.5, alternating between consolidation and shearing phases under different normal stress conditions. During the consolidation phase, the sample was subjected to the maximum applied normal load, while the trough rotated clockwise. This phase serves to standardize the initial packing state, compensating for the material's history-dependent mechanical behaviour. When the steady state condition was observed, the rotation was reversed

allowing the shear stress to relax toward zero, thereby preparing the system for the subsequent shearing step.
In the shearing phase, the normal stress was reduced, and clockwise rotation resumed. The evolution of shear stress was monitored to detect the onset of flow, typically preceded by a transient increase due to elastic deformation and particle rearrangement. This initial peak defines the failure condition, marking the transition from static to dynamic behaviour. The relationship between consolidation pressure and shear strength was evident: higher consolidation loads consistently resulted in higher failure thresholds. After each failure point was reached, the system underwent a new consolidation cycle, ensuring repeatability and comparability across all test conditions.

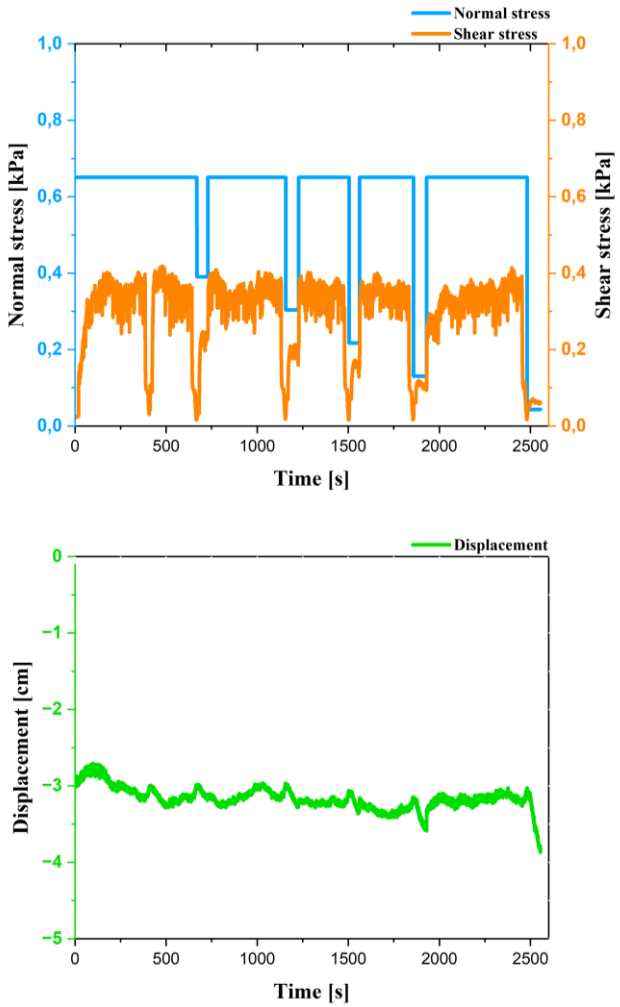

Figure IV.3 Time-resolved experimental data showing normal load (grey), shear stress (orange), and displacement (blue).

An example of the time-resolved data acquired during testing is presented in Figure IV.3, which illustrates the evolution of normal force, shear force and displacement throughout the consolidation and shearing phases. It is important to clarify that the negative displacement values observed in the dataset result from the specific convention adopted by the Schulze shear tester's data acquisition system. According to this convention, a reduction in sample height is considered a positive displacement. This typically occurs when a load is applied and the particles rearrange, increasing their number of contact points and compacting into a denser configuration. As the bulk density increases, the lid moves downward, and this movement is recorded as a positive value. Conversely, when the displacement is recorded as negative, it indicates that the distance between the lid and the trough has increased. This may happen due to local rearrangements within the sample, temporary expansion effects, or uneven force transmission. Such behaviour should not be interpreted as a decrease in density but rather as a transient mechanical response where the lid is momentarily lifted relative to its initial position.
Conversely, when the measured displacement is negative, it indicates that the distance between the lid and the trough has increased. This behaviour may arise from local rearrangements, arching effects, or transient expansions within the sample, and should not be misinterpreted as a decrease in density. Instead, it reflects a momentary mechanical response where the lid is lifted slightly relative to its initial position, possibly due to uneven force transmission or delayed settling of the granular bed.
This representation highlights the dynamic response of the material under controlled boundary conditions and serves as a reference for interpreting the mechanical behaviour observed across different test configurations. The corresponding test parameters and applied stress levels for both particle sizes are reported in Table IV.1, providing a comprehensive overview of the experimental conditions investigated.

Table IV.1 Normal stress conditions investigated using the Schulze rotational cell and wooden spheres.

Pre-shear [kPa]	0.65	1.09	2.17
Shear [kPa]	0.39	0.65	1.30
	0.30	0.43	0.87
	0.22	0.22	0.43
	0.13	0.13	0.13
	0.04	0.04	0.04

Both available samples, which differed in their characteristic dimensions, were analysed under the three pre-shear load conditions listed in

Table IV.1.respectively equal to of 0.65 kPa, 1.09 kPa, and 2.17 kPa. These particular values (with decimal precision) are a direct consequence of the way the stress is applied to the system, namely through calibrated weights. Accordingly, the preshear stresses were obtained by applying 5.00 kg, 2.50 kg, and 1.50 kg, respectively.

Each test condition was repeated three times to ensure statistical consistency and reproducibility. The use of kilograms as the unit of measurement reflects the specific loading mechanism of the Schulze rotational shear cell, where compression is applied by placing calibrated weights onto a mechanical hangar that transfers the load directly to the sample lid.

From the shear stress vs. time data, the failure conditions (defined by the peak shear stress preceding flow) were systematically identified. These values were then plotted on $\sigma - \tau$ diagrams, allowing the construction of yield loci for each test configuration.

Figure IV.4 presents the yield loci obtained from tests conducted with 6 mm spheres, grouped according to the compressive load applied during the pre-shear phase. Each curve reflects the outcome of three independent repetitions under identical loading conditions, allowing for assessment of repeatability and statistical dispersion.

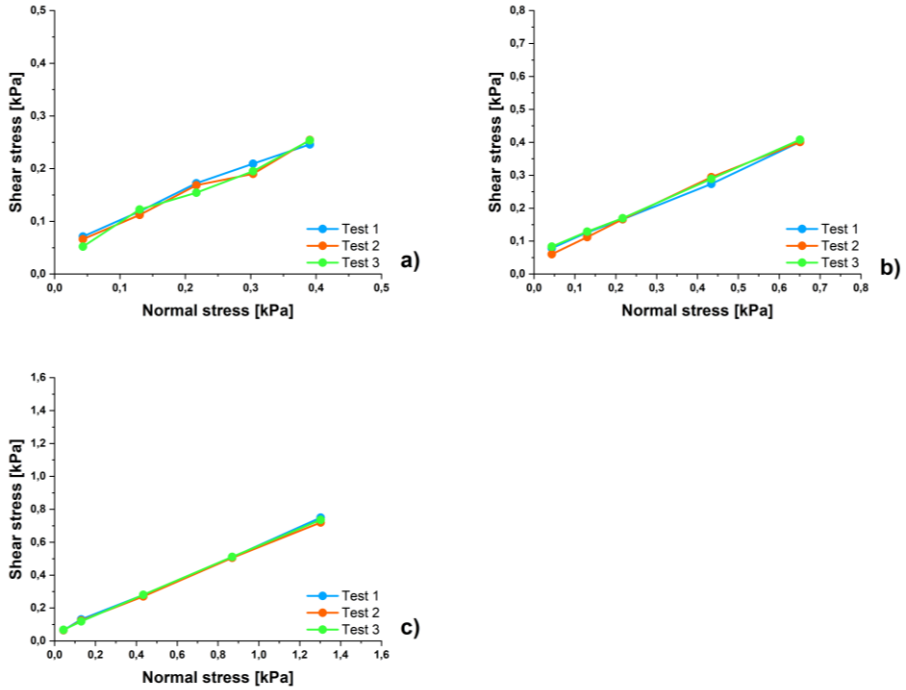

Figure IV.4 Yield loci obtained from tests with 6 mm spheres, grouped according to the compressive load applied during the pre-shear phase: (a) 0.65 kPa, (b) 1.09 kPa, and (c) 2.17 kPa.

Figure IV.5 shows the corresponding yield loci derived from tests with 10 mm spheres, processed using the same protocol and grouping criteria.

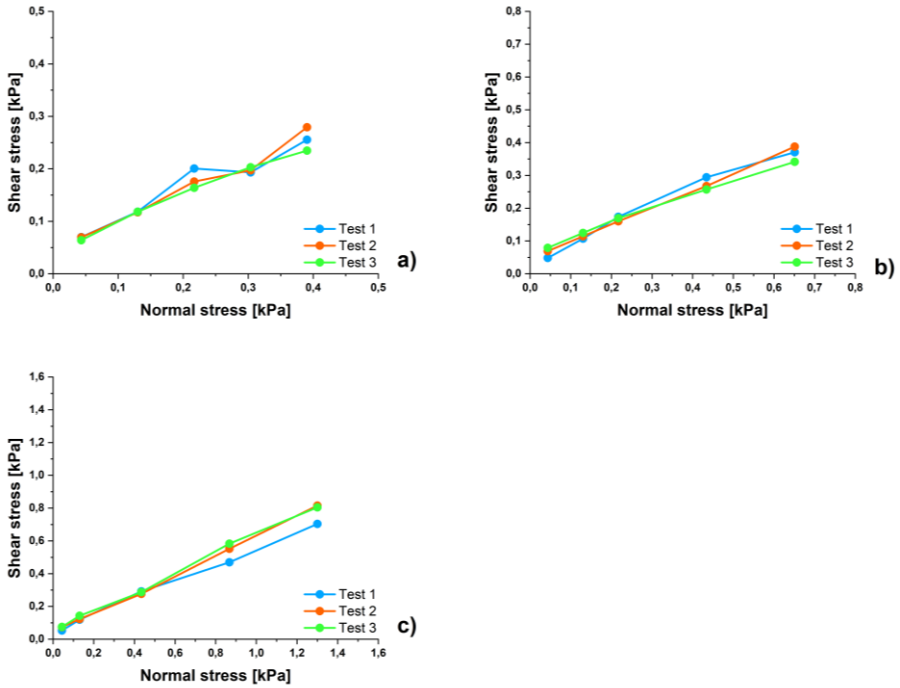

Figure IV.5 Yield loci obtained from tests with 10 mm spheres, grouped according to the compressive load applied during the pre-shear phase: a) 0.65 kPa, (b) 1.09 kPa, and (c) 2.17 kPa.

The graphs reveal a clear linear relationship between the measured shear force and the applied normal load, indicating that the spheres behave as Colburn-type materials. This classification refers to granular solids whose shear resistance increases proportionally with the applied compressive stress, following a linear failure criterion.

Based on this interpretation, the experimental data were linearly interpolated for each test condition. From these interpolations, the internal friction angle and cohesion values were extracted, corresponding respectively to the slope and intercept of the fitted lines. These parameters are reported in Table IV.2, providing a quantitative description of the mechanical behaviour of the two sample types under the investigated loading conditions.

Table IV.2 Values of internal friction angle (α) and cohesion (C) derived from the linearization of yield loci obtained at different consolidation loads and for the various sphere sizes investigated.

Sphere diameter [mm]	Pre-shear [kPa]	α [°]	C [kPa]
6	0.65	30.2	0.050
	1.09	29.9	0.054
	2.17	30.0	0.045
10	0.65	30.8	0.047
	1.09	29.3	0.048
	2.17	32.7	0.045

This comparative analysis enables a direct evaluation of how particle size influences the shear response and consolidation behaviour of the granular material. As anticipated, across all tested conditions, the cohesion between the spheres remains negligible. This outcome is consistent with their geometric characteristics and the absence of interparticle mechanisms, such as capillary bridges or surface adhesion, that could induce cohesive behaviour. Accordingly, the intercept values derived from the yield loci are close to zero, confirming that the material behaves as non-cohesive.

In contrast, the internal friction angle appears insensitive to variations in the applied compressive load within the range investigated. This suggests that, for the tested configurations, the frictional resistance is primarily governed by particle geometry and contact mechanics rather than confinement intensity. It should be noted, however, that higher compressive loads could not be explored due to instrumental limitations, which may restrict the generalizability of this observation.

Beyond the graphical representation of shear strength as a function of axial stress, these results serve to validate the experimental approach adopted for characterizing the frictional behaviour of unconventional granular materials. The high repeatability observed, particularly with the 6 mm spheres, and the consistency of the extracted parameters reinforce the reliability of the methodology and support its application in broader studies involving non-standard particulate systems.

IV.2. Effect of lid geometry

A comparison between figures IV.4 and IV.5 shows that as the size of the spheres increases the experimental data exhibits a greater deviation. To

investigate this phenomenon, it was decided to adapt the lid to the size of the material being tested.

As discussed in Section 2.3, the geometry of the lid plays a critical role in defining the shear interface within the sample. Specifically, a stagnant region of solid material forms between the vanes of the lid, where particles are mechanically constrained. In contrast, the bulk material within the trough remains free to rotate with the motion of the base, thereby generating a shear plane to the depth of edge vanes immersed in the granular medium.

For materials with particle sizes below a few millimetres, the standard vane geometry of commercial lids is sufficient to induce this stagnant zone. However, in the case of the 10 mm wooden spheres used in this study, the 5 mm-high vanes of the original lid were inadequate to achieve effective confinement. To address this limitation, a custom lid design was developed, maintaining the original body geometry and materials but modifying the vanes configuration.

The redesigned lid features two alternating sets of radial vanes, each group comprising 10 elements, arranged equally spaced across the contact surface. While both vane types share the same thickness (1 mm) and width (48 mm), they differ in height: one set measures 1 mm, and the other 12 mm.

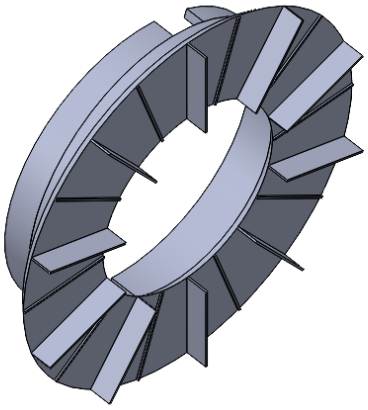

Figure IV.6 Representation of the modified lid modelled in SolidWorks.

This configuration allows the taller vanes to penetrate the sample more deeply, reaching a depth sufficient to engage at least one full sphere. The alternating vane heights increase the number of particles constrained between the taller vanes, thereby reducing particle mobility and self-rotation, and enhancing the formation of a stable shear interface.

Three repetitions were conducted using 10 mm diameter wooden spheres, applying the maximum preshear load investigated in this study. The test conditions correspond to those listed in Table 6, specifically under the 2.17 kPa pre-shearing column. This configuration was selected because, for this particle size and load level, the resulting yield loci exhibited the greatest

deviation from the average across repetitions, making it a suitable case for evaluating the impact of lid geometry. The data acquisition and processing protocol remained consistent with the methodology described in previous sections.

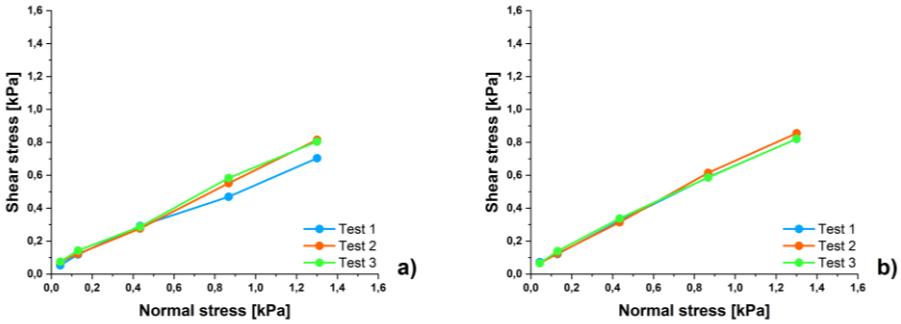

Figure IV.7 Comparison of yield loci obtained with 10 mm spheres under the same consolidation load (2.17 kPa), using the commercial lid (a) and the modified lid (b).

Figure IV.7 presents a comparison between the standard lid (a) and the modified lid equipped with redesigned vanes (b). The graphical output clearly shows that, with the new vane configuration, the yield curves are more closely aligned, indicating improved repeatability and reduced variability in the shear response. This observation is further supported by the numerical data reported in Table IV.3, which quantitatively confirms the enhanced consistency achieved through the modified lid design.

Table IV.3 Force values from tests conducted with a consolidation load of 5 kg using the commercial and modified lids, reported together with the standard deviation on a population basis. The internal friction angle (α) and cohesion (C), derived from the linearization of yield loci are also reported.

Standard lid	Measured Force [kPa]					
Pre-shear [kPa]	Test 1	Test 2	Test 3	STDev.P [kPa]	α [°]	C [kPa]
2.17	0.68	0.87	0.79	0.080	32.7	0.045
	0.50	0.60	0.58	0.043		
	0.29	0.25	0.30	0.021		
	0.11	0.13	0.13	0.010		
	0.06	0.07	0.08	0.009		

Modified lid	Measured Force [kPa]					
Pre-shear [kPa]	Test 1	Test 2	Test 3	STDev.P [kPa]	α [°]	C [kPa]
2.17	0.88	0.81	0.90	0.040	35.6	0.047
	0.54	0.57	0.60	0.025		
	0.36	0.31	0.31	0.024		
	0.12	0.13	0.14	0.008		
	0.07	0.07	0.06	0.003		

Table IV.3 presents the time-resolved measurements of the force required to maintain lid position during testing. For each of the three repetitions, the internal friction angle, cohesion, and the population-based standard deviation (STDev.P) were calculated. The latter serves as a quantitative indicator of repetition quality, reflecting the consistency of the measured shear response under identical test conditions.

As shown in the table, the STDev.P values for both lid configurations remain well below 0.08 kPa, confirming good repeatability. However, the modified lid yields a drastically lower standard deviation, particularly under higher shear loads, where variability is typically more pronounced. In fact, the deviation recorded with the new lid is approximately one-third of that observed with the standard configuration.

While the results do not suggest significant differences in the material's intrinsic properties, as the friction angle and cohesion remain comparable across configurations, they do confirm that lid geometry directly influences the quality of the measurement. The redesigned vanes enhance the mechanical coupling between the lid and the granular medium, particularly for larger particle sizes, thereby preserving the shear interface integrity and enabling more accurate and reproducible characterization of the material's frictional behaviour.

IV.3. Effect of cohesive forces

Building on the improved measurement consistency achieved with the modified lid, the experimental setup was further advanced by introducing a controlled form of interparticle cohesion. This enhancement was driven by the overarching goal of developing a DEM model capable of reproducing the behaviour of iron oxide pellets during their reduction to metallic iron: a transformation in which cohesive forces between particles are fundamentally involved. To calibrate and validate a preliminary model for simulations, it was

necessary to replicate mechanical conditions representative of cohesive granular systems.
To simulate such cohesion under ambient conditions, where natural adhesive forces between the wooden spheres are negligible, a commercial silicone-based adhesive, VIKY grease 51c, was introduced. The tested material consisted of 6 mm wooden spheres, which were coated with a uniform 0.5 mm-thick layer of grease. The required mass of grease was estimated based on the number of spheres per sample, typically around 4.400 units, and the volume difference between the uncoated and coated spheres. This volume increment was then converted into mass using the grease density, approximately 860 kg/m³.
The coating process was carried out using a Wab Turbula mixer, operating at 44 rpm for 15 minutes, to ensure homogeneous distribution of the adhesive across the entire surface of the sample.

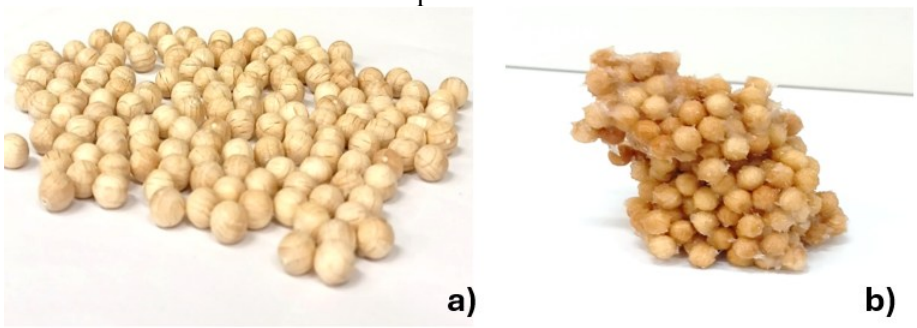

Figure IV.8 Photographic images of wooden spheres: (a) uncoated and (b) coated.

Even prior to the execution of shear tests, several qualitative observations can be made regarding the influence of grease on the behaviour of the spheres. In their uncoated state, the spheres exhibit negligible cohesion, with interparticle forces significantly weaker than gravity. As a result, when poured onto a flat surface, they fail to form stable structures, instead spreading freely to create a single, loosely packed layer.
By contrast, the introduction of silicone grease radically alters this behaviour. The coated spheres display visible cohesive interactions, enabling the formation of complex, self-supporting structures. These assemblies remain stable even in the absence of confinement, indicating that the adhesive layer introduces sufficient interparticle attraction to counteract gravitational dispersion. This transformation in mechanical behaviour is visually illustrated in Figure IV.8, which captures the contrast between the non-cohesive (a) and cohesive configurations (b).
The sample preparation followed the same protocol described earlier, including the application of the two-step consolidation and shearing procedure. For the tests involving cohesive spheres, the modified lid was employed to ensure effective mechanical interaction with the coated particles. The applied weight forces for each test condition are listed in Table IV.4.

Table IV.4 Normal stress conditions applied in both consolidation and shear phases of testing involving coated and uncoated 6mm wooden spheres.

	Set 1	Set 2
Pre-shear [kPa]	1.30	2.17
Shear [kPa]	0.87 0.43 0.22 0.13 0.04	1.30 0.87 0.43 0.22 0.13 0.04

For each configuration, three repetitions were performed using 6 mm wooden spheres, both with and without grease coating. From the resulting shear stress data, the corresponding yield loci were constructed and then averaged for each condition and sample type. The resulting trends are illustrated in Figure IV.9, which provides a comparative view of the material's behaviour under cohesive and non-cohesive conditions.

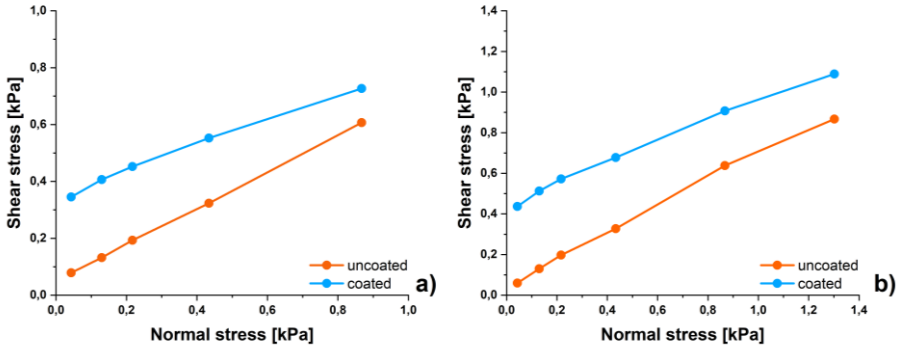

Figure IV.9 Comparison of yield loci averaged over three repetitions conducted on 6mm coated and uncoated spheres, with consolidation loads of (a) 1.3 kPa and (b) 2.17 kPa.

Specifically, Figure IV.9.a displays the average yield loci obtained under a 1.3 kPa consolidation load, while Figure IV.9.b presents the results for a 2.17 kPa of normal stress. In both cases, the graphs show the averaged response for coated and uncoated spheres, allowing a direct assessment of the influence of simulated cohesion on the material's shear strength and failure behaviour.
Even in the case of coated spheres, the experimental data revealed a linear relationship between the applied normal load and the shear force measured at failure.
Accordingly, the internal friction angle and cohesion values required to describe the four test configurations illustrated in Figure IV.9 are summarized in Table IV.5. These parameters provide a quantitative basis for comparing the

mechanical behaviour of cohesive and non-cohesive granular systems and serve as reference inputs for the calibration of simulation models.

Table IV.5 Comparison of internal friction angle (α) and cohesion (C) derived from coated and uncoated wooden spheres subjected to pre-shear loads of 3.0 kg and 5.0 kg.

Pre shear [kg]	1.30		2.17	
	Coated	Uncoated	Coated	Uncoated
α [°]	25.8	36.6	29.2	37.0
C [kPa]	0.344	0.050	0.445	0.048

The analysis of the data presented in Table IV.5 clearly indicates that cohesion is the parameter most affected by the presence of grease. In the absence of coating, cohesion remains negligible (close to zero) whereas the introduction of simulated cohesion via silicone grease results in a marked increase, exceeding 0.30 kPa. This substantial change confirms the effectiveness of the adhesive layer in generating measurable interparticle attraction.

Importantly, despite this increase in cohesion, the fundamental shear behaviour of the material remains unchanged. The data continue to exhibit a linear relationship between normal stress and shear stress at failure, validating the applicability of a linear failure criterion even in the presence of simulated cohesion.

These findings demonstrate that traditional experimental setups, such as the rotational shear cell, can be reliably used to quantify cohesive and frictional properties of granular materials, including those composed of coarse particles. The ability to simulate and measure cohesion under controlled conditions opens the door to more accurate calibration of numerical models and enhances the experimental characterization of unconventional particulate systems.

IV.3.1. Discrete Element Modelling calibration

To contextualize the use of the experimental data, it is first necessary to introduce the Discrete Element Method (DEM), a numerical technique designed to simulate systems composed of discrete particles. DEM resolves particle interactions with high temporal resolution, making it suitable for modelling dense granular systems under both static and dynamic conditions, and accommodating a wide range of particle shapes and sizes (Scheffler and Coetzee, 2023)(Scheffler and Coetzee, 2023).

In DEM, the motion of each particle is governed by the total forces and torques acting upon it. These are computed at every time step and used to solve

Newton's equations for translational motion (eq. (68)) and Euler's equations for rotational dynamics (eq. (69)). This framework allows for the detailed tracking of particle trajectories and contact histories.

$$m_i \cdot \frac{d^2\vec{x}_i}{dt^2} = \sum_{j=1}^{N} \vec{F}_{ij} + m_i\,\vec{g} = \vec{F}_i + m_i\,\vec{g} \tag{68}$$

$$\theta_i \cdot \frac{d^2\vec{\varphi}_i}{dt^2} = \sum_{j=1}^{N} \vec{M}_{ij} + M_i^r = \sum_{j=1}^{N} \vec{r}_i \times \vec{F}_{ij} + \vec{M}_i^r = \vec{M}_i \tag{69}$$

The translational motion is determined by the particle's mass $m_i$and linear acceleration $d^2\vec{x}_i/dt^2$, while the rotational motion depends on its moment of inertia $\Theta_i$and angular acceleration $d^2\vec{\phi}_i/dt^2$.

The total force $\vec{F}_i$acting on particle i is obtained by summing all contact forces $\vec{F}_{ij}$ exerted by neighbouring particles $j = 1 \dots N$, along with any external forces. Similarly, the total moment $\vec{M}_i$ includes the sum of contact moments $\vec{M}_{ij}$ from all interacting particles, as well as the rolling friction moment $\vec{M}_i^r$, which accounts for resistance to rotation due to surface interactions.

The cohesive force model inspired by Luding et al. [138] is adopted to simulate the effects of adhesion and mechanical interlocking between particles. The model describes how two particles interact when they touch and then move apart. It's based on how much they overlap, which is a way to measure how deeply they press into each other during contact.

When two particles come into contact, they start to repel each other like a spring being compressed. This repulsive force grows linearly with the overlap and is controlled by a stiffness value called k_1. As the particles begin to separate, the overlap decreases. Initially, the same spring stiffness $k_1$governs this phase, meaning the force decreases gradually. But once the overlap becomes very small, below a threshold called δ_{limit}, the system switches to a stiffer spring with stiffness k_2. This causes the force to drop more sharply, mimicking a sudden release of stored energy.

If the particles continue to move apart beyond a certain point, called the equilibrium overlap δ_0, the force becomes negative, meaning the particles are now attracting each other. This is the adhesion phase, and the strongest attractive force occurs at δ_{min}. Beyond δ_{min}, the particles are still close, but the attractive force starts to fade.

A softer spring with stiffness k_c is used to model this gradual detachment, which reflects how energy is dissipated as the particles finally separate.

The calibration of the cohesive force model follows an iterative approach, in which the parameters k_2 and k_c are systematically adjusted to reproduce the observed mechanical behaviour, once δ_{min} and δ_{limit} are fixed. This strategy allows the model to be tuned for different cohesive regimes, enabling a

controlled representation of adhesion and detachment dynamics between particles. To evaluate the model's fidelity, Figure IV.10 presents a visual comparison between the experimental and simulated configurations, captured both before and after the application of a 2.17 kPa normal stress. This assessment offers a qualitative validation of the model's ability to replicate the structural response of cohesive granular assemblies under compression.

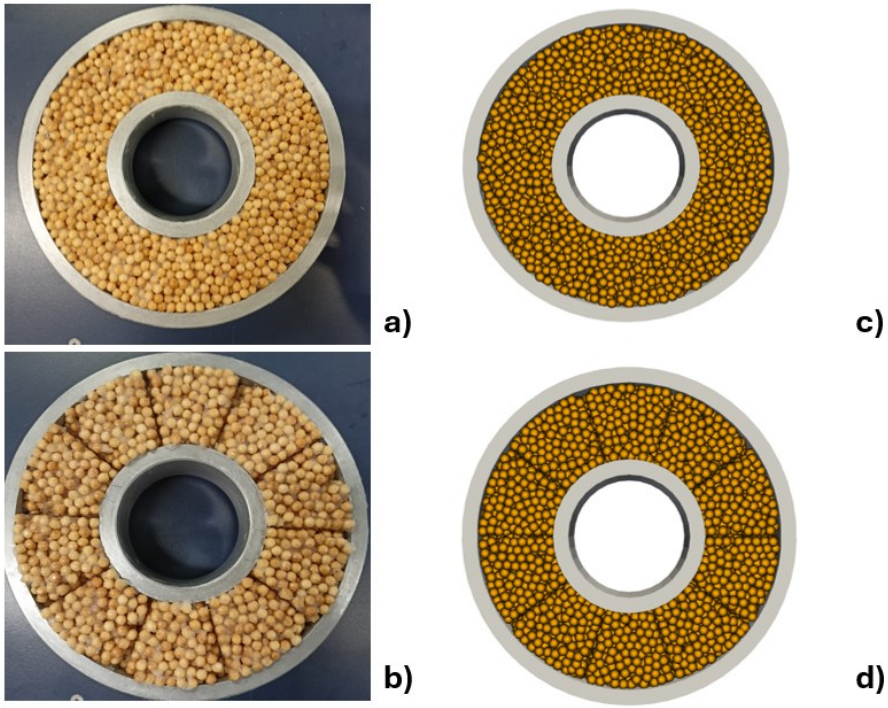

Figure IV.10 Comparison of real sample conditions before (a) and after (b) shear testing with DEM simulations before (c) and after (d) [139].

The calibration parameters adopted for the simulations involving coated particles are summarized in Table IV.6, while the corresponding simulation outcomes are presented in Figure IV10. In particular, Figure IV.10.a illustrates the comparison between the experimental torque time series and the simulated response. Figure IV.10.b presents the comparison between the mean yield loci obtained from both experimental and numerical data, under identical consolidation conditions.

Table IV.6 Calibration parameters of the DEM model, reported for both sphere–sphere and sphere–wall interaction cases [139].

Parameters	*Sphere – Sphere*	*Sphere – Wall*
k_1 (kg/s^2)	9.0×10^5	1.5.0×10^6
k_2 (kg/s^2)	1.8×10^6	3×10^6
k_c (kg/s^2)	9.0×10^5	1.5×10^6
γ^n (kg/s)	920	710
γ^t (kg/s)	460	355
δ_0 (m)	4.0×10^{-3}	4.0×10^{-3}
δ_{min} (m)	3.5×10^{-3}	3.5×10^{-3}
δ_{limit} (m)	7.5×10^{-3}	7.5×10^{-3}

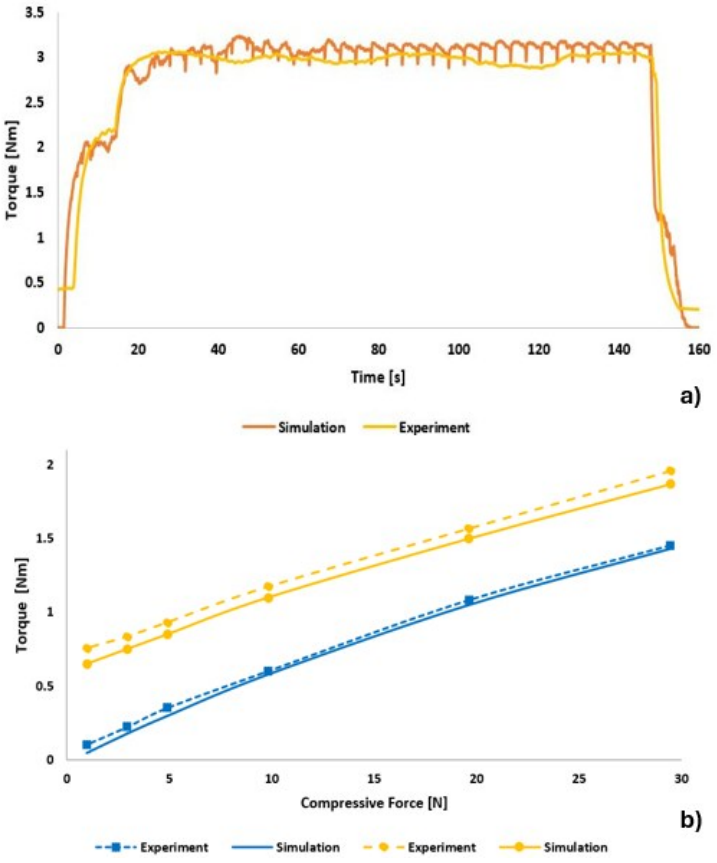

Figure IV.11 Comparison between experimental data and DEM simulations: (a) temporal evolution of the recorded torque versus that obtained from the DEM model resolution, and (b)

yield loci estimated from experimental measurements compared with those derived from DEM simulations [139].

The DEM analysis was conducted on selected time segments of the experimental tests, focusing specifically on the steady-state phases associated with preshear and shear conditions. This targeted approach allows the simulation to capture the most mechanically informative stages of the test, where force transmission, contact dynamics, and structural rearrangements are most representative of the material's behaviour.

This segmentation is necessary due to the computational limitations inherent to DEM simulations. As the number of particles increases and the contact interactions become more complex, the computational cost of resolving the equations of motion, particularly the force and moment balances, rises sharply. Simulating long-duration tests with high-resolution contact physics becomes impractical, especially for dense systems like iron oxide pellets. This strategy ensures that the DEM results remain both computationally tractable and physically meaningful, while still providing valuable insight into the transient and steady-state behaviours observed experimentally.

The strong agreement observed in both torque evolution and yield behaviour confirms that the calibrated DEM model successfully captures the mechanical response of the cohesive granular system. This consistency across different shear conditions demonstrates the model's robustness and predictive capability. It also reinforces the notion that DEM modelling is a reliable and versatile tool for characterizing granular materials, including those with non-standard geometries or cohesive interactions, such as coated or irregular particles.

IV.4. Effect of solid properties

This section shifts the focus toward evaluating the applicability of the previously described methods and procedures to denser granular solids, specifically iron oxide pellets. While the initial tests focused on coated wooden spheres, chosen for their controllable cohesion and geometric uniformity, the ultimate goal is to simulate and characterize materials relevant to industry, mechanically robust, and of complex composition.

The pellets examined in this section are representative of the feedstock typically used in BF processes. They exhibit a size distribution between 10 and 13 mm and a sphericity of approximately 0.9, reflecting the controlled morphology resulting from standardized pelletisation and thermal processing. Their composition is dominated by alloyed iron species, with detailed weight percentages of the constituent oxides and additives reported in Table IV.7.

Table IV.7 Chemical composition of pellets.

Fe	SiO_2	CaO	MgO	Al_2O_3	FeO
64.6	2.88	2.1	1.34	0.64	<0.1

The chemical analysis reveals a high iron content by weight, though the iron is not present in its metallic form. Instead, it is chemically bound to oxygen, predominantly as ferric oxide (Fe_2O_3), with ferrous oxide (FeO) appearing only in minor quantities. This distribution of oxidized species is typical of pre-reduction iron-bearing materials and aligns well with compositions commonly reported in the literature for pelletized feedstock used in metallurgical applications, particularly in blast furnace and direct reduction processes [96].
The experimental procedure adopted for the iron oxide pellets closely mirrors that previously applied to the wooden spheres. The pellets were carefully loaded into the shear trough, and the surface was manually levelled to ensure uniform initial conditions. To accommodate the mechanical characteristics of the denser material, the modified lid was again employed, ensuring consistent contact and load transmission during testing.

Figure IV.12 Photographic image of the tank containing the pellets at the end of the sample preparation phase.

A visual overview of the iron oxide pellets is presented in Figure IV.12, which captures the material loaded into the test M-sized trough prior to mechanical testing. One of the most notable distinctions compared to the earlier trials with wooden spheres is the mass of the sample. Owing to the high particle density of the pellets (approximately 4000 kg/m³) the average sample weight reaches nearly 5000 g, a substantial increase relative to the 415 g typical of the wooden sphere configurations.
The tests followed the established two-step protocol, consisting of a consolidation phase followed by shear. A normal stress of 2.17 kPa was applied during consolidation, replicating the conditions used in earlier trials.

The full set of experimental parameters and test conditions is summarized in Table IV.8.

Table IV.8 Consolidation and shear conditions investigated in tests with iron oxide pellets at room temperature.

Pre-shear [kPa]	2.17
Shear [kPa]	1.30
	0.87
	0.43
	0.13
	0.04

For each configuration, three independent repetitions were performed to ensure statistical reliability. The resulting data, comprising the time series of applied normal load, the torque required to prevent lid rotation, and the displacement of the specimen, are presented in Figure IV.13.

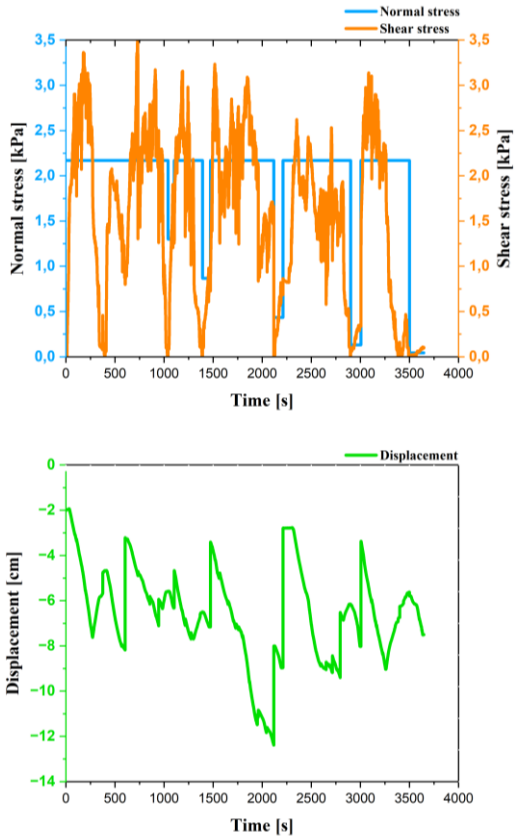

Figure IV.13 Experimental data recorded during the test conducted with the Schulze rotational cell using iron oxide pellets under a pre-shear load of 2.17 kPa.

The graph reveals two key behaviours: pronounced oscillations in the measured force and sudden changes in lid height, with displacements comparable to the diameter of the pellets. These phenomena are closely linked to the formation of force chains within the granular bed during shear.

Force chains are transient, load-bearing structures that emerge when particles align in such a way that they transmit stress along preferential paths. In dense granular systems like iron oxide pellets, where particles are stiff, heavy, and relatively uniform in shape, the applied load is not distributed evenly across the entire assembly. Instead, it becomes concentrated along these chains of contacting particles, which act as internal scaffolds resisting deformation.

As the trough rotates, the contact network within the sample continuously reorganizes. Some chains strengthen and carry more load, while others collapse or shift, redistributing stress throughout the system. This dynamic restructuring leads to the oscillatory force response: each time a dominant chain fails or a new one forms, the resistance to shear changes abruptly,

producing the observed fluctuations. Therefore, the force read is not a function of the properties of the material, but of the work required to break the chains. Similarly, the sudden changes in lid height (comparable to the size of a single pellet) can be attributed to the collapse or reorientation of these chains. When a force chain that was supporting part of the lid fails, the local structure may expand slightly, causing the lid to lift. These vertical displacements reflect the granular system's tendency to respond to shear, under these confined conditions, not as a uniform continuum, but as a network of discrete, evolving contact structures.

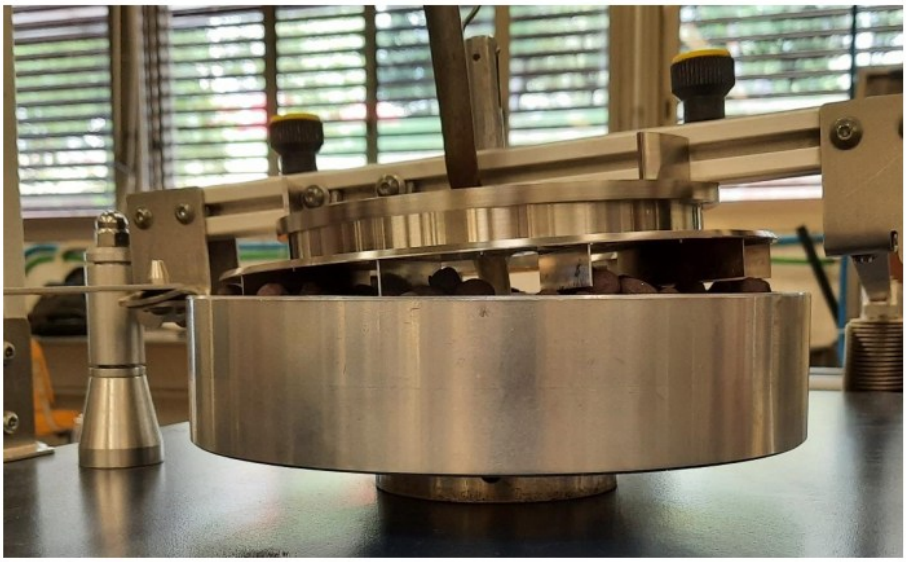

Figure IV.14 Photographic image of the Schulze rotation cell during the shear test with iron oxides, highlighting the lid leakage observed during the tests.

In contrast to finer or more deformable materials, where force transmission is more diffuse, the mechanical properties of iron oxide pellets make force chains the dominant mechanism governing both shear resistance and vertical compaction behaviour.

Figure IV.14 captures the Schulze shear cell during the measurement phase, where the tilted position of the lid clearly reveals a non-uniform distribution of internal forces within the sample. This asymmetry causes the lid to partially lift or protrude from the granular bed, leading to an increase in measured displacement and an uneven transmission of forces to the load cells. As a result, the force readings become spatially biased, and the mechanical response of the system no longer reflects a uniform stress state. This deviation from ideal conditions undermines the validity of standard characterization protocols and compromises the reproducibility of the procedures previously applied to less demanding materials.

While increasing the applied normal load could, in principle, reduce this instability by enhancing confinement and suppressing local rearrangements,

such an approach is constrained by the mechanical limits of the testing apparatus. The high density and stiffness of the iron oxide pellets amplify the formation of force chains, which dominate both the shear resistance and the vertical compaction behaviour of the material. These chains concentrate stress along discrete paths, making the system highly sensitive to perturbations and prone to sudden structural rearrangements.

The key insight data interpretation is that the measured force is not simply a function of the material's intrinsic properties, but rather of the mechanical work required to disrupt these force chains. The heavier the material, the more robust these chains become, and the greater the energy needed to break them. This observation underscores two critical needs: first, the development of new experimental protocols tailored to the characterization of dense, stiff granular solids, aimed at reducing the effect of force chains on the measured value and the effects that these accumulations of force can have on the structure of the solid; and second, the design of more robust testing equipment capable of withstanding and accurately capturing the complex mechanical responses that emerge under such demanding conditions.

IV.4.1. The effect of time

The findings discussed in Section 4.4 clearly demonstrate that standard characterization protocols and commercial shear testing equipment face substantial limitations when applied to granular solids of high density and size, such as iron oxide pellets. These constraints are primarily mechanical: the equipment is not designed to accommodate the elevated internal stresses, abrupt force redistributions, and non-uniform contact dynamics that emerge in such systems. As a result, both the accuracy of the measurements and the reliability of the protocols are compromised.

To address these challenges, a collaborative solution was proposed in partnership with the University of Bochum, focusing on the integration of experimental data with Discrete Element Method (DEM) modelling. This hybrid approach allows for a more nuanced interpretation of the mechanical behaviour by linking observed macroscopic responses to the underlying particle-scale interactions. However, DEM simulations are inherently limited by computational cost, particularly when dealing with large, dense assemblies. As highlighted in Section 4.3.1, the simulations are constrained to short time windows and are typically used to replicate specific segments of the experimental tests rather than full-duration scenarios.

In light of this, a targeted experimental campaign was conducted using the Schulze shear cell equipped with the modified lid, specifically designed to capture the short-term mechanical response of the pellet bed.

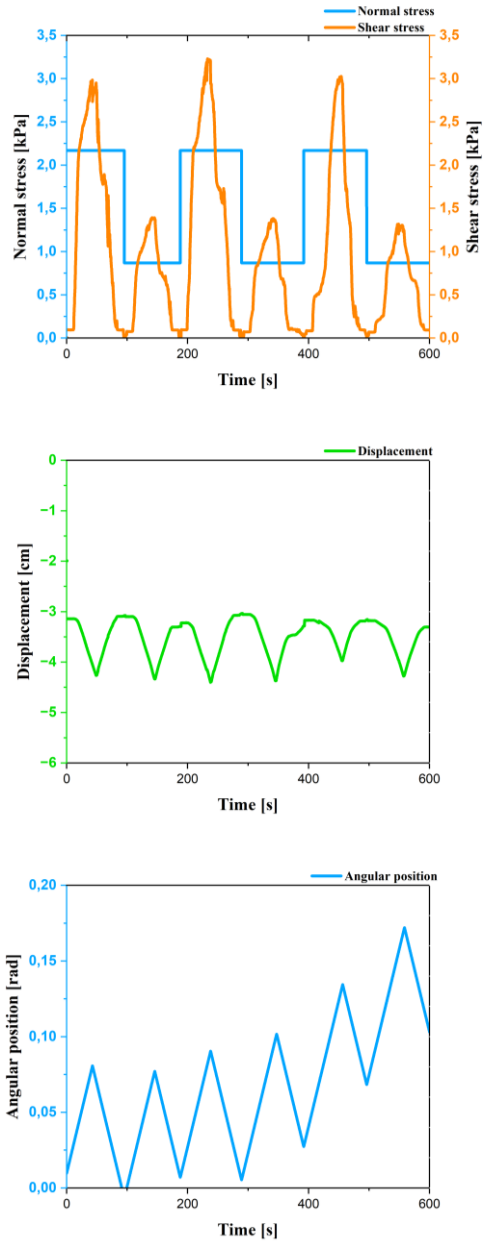

Figure IV.15 Experimental data obtained with iron oxide pellets, showing applied normal stress (light blue), measured shear stress (orange), lid displacement (green), and trough angular position (blue).

While the sample preparation and the applied loads remain consistent with those reported in Table IV.8, the measurement procedure has undergone a substantial revision to better align with the temporal constraints of DEM

simulations. Figure IV.15 presents the recorded traces from the test, including the applied normal load, the measured force, the vertical displacement, and the angular position of the trough.

To capture the repetitive mechanical behaviour of the material within a timeframe compatible with DEM analysis, the focus was shifted to the elastic response phase: specifically, the initial moments following the application of shear. In this revised protocol, the traditional distinction between consolidation and shear load is no longer maintained. Although the procedure still alternates between two load levels, only the behaviour within the plastic deformation region is monitored, where the system is still in reversible rearrangements.

For each load pair, three consecutive repetitions were performed to assess the repeatability of the observed phenomena. To minimize the influence of uncontrolled spatial rearrangements, the trough was rotated clockwise for a fixed duration, then counter-rotated under the same load and time conditions to restore the sample to its initial configuration. Once the measured shear stress returned to zero, the normal load was reduced and the trough was rotated again in the opposite direction, initiating a new cycle.

This alternating rotation sequence was repeated six times per sample, allowing for a controlled investigation of the material's short-term mechanical response. The resulting data, obtained under normal stress of 2.17 kPa, are shown in Figure IV.15, and provide a detailed view of the system's behaviour under cyclic shear, underlining the position of the trough. By comparing the initial and final positions recorded under the same normal load, it becomes evident that the variation in angular displacement is negligible. This observation confirms that the alternating rotation procedure (clockwise followed by counterclockwise) effectively restores the sample's spatial configuration, minimizing cumulative drift and ensuring that each cycle begins from a comparable mechanical state. This repeatability is essential for isolating the short-term mechanical response of the material and for maintaining consistency across test repetitions.

At this stage, no quantitative data has been extracted from the calibration of the DEM models, as the simulations are still undergoing validation and refinement.

IV.5. Fine powder from iron ore pellets

Before initiating the prototype analysis, the sensitivity of the iron oxide pellets' shear properties to temperature variations was assessed. As previously discussed, one of the principal limitations of commercial shear testing equipment is its inability to operate under elevated thermal conditions. To overcome this constraint, the experimental campaign was conducted using a custom-built device developed at the Powder Technology Laboratory of the University of Salerno: High Temperature Annular Shear Cell.

This apparatus is a size-reduced version of the Schulze rotational shear cell, specifically engineered to reach and maintain high temperatures during testing. Both the trough and the lid are in direct contact with electrical resistors, which serve as the heating elements. To minimize thermal losses, the steel components are enveloped in insulating material, with the resistors positioned between the metal surfaces and the insulation. A water-cooled jacket, placed between the trough and the rotary motor, ensures thermal protection of the drive system and maintains operational integrity.

The measurement system mirrors that of the Schulze cell: two load cells secure the lid and record the torque required to prevent its rotation and the normal load is applied via hanger. However, the current configuration does not permit control over the reaction atmosphere, and the partial exposure of heated components facilitates some degree of heat dissipation. To mitigate this and promote a uniform temperature distribution, the internal volume of the cell was deliberately minimized. The trough features an internal diameter of 60 mm, an external diameter of 120 mm, and a height of 10 mm, resulting in a compressive volume of approximately 95 mm^3.

The lid was custom designed to enhance shear transmission and thermal uniformity. It has an internal diameter of 62 mm, an external diameter of 118 mm, and is equipped with 20 radial fins, each 4 mm high, arranged equidistantly across the surface. These fins improve mechanical interlocking with the sample and promote consistent shear stress distribution.

Figure IV.16 provides a visual reference of the High Temperature Annular Shear Cell, illustrating its compact design and the integration of heating and cooling systems tailored for high-temperature granular testing.

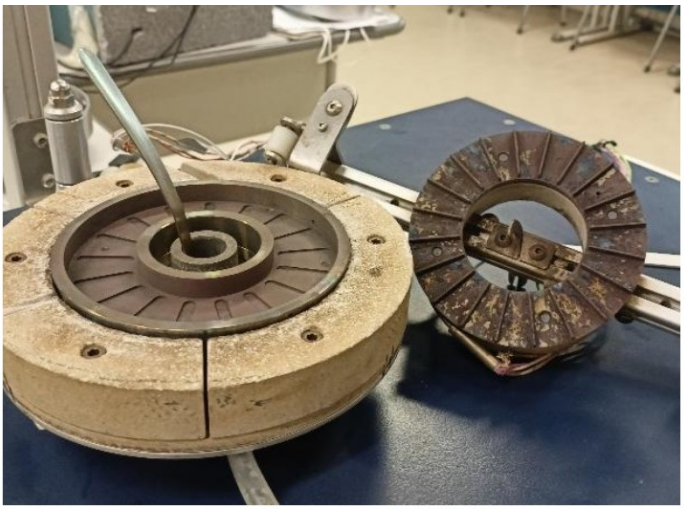

Figure IV.16 Photographic image of the High Temperature Annular Shear Cell.

Due to the limited internal volume of the High Temperature Annular Shear Cell and the size of iron ore pellets, it was not feasible to perform tests directly on intact iron oxide pellets. To adapt the material to the cell's dimensions and thermal configuration, the pellets were first ground using a laboratory blender, producing a fine powder suitable for high-temperature shear testing. The resulting material was then sieved with a hammer sieve, and the fraction between 125 and 180 micrometres was selected for analysis, representing the most widely processed product.

Three temperature conditions were investigated: ambient (25 °C), intermediate (400 °C), and maximum operating temperature (660 °C). These values were chosen to explore the thermal sensitivity of the material's shear behaviour, particularly in relation to potential softening, sintering, or changes in interparticle friction.

The tests were conducted following the standard two-step procedure, consisting of a consolidation phase followed by shear, in accordance with established protocols for fine granular materials. A 2.17 kPa as normal stress was applied both during the consolidation while the shear conditions explored are detailed in Table IV.9.

Table IV.9 Conditions investigated on iron oxide powders in an uncontrolled environment, with the High-Temperature Annular Shear Cell.

Pre-shear [kPa]	2.17
Shear [kPa]	1.30
	0.87
	0.43
	0.13
	0.04
	2.17

The experimental data recorded during the test at 400 °C, presented in Figure IV.17, clearly illustrates the alternation between consolidation and shear phases, as evidenced by the periodic trend of the applied load curve.

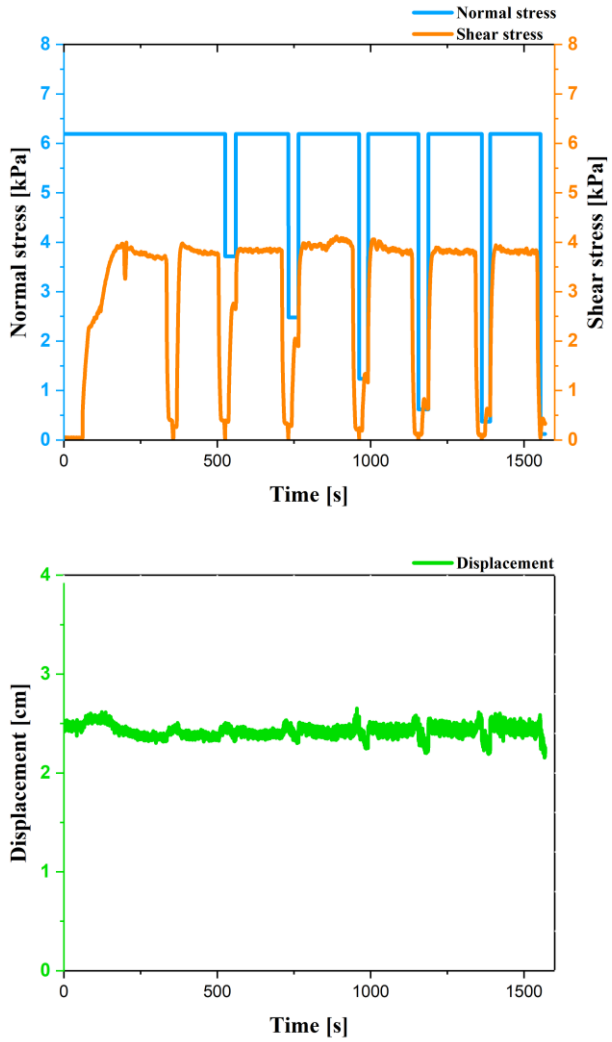

Figure IV.17 Example of experimental data recorded during the shear test with iron oxide powder under a compressive load of 2.17 kPa and at 400°C.

A particularly notable aspect is the behaviour of the lid displacement, which consistently assumes positive values throughout the measurement. This indicates that the lid gradually descends into the sample, compacting the powder under the influence of the applied load. Initially, the surface of the granular bed is aligned with the free edge of the trough, but as the load is applied, the powder densifies and the lid penetrates deeper into the material.
For each temperature condition, three independent repetitions were performed to ensure statistical reliability. From each test, the failure points were used to construct the corresponding yield locus on the $\sigma - \tau$ plot.

The three yield loci obtained for each temperature were then averaged, and the resulting mean yield loci are plotted together in Figure IV.18.

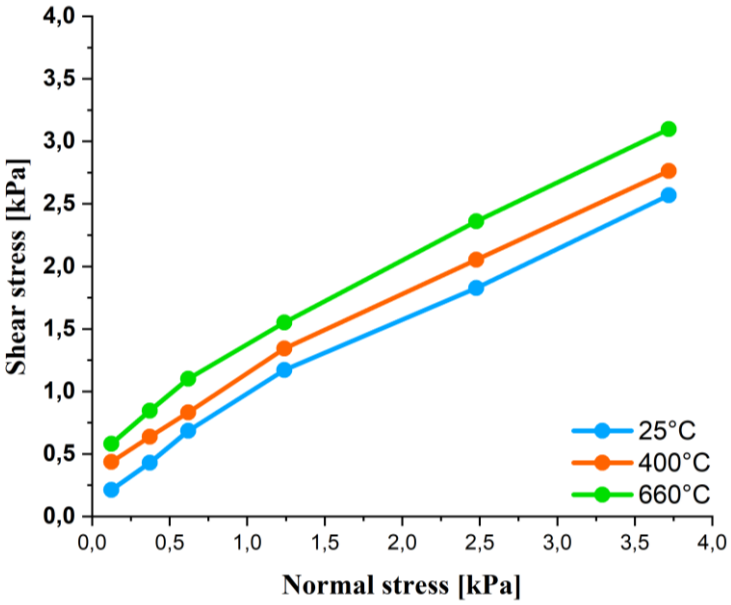

Figure IV.18 Yield loci averaged at various temperatures.

The graph reveals a consistent trend: the material's behaviour across all temperatures can be accurately described by a linear relationship between shear stress and normal stress, indicating that the fundamental frictional response remains stable despite thermal variation.
Based on this observation, the internal friction angle and cohesion were calculated for each temperature condition using linear regression of the average data. These values are presented in Table IV.10, providing a comparative view of how thermal exposure influences the shear parameters.

Table IV.10 Values of internal friction angle and cohesion obtained from the linearization of yield loci averaged at different temperatures.

Temperature [°C]	α [°]	C $[kPa]$
25	36.7	0.235
400	36.9	0.427
660	39.4	0.611

In agreement with the data presented in Table IV.10, the yield loci corresponding to the three investigated temperatures exhibit similar slopes, indicating that the internal friction angle of the particulate material remains substantially unaffected by thermal variation. This suggests that the

interparticle sliding resistance, governed primarily by surface roughness and contact mechanics, is relatively stable across the tested temperature range.
However, the cohesion values show a marked increase with temperature, rising from approximately 0.234 kPa at 25 °C to 0.611 kPa at 660 °C. This represents an increase of nearly 150%, highlighting a pronounced temperature dependence of the material's cohesive strength, even under relatively modest compressive loads.
Having established the influence of temperature on the material's shear parameters, further investigation was carried out to assess the sensitivity of torque to thermal variation under controlled loading conditions. In this series of tests, the pre-shear normal load was fixed at 2.17 kPa, while the normal load during shear was set at 1.30 kPa. The temperature increased from 400 °C to 660 °C, in steps of 20 °C, and at each step, the failure point was identified.

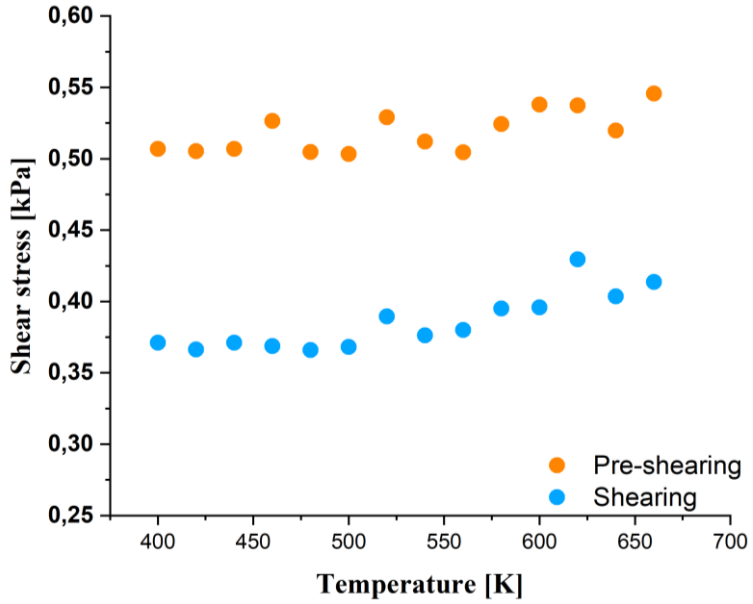

Figure IV.19 Steady-state (orange) and failure (light blue) conditions obtained with consolidation load of 2.17 kPa and failure load of 1.30 kPa, investigated at temperatures between 400 °C and 660 °C.

The results, presented in Figure IV.19, show the evolution of torque as a
The results shown in Figure IV.19 illustrate the evolution of torque with temperature, distinguishing between the steady-state torque associated with consolidation and the peak torque corresponding to failure. The steady-state values remain essentially unchanged across the investigated temperature range, indicating that the consolidation phase, and thus the frictional resistance mobilised during initial compaction, is only marginally affected by thermal variation under the applied load. In contrast, the torque at failure increases

systematically with temperature, reducing the gap between the two curves. This behaviour confirms that cohesion is the parameter most sensitive to thermal effects, whereas internal friction remains comparatively stable. The increase in the torque measured at failure directly translates into a higher value of the corresponding failure point in the stress space. Since cohesion is obtained from the intercept of the failure envelope constructed through these discrete points, a systematic upward shift of the failure values with temperature implies an increase in the apparent cohesion of the material. This effect cannot be attributed to chemical reactions, given both the inert nature of the solid and the absence of reactive species in the gas phase. A more plausible explanation is the behaviour of the finest fraction of the material, which at elevated temperatures may begin to soften, compact, or partially melt. These processes promote the formation of transient cohesive bridges within the granular assembly, increasing the resistance to shear at failure. Consequently, the material exhibits a higher apparent cohesion, while the frictional component remains largely unaffected by temperature.

IV.6. Prototype: preliminary tests

The experimental campaign with the newly developed prototype begins with a series of preliminary tests aimed at verifying its usability and operational reliability under simplified conditions. These initial trials were conducted using iron oxide pellets subjected to low compression loads, an uncontrolled atmospheric environment, and the temperature progressively increased until reaching 900°C. A secondary goal of these tests is to establish a baseline for refining the experimental procedure for generating data to support DEM model calibration.

The trough filling procedure adopted for these tests remains consistent with the standard protocol. As in previous studies involving wooden spheres, the surface of the sample was manually levelled by selectively removing pellets from the uppermost layer. This ensures a uniform initial surface, minimizing geometric irregularities and promoting consistent contact between the lid and the granular bed.

Figure IV.20 Photographic image of the trough filled with 10–13 mm iron oxide pellets after the sample preparation procedure.

Figure IV.20 presents a photographic image of the trough filled with 10-13 mm iron oxide pellets, illustrating the sample configuration prior to testing.

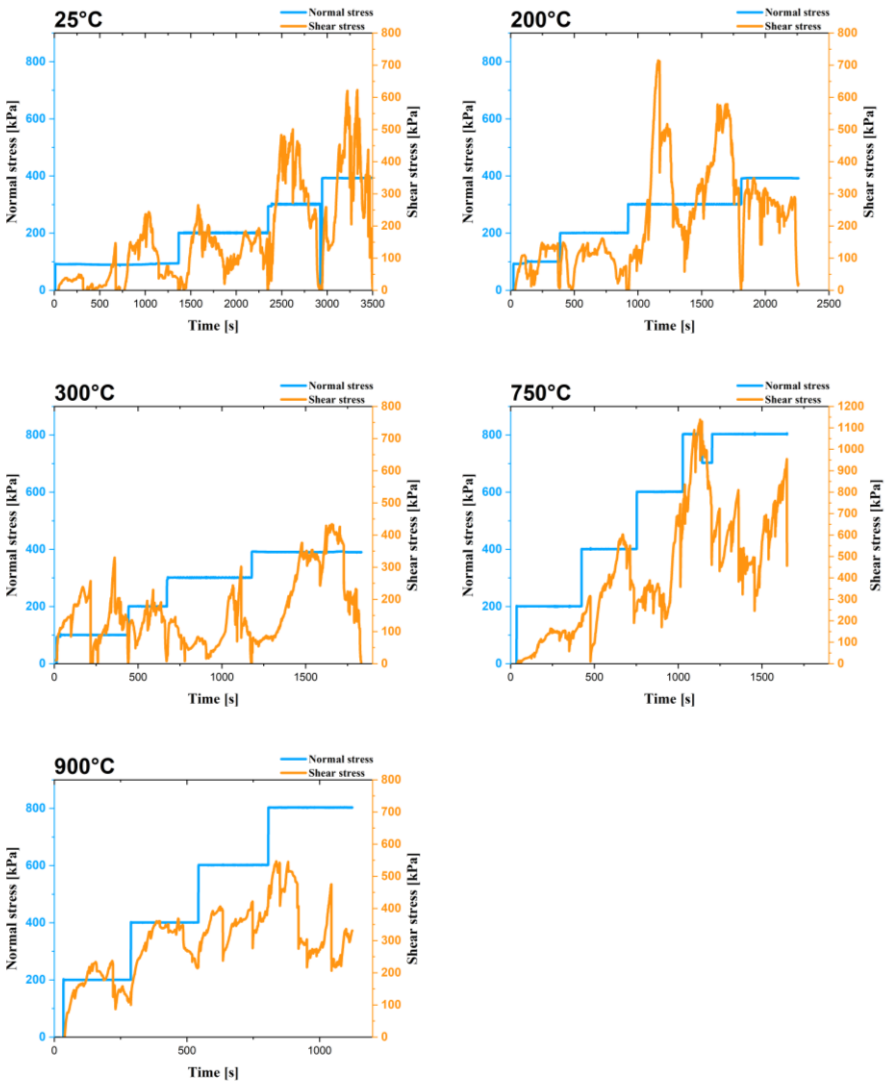

Figure IV.21 Experimental time-series data obtained with iron oxide pellets using the prototype and the procedure adapted to coarse particles. The applied load is shown in blue (maximum of 400 kPa compressive stress for temperatures up to 400 °C and 800 kPa for temperatures up 900°C, highlighting the stepwise behaviour of the new protocol. The measured torque is shown in yellow.

These tests were essential to ensure that the sensors embedded in the system could accurately record torque and displacement across a range of thermal environments. The first three trials were conducted at 25 °C, 200 °C, and 300 °C, providing a preliminary assessment of the system's performance under increasing thermal stress.

The testing procedure was shaped by the constraints outlined in Sections 4.4 and 4.3.1, which highlight two critical challenges: the limited temporal scope of DEM simulations, and the dominant role of force chains in the mechanical behaviour of coarse granular materials.
The procedure, which will be consistently applied throughout the pellet-based experimental campaign, involves a stepwise increase in normal stress, with each load held constant while the torque required to prevent lid rotation is recorded while the trough is rotating.
The normal stress investigated in these preliminary tests were 100, 200, 300, and 400 kPa, and are presented with the corresponding torque values in Figure IV.21 using a double system of axes; providing an initial mapping of the material's resistance to rotational displacement under controlled vertical confinement and confirming the applicability of the measurement procedure adapted to the case of pellets.
The subsequent experimental tests followed the same protocol established during the preliminary phase, maintaining consistency in both sample preparation and measurement procedure, while extending the operating conditions to more demanding regimes. Specifically, the normal stress values were doubled, and the maximum temperature was raised to 900 °C.
The torque curves obtained from the tests conducted at 750 °C and 900 °C, presented in Figure IV.21, reveal a pronounced randomness in the measured values, particularly evident in the yellow torque trace. This variability is attributed to the formation and collapse of force chains, which dominate the distribution of stress in coarse granular systems.
The appearance and disappearance of force chains, and their influence on the measured torque, can be interpreted through finite-size scaling. In the present prototype, pellets with a diameter (d_p) of 10-13 mm occupy a significant fraction of the 80 mm trough diameter (D), giving a ratio d_p/D of about 0.14. Due to the geometry of the system, the formation and persistence of force chains might be more strongly governed by the cell thickness (h). Since force chains tend to align along the principal stress direction, approximately 45° in a pseudo-continuous granular medium, the number of particles that can participate in a chain is better estimated as $h\sqrt{2}/d_p$. This highlights that the effective distance between the trough bottom and the lid plays a dominant role in determining whether force chains can develop and transmit load. Under geometrically similar conditions, both d_p/D and d_p/h remain useful reference ratios, but the latter more directly captures the constraints controlling force-chain stability.
As this ratio increases, the likelihood that force chains form and persist grows accordingly. At sufficiently high values, force chains can span the entire sample, creating continuous load-bearing structures between opposite walls. When this occurs, the granular medium may shift from a plastic-like regime, characterised by distributed deformation and intermittent rearrangements, to

a behaviour dominated by rigid-body-like motion. In such a state, stresses are transmitted through a small number of persistent chains rather than through collective particle rearrangements, markedly altering the stress–strain response.

This mechanism has direct implications for interpreting the experimental results. System-spanning force chains can trigger premature pellet failure and fragmentation, effects that would be far less pronounced under industrial conditions, where d_p/D is typically much smaller. The present observations therefore suggest that for $d_p/D \geq 0.14$ or equivalently $h\sqrt{2}/d_p \geq 5.9$, force-chain effects become sufficiently strong and frequent to influence the torque signal and the overall mechanical response of the sample.

For these reasons, a valuable direction for future work would be a systematic investigation of finite-size effects, particularly the influence of d_p/D or $h\sqrt{2}/d_p$on the shear–strain relationship and on the onset of pellet breakage. Reducing particle size would allow the transition between plastic-like and rigid-body-like behaviour to be quantified, providing a more complete understanding of how confinement and particle size jointly govern the rheology of the granular bed.

Due to the presence of the force chains, it becomes impractical to associate a specific normal stress with a deterministic torque value, underscoring the limitations of direct interpretation and reinforcing the need for DEM modelling to extract meaningful descriptive parameters.

Figure IV.22 Photographic image of the iron oxide sample at the end of the shear test.

Figure IV.22 also includes a photographic image of the sample during recovery from the reactive chamber, where localized pellet fragmentation is visible. These breakage events are likely caused by stress concentration at discrete contact points, again linked to the dynamic behaviour of force chains. However, even under the most extreme conditions tested (900 °C and 8 bar) fragmentation remains limited, and the pellets retain their structural integrity, confirming their mechanical suitability for use across the full operating range.

Given these findings, the next phase of investigation must focus on the effects of the reaction reduction on the material's behaviour, as chemical transformation may alter both the mechanical properties and the internal stress transmission mechanisms of the pellet bed.

IV.7. Prototype: reduced pellets

Although the prototype was engineered to withstand reactive environments, the iron oxide reduction tests were not conducted directly within it but rather approached through a stepwise methodology. For this phase of the experimental campaign, the reduced materials were supplied by Łukasiewicz: Górnośląski Instytut Technologiczny (Ł-GIT), enabling us mechanical testing on samples that had already undergone hydrogen-based reduction.

The reduction process was conducted in a dedicated high-temperature reactor, capable of operating under strongly reducing conditions. The reactor was maintained at a constant temperature of 950 °C, with a continuous flow of pure hydrogen at 300 L/h. The key variable in this setup was reaction time, which was modulated to produce samples with varying degrees of reduction. Four distinct tests were performed, with reaction durations ranging from 30 to 180 minutes, yielding four material states for comparative analysis.

At Ł-GIT, the reduced samples were prepared from 300 g of raw iron oxide pellets, processed in a horizontal rector. The degree of reduction was determined through chemical analysis, based on FeO content (0.55%), total iron content (64.3%), and mass loss during the reduction process. After 180 minutes, the material reached a near-complete reduction of 99%, confirming the effectiveness of the procedure.

Additionally, the degree of metallization was calculated by comparing the total iron content with the metallic iron fraction in the reduced samples, providing a quantitative measure of the transformation from oxide to metal. All relevant data, including reduction time, reduction conditions, and metallization degree, are summarized in Table IV.11.

Table IV.11 Conditions used for the reduction of iron oxides in a controlled environment, reported in terms of reaction time, gas flow rate, and hydrogen purity. The degree of reduction and metallization downstream of the reaction are also presented.

Temperature [°C]	Time [min]	Gas flow [l / min]	H_2 [m^3/m^3]	Reduction degree [%]	Metallisation degree [%]
950	30	300	100	39.8	18.2
950	60	300	100	65.2	71.1
950	90	300	100	79.6	78.4
950	180	300	100	99.0	89.9

Given the limited quantity of reduced materials available, the subsequent investigations were structured around the preparation of a single sample, which was then subjected to multiple temperatures and load cycles. This approach allowed for a comprehensive evaluation of the material's behaviour under varying thermal and mechanical conditions, while optimizing the use of the reduced pellet batch.

Once the material characteristics were defined, it became necessary to establish a dedicated testing protocol tailored to the thermal and structural constraints of the system. The protocol required the sample to be heated to high temperatures, with a pre-heating phase of approximately 10 hours, followed by mechanical testing lasting around 1 hour and 20 minutes, and a cooling phase of 12 hours to ensure safe recovery and handling of the sample. The conditions investigated, including temperature levels, load configurations, and reduction states, are summarized in Table IV.12. These were selected to explore the mechanical response of both reduced and non-reduced pellets, and the reason behind each condition will be detailed in the following section.

Table IV.12 Experimental conditions investigated with reduced and non-reduced iron oxide pellets, expressed in terms of degree of conversion, temperature, and applied normal stress.

	Reduction Degree [%]	0	79.6	39.8	65.2	99.0
Temperature [°C]	250	x	x	x	x	x
	500	x	x	x	x	x
	800	x	x	x	x	x
	1000	x	x	x	x	x
Normal Stress [kPa]	50		x	x		x
	100				x	
	200	x			x	
	300				x	
	400	x			x	
	600	x				
	800	x				

Since the reduced material remains chemically reactive, all tests conducted in this section were performed under a controlled nitrogen atmosphere throughout the heating, measurement, and cooling phases. This inert environment was essential to preserve the chemical composition of the reduced solid, preventing unwanted reoxidation or secondary reactions that could compromise the integrity of the sample.
Therefore, this precaution was particularly critical given the high temperatures involved and the extended exposure times required by the experimental protocol.

IV.7.1. Iron ore pellets: 0% reduction degree

The investigation of the flow properties of pellets with varying degrees of reduction under inert conditions began with a series of tests using unreduced raw iron ore pellets, with diameters ranging from 10 to 13 mm. These pellets were subjected to:

- Compressive stresses of 200, 400, 600, and 800 kPa.
- Temperatures of 230, 500, 800, and 1000 °C.
- A nitrogen atmosphere maintained throughout the heating, measurement, and cooling phases.

The experimental results are presented in Figure IV.23.a, which displays a composite graph with dual vertical axes: the normal load, shown in blue, and the corresponding shear stress, shown in yellow, are plotted across the different temperature conditions, where it is possible to recognize the graphic trend of the applied load and observe its evolution throughout the test sequence. The temperature profiles recorded during the measurement phase are shown in Figure IV.23.b, where the red curves illustrate the thermal stability achieved during testing (intermediate heating stages are omitted for clarity).

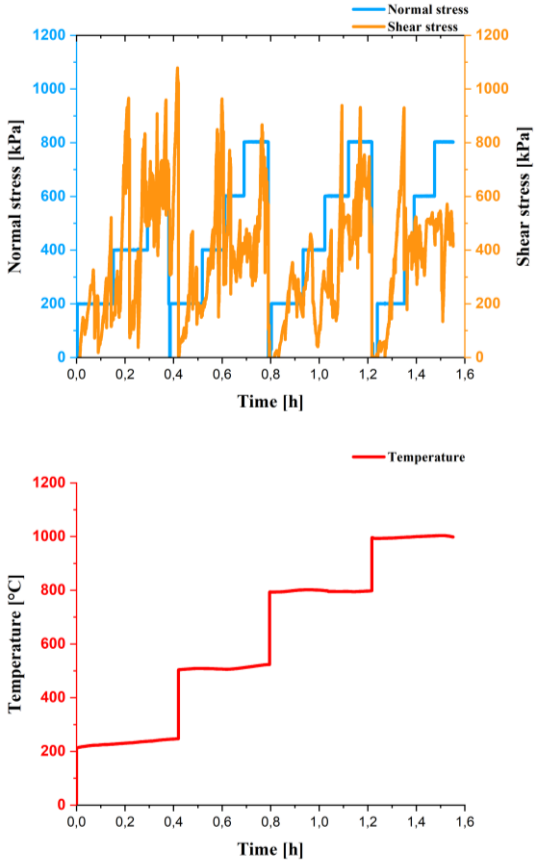

Figure IV.23 Experimental data obtained with unreduced pellets using the prototype in a controlled environment. (a) Applied normal stress between 200 and 800 kPa (blue) and recorded torque (orange). (b) Temperature profiles under measurement conditions.

The temperature profile remains stable throughout the measurement phase at all investigated levels, confirming optimal control of thermal conditions and ensuring consistent mechanical response. This stability is critical for isolating the material's behaviour under defined thermal and mechanical loads.

The stress graph reveals significant fluctuations in the recorded shear stress signal, reflecting the dynamic nature of force chain formation and collapse within the granular bed. An important observation must be made regarding the test conducted at 25 °C. Under these conditions, pronounced force-chain structures developed within the sample, resulting in abnormally high torque values. To prevent potential damage to the equipment, the applied load had to be limited, as further compression would have amplified the effect of these chains and caused an excessive rise in torque. Consequently, the sample could not be compressed up to the target value of 800 kPa. As shown in the graph, peak torque values correlate strongly with both the applied compressive stress and the temperature, indicating a complex interplay between thermal softening and mechanical confinement.

To protect the torque transducer, which has a maximum capacity of 100 Nm, the test was capped at a maximum compressive stress of 600 kPa. Despite this precaution, a critical issue emerged at the end of the test: the sample exhibited extensive fragmentation, as documented in Figure IV.24, which shows the recovered material post-test. This fragmentation, caused by excessive compressive forces, significantly compromised the accuracy of the shear stress measurements, as the signal is extremely sensitive to particle size distribution.

Figure IV.24 Photographic image of the sample downstream of the shear tests, where the effects of fragmentation are evident.

This fragmentation was notably more intense than that observed during the 900 °C test, despite the lower temperature applied in this case. The increased severity is attributed to the higher compressive stresses used in the initial trials, which exceeded the mechanical tolerance of the pellet structure. The

resulting damage not only compromised the specimen's integrity but also introduced significant variability in particle size, further complicating the interpretation of the shear stress signal and its reproducibility.
The alteration in grain size and the broadening of the particle size spectrum rendered the recorded data difficult to interpret and unsuitable for direct DEM simulation. To mitigate this, the compressive stress was reduced in all subsequent tests, ensuring better preservation of specimen integrity and improving the reliability of the mechanical characterization.

IV.7.2. Iron ore pellets: 79.6% reduction degree

The first sample exhibited a reduction rate of 79.6%, under the following conditions:

- compressive stresses of 100, 200, 300, and 400 kPa.
- temperatures of 270, 500, 800, and 1000 °C.
- inert nitrogen atmosphere.

The maximum compressive stress was therefore halved, and the experimental observations are reported in Figure IV.25, where the stress (normal, in blue) and torque (in yellow) components are plotted together on a dual-axis graph. Figure IV.25.a shows the results of the four tests, while the temperature profile for the measurement phase (Figure IV.25.b) and the lid displacement (Figure IV.25.c) are also presented.

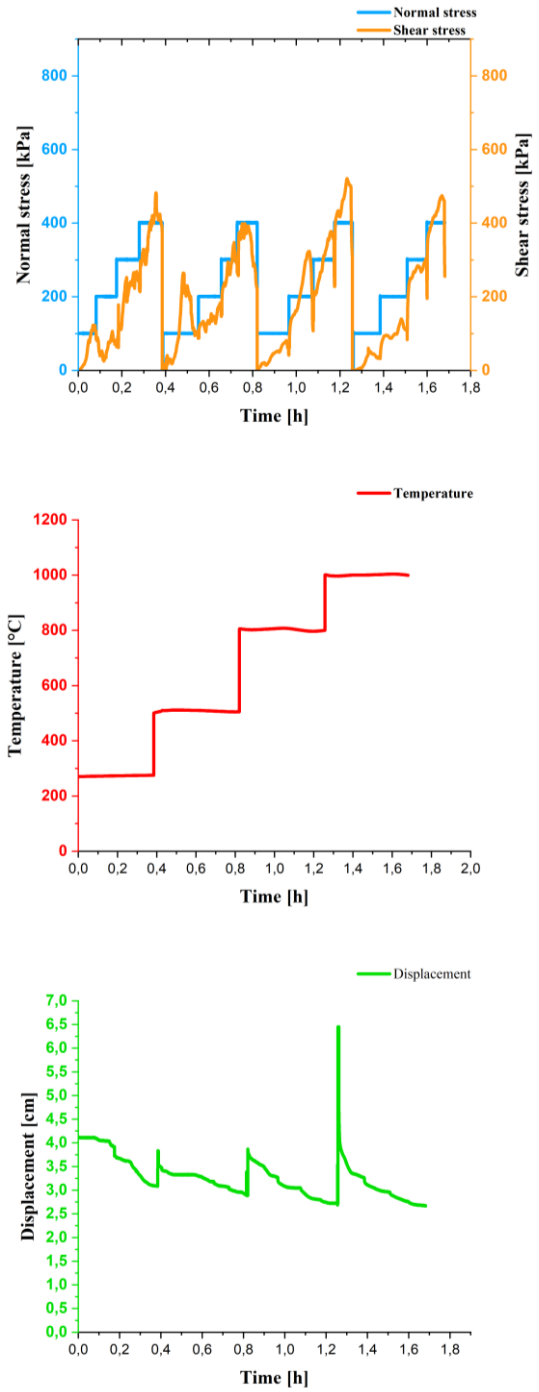

Figure IV.25 Experimental data obtained in a controlled environment, showing (a) normal stresses (blue) and torque (yellow), (b) temperature profiles during measurement, and (c) lid displacement.

From the stress graph, a gradual reduction in shear stress fluctuations can be observed with increasing compressive stress and temperature. This behaviour coincides with a variation in lid height, indicating a progressive densification of the sample. At the beginning of the test, the sample height measured approximately 4.3 cm, which gradually decreased to about 2.6 cm, confirming a significant increase in bulk density.

Figure IV.26 Photographic images of the sample containing reduced pellets: (a) before the test; (b) after the test.

The phenomena underlying these behaviours are illustrated in Figure IV.26, which shows the sample before (a) and after (b) the test. As evident in Figure IV.26.b, the fragmentation of the reduced material is considerably more pronounced than that observed in unreduced pellets. A nearly complete comminution process occurs, accompanied by partial sintering induced by the combined effects of temperature and compression.

This fragmentation explains the reduction in torque fluctuations, since the formation of fine particles progressively eliminates the force chains that typically govern stress transmission in granular systems. At the same time, the continuous reduction in particle size accounts for the increase in apparent density observed during the test.

However, the experimental results obtained at highest normal stress reveal a phenomenon that is not observed under industrial conditions: the extensive comminution of the pellets. Although fragmentation is an inherent feature of many process stages, the complete breakdown of pellets seen in the tests does not reflect industrial behaviour, where pellets generally retain their overall geometry despite exhibiting swelling, cracking and limited fragmentation. The severity of the comminution observed in the study therefore suggests that the extreme normal loads applied in the laboratory generate highly localised stresses rather than representing the global stress state experienced by pellets in a real furnace. This distinction is important, as it broadens our understanding of how pellets respond to intense, short range mechanical

interactions and provides insight into degradation mechanisms that extend beyond the conditions typically reported in industrial practice and in the literature.
The unexpected fragility of the reduced pellets highlighted the need for a more detailed investigation of the physical properties of subsequent samples, leading to a redesign of the operating conditions to mitigate fragmentation phenomena and preserve specimen integrity considering a drastic reduction in normal stress for subsequent tests.

IV.7.3. Iron ore pellets: 39.8, 65.2 and 99.0% of reduction degree

Based on observations from previous tests, experimental tests conducted on the remaining samples with reduction degrees of 39.8%, 65.2%, and 99.0% were adapted not in terms of temperature, but in terms of applied compressive stress. Therefore, the conditions tested are:

- Compressive stress of 50 kPa.
- Temperatures of 270, 500, 800, and 1000 °C.
- Inert nitrogen atmosphere.

A single compressive stress value was applied for the entire duration of the experimental test and for all temperatures investigated. Consequently, the observations from earlier trials led to a further variation in the measurement protocol. The experimental data collected in terms of normal stress, shear stress, and temperature are reported in Figure IV.27, following the same format as in the previous case.

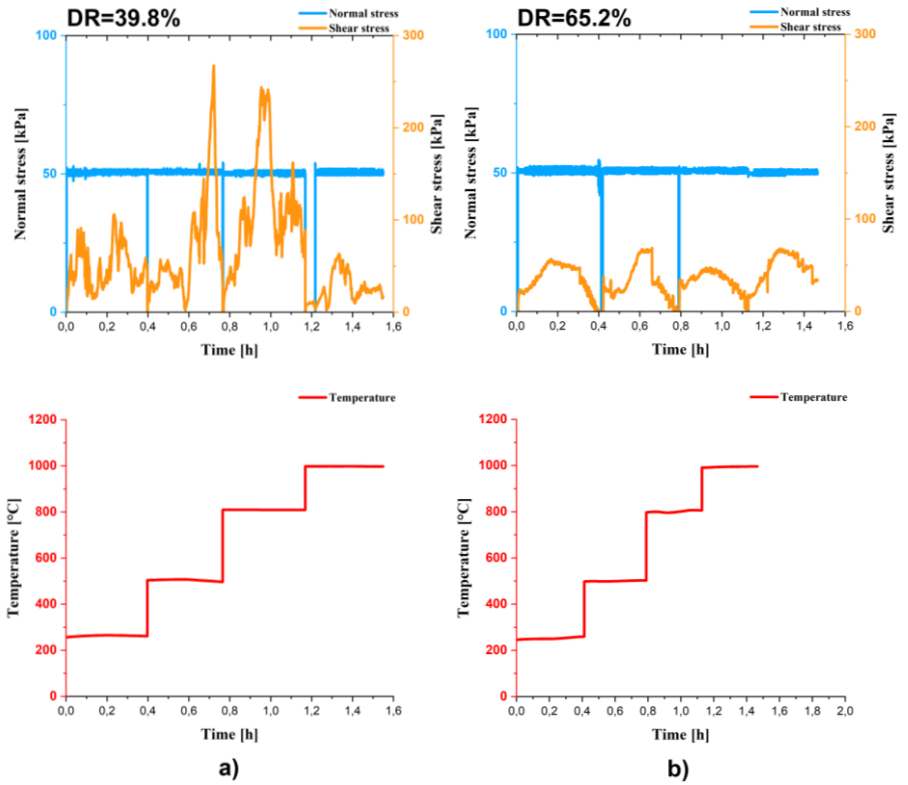
DR=39.8%
Normal stress
Shear stress
Normal stress [kPa]
Shear stress [kPa]
Time [h]
DR=65.2%
Normal stress
Shear stress
Normal stress [kPa]
Shear stress [kPa]
Time [h]
Temperature
Temperature [°C]
Time [h]
a)
Temperature
Temperature [°C]
Time [h]
b)

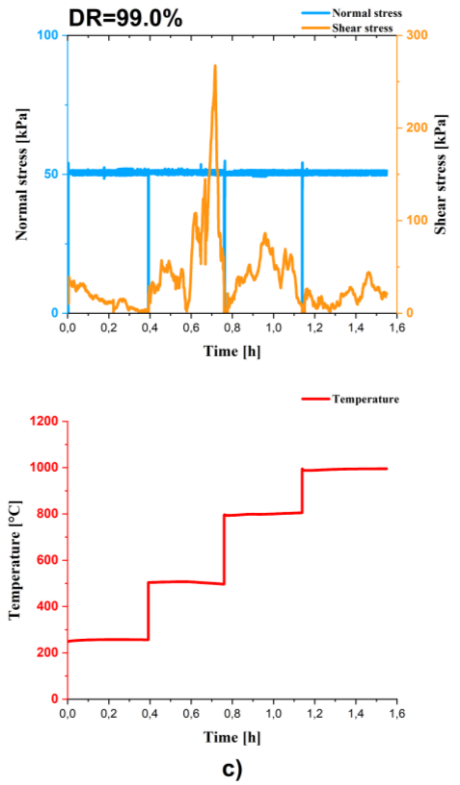

Figure IV.27 Experimental data obtained with pellets at different degrees of reduction: (a) 39.8%, (b) 65.2%, (c) 99.0%. The compressive load is shown in blue, illustrating the new procedure based on the use of a constant load across the investigated temperatures.

Analysis of the graphs confirms that the temperature profile is aligned with the target values, demonstrating that the new configuration successfully replicates and maintains stable thermal conditions throughout the test. Moreover, the oscillations in shear stress decrease with increasing temperature, indicating a progressive reduction in the influence of force chains on the measured stress values.

This effect could hypothetically be explained by temperature-induced softening, microcracking, or partial sintering of the pellets, which may reduce the rigidity of interparticle contacts. Under these conditions, the granular skeleton might become less capable of sustaining strong, discrete load-bearing chains, leading to a more homogeneous stress distribution. As a result, the formation and collapse of force chains, which at lower temperatures generate sharp oscillations in shear stress, would be expected to become less pronounced, producing smoother torque signals.

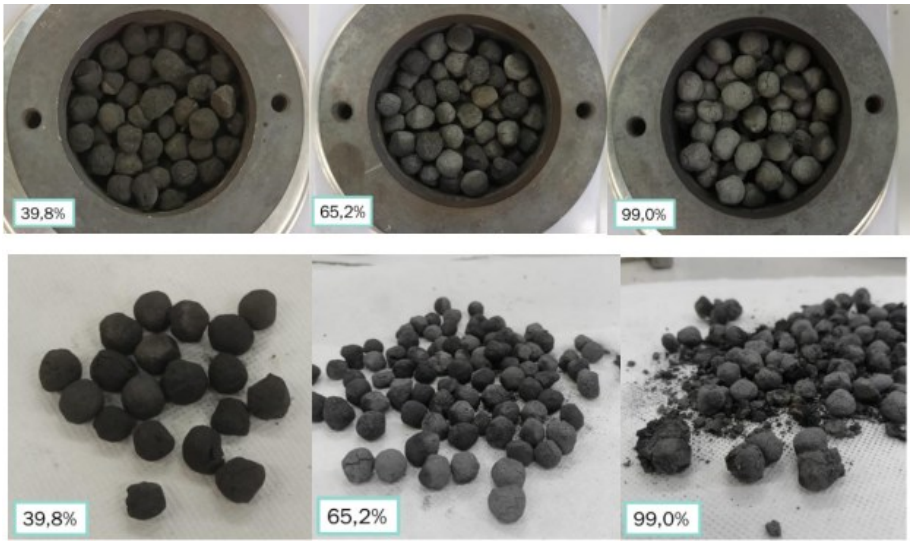

Figure IV.28 Photographic images of the samples formed by reduced iron oxide pellets before testing (top) and after testing (bottom).

Figure IV.28 also presents photographic images of the samples taken before and after the tests for the three analysed reduction degrees. As shown in Figure IV.26.a, the pre-reduced pellets exhibited the formation of increasingly deep cracks, a direct consequence of the structural transformations that had already occurred during the reduction process. The removal of oxygen from the oxide lattice had weakened the material, resulting in a gradual loss of mechanical strength. Even under the relatively low compressive stress applied, partial fragmentation was observed in samples with a degree of reduction of 99%. The fragments generated during testing facilitated the formation of bonds between adjacent pellets, ultimately leading to pellet aggregation and altering the bulk mechanical response of the system.

The progressive fragmentation and weakening of these reduced iron ore pellets can be explained by the microstructural evolution induced by reduction, which directly affects their mechanical strength. As oxygen is removed, the pellet's structure evolves from dense hematite (Fe_2O_3) to magnetite (Fe_3O_4), wüstite (FeO), and finally metallic iron. Each stage introduces porosity, microcracks, and stress concentrations, progressively reducing the pellet's ability to sustain compressive and shear loads. Hematite pellets, in their initial oxide state, are relatively dense and exhibit high cold crushing strength due to their compact lattice and strong intergranular bonding. In contrast, the intermediate phases generate oxygen vacancies and porosity, destabilizing the lattice and promoting crack propagation along grain boundaries. This stage is particularly critical, as pellets lose essential bonds and begin to fragment under mechanical stress.

In the final metallic iron phase, the crystal structure differs significantly from that of the oxides and exhibits lower hot strength. While fine fragments may

undergo partial sintering at elevated temperatures, the bulk pellet loses its integrity and shows reduced resistance to compressive forces. Experimental studies confirm that pellet strength can decrease to as little as 20-40% of its initial value during reduction, depending on temperature and reduction degree [120], [140], [141]. This explains why the tests on highly reduced samples (e.g., DR = 99%) revealed deep cracks and partial fragmentation even under relatively low compressive stress.

The mechanisms underlying this behaviour include the increase in porosity, which reduces load-bearing capacity; the disruption of pellets due to force chains in which fine particles replace larger grains and eliminate stable stress transmission paths; thermal effects, which accelerate crack propagation and promote partial sintering that encourages pellet aggregation but does not restore strength; and chemical weakening, since the reduction reaction itself destabilizes the oxide lattice, leaving the material more brittle and prone to comminution.

In summary, the tests conducted on the reduced materials revealed unexpected pellet behaviour under high loads and advanced degrees of reduction. These findings provide the basis for a more detailed description of pellet performance during process steps, emphasizing the mechanical limitations of the material, which are strongly influenced by operating conditions. Fragmentation thus emerges as a recurrent phenomenon throughout the reduction pathway, a trend clearly confirmed by experimental analyses.

The adapted protocol, employing a single compressive stress of 50 kPa across all investigated temperatures, proved effective in mitigating the excessive fragmentation observed in earlier trials, while still yielding valuable data on the mechanical response of pellets at different reduction degrees. At the same time, the progressive weakening of pellet structure with increasing reduction was evident in the formation of cracks and partial fragmentation, particularly in fully reduced samples. This behaviour underscores the dual effect of reduction: while enhancing metallization, it simultaneously diminishes mechanical strength, thereby altering stress transmission mechanisms and particle reorganization within the bed. The observed aggregation of fragmented pellets further suggests that sintering phenomena may contribute to modifying the bulk response of the reduced material.

Overall, the results demonstrate that the mechanical properties of iron oxide pellets are highly dependent on the degree of reduction, with cohesion and structural integrity decreasing as oxygen is progressively removed from the lattice. This conclusion provides a solid foundation for refining the experimental protocol and calibrating DEM simulations, ensuring that both the brittleness of reduced pellets and their tendency toward densification through fragmentation are properly incorporated into predictive modeling.

IV.8. Case study

While the mutual collaboration between DEM simulations and experimental testing is essential for the characterization of pellets, the evaluation of standard materials can be effectively carried out through experimental testing alone, supported by using a prototype. To illustrate this, the present section introduces a case study focused on the mechanical properties of a widely studied and thermally stable material: quartz sand. Sand was selected as the reference material for both the validation and study phases due to its well-established ability to withstand high temperatures while maintaining rigidity and mechanical resistance, even under significant applied pressures.
For this investigation, the characterization procedure defined by the ASTM D6773 standard was adopted, alternating consolidation and shear phases in accordance with the protocol. The stress conditions applied are reported in Table IV.13.

Table IV.13 Conditions investigated using the prototype with sand, expressed in terms of normal pre-shear and shear stresses.

Pre-shearing normal stress [kPa]	200	400	600	800
Shearing normal stress [kPa]	160	320	480	640
	120	240	360	480
	80	160	240	320
	50	100	150	200

To define the shear conditions, a series of values ranging between 25% and 80% of the consolidation stress was chosen, consistent with the standard methodology. The experimental program was conducted at temperatures of 25, 200, 400, 600, and 800 °C, thereby enabling the assessment of quartz sand behaviour across a wide thermal range.

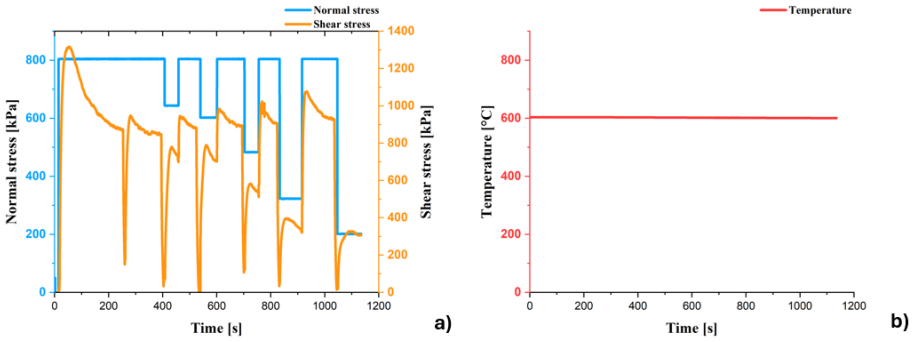

Figure IV.29 Graphical representation of experimental data obtained from the test at 600 °C with a compressive stress of 800 kPa for consolidation with sand. (a) Normal stresses (blue) and torque (orange). (b) Temperature profile during the test.

The experimental data are presented in Figure IV.29, which shows a representative time series obtained using quartz sand at 600 °C with a pre-shear normal stress of 800 kPa. In Figure IV.29a, the applied normal stress is plotted in blue, while the measured shear stress is plotted in orange, clearly illustrating the application of the two-step procedure consisting of consolidation followed by shear. To improve repeatability and reliability, the test protocol was designed to begin with two consecutive consolidation cycles. Figure IV.29.b reports the recorded temperature profile, which remained uniform throughout the entire measurement period, thereby validating both the prototype's control system and the thermal stability of the reaction chamber. From these data, the failure conditions were determined for each combination of temperature and consolidation stress, enabling the derivation of the descriptive yield loci of the material.

The graphical representation of the data shows that the system reaches a steady-state condition, though with different shear stress values. This behaviour is typical of shear tests and can occur even under lower applied loads. In such cases, it is necessary to normalize the readings with respect to the mean pre-shear value, a correction procedure known as pro-rating [142].

To apply this correction, four pre-shear stress values, τ_{pi}, were calculated from the time series as the average shear stresses recorded at the steady-state condition corresponding to consolidation prior to each shear phase.

Once the failure conditions were established, eq. (70) was applied to the four shear stress values at failure, τ_i, to normalize the data and account for fluctuations in pre-shear stress that could otherwise introduce variations in powder consolidation during different shear steps. In this equation, the corrected shear stress at failure, τ_i', is related to the measured shear stress, τ_i, considering the corresponding pre-shear stress, τ_{pi}, and the mean value, τ_{pm}, obtained as the average of the four τ_{pi}recorded under the same temperature and consolidation conditions.

$$\tau_i' = \tau_i \left(\frac{\tau_{pm}}{\tau_{pi}} \right) \quad (70)$$

The results of these calculations are reported in Figure IV.30, which presents the yield loci obtained at the four investigated temperatures. Providing a descriptive framework for the mechanical behaviour of quartz sand under varying thermal and stress conditions, confirming both the robustness of the experimental protocol and the reliability of the prototype in reproducing controlled consolidation-shear cycles.

Table IV.14 Values of cohesion and internal friction angle derived from linearized yield loci of sand across different temperatures.

Temperature [°C]	Cohesion [kPa]	Angle of internal friction [deg]
25	22	17
200	27	19
400	21	20
600	21	18
800	38	16

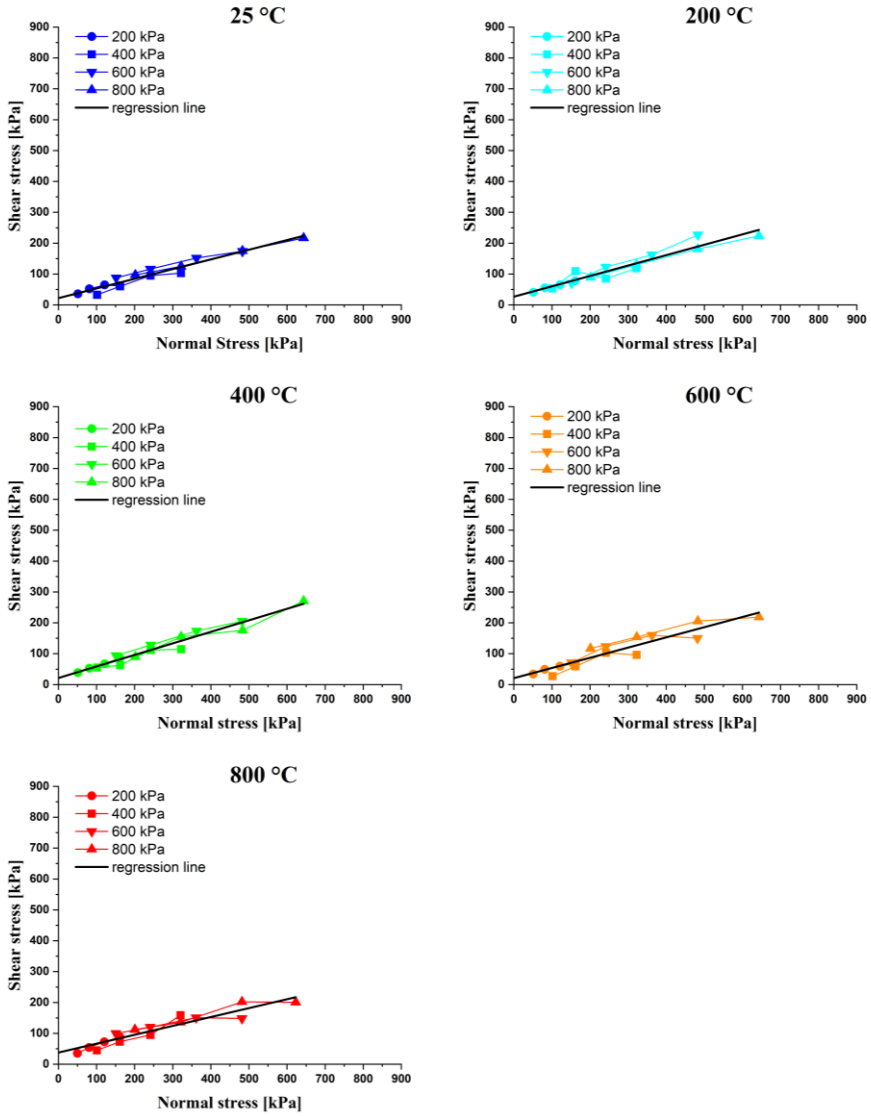

Figure IV.30 Comparison of yield loci obtained at identical temperature conditions with varying consolidation stresses.

From the yield loci, the internal friction angle and cohesion values were estimated and are reported in Table IV.14. The internal friction angles obtained are consistent with values reported in the literature, where quartz sand typically exhibits an interparticle friction angle between 22° and 35°,

accompanied by characteristically low cohesion. The limited variation observed in the internal friction angle confirms the expected minimal influence of temperature on the flow properties of quartz sand across the investigated thermal range.

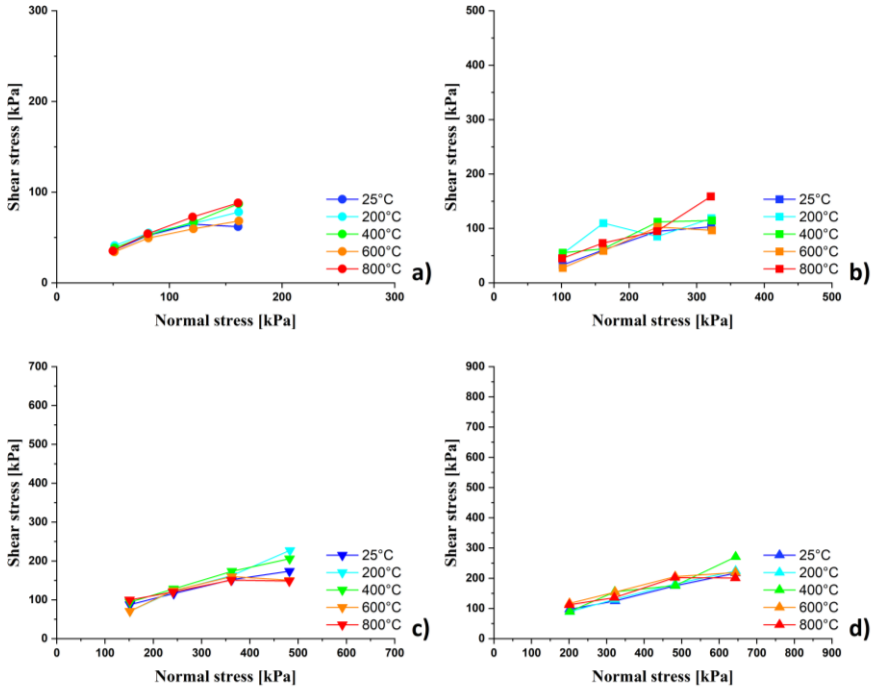

Figure IV.31 Yield loci compared across different temperatures at constant compression loads of 200, 400, 600, and 800 kPa.

This temperature-insensitive behaviour is further validated in Figure IV.31, which presents yield loci at different temperatures grouped by identical pre-shear conditions. The close similarity between these loci highlights the negligible impact of thermal variation on the fracture response under comparable states of consolidation. This outcome is consistent with the well-established thermal stability of quartz sand, whose crystalline structure and interparticle contacts remain largely unaffected by heating up to 800 °C. The absence of significant thermal effects on the yield loci confirms that the dominant mechanisms governing quartz sand behaviour are primarily mechanical rather than thermally driven. Stress transmission and failure response are controlled by particle geometry, packing density, and intergranular friction, rather than by temperature-induced changes in cohesion or strength. This stability ensures that quartz sand provides a reliable benchmark for validating prototype performance, as it allows the influence of the testing apparatus and measurement protocol.

Overall, these results reinforce the suitability of quartz sand as a reference material and a perfect case study for prototype validation. Its mechanical stability, reproducibility, and insensitivity to thermal variation across a wide range of operating conditions make it an ideal baseline for comparative analyses. By confirming that the yield loci remain consistent regardless of temperature, the study establishes quartz sand as a model case study that demonstrates the robustness of the experimental framework and provides confidence in extending the methodology to more complex or reactive materials.

V. Conclusion

The work presented in this thesis has focused on the design, use, and validation of a prototype apparatus for the thermo-mechanical characterization of granular materials under controlled conditions of temperature, atmosphere, and applied stress. The prototype was conceived to address a critical gap in the experimental study of granular systems: the need for a versatile instrument capable of reproducing consolidation-shear cycles at elevated temperatures while ensuring precise control of thermal stability and mechanical loading. The results confirm that the prototype is both technically reliable and scientifically robust, providing reproducible data that can be directly employed for the calibration of Discrete Element Method (DEM) simulations. This is particularly relevant for the characterization of coarse granular materials, where numerical modelling is essential to capture particle interactions and bulk behaviour due to the considerable impact of force chains during the measurement. At the same time, for fine materials, the prototype can be used directly to quantify flow properties in accordance with standardized protocols (such as ASTM D6773). This dual applicability underscores its versatility, positioning the prototype as both a calibration tool for DEM in complex, coarse systems and a direct measurement instrument for fine powders, thereby bridging experimental practice and computational modelling in the study of granular materials under severe conditions.

In its overall configuration, the prototype shares several similarities with commercial rotational shear testers used in powder mechanics, particularly those designed for room-temperature characterization according to ASTM or ISO standards. At its core lies the rotational shear cell, composed of two parts: a lid, which applies compression and measures shear forces, and a rotating trough, which houses the material. The prototype extends commercial devices capabilities by enabling high-temperature operation under controlled atmospheres (a feature not commonly available in standard instruments) and by allowing higher compressive stresses to be applied to granular samples.

The assembly followed a systematic approach, integrating mechanical, thermal, and electronic subsystems into a reliable unit.

The mechanical parts were fabricated from high-strength alloy: AISI310; selected for its thermal stability and resistance to deformation, ensuring durability and dimensional accuracy even at elevated temperatures.
Specific mechanical elements were incorporated to perform distinct functions: a linear actuator provides precise normal stress on the sample, and a rotational engine drives the shear motion of the trough.
The skeleton was designed to provide rigidity and precise alignment of all loading components. Its structural stiffness minimizes mechanical drift, thereby preserving measurement accuracy. The frame also offers modularity, allowing the integration of heating elements, insulation, and sensors without compromising stability.
The reaction chamber, designed in AISI310, contains the shear cell and allows the control of the atmosphere surrounding the material to avoid unwanted reactions. The heating subsystem surrounds the reaction, ensuring uniform temperature distribution up to 1000 °C. While the electrical components include thermocouples for continuous monitoring of thermal stability, and torque meter for shear stress measurement.
Operation of the prototype is managed through a dedicated software interface developed in LabVIEW. The software coordinates actuator control, thermal regulation, and data acquisition, enabling real-time monitoring of stress, torque, temperature, and displacement of the sample.
This enhancement allows the investigation of materials under conditions that closely replicate metallurgical industrial processes, such as direct reduction, sintering, or high-temperature storage and this condition can be summarized as:

- Temperature up to 1000°C.
- Compressive force up to 800kPa.
- Reactive/inert environment.

The experimental program was conducted on two granular materials. The first comprised reduced and unreduced iron oxide pellets, characterized by non-standard dimensions and high density, representative of reactive systems undergoing structural transformation during reduction. The second was quartz sand, selected as a conventional rigid material whose well-established mechanical stability makes it ideally suited for the standardized characterization of flow properties.
The investigation of reduced iron ore pellets revealed a set of behaviours of considerable relevance to both fundamental science and industrial practice. The experiments demonstrated that the degree of reduction (DR) exerts a decisive influence on pellet strength and structural integrity. At intermediate reduction degrees, pellets showed the onset of microcracking and partial fragmentation, whereas at high reduction degrees (e.g., DR = 99%), fragmentation became pronounced even under relatively low compressive stresses.

Although a direct measurement of sliding properties is not feasible due to the influence of force chains within the granular assembly, meaningful evaluations can however be derived from macroscopic observations of the materials before and after testing.

The observed fragility is potentially linked to the microstructural transformations induced by oxygen removal, which progressively weaken the oxide lattice and increase porosity, thereby reducing the material's ability to sustain mechanical loads.

The aggregation of fragmented pellets suggests that partial sintering phenomena may play a role in modifying the bulk response of the reduced material. While sintering can promote bonding between adjacent fragments, it does not restore the original strength of the pellets. Instead, it alters the pathways of stress transmission and contributes to the densification of the bed, thereby changing the collective mechanical behaviour of the system. This dual reduction effect (improved metallisation and simultaneous decrease in mechanical strength) has direct implications for industrial processes such as direct reduction and blast furnace operation, where pellet integrity is critical to maintaining permeability, reactivity and overall process efficiency. As the pellets descend through the shaft furnace, their progressive weakening, caused first by thermally induced cracking, then by mechanical stresses and those associated with chemical reactions, makes them increasingly susceptible to fragmentation. The transition region from hematite to magnetite is particularly critical, as lattice-expansion stresses can promote the propagation of coarse cracks and generate fine particles that accumulate within the charge, limiting gas flow and altering reduction kinetics [85], [87]. At higher temperatures, slag softening and the development of binding phases partially stabilise the structure, while the growth of iron whiskers contributes to local densification and partial healing of previous cracks. Only in the final metallisation zone does sintering of metallic iron restore sufficient strength to limit further degradation. Understanding how these sequential mechanisms interact with the evolving mechanical properties of the pellet is therefore essential for predicting fines generation, burden permeability and the overall stability of the reduction process. Taken together, these observations clarify how reduction-induced weakening interacts with the fragmentation mechanisms occurring along the shaft-furnace descent; despite these localised degradation processes, no evidence of severe or complete pellet fragmentation has been reported either in the literature or in industrial shaft-furnace operations, where pellets generally retain their overall geometry even under demanding reduction conditions.

To preserve pellets integrity, the preliminary tests conducted on these materials enabled the development of an ad hoc experimental protocol tailored to the specific characteristics of reduced pellets. The adapted procedure, based on the application of a single compressive stress of 50 kPa across all investigated temperatures, proved effective in mitigating excessive

fragmentation while still providing descriptive data on pellet mechanics. This adjustment ensured that the prototype could capture the essential features of pellet behaviour without compromising pellets dimensions and integrity.

The results obtained underline the importance of tailoring experimental protocols to reactive materials, thereby enabling the collection of reliable data that can be directly employed for the calibration of Discrete Element Method (DEM) simulations.

Quartz sand was selected as the second material tested, chosen as the ideal reference medium owing to its well-documented ability to withstand high temperatures while maintaining rigidity and mechanical strength. Its characterization followed the ASTM D6773 standard, alternating consolidation and shear phases, and standard data elaboration to derive the relevant mechanical response of the material.

The experimental data confirmed that quartz sand exhibits temperature-insensitive behaviour across the investigated range (25-800 °C) under compressive stress up to 800 kPa. Yield loci obtained at different temperatures showed consistent trends, with internal friction angles and cohesion values closely matching those reported in the literature. The limited variation in friction angle validated the expectation of minimal thermal influence on its flow properties, indicating that stress transmission and failure response are governed primarily by particle geometry, packing density, and intergranular friction.

This stability established quartz sand as a perfect case study for prototype validation. Its reproducibility and mechanical robustness ensured that the role of the testing apparatus and measurement protocol could be isolated from material-specific effects, thereby reinforcing the reliability of the experimental framework and supporting its extension to more complex or reactive granular systems.

The combined investigation of quartz sand and iron oxides provided confidence to extend the methodology to more complex or reactive granular systems, ultimately strengthening the prototype's suitability for both scientific research and industrial applications.

References

[1] S. R. Taylor, “Abundance of chemical elements in the continental crust: a new table,” *Geochim. Cosmochim. Acta*, vol. 28, no. 8, pp. 1273–1285, Aug. 1964, doi: 10.1016/0016-7037(64)90129-2.

[2] Liming. Lu, “Iron ore : mineralogy, processing and environmental sustainability,” p. 842, 2022, Accessed: Sep. 10, 2025. [Online]. Available: https://books.google.com/books/about/Iron_Ore.html?hl=it&id=fTFJEAAAQBAJ

[3] D. Spreitzer and J. Schenk, “Reduction of Iron Oxides with Hydrogen—A Review,” *Steel Res. Int.*, vol. 90, no. 10, p. 1900108, Oct. 2019, doi: 10.1002/SRIN.201900108.

[4] Y. Xiao, K. Zhu, S. Ye, Z. Xie, Y. Zhang, and X. Lu, “Hydrogen on softening-melting and slag forming behavior under the operation of blast furnace with iron coke charging,” *Int. J. Hydrogen Energy*, vol. 47, no. 73, pp. 31129–31139, Aug. 2022, doi: 10.1016/j.ijhydene.2022.07.035.

[5] I. Tomasetta, D. Barletta, and M. Poletto, “The Effect of Temperature on Flow Properties of Fine Powders.”

[6] C. Ramakgala and G. Danha, “A review of ironmaking by direct reduction processes: Quality requirements and sustainability,” *Procedia Manuf.*, vol. 35, pp. 242–245, Jan. 2019, doi: 10.1016/J.PROMFG.2019.05.034.

[7] Y. Kaymak, T. Hauck, R. Lin, and H. Rausch, “VDEh-Betriebsforschungsinstitut GmbH Simulation of Slag / Gas and Slag / Iron Interface Tilting in Blast Furnace Hearth during Slag Tapping,” *Engineering, Materials Science*, 2017.

[8] Seshadri. Seetharaman, Alexander. McLean, R. I. L. . Guthrie, and Seetharaman. Sridhar, “Treatise on process metallurgy. Volume 3, Industrial processes,” p. 1745, 2014.

[9] A. Ghosh and A. Chatterjee, “IRON MAKING AND STEEL MAKING- Theory and Practice,” *Ironmaking and Steelmaking*, vol. 1, p. 482, 2008, Accessed: Sep. 12, 2025. [Online]. Available: https://books.google.com/books/about/IRON_MAKING_AND_STEELMAKING.html?hl=it&id=7_GcmB4i_dsC

[10] “Total production of crude steel.” Accessed: Sep. 10, 2025. [Online]. Available: https://worldsteel.org/data/annual-production-steel-data/?ind=P1_crude_steel_total_pub/CHN/IND

[11] C. E. Loo, L. T. Matthews, and D. P. O’Dea, “Lump ore and sinter behaviour during softening and melting,” *ISIJ International*, vol. 51,

no. 6, pp. 930–938, Jun. 2011, doi: 10.2355/ISIJINTERNATIONAL.51.930.
[12] M. Abdul Quader, S. Ahmed, S. Z. Dawal, and Y. Nukman, "A review on low carbon emissions projects of steel industry in the World," *J. Clean. Prod.*, vol. 306, p. 127259, Jul. 2021, doi: 10.1016/j.rser.2015.10.101.
[13] E. Worrell and G. Boyd, "State-of-the-art review on the steel decarbonization technologies based on process system engineering perspective," *Fuel*, vol. 347, p. 128459, Sep. 2023, doi: 10.1016/j.jclepro.2021.129758.
[14] G. Di Foggia and M. Beccarello, "Decarbonization in the European steel industry: Strategies, risks, and commitments," *Environmental Challenges*, vol. 16, p. 100988, Aug. 2024, doi: 10.1016/J.ENVC.2024.100988.
[15] B. Kazmi, S. A. A. Taqvi, and D. Juchelková, "State-of-the-art review on the steel decarbonization technologies based on process system engineering perspective," *Fuel*, vol. 347, p. 128459, Sep. 2023, doi: 10.1016/J.FUEL.2023.128459.
[16] "Industrial Transformation 2050 - Pathways to Net-Zero Emissions from EU Heavy Industry | Material Economics." Accessed: Oct. 01, 2025. [Online]. Available: https://materialeconomics.com/node/13
[17] "Maximise H2 Enrichment in Direct Reduction Shaft Furnaces | MaxH2DR | Project | Fact Sheet | HORIZON | CORDIS | European Commission." Accessed: Oct. 01, 2025. [Online]. Available: https://cordis.europa.eu/project/id/101058429
[18] B. Anameric and S. K. Kawatra, "Properties and features of direct reduced iron," *Mineral Processing and Extractive Metallurgy Review*, vol. 28, no. 1, pp. 59–116, Jan. 2007, doi: 10.1080/08827500600835576.
[19] D. Schulze, "Flow Properties of Powders and Bulk Solids and Silo Design for Flow," 2011.
[20] V. Ganesan, K. A. Rosentrater, and K. Muthukumarappan, "Flowability and handling characteristics of bulk solids and powders – a review with implications for DDGS," *Biosyst. Eng.*, vol. 101, no. 4, pp. 425–435, Jan. 2008, doi: 10.1016/j.biosystemseng.2008.09.008.
[21] "Powder Flowability: Understanding its Importance and Influencing Factors," 2024, doi: 10.4172/2168-9806.1000452.
[22] H. M. Jaeger, S. R. Nagel, and R. P. Behringer, "Granular solids, liquids, and gases," *Rev. Mod. Phys.*, vol. 68, no. 4, p. 1259, Oct. 1996, doi: 10.1103/RevModPhys.68.1259.
[23] O. C. Scheffler and C. Coetzee, "DEM calibration for simulating bulk cohesive materials," *Comput. Geotech.*, vol. 161, p. 105476, Sep. 2023, doi: 10.1016/J.COMPGEO.2023.105476.

[24] L. Scholtès, B. Chareyre, F. Nicot, and F. Darve, “Micromechanics of granular materials with capillary effects,” *Int. J. Eng. Sci.*, vol. 47, no. 1, pp. 64–75, Jan. 2009, doi: 10.1016/j.ijengsci.2008.07.002.

[25] G. A. D’Addetta, F. Kun, and E. Ramm, “On the application of a discrete model to the fracture process of cohesive granular materials,” *Granul. Matter*, vol. 4, no. 2, pp. 77–90, Jul. 2002, doi: 10.1007/s10035-002-0103-9.

[26] C. Kloss, C. Goniva, A. Hager, S. Amberger, and S. Pirker, “Models, algorithms and validation for opensource DEM and CFD-DEM,” *Progress in Computational Fluid Dynamics*, vol. 12, no. 2–3, pp. 140–152, 2012, doi: 10.1504/PCFD.2012.047457.

[27] H. P. Zhu, Z. Y. Zhou, R. Y. Yang, and A. B. Yu, “Discrete particle simulation of particulate systems: Theoretical developments,” *Chem. Eng. Sci.*, vol. 62, no. 13, pp. 3378–3396, Jul. 2007, doi: 10.1016/j.ces.2006.12.089.

[28] R. L. . Brown and J. C. . Richards, *Principles of Powder Mechanics: Essays on the Packing and Flow of Powders and Bulk Solids*, 1st ed. Oxford: Pergamon Press, 1970.

[29] E. R. Tuttle, “Mohr’s circle and the determination of moments of inertia,” *Am. J. Phys.*, vol. 45, no. 4, pp. 396–397, Apr. 1977, doi: 10.1119/1.10853.

[30] Y. Wan, G. Luo, Y. Wang, F. Zhang, and H. Guan, “Stability Analysis of Cracked Clay Slopes Using a Modified Mohr–Coulomb Criterion,” *Geotechnical and Geological Engineering 2025 43:6*, vol. 43, no. 6, pp. 298-, Jul. 2025, doi: 10.1007/s10706-025-03249-1.

[31] J. Zhou, C. Li, P. G. Asteris, X. Shi, and D. J. Armaghani, “Chart-Based Granular Slope Stability Assessment Using the Modified Mohr–Coulomb Criterion,” *Arab. J. Sci. Eng.*, vol. 48, no. 4, pp. 5549–5569, Apr. 2023, doi: 10.1007/s13369-022-07478-x.

[32] H. Shi *et al.*, “Effect of Particle Size and Cohesion on Powder Yielding and Flow,” *Kona*, vol. 2018, no. 35, pp. 226–250, Jan. 2018, doi: 10.14356/kona.2018014.

[33] O. Pouliquen, “Powders and cohesive granular media: a rheological perspective,” *Rheologica Acta 2025 64:4*, vol. 64, no. 4, pp. 195–207, Apr. 2025, doi: 10.1007/s00397-025-01490-2.

[34] “Storage and flow of solids. Bulletin No. 123; Vol. 53, No. 26, November 1964 - UNT Digital Library.” Accessed: Aug. 05, 2025. [Online]. Available: https://digital.library.unt.edu/ark:/67531/metadc1067072/

[35] M. Ghadiri *et al.*, “Cohesive Powder Flow: Trends and Challenges in Characterisation and Analysis,” *KONA Powder and Particle Journal*, vol. 37, pp. 3–18, Jan. 2020, doi: 10.14356/kona.2020018.

[36] C. J. Coetzee and O. C. Scheffler, “Review: The Calibration of DEM Parameters for the Bulk Modelling of Cohesive Materials,” *Processes 2023, Vol. 11,* vol. 11, no. 1, Dec. 2022, doi: 10.3390/pr11010005.

[37] S. W. Jeong and S. S. Park, “Effect of the Surface Roughness on the Shear Strength of Granular Materials in Ring Shear Tests,” *Applied Sciences 2019, Vol. 9,* vol. 9, no. 15, Jul. 2019, doi: 10.3390/app9152977.

[38] V. Ganesan, K. Muthukumarappan, and K. A. Rosentrater, “Flow properties of DDGS with varying soluble and moisture contents using jenike shear testing,” *Powder Technol.*, vol. 187, no. 2, pp. 130–137, Oct. 2008, doi: 10.1016/J.POWTEC.2008.02.003.

[39] Y. Jiang, G. Wang, and T. Kamai, “Fast shear behavior of granular materials in ring-shear tests and implications for rapid landslides,” *Acta Geotechnica 2016 12:3*, vol. 12, no. 3, pp. 645–655, Dec. 2016, doi: 10.1007/s11440-016-0508-y.

[40] T. Swize, F. Osei-Yeboah, M. L. Peterson, and P. Boulas, “Impact of Shear History on Powder Flow Characterization Using a Ring Shear Tester,” *J. Pharm. Sci.*, vol. 108, no. 1, pp. 750–754, Jan. 2019, doi: 10.1016/j.xphs.2018.07.003.

[41] J. Schwedes and D. Schulze, “Measurement of flow properties of bulk solids,” *Powder Technol.*, vol. 61, no. 1, pp. 59–68, Apr. 1990, doi: 10.1016/0032-5910(90)80066-8.

[42] F. Radjai, S. Roux, and J. J. Moreau, “Contact forces in a granular packing,” *Chaos: An Interdisciplinary Journal of Nonlinear Science*, vol. 9, no. 3, pp. 544–550, Sep. 1999, doi: 10.1063/1.166428.

[43] Y. Forterre and O. Pouliquen, “Flows of dense granular media,” *Annu. Rev. Fluid Mech.*, vol. 40, no. Volume 40, 2008, pp. 1–24, Jan. 2008, doi: 10.1146/annurev.fluid.40.111406.102142.

[44] P. W. Rowe, “The stress-dilatancy relation for static equilibrium of an assembly of particles in contact,” *Proceedings of the Royal Society of London. A. Mathematical and Physical Sciences*, vol. 269, no. 1339, pp. 500–527, Oct. 1962, doi: 10.1098/rspa.1962.0193.

[45] P. Guo, S. Zhou, and D. Stolle, “Analysis of dilatancy relation and shear-band formation in granular materials based on Eshelby-Mandel tensor,” *Int. J. Numer. Anal. Methods Geomech.*, vol. 47, no. 9, pp. 1699–1717, Jun. 2023, doi: 10.1002/nag.3535.

[46] X. Li, H. Zhu, and Q. Yuan, “Dilatancy Equation Based on the Property-Dependent Plastic Potential Theory for Geomaterials,” *Fractal and Fractional 2023, Vol. 7,* vol. 7, no. 11, Nov. 2023, doi: 10.3390/fractalfract7110824.

[47] D. Schulze, J. Schwedes, and J. W. Carson, *Powders and bulk solids: Behavior, characterization, storage and flow*, Second Edition. Springer Berlin Heidelberg, 2008. doi: 10.1007/978-3-540-73768-1/COVER.

[48] W. A. Beverloo, H. A. Leniger, and J. Van De Velde, “The flow of granular solids through orifices.”

[49] S. A. Hall *et al.*, “Discrete and Continuum analysis of localised deformation in sand using X-ray CT and Volumetric Digital Image Correlation,” *Volumetric Digital Image Correlation. Geotechnique*, no. 5, pp. 315–322, 2010, doi: 10.1680/geot.2010.60.5.315ï.

[50] “Standard Test Method for Bulk Solids Using Schulze Ring Shear Tester 1,” 2016. doi: 10.1520/D6773-16.

[51] H. Salehi, D. Barletta, and M. Poletto, “A comparison between powder flow property testers,” *Particuology*, vol. 32, pp. 10–20, Jun. 2017, doi: 10.1016/J.PARTIC.2016.08.003.

[52] M. Wojtkowski *et al.*, “Effect of cohesive forces on fluctuations in granular flows: linking experiments and simulations,” *EPJ Web Conf.*, vol. 224, pp. 13–21, 2012.

[53] D. J. Lacks and R. Mohan Sankaran, “Contact electrification of insulating materials,” *J. Phys. D Appl. Phys.*, vol. 44, no. 45, p. 453001, Oct. 2011, doi: 10.1088/0022-3727/44/45/453001.

[54] N. P. Kruyt and O. Millet, “An analytical theory for the capillary bridge force between spheres,” *J. Fluid Mech.*, vol. 812, pp. 129–151, Feb. 2017, doi: 10.1017/jfm.2016.790.

[55] S. M. Iveson, J. D. Litster, K. Hapgood, and B. J. Ennis, “Nucleation, growth and breakage phenomena in agitated wet granulation processes: a review,” *Powder Technol.*, vol. 117, no. 1–2, pp. 3–39, Jun. 2001, doi: 10.1016/S0032-5910(01)00313-8.

[56] Y. Man, J. X. Feng, F. J. Li, Q. Ge, Y. M. Chen, and J. Z. Zhou, “Influence of temperature and time on reduction behavior in iron ore-coal composite pellets,” *Powder Technol.*, vol. 256, pp. 361–366, 2014, doi: 10.1016/j.powtec.2014.02.039.

[57] Y. Lu, S. Wu, B. Du, and H. Zhou, “Increasing the softening as well as melting behaviors for iron ore materials within the blast furnace cohesive zone through the high-temperature interactivity,” *ISIJ International*, vol. 60, no. 7, pp. 1461–1468, 2020, doi: 10.2355/ISIJINTERNATIONAL.ISIJINT-2019-713.

[58] Masaru Matsumura, Masahiko Hoshi, and Takazo Kawaguchi, “improvement of sinter softening property and reducibility by controlling chemical composition”.

[59] S. L. Wu, H. F. Xu, and Y. Q. Tian, “Evaluation of lump ores for use in modern blast furnaces as part of mixed burden practice,” *Ironmaking and Steelmaking*, vol. 36, no. 1, pp. 19–23, Jan. 2009, doi: 10.1179/174328107X167931.

[60] F. R. Silva, L. R. Lemos, P. de Freitas Nogueira, and M. Bressan, “Effect of Ternary Basicity of Iron Ore-Fluxed Pellets on Melting and Softening Properties in a Blast Furnace,” *Metallurgical and Materials Transactions B: Process Metallurgy and Materials Processing*

Science, vol. 52, no. 1, pp. 69–76, Feb. 2021, doi: 10.1007/s11663-020-01917-6.

[61] Y. Qie *et al.*, "Effect of Hydrogen Addition on Softening and Melting Reduction Behaviors of Ferrous Burden in Gas-Injection Blast Furnace," *Metallurgical and Materials Transactions B: Process Metallurgy and Materials Processing Science*, vol. 49, no. 5, pp. 2622–2632, Oct. 2018, doi: 10.1007/s11663-018-1299-3.

[62] S. Natsui, M. Tanaka, A. S. Siahaan, and H. Nogami, "Dynamic Model of High-Temperature Sintered Iron Ore Plastic Deformation Considering Reduction Degree," *Metallurgical and Materials Transactions B: Process Metallurgy and Materials Processing Science*, vol. 53, no. 6, pp. 3842–3855, Dec. 2022, doi: 10.1007/s11663-022-02646-8.

[63] F. Patisson, O. Mirgaux, and J. P. Birat, "Hydrogen steelmaking. Part 1: Physical chemistry and process metallurgy," *Materiaux et Techniques*, vol. 109, no. 3–4, 2021, doi: 10.1051/MATTECH/2021025.

[64] T. Han, "Comparison of Wall Friction Measurements by Jenike Shear Tester and Ring Shear Tester," *KONA Powder and Particle Journal*, vol. 29, pp. 118–124, 2011, doi: 10.14356/KONA.2011014.

[65] J. Härtl and J. Y. Ooi, "Numerical investigation of particle shape and particle friction on limiting bulk friction in direct shear tests and comparison with experiments," *Powder Technol.*, vol. 212, no. 1, pp. 231–239, Sep. 2011, doi: 10.1016/j.powtec.2011.05.022.

[66] S. V. Søgaard, T. Pedersen, M. Allesø, J. Garnaes, and J. Rantanen, "Evaluation of ring shear testing as a characterization method for powder flow in small-scale powder processing equipment," *Int. J. Pharm.*, vol. 475, no. 1–2, pp. 315–323, Nov. 2014, doi: 10.1016/j.ijpharm.2014.08.060.

[67] X. Ding, L. Liu, and M. S. A. Bradley, "New Instrument PFT for Powder Flow Researching," *Adv. Mat. Res.*, vol. 508, pp. 141–145, 2012, doi: 10.4028/www.scientific.net/AMR.508.141.

[68] H. Salehi, D. Sofia, D. Schütz, D. Barletta, and M. Poletto, "Experiments and simulation of torque in Anton Paar powder cell," *Particulate Science and Technology*, vol. 36, no. 4, pp. 501–512, May 2018, doi: 10.1080/02726351.2017.1409850.

[69] K. K. Moravkar, S. D. Korde, B. A. Bhairav, S. B. Shinde, S. V Kakulade, and S. S. Chalikwar, "Traditional and Advanced Flow Characterization Techniques: A Platform Review for Development of Solid Dosage Form", Accessed: Feb. 14, 2026. [Online]. Available: www.ijpsonline.com

[70] I. Tomasetta, D. Barletta, and M. Poletto, "The High Temperature Annular Shear Cell: A modified ring shear tester to measure the flow properties of powders at high temperature," *Advanced Powder*

Technology, vol. 24, no. 3, pp. 609–617, May 2013, doi: 10.1016/J.APT.2012.11.007.

[71] I. Tomasetta, D. Barletta, and M. Poletto, "Correlation of powder flow properties to interparticle interactions at ambient and high temperatures," *Particuology*, vol. 12, no. 1, pp. 90–99, Feb. 2014, doi: 10.1016/J.PARTIC.2013.02.002.

[72] M. Ripp and S. Ripperger, "Influence of temperature on the flow properties of bulk solids," *Chem. Eng. Sci.*, vol. 65, no. 13, pp. 4007–4013, Jul. 2010, doi: 10.1016/J.CES.2010.03.046.

[73] D. Macri *et al.*, "Characterization of the Bulk Flow Properties of Industrial Powders from Shear Tests," *Processes 2020, Vol. 8, Page 540*, vol. 8, no. 5, p. 540, May 2020, doi: 10.3390/PR8050540.

[74] R. Chirone, D. Barletta, P. Lettieri, and M. Poletto, "Bulk flow properties of sieved samples of a ceramic powder at ambient and high temperature," *Powder Technol.*, vol. 288, pp. 379–387, Jan. 2016, doi: 10.1016/J.POWTEC.2015.11.040.

[75] D. Macrì, M. Poletto, D. Barletta, S. Sutcliffe, and P. Lettieri, "Analysis of industrial reactive powders flow properties at high temperature," *Powder Technol.*, vol. 316, pp. 131–138, Jul. 2017, doi: 10.1016/J.POWTEC.2016.10.064.

[76] R. Gannoun, J. M. P. Ebrí, A. T. Pérez, and J. M. Valverde, "The Sevilla Powder Tester: A Tool for Measuring the Flow Properties of Cohesive Powders at High Temperatures," *KONA Powder and Particle Journal*, vol. 39, pp. 29–44, Jan. 2022, doi: 10.14356/KONA.2022008.

[77] M. Manokaran, M. Morgeneyer, and D. Weis, "Effect of Microscopic Properties on Flow Behavior of Industrial Cohesive Powder," *Powders 2024, Vol. 3, Pages 324-337*, vol. 3, no. 3, pp. 324–337, Jun. 2024, doi: 10.3390/POWDERS3030019.

[78] A. Castellanos, M. A. S. Quintanilla, J. M. Valverde, and C. Soria-Hoyo, "Novel instrument to characterize dry granular materials at low consolidations," *Review of Scientific Instruments*, vol. 78, no. 7, Jul. 2007, doi: 10.1063/1.2751096/379989.

[79] L. K. Zoet, P. Sobol, N. Lord, and D. D. Hansen, "A ring shear device to simulate cryosphere processes," *Review of Scientific Instruments*, vol. 94, no. 4, Apr. 2023, doi: 10.1063/5.0142933/2878599.

[80] L. Yi, Z. Huang, T. Jiang, R. Zhong, and Z. Liang, "Iron ore pellet disintegration mechanism in simulated shaft furnace conditions," *Powder Technol.*, vol. 317, pp. 89–94, Jul. 2017, doi: 10.1016/j.powtec.2017.04.056.

[81] J. R. Kim *et al.*, "Real-time microradiology of disintegration of iron ore sinteres," *Nucl. Instrum. Methods Phys. Res. B*, vol. 199, no. 7, pp. 441–445, Jan. 2003, doi: 10.1016/S0168-583X(02)01550-1.

[82] M. Nabeel, A. Karasev, and P. G. Jönsson, "Friction Forces and Mechanical Dust Generation in an Iron Ore Pellet Bed Subjected to

Varied Applied Loads," *ISIJ International*, vol. 57, no. 4, pp. 656–664, Apr. 2017, doi: 10.2355/isijinternational.ISIJINT-2016-514.

[83] H. T. Wang, Y. Bin Wang, S. X. Zhu, Q. M. Meng, T. J. Chun, and H. M. Long, "Mechanism of thermal compressive strength evolution of carbon-bearing iron ore pellet without binders during reduction process," *Journal of Iron and Steel Research International 2024 32:4*, vol. 32, no. 4, pp. 871–882, May 2024, doi: 10.1007/s42243-024-01245-y.

[84] M. Iljana *et al.*, "Effect of adding limestone on the metallurgical properties of iron ore pellets," *Int. J. Miner. Process.*, vol. 141, pp. 34–43, Aug. 2015, doi: 10.1016/j.minpro.2015.06.004.

[85] T. Umadevi, P. Kumar, N. F. Lobo, M. Prabhu, P. C. Mahapatra, and M. Ranjan, "Influence of Pellet Basicity (CaO/SiO2) on Iron Ore Pellet Properties and Microstructure," *ISIJ International*, vol. 51, no. 1, pp. 14–20, Jan. 2011, doi: 10.2355/isijinternational.51.14.

[86] S. Dwarapudi and M. Ranjan, "Influence of Oxide and Silicate Melt Phases on the RDI of Iron Ore Pellets Suitable for Shaft Furnace of Direct Reduction Process," *ISIJ International*, vol. 50, no. 11, pp. 1581–1589, Nov. 2010, doi: 10.2355/isijinternational.50.1581.

[87] Z. Huang, L. Yi, and T. Jiang, "Mechanisms of strength decrease in the initial reduction of iron ore oxide pellets," *Powder Technol.*, vol. 221, pp. 284–291, May 2012, doi: 10.1016/j.powtec.2012.01.013.

[88] T. Sharma, R. C. Gupta, and B. Prakash, "Effect of Porosity on the Swelling Behaviour of Iron Ore Pellets and Briquettes," *ISIJ International*, vol. 31, no. 3, pp. 312–314, Mar. 1991, doi: 10.2355/isijinternational.31.312.

[89] R. C. Gupta and B. Prakash, "Swelling of Iron Ore Pellets by Statistical Design of Experiment," *ISIJ International*, vol. 32, no. 12, pp. 1268–1275, Dec. 1992, doi: 10.2355/isijinternational.32.1268.

[90] T. Sharma, "Swelling of Iron Ore Pellets under Non-isothermal Condition," *ISIJ International*, vol. 34, no. 12, pp. 960–963, Dec. 1994, doi: 10.2355/isijinternational.34.960.

[91] T. Sharma, R. C. Gupta, and B. Prakash, "Effect of Reduction Rate on the Swelling Behaviour of Iron Ore Pellets," *ISIJ International*, vol. 32, no. 7, pp. 812–818, Jul. 1992, doi: 10.2355/isijinternational.32.812.

[92] S. Hayashi and Y. Iguchi, "Abnormal Swelling during Reduction of Binder Bonded Iron Ore Pellets with CO-CO2 Gas Mixtures," *Isij International*, vol. 43, no. 9, pp. 1370–1375, 2003, doi: 10.2355/isijinternational.43.1370.

[93] O. Kovtun, M. Levchenko, E. Oldinski, M. Gräbner, and O. Volkova, "Swelling Behavior of Iron Ore Pellets during Reduction in H2 and N2/H2 Atmospheres at Different Temperatures," *Steel Res. Int.*, vol. 94, no. 10, p. 2300140, Oct. 2023, doi: 10.1002/srin.202300140.

[94] X. Dong, Y. Tian, G. An, J. Chen, S. He, and W. Wu, "Research on influence of grinding blast furnace return ore on reduction swelling index of low silicon fluxed pellets and production practice," *Metallurgical Research & Technology*, vol. 121, no. 3, p. 305, 2024, doi: 10.1051/metal/2024025.

[95] M. Iljana *et al.*, "Dynamic and Isothermal Reduction Swelling Behaviour of Olivine and Acid Iron Ore Pellets under Simulated Blast Furnace Shaft Conditions," *ISIJ International*, vol. 52, no. 7, pp. 1257–1265, 2012, doi: 10.2355/isijinternational.52.1257.

[96] L. Yi, Z. Huang, T. Jiang, R. Zhong, and Z. Liang, "Iron ore pellet disintegration mechanism in simulated shaft furnace conditions," *Powder Technol.*, vol. 317, pp. 89–94, Jul. 2017, doi: 10.1016/J.POWTEC.2017.04.056.

[97] B. Wang *et al.*, "Experimental Study about the Low Temperature Pulverization of Pellets," *Proceedings of the 5th International Conference on Information Engineering for Mechanics and Materials*, vol. 21, pp. 1647–1651, Jul. 2015, doi: 10.2991/icimm-15.2015.305.

[98] Q. Cai *et al.*, "Phase Evolution Behavior during the Reduction Process of Medium-Silica Fluxed Pellets," *Steel Res. Int.*, vol. 95, no. 7, p. 2400021, Jul. 2024, doi: 10.1002/srin.202400021.

[99] Y. Chai *et al.*, "Effect of Basicity on the Reduction Swelling Performance of Pellets Prepared from Bayan Obo Iron Ore Concentrate Based on Microscopic Characterization," *Crystals 2022, Vol. 12,* vol. 12, no. 10, Oct. 2022, doi: 10.3390/cryst12101399.

[100] R. K. Dishwar, A. K. Mandal, and O. P. Sinha, "Studies on Highly Fluxed Iron Ore Pellets Hardened at 1100 °C to 1200 °C," *Metallurgical and Materials Transactions B 2019 50:2*, vol. 50, no. 2, pp. 617–621, Jan. 2019, doi: 10.1007/s11663-019-01506-2.

[101] R. Prasad, S. Soren, L. A. Kumaraswamidhas, C. Pandey, and S. K. Pan, "Experimental Investigation of Different Fineness and Firing Temperatures on Pellets Properties of Different Iron Ore fines from Indian Mines," *Materials (Basel).*, vol. 15, no. 12, Jun. 2022, doi: 10.3390/ma15124220.

[102] B. Yur'ev and V. Dudko, "Development of the Process for Obtaining Iron-Ore Pellets with Required Metallurgical Properties," *Materials Science Forum*, vol. 946, pp. 450–455, 2019, doi: 10.4028/www.scientific.net/MSF.946.450.

[103] A. Kemppainen *et al.*, "Softening behaviors of acid and olivine fluxed iron ore pellets in the cohesive zone of a blast furnace," *ISIJ International*, vol. 55, no. 10, pp. 2039–2046, 2015, doi: 10.2355/isijinternational.ISIJINT-2015-023.

[104] M. Iljana, A. Kemppainen, T. Paananen, O. Mattila, E. P. Heikkinen, and T. Fabritius, "Evaluating the reduction-softening behaviour of blast furnace burden with an advanced test," *ISIJ International*, vol.

56, no. 10, pp. 1705–1714, 2016, doi: 10.2355/isijinternational.ISIJINT-2016-117.
[105] J. Sterneland and A. K. Lahiri, “Contraction and meltdown behaviour of olivine iron ore pellets under simulated blast furnace conditions,” *Ironmaking & Steelmaking*, vol. 26, no. 5, pp. 339–348, 1999, doi: 10.1179/030192399677194.
[106] V. Shatokha and O. Velychko, “Study of softening and melting behaviour of iron ore sinter and pellets,” *High Temperature Materials and Processes*, vol. 31, no. 3, pp. 215–220, Jun. 2012, doi: 10.1515/htmp-2012-0027.
[107] T. Nishimura, K. Higuchi, M. Naito, and K. Kunitomo, “Evaluation of softening, shrinking and melting reduction behavior of raw materials for blast furnace,” *ISIJ International*, vol. 51, no. 8, pp. 1316–1321, Aug. 2011, doi: 10.2355/isijinternational.51.1316.
[108] D. J. Gavel *et al.*, “A comparative study of pellets, sinter and mixed ferrous burden behaviour under simulated blast furnace conditions,” *Ironmaking and Steelmaking*, vol. 48, no. 4, pp. 359–369, 2021, doi: 10.1080/03019233.2020.1786644.
[109] X. Fan *et al.*, “Relationship between interaction under non-load condition and softening & melting behaviour of typical blast furnace feed,” *Ironmaking and Steelmaking*, vol. 49, no. 6, pp. 626–633, 2022, doi: 10.1080/03019233.2022.2036085.
[110] H. Guo, X. Jiang, F. Shen, H. Zheng, Q. Gao, and X. Zhang, “Influence of SiO2 on the Compressive Strength and Reduction-Melting of Pellets,” *Metals 2019, Vol. 9,* vol. 9, no. 8, Aug. 2019, doi: 10.3390/met9080852.
[111] O. Kovtun, M. Levchenko, E. Oldinski, M. Gräbner, and O. Volkova, “Swelling Behavior of Iron Ore Pellets during Reduction in H2 and N2/H2 Atmospheres at Different Temperatures,” *Steel Res. Int.*, vol. 94, no. 10, Oct. 2023, doi: 10.1002/srin.202300140.
[112] S. Wang, F. Shen, X. Zhang, H. Zheng, X. Jiang, and Q. Gao, “Studies of the expansion mechanism on different pellets under hydrogen-rich reducing atmosphere,” *Canadian Metallurgical Quarterly*, vol. 64, no. 4, pp. 2566–2574, Oct. 2025, doi: 10.1080/00084433.2024.2447644.
[113] Z. C. Huang, D. G. Yang, and L. Y. Yi, “Effect of thermal charging of iron ore pellets on the reduction rate and compressive strength in gas-based reduction process,” *Adv. Mat. Res.*, vol. 532–533, pp. 262–266, 2012, doi: 10.4028/www.scientific.net/AMR.532-533.262.
[114] R. C. Gupta and J. P. Gautam, “The Effect of Additives and Reductants on the Strength of Reduced Iron Ore Pellet,” *ISIJ International*, vol. 43, no. 12, pp. 1913–1918, 2003, doi: 10.2355/isijinternational.43.1913.
[115] D. Zhu *et al.*, “Direct reduction behaviors of composite binder magnetite pellets in coal-based grate-rotary kiln process,” *ISIJ*

International, vol. 51, no. 2, pp. 214–219, 2011, doi: 10.2355/isijinternational.51.214.

[116] F. O. Boechat, L. T. da Rocha, R. M. de Carvalho, S. M. Jung, and L. M. Tavares, "Amenability of reduced iron ore pellets to mechanical degradation," *ISIJ International*, vol. 58, no. 6, pp. 1028–1033, 2018, doi: 10.2355/isijinternational.ISIJINT-2017-734.

[117] A. Shams and F. Moazeni, "Modeling and Simulation of the MIDREX Shaft Furnace: Reduction, Transition and Cooling Zones," *JOM 2015 67:11*, vol. 67, no. 11, pp. 2681–2689, Aug. 2015, doi: 10.1007/s11837-015-1588-0.

[118] A. Zare Ghadi, M. S. Valipour, and M. Biglari, "CFD simulation of two-phase gas-particle flow in the Midrex shaft furnace: The effect of twin gas injection system on the performance of the reactor," *Int. J. Hydrogen Energy*, vol. 42, no. 1, pp. 103–118, Jan. 2017, doi: 10.1016/j.ijhydene.2016.11.053.

[119] S. Yadav, C. Srishilan, and A. K. Shukla, "Static Thermochemical Model of MIDREX: Genetic Algorithm Validation and Green Ironmaking with Hydrogen and Coke Oven Gas Injection," *Steel Res. Int.*, vol. 95, no. 11, p. 2400082, Nov. 2024, doi: 10.1002/srin.202400082.

[120] H. A. Petit, A. Philippe, A. D. Thomazini, and L. M. Tavares, "Modeling breakage by impact of fragments of fired iron ore pellets," *Powder Technol.*, vol. 398, p. 117059, Jan. 2022, doi: 10.1016/J.POWTEC.2021.117059.

[121] M. Sperl, "Experiments on corn pressure in silo cells - Translation and comment of Janssen's paper from 1895," *Granul. Matter*, vol. 8, no. 2, pp. 59–65, May 2006, doi: 10.1007/S10035-005-0224-Z/METRICS.

[122] S. K. Dwivedi and M. Vishwakarma, "Hydrogen embrittlement in different materials: A review," *Int. J. Hydrogen Energy*, vol. 43, no. 46, pp. 21603–21616, Nov. 2018, doi: 10.1016/J.IJHYDENE.2018.09.201.

[123] P. G. Shewmon, "Hydrogen attack of carbon steel," *Metallurgical Transactions A 1976 7:2*, vol. 7, no. 2, pp. 279–286, Feb. 1976, doi: 10.1007/BF02644468.

[124] S. P. Lynch, "Hydrogen embrittlement (HE) phenomena and mechanisms," *Stress corrosion cracking: Theory and practice*, pp. 90–130, Jan. 2011, doi: 10.1533/9780857093769.1.90.

[125] K. Poorhaydari, "A Comprehensive Examination of High-Temperature Hydrogen Attack—A Review of over a Century of Investigations," *Journal of Materials Engineering and Performance 2021 30:11*, vol. 30, no. 11, pp. 7875–7908, Aug. 2021, doi: 10.1007/S11665-021-06045-Z.

[126] Y. W. Yen, F. Y. Hung, J. R. Zhao, B. D. Wu, and H. Y. Hsieh, "A study on thermal-induced phase transformation behavior and deterioration

mechanism of 310S stainless steel," *Journal of Alloys and Metallurgical Systems*, vol. 6, p. 100069, Jun. 2024, doi: 10.1016/J.JALMES.2024.100069.

[127] E. Kamel, S. S. A. ElMoamen, E. El-Kashif, and L. Z. Mohamed, "A comparative study of stainless steel 310 and N350 in high temperature oxidation," *Egypt. J. Chem.*, vol. 68, no. 4, pp. 37–52, Apr. 2025, doi: 10.21608/EJCHEM.2024.303345.9987.

[128] C. Parrens, B. Malard, J. L. Dupain, and D. Poquillon, "Metallurgy and Creep Behavior of Type 310S Stainless Steel at High Temperature in Different Atmospheres and Loading Conditions," *Characterization of Minerals, Metals, and Materials 2016*, pp. 193–200, Jan. 2016, doi: 10.1007/978-3-319-48210-1_23.

[129] J. M. Garcia, A. C. A. Monteiro, A. de M. B. Casanova, N. R. Checca Huaman, S. N. Monteiro, and L. P. Brandao, "Microstructural analysis of phase precipitation during high temperature creep in AISI 310 stainless steel," *Journal of Materials Research and Technology*, vol. 23, no. 10, pp. 5953–5966, Mar. 2023, doi: 10.1016/j.jmrt.2023.02.175.

[130] M. Z. Yang, Q. Yang, and J. L. Luo, "Effects of hydrogen on passive film and corrosion of aisi 310 stainless steel," *Corros. Sci.*, vol. 41, no. 4, pp. 741–745, Apr. 1999, doi: 10.1016/S0010-938X(98)00147-4.

[131] S. T. Iso and J. A. Pask, "Reaction of Silicate Glasses and Mullite with Hydrogen Gas," *Journal of the American Ceramic Society*, vol. 65, no. 8, pp. 383–387, Aug. 1982, doi: 10.1111/J.1151-2916.1982.TB10489.X.

[132] G. E. Dieter, *Mechanical metallurgy*. New York: McGraw-Hill, 1961. Accessed: Feb. 14, 2026. [Online]. Available: https://archive.org/details/mechanicalmetall00diet/mode/2up

[133] K. G. Wynnyk, B. Hojjati, and R. A. Marriott, "Sour Gas and Water Adsorption on Common High-Pressure Desiccant Materials: Zeolite 3A, Zeolite 4A, and Silica Gel," *J. Chem. Eng. Data*, vol. 64, no. 7, pp. 3156–3163, Jun. 2019, doi: 10.1021/ACS.JCED.9B00233.

[134] E. Webster and P. Saunders, "Characterizing Drift Behavior in Type S Thermocouples to Predict In-use Temperature Errors," *International Journal of Thermophysics 2019 41:1*, vol. 41, no. 1, pp. 5-, Dec. 2019, doi: 10.1007/S10765-019-2579-0.

[135] J. Tomas, "Product design of cohesive powders - Mechanical properties, compression and flow behavior," *Chem. Eng. Technol.*, vol. 27, no. 6, pp. 605–618, Jun. 2004, doi: 10.1002/CEAT.200406134.

[136] "Test Method for Bulk Solids Using Schulze Ring Shear Tester," Feb. 01, 2016, *ASTM International, West Conshohocken, PA*. doi: 10.1520/D6773-16.

[137] O. C. Scheffler and C. Coetzee, “DEM calibration for simulating bulk cohesive materials,” *Comput. Geotech.*, vol. 161, p. 105476, Sep. 2023, doi: 10.1016/J.COMPGEO.2023.105476.

[138] S. Luding, “Shear flow modeling of cohesive and frictional fine powder,” *Powder Technol.*, vol. 158, no. 1–3, pp. 45–50, Oct. 2005, doi: 10.1016/J.POWTEC.2005.04.018.

[139] K. Qyteti, S. la Manna, E. Illana, D. Barletta, M. Poletto, and V. Scherer, “Discrete element modeling of shear cell experiments with cohesive wooden spheres,” *Particuology*, vol. 107, pp. 300–312, Dec. 2025, doi: 10.1016/J.PARTIC.2025.10.006.

[140] H. Pousette and N. Kojola, “Factors influencing physical and mechanical properties of direct reduced iron ore pellets”, doi: 10.1177/03019233241277422.

[141] I. S. Bersenev, V. V. Bragin, Y. A. Chesnokov, A. I. Gruzdev, E. R. Sabirov, and N. A. Spirin, “Peculiarities of fracture of iron–ore pellets in the course of reduction heat treatment,” *Metallurgist 2025 69:3*, vol. 69, no. 3, pp. 349–357, Jul. 2025, doi: 10.1007/S11015-025-01949-W.

[142] D. Barletta, M. Poletto, and A. C. Santomaso, “Bulk Powder Flow Characterisation Techniques,” *Powder Flow*, pp. 64–146, Jul. 2019, doi: 10.1039/9781788016100-00064.

[143] D. W. Green and R. H. Perry, *Perry’s Chemical Engineers’ Handbook*, 8th ed. New York, NY: McGraw-Hill, 2008.

List of symbols

α	Angle of internal friction, rad
δ_0	Equilibrium overlap, m
δ_{limit}	Overlap threshold, m
δ_{min}	Minimum overlap, m
ϕ	Inclination from vertical axis of principal plane, rad
ϕ_e	Effective angle of internal friction, rad
ϵ_{eq}	Equivalent solid deformation, -
ϵ_i	Solid component deformation, -
ρ_b	Solid bulk density, kg m^{-3}
σ	Normal stress, kPa
σ_1	Major principal stress, kPa
σ_2	Minor principal stress, kPa
$\sigma_{eq,vM}$	von Mises equivalent stress, Pa
σ_{adm}	Yield stress, kPa
σ_{ij}	Normal stress component, kPa
σ_p	Hydrostatic normal stress, kPa
τ	Shear stress, kPa
τ_i	Shear stress at failure, Pa
τ_i'	Corrected shear stress at failure, Pa
τ_{ij}	Shear stress component, kPa
τ_{pi}	Pre-shearing stress, Pa
τ_{pm}	Averaged pre-shearing stress, Pa
μ_w	Wall friction coefficient, -
ν	Poisson's ratio, -
A	Cross section, m^2
A_{rod}	Rod's cross-sectional area, m^2
C	Cohesion, kPa
Cp	Specific heat at constant pressure, J mol^{-1} K^{-1}
d	Mohr circle diameter, kPa
D	Bin diameter, m
D_{rod}	Rod diameter, m
E	Young's modulus, -
F	Force, N
f_i	Deflection, -
g	Gravitational acceleration, m s^{-2}

I	Mass moment of inertia, kg m²
I_p	Polar moment of the cross-section, m⁴
K	Lateral stress ratio, -
k_1	Primary repulsive stiffness, N m⁻¹
k_2	Secondary repulsive stiffness, N m⁻¹
k_c	Cohesive stiffness, N m⁻¹
k_s	Solid thermal conductivity, W m⁻¹ K⁻¹
L	Height of the cooling chamber, m
M_b	Bending moment, N m
M_e	Torque, N m
M_t	Torsional moment, N m
N	Total normal force, N
q	Heat flow, W m⁻²
$\dot{Q}$	Thermal power, W
r	Mohr circle radius, kPa
S	Stress tensor, kPa
T	Temperature, K
T_{bottom}	Rod temperature at lower boundary, K
T_{top}	Rod temperature at upper boundary, K
U_D	Distortion energy, Pa
U_{D_l}	Limit distortion energy, Pa
U_T	Total elastic strain energy, Pa
U_V	Volumetric energy, Pa
$\dot{V}$	Volumetric flow rate, m³ s⁻¹
z	Depth from free surface, m

Appendix A

Orthographic projections and dimensions

Lid

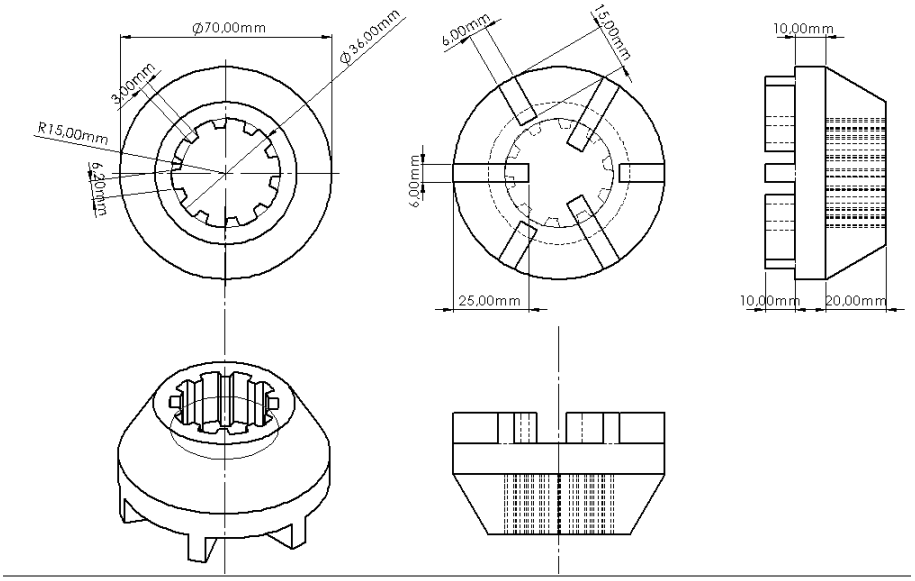

Trough

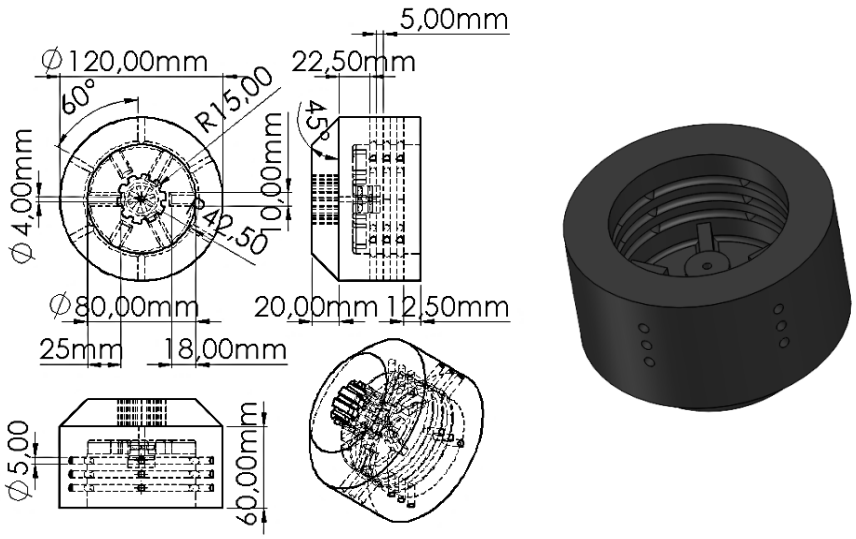

Upper rod

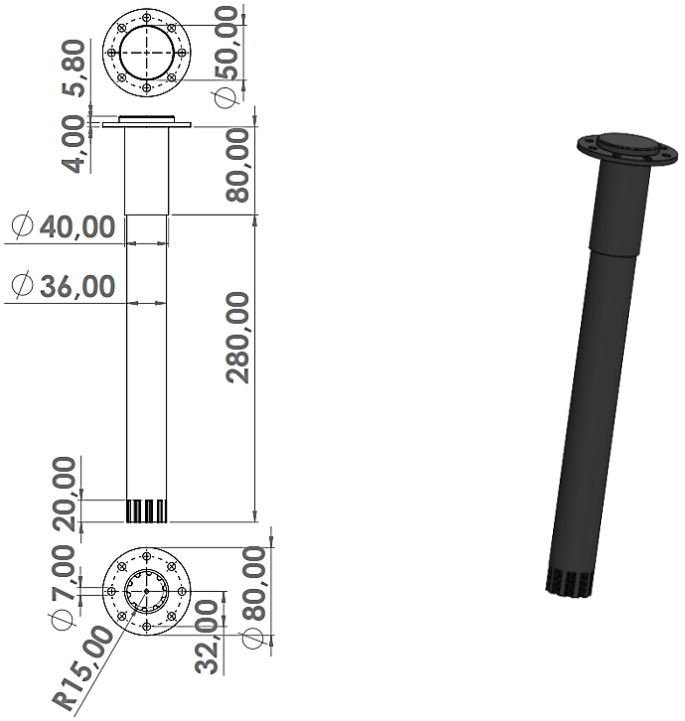

Lower rod

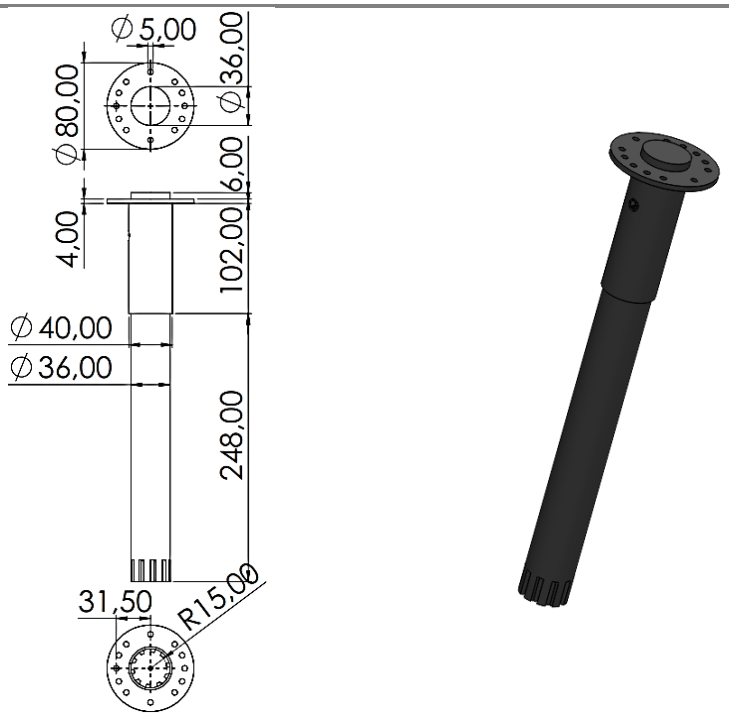

Reactive chamber

I) II)

Reactive chamber I

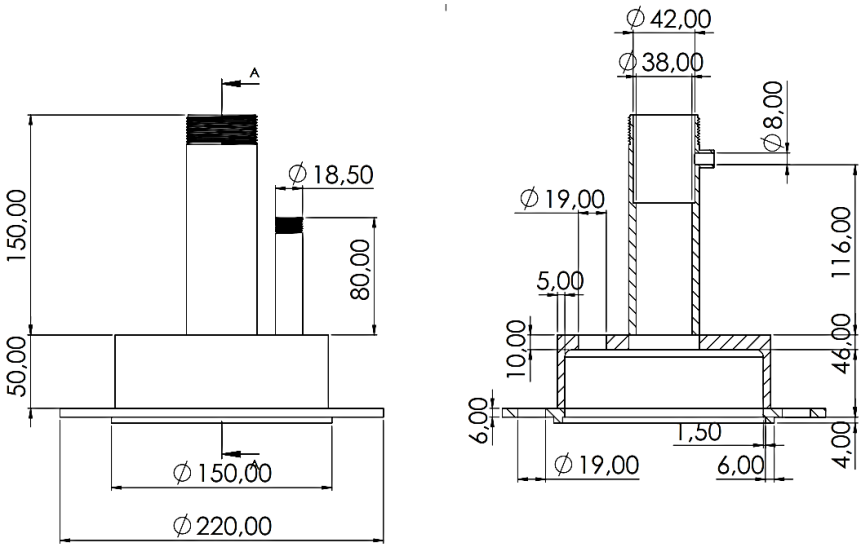

Reactive chamber II

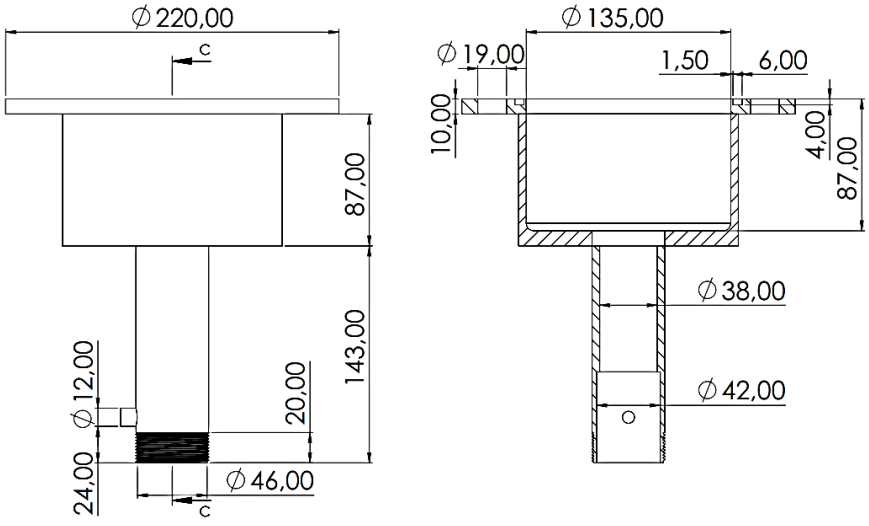

Skeleton

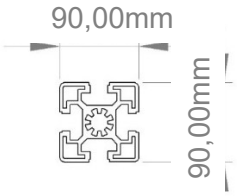

Type:	length [mm]:	Qt.:
I	1750	4
II	420	18
III	180	2

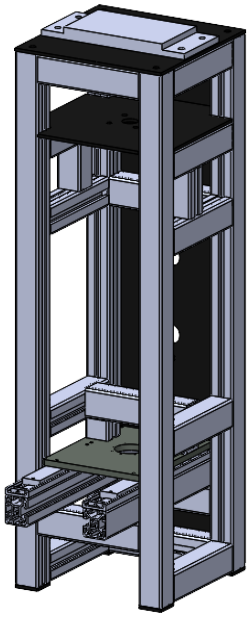

Skeleton top wall

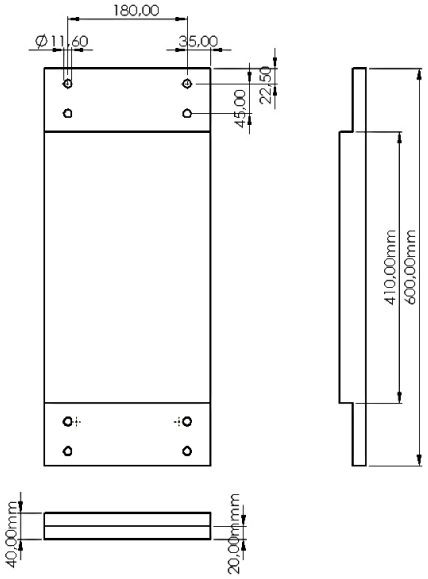

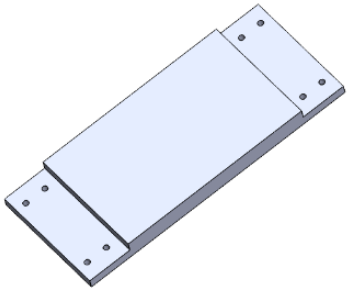

Skeleton upper plane

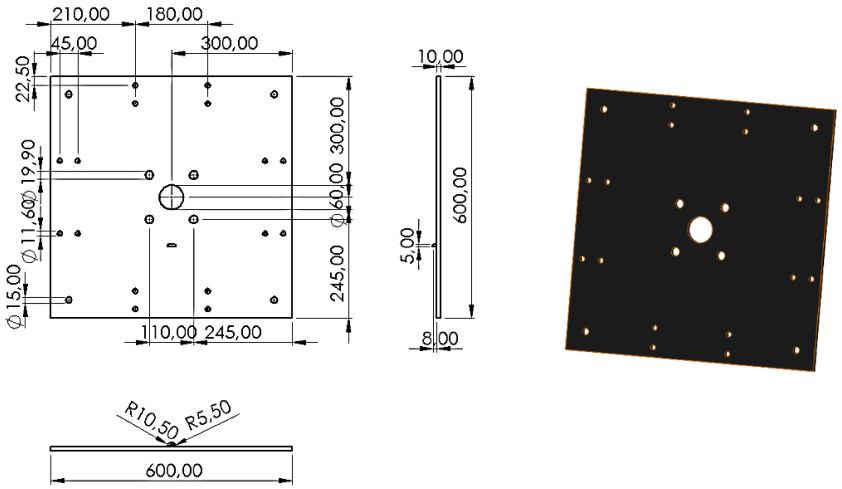

Skeleton middle plane

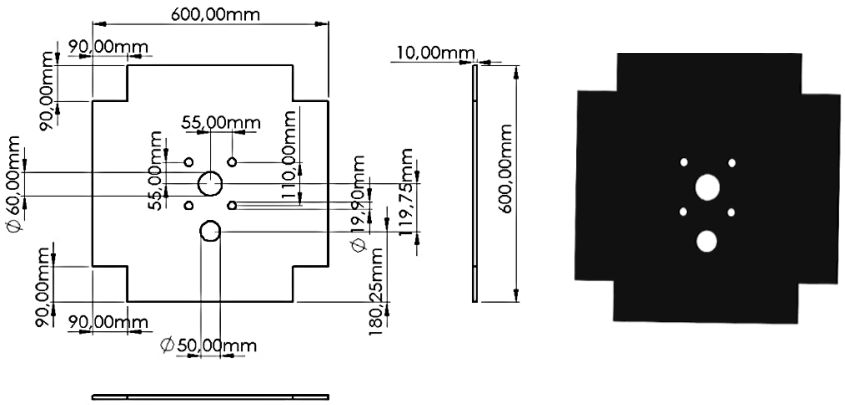

Skeleton back wall

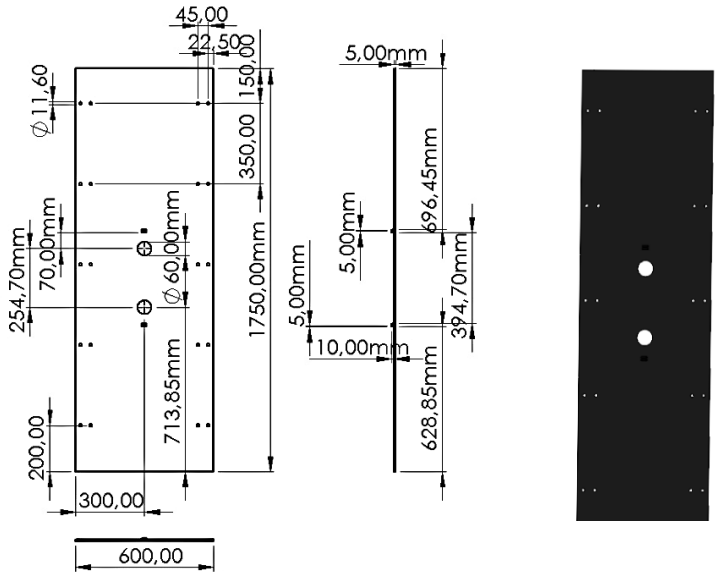

Sliding board

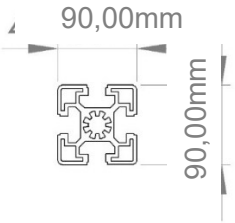

Type:	length [mm]:	Qt.:
I	840	2
II	420	1
III	65	2

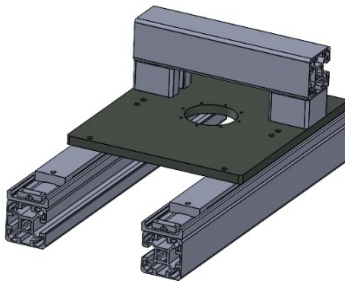

Sliding plane

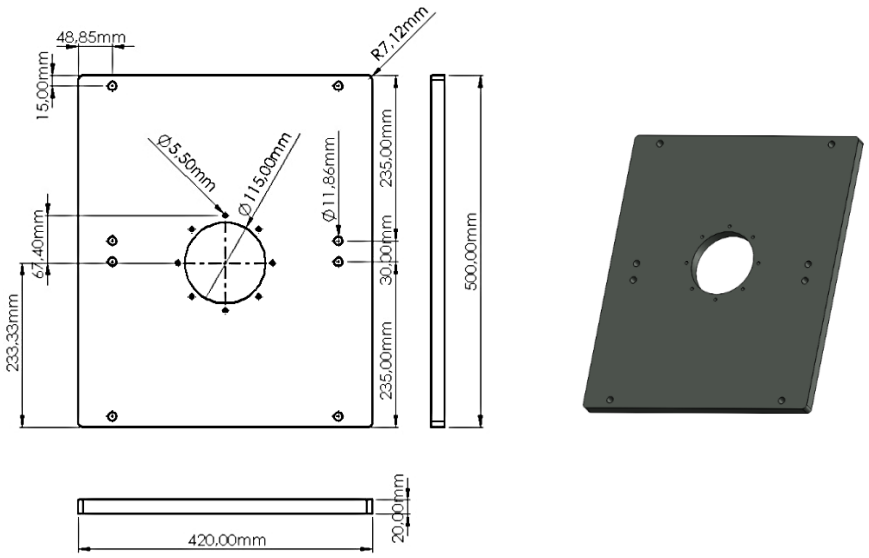

Position sensor connector

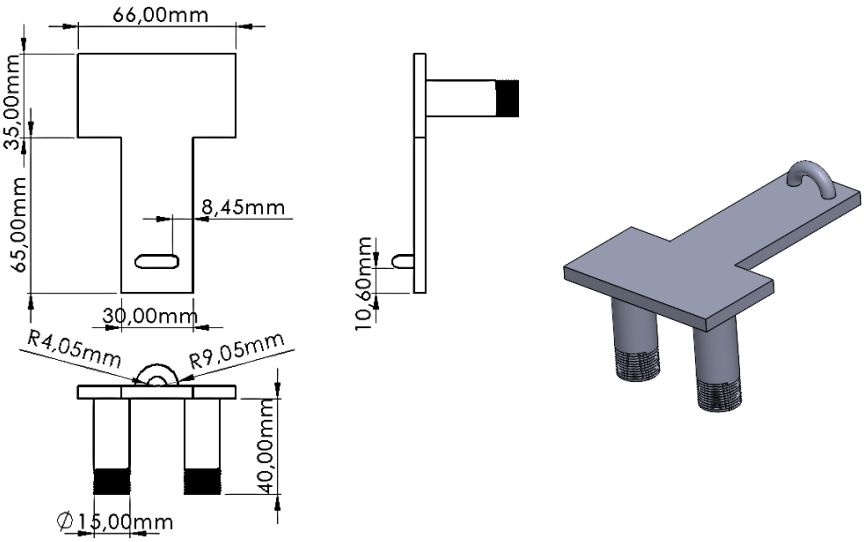

Torquemeter connectors

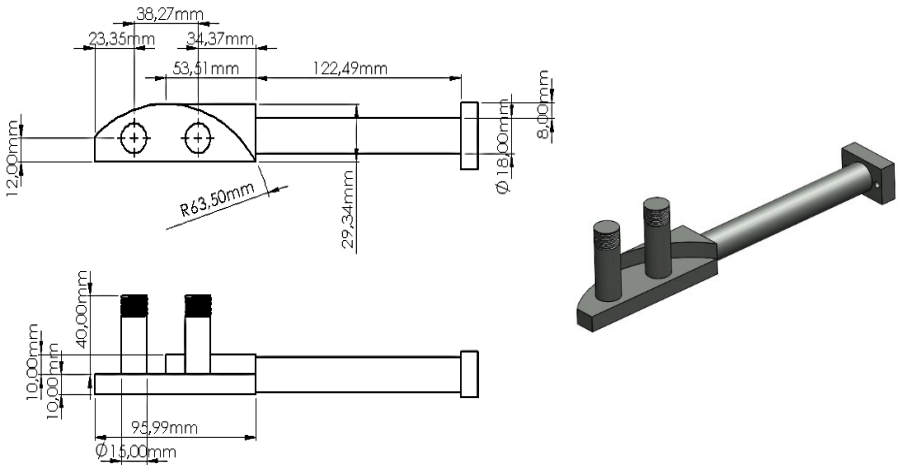

Upper rod connector

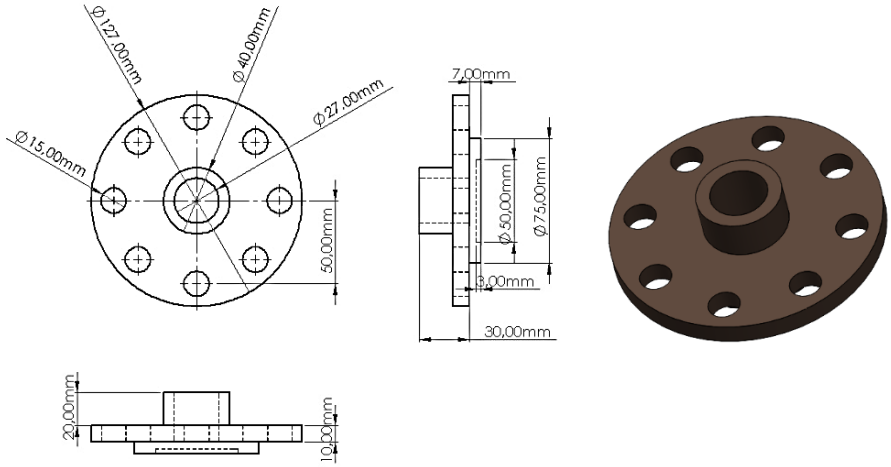

Structural support I

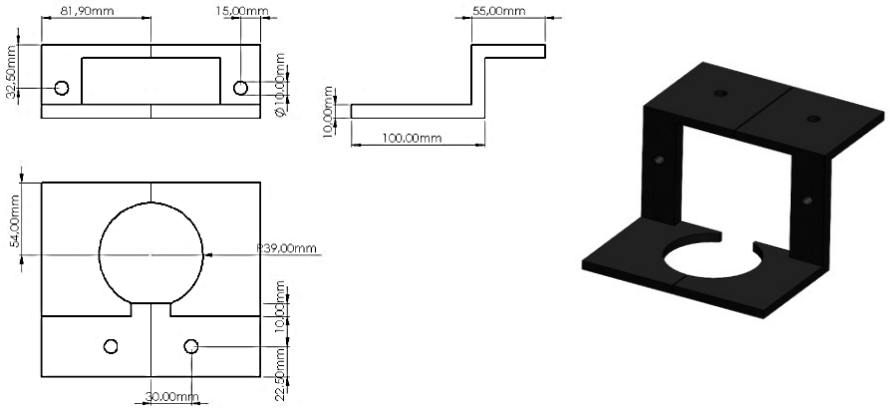

Structural support II

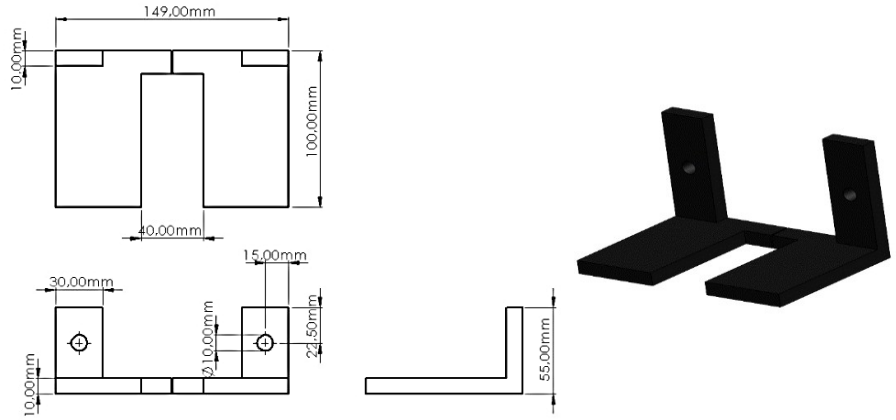

Appendix B

Measurement trasducers and Data-Acquisition Architecture

USB-6341, X Series DAQ (16 AI, 24 DIO, 2 AO)

Analog Inputs (AI)

- 16 single-ended channels / 8 differential channels
- 16-bit ADC
- Max sampling rate: 500 kS/s
- Input ranges: ±10 V
- Accuracy: 2,190 µV
- Input impedance: >10 GΩ ‖ 100 pF
- Overvoltage protection: ±25 V
- Small-signal bandwidth: 1.2 MHz
- Max accepted current: ±5 mA

Analog Outputs (AO)

- 2 independent channels
- 16-bit DAC
- Update rate: 900 kS/s (1 ch), 840 kS/s (2 ch)

- Output type: voltage
- Output range: ±10 V
- Power-on level: ±20 mV

Digital I/O (DIO) and PFI

- 24 total digital lines
- Port 0: 8 hardware-timed lines (up to 1 MHz)
- PFI 0-15: trigger/clock/static I/O
- Input protection: ±20 V (2 pins max)
- Pull-down resistor: 50 kΩ

Counters / Timers

- 4 counters, 32-bit
- Supported modes: pulse counting, frequency, PWM, quadrature
- Internal timebase: 100 MHz

Hardware / Software

- NI-STC3 timing engine
- NI Signal Streaming over USB
- Screw-terminal
- Supported by NI-DAQmx (v9.5+)
- Compatible with LabVIEW, MATLAB, Python, C#, C++

NI USB-6341 Screw Terminal Pin Configuration

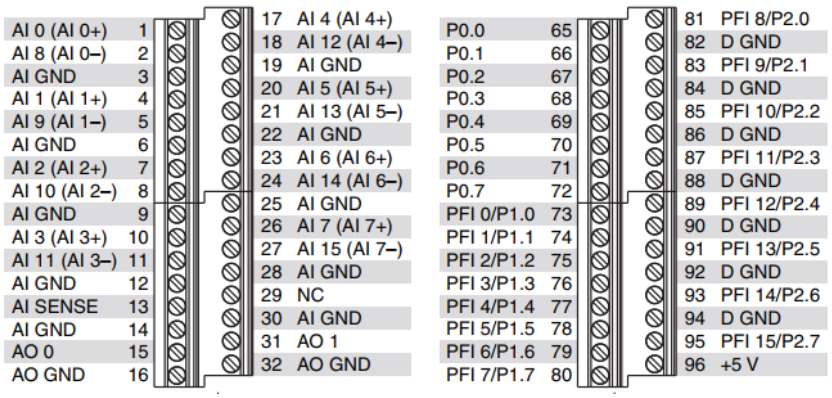

DAT converters

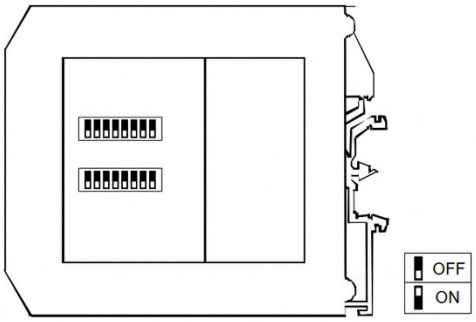

Input

- Configurable via DIP-switch
- Voltage ranges: 0–10 V, 2–10 V
- Current ranges: 0–20 mA, 4–20 mA (active/passive)
- Input impedance (voltage): ≥1 MΩ
- Input impedance (current): ~50 Ω

Output

- 2 independent analog channels
- Signal type: voltage or current (selectable)
- Voltage output: 0-10 V, 2-10 V (min load 1 kΩ)
- Current output: 0-20 mA, 4-20 mA (max load 500 Ω)

Transmission Performance

- Accuracy: ±0.1% FS
- Linearity: ±0.05% FS
- Temperature coefficient: 0.02% / °C
- Response time: ~40 ms (10%-90%)

Isolation and Protection

- 3-way galvanic isolation (input / output / power)
- Isolation voltage: 1500 V AC
- EMC compliance: CE (industrial environment)

Power and Physical

- Supply voltage: 18-30 V DC
- Current consumption: ~90 mA (active outputs)
- Mounting: DIN rail
- Connectors: screw terminals
- Operating temperature: -20 °C to +60 °C

The DIP-switches were configured according to the selected data source in the Input settings, and the output was set to match the signal required in the Output settings.
Dedicated zero and full-scale DIP-switches are available for the thermocouple module, while the excitation voltage is supplied for the flange torque meter.
Along the upper and lower sides of each converter are the screw terminals, identified by capital letters. The terminals used in this work are highlighted in blue, including the differential notation (+/−) for channels. These terminals include the power supply, the input signal (Voltage In) coming from the transducer during measurement or from the DAQ during control, and the output signal (Voltage Out) sent either to the acquisition unit (reading mode) or to the controller (control mode).

- **Thermocouple**

DAT-4531/A DIP-switch configuration

Input setting	Thermocouple K	
Output setting	0 – 10 V	
Zero	0°	
Full Scale	1100°	

DAT-4531/A screw terminals connection

Voltage In -		I G E	L H F	Voltage In +
Voltage Out -		M O	N P	Voltage Out +
Power supply +		Q	R	Power supply -

- **Torquemeter**

DAT-5025 DIP-switch configuration

Input setting	±10 V	
Output setting	0 – 10 V	
Excitation voltage	10 Vdc	

DAT-5025 screw terminals connection

Voltage In -		I	L		
Voltage In +		G	H		
Excitation +		E	F		Excitation -
Ground		M	N		Voltage Out +
		O	P		
Power supply +		Q	R		Power supply -

- **Proportional control valve**

DAT-4532/D DIP-switch configuration

Channel A: reading mode		
Input setting	4 – 20 mA	
Output setting	0 – 10 V	
Channel B: control mode		
Input setting	0 – 10 V	
Output setting	4 – 20 mA	

DAT-5025 screw terminals connection

Channel A					
Current In -		I	L		Current Out +
		G	H		
		E	F		
Voltage Out -		M	N		Voltage Out +
Channel B					
Current In -		O	P		Current In +
		G	H		Voltage Out +
Voltage Out -		E	F		
Power supply +		Q	R		Power supply -

- **Position sensor**

Grafen PCIR 101

Brown cable		1	2		Yellow cable
Blue cable		3	4		ground

- **Transformer**

Trasformatore EDR-120-24

An EDR-120-24 series power supply module is employed to convert the 240 V AC mains voltage into a regulated 24 V DC output. This unit provides stable power for all conditioning modules and auxiliary electronics, ensuring proper operation under varying load conditions. The device features industrial-grade protections, including overload, overvoltage, and short-circuit safeguards, and is designed for DIN-rail mounting to integrate cleanly within the electrical enclosure.
At the lower side of the module are the 240 V AC input terminals, providing connections for phase, neutral, and protective ground. The upper side hosts the 24 V DC output terminals, which supply regulated power to the conditioning modules and auxiliary electronics.

Appendix C

Momentum and Heat balances

In this section, the mathematical models describing the region located below the cooling chamber (Section III.3.5) are presented. This portion of the system consists of a central cylindrical steel rod, surrounded by a thin outer steel wall, with nitrogen flowing through the annular gap between them.

To solve the momentum and energy balance the properties of the phases and species involved are needed. The thermophysical properties of the solid phase are reported in Section III.2, whereas the properties of the gaseous and liquid phases were obtained from the literature [143]. These include density ρ $[kg\ m^{-3}]$, thermal conductivity k $[W\ m^{-1}\ K^{-1}]$, viscosity $\mu[Pa\ s]$, and specific heat capacity at constant pressure cp $[J\ kg^{-1}K^{-1}]$. The governing equations applied in the analysis are summarized in eqs. (C.1) to (C.12), in which for the gaseous species the properties are estimated by considering a constant pressure value of 1 bar.

For the nitrogen:

$$\rho_{n_2} = 10^{-8}T^2 - 3 * 10^{-5} * T + 0.0291 \quad \text{(C.1)}$$

$$k_{n_2} = -6 * 10^{-6}T^2 - 0.0573 * T + 26.741 \quad \text{(C.2)}$$

$$\mu_{n_2} = -5 * 10^{-6}T^2 - 0.0573 * T + 18.709 \quad \text{(C.3)}$$

$$cp_{n_2} = 6.5 + 0.000100 * T \quad \text{(C.4)}$$

For the air:

$$\rho_{air} = 3 * 10^{-8}T^2 - 5 * 10^{-5} * T + 0.0341 \quad \text{(C.5)}$$

$$k_{air} = -10^{-6}T^2 - 0.0655 * T + 25.637 \quad \text{(C.6)}$$

$$\mu_{air} = -9 * 10^{-6}T^2 - 0.0410 * T + 18.273 \quad \text{(C.7)}$$

$$cp_{air} = -10^{-9} * T^2 + 8 * 10^{-6} * T + 0.0281 \quad \text{(C.8)}$$

For the liquid water:

$$\rho_{H_2O} = -0.0014 * T + 55.356 \quad \text{(C.9)}$$

$$k_{H_2O} = 0.943 * T + 584.86 \quad \text{(C.10)}$$

$$\mu_{H_2O} = \exp\left(-52.843 + \frac{3703.6}{T} + 5.866 * \ln T + -5.879 * 10^{-29} * T^{10}\right) \quad \text{(C.11)}$$

$$cp_{H_2O} = 276370 - 2090.1 * T + 8.125 * T^2 + -0.017116 * T^3 + 9.3701 * 10^{-6} * T^4 \quad \text{(C.12)}$$

The first step is to characterize the behavior of the gas within this confined volume, i.e., the space between the rod and the inner wall of the reaction chamber. In order to adequately describe the system, it is essential to characterize the behaviour of the gas, particularly by constraining the degree of freedom associated with the inlet flow rate.

To evaluate the resulting flow regime and driving mechanisms, three dimensionless numbers were considered: the Reynolds number Re, the Grashof number Gr, and the Richardson number Ri; where for calculation purposes, the nitrogen flow rate was fixed at 10 l/h.

$$Re = \frac{\rho v D_h}{\mu} = \frac{\rho v}{\mu} \frac{2(R_2^2 - R_1^2)}{(R_2 - R1)} = 8.96 \quad \text{(C.13)}$$

$$Gr = \frac{\bar{\rho} g (R_2 - R_1)^3 \Delta\rho}{\mu^2} = 2.28 \quad \text{(C.14)}$$

$$Ri = \frac{Gr}{Re^2} = 0.03 \quad \text{(C.15)}$$

In which D_h is the hydraulic diameter, R_1 is the radius of the rod and R_2 is the internal radius of the reactive chamber.

Re number, that quantifies the ratio of inertial to viscous forces, assumed an extremely low value authorizing that the flow regime in the design hypotheses was laminar. The Grashof number, which measures the relative importance of buoyancy forces compared to viscous forces, indicating that buoyancy effects are present but remain secondary with respect to the imposed flow. The Richardson number, which expresses the ratio of natural to forced convection, yielded a value much less than unity, implying that, although the imposed flow rate is low, the gas motion is primarily sustained by the pressure difference across the system, while the contribution of natural convection is negligible.

Once the fluid dynamic behaviour has been established, it becomes possible to formulate the corresponding balance equations. Starting from the continuity equation (eq. (C.16)) for the gas and assuming steady-state conditions and negligible velocity variations in the angular and radial directions, the partial differential equation simplifies significantly (eq. (C.17)).

$$\frac{\delta\rho}{\delta t} + \frac{1}{r}\frac{\delta}{\delta r}(\rho r v_r) + \frac{1}{r}\frac{\delta}{\delta\theta}(\rho v_\theta) + \frac{\delta}{\delta z}(\rho v_z) = 0 \tag{C.16}$$

$$\frac{\delta}{\delta z}(\rho v_z) = 0 \tag{C.17}$$

As a result, the vertical velocity component emerges as the only non-zero term, expressed as a function of the radial coordinate r.

$$v_z = v_z(r) \tag{C.18}$$

The velocity profile in the radial direction can then be derived by applying the momentum balance. This equation is simplified by the aforementioned assumptions and by considering steady-state operation.

$$\begin{aligned}\rho\left(\frac{\delta v_z(r)}{\delta t} + v_r\frac{\delta v_z}{\delta r} + \frac{v_\theta}{r}\frac{\delta v_z}{\delta\theta} + v_z\frac{\delta v_z}{\delta z}\right) \\ = -\frac{\delta p}{\delta z} + \mu\left[\frac{1}{r}\frac{\delta}{\delta r}r\left(\frac{\delta v_z}{\delta r}\right) + \frac{1}{r^2}\frac{\delta^2 v_z}{\delta\theta^2} + \frac{\delta^2 v_z}{\delta z^2}\right] \\ + \rho g_z\end{aligned} \tag{C.19}$$

In this framework, the pressure term and the gravitational contribution are combined into a single modified pressure, defined as $P = p + \rho g_z$.

$$\frac{dP}{dz} = \mu\left[\frac{1}{r}\frac{d}{dr}r\frac{dv_z}{dr}\right] \tag{C.20}$$

With this definition, the governing equation can be integrated along the axial direction, from 0 to the rod length L.

$$\frac{\Delta P}{\mu L}r = \frac{d}{dr}r\frac{dv_z}{dr} \tag{C.21}$$

Rearranging the terms yields a differential equation that, upon separation of variables and successive integration, provides the functional form of the velocity distribution.

$$\frac{dv_z}{dz} = \frac{\Delta P}{2\mu L}r + \frac{C_1}{r} \tag{C.22}$$

$$v_z = \frac{\Delta P}{2\mu L}r^2 + C_1\ln(r) + C_2 \tag{C.23}$$

To fully characterize the velocity profile, boundary conditions must be imposed. Specifically, the non-slip condition at the solid surfaces requires:

$$\begin{cases} r = R_1 & \begin{cases} v_z = 0 \\ v_z = 0 \end{cases} \\ r = R_2 \end{cases} \tag{C.24}$$

These boundary conditions determine the complete velocity profile, which allows the subsequent resolution of the energy balance.

$$v_z = \frac{\Delta P}{2\mu L} R_2^2 \left[1 - \left(\frac{r}{R_2} \right)^2 - \frac{(R_2^2 - R_1^2)}{R_2^2 \ln\left(\frac{R_2}{R_1}\right)} \ln\left(\frac{R_2}{r}\right) \right] \tag{C.25}$$

The laminar flow regime also allows determination of the gas-side heat transfer coefficients, which are essential for evaluating the internal thermal profile of the piston. It is necessary to calculate the Nusselt number Nu, which represents the dimensionless ratio between convective and conductive heat transfer; the Prandtl number Pr, which expresses the ratio between momentum diffusivity and thermal diffusivity, thereby linking fluid flow to heat transfer characteristics; and the Biot number Bi, which represents the ratio between internal conduction resistance within the solid and external convective resistance at its surface. To estimate the Nusselt number, the constant value associated with laminar motion in a fully developed velocity profile was considered and corrected to account for the annular geometry of the system. The corresponding expression is:

$$Pr = \frac{\mu C_p}{k_{gas}} = 0.678 \tag{C.26}$$

$$Nu = \left(0.4 * Re^{0.5} + 0.06 Re^{\frac{2}{3}} \right) * (\mathrm{Pr})^{0.4} \left(\frac{\mu_{\mathrm{inf}}}{\mu_0} \right)^{0.2} * 0.86 * \\ * \left(\frac{\mathrm{D_1}}{\mathrm{D_2}} \right)^{-0.16} * \left(\frac{\mathrm{D_1}}{\mathrm{D_2}} \right) = 4.01 \tag{C.27}$$

It should be emphasized that the calculation results reported later were obtained by estimating the thermophysical properties of the species at a reference temperature of 1000 °C. However, it can be readily demonstrated that both the Nusselt number and the convective heat transfer coefficient exhibit only minor sensitivity to temperature variations. In fact, these parameters are predominantly governed by the geometric characteristics of the system, rather than by the specific values of the fluid properties.
Once the Nusselt number is known, the convective heat transfer coefficient h_1 can be determined:

$$h_1 = \frac{Nu\, k_{gas}}{D_h} = 3.00 \left[\frac{W}{m^2 K}\right] \tag{C.28}$$

With the heat transfer coefficient established, the Biot number can then be calculated:

$$Bi = \frac{h_1 L}{k_{solid}} = 0.02 \tag{C.29}$$

An important assumption was introduced in this step: the height affected by the temperature gradient is taken to be equal to the height of the reactive chamber wall surrounding the piston. Accordingly, the characteristic length L is set to 0.19 m. Under these conditions, the immersed base of the piston is assumed to be at 1000 °C, while the remaining portion of the solid is subjected to detailed thermal analysis.

Since the value obtained is significantly less than 0.1, the thermal behaviour of the piston can be approximated as uniform, meaning that the internal temperature profile of the solid can be considered flat and independent of the radial direction.

Building upon the assumptions established thus far, the next step involves the formulation and resolution of the energy balances, beginning with the thermal balance on the rod. This analysis provides the foundation for quantifying heat transfer within the system and serves as the starting point for the subsequent evaluation of the overall thermal behaviour of the reactive chamber.

Considering a differential element along the axial direction z of the rod, the heat transfer phenomena to which it is subjected include internal conduction within the solid, forced convection with the gas at the interface surface, and thermal radiation, where the exchange between the two metallic faces. Therefore, at steady state conditions, the energy balance becomes:

$$\begin{aligned} 0 = \frac{\delta}{\delta z}\left(k\frac{\delta T_1}{\delta z}\right) - \frac{h_1 P_1}{S_1}\frac{\delta}{\delta z}\left(T_1 - T_{gas}\right) \\ - \frac{e\sigma P_2}{S_2}(T_1^2 + T_2^2)(T_1 + T_2)\frac{\delta}{\delta z}(T_1 - T_2) \end{aligned} \tag{C.30}$$

In which the condition is expressed through Fourier's law of conduction, while the radiative contribution is accounted for using the Stefan-Boltzmann law. S_1 denotes the section of the solid cylinder, P_1 is its perimeter, e is the Stefan–Boltzmann constant, taken as $1.355*10^{-12}$ cal/(s cm^3 K), σ is the surface emissivity assumed equal to 0.8, and T_1 and T_2 are respectively the temperature of the rod and the temperature of the external wall exposed by the reactive chamber.

The energy balance on the central solid inherently provides information about the temperature of the surrounding gas phase. To fully capture this interaction, the analysis must be extended to the gas flowing between the two cavities,

where heat transfer occurs by forced convection, with both walls maintained at different temperatures. In order to evaluate the convective heat transfer coefficient on the outer wall, the Nusselt number must be recalculated, incorporating the correction factor for annular geometries with a heated outer boundary. This adjustment ensures that the convective exchange is accurately represented under the specific thermal and geometric conditions of the system:

$$Nu = \left(0.4 * Re^{0.5} + 0.06Re^{\frac{2}{3}}\right) * \\ * (\mathrm{Pr})^{0.4}\left(\frac{\mu_{\inf}}{\mu_0}\right)^{0.2}\left[1 - 0.14 * \left(\frac{\mathrm{D}_1}{\mathrm{D}_2}\right)^{0.6}\right] * \left(\frac{\mathrm{D}_1}{\mathrm{D}_2}\right) \\ = 4.03 \tag{C.31}$$

$$h_1 = \frac{Nu\, k_{gas}}{D_h} = 3.03\left[\frac{W}{m^2K}\right] \tag{C.32}$$

Once the two convective heat transfer coefficients have been determined, the energy balance can be formulated. This balance is developed by incorporating all the assumptions and observations established thus far regarding the dependencies of the relevant variables, and it is resolved under steady-state operating conditions.

$$\rho\widehat{C_p}v_z(r)\frac{\delta T_{gas}}{\delta z} = \frac{h_1 P}{S}\frac{\delta}{\delta z}\left(T_1 - T_{gas}\right) + \frac{h_2 P}{S}\frac{\delta}{\delta z}\left(T_2 - T_{gas}\right) \tag{C.33}$$

The temperature of the reactive chamber remains an unknown variable; however, it can be determined from a final energy balance. This solid region is subjected to multiple heat transfer mechanisms: natural convection at the outer wall, exposed to ambient air; internal conduction within the solid material; forced convection at the inner wall, driven by the gas flow; and radiative exchange with the adjacent rod.

For natural convection, the thermophysical properties were evaluated at the film temperature, defined as the arithmetic mean between the wall temperature and the ambient air temperature at infinite distance. Consequently, the film temperature varies along the axial coordinate z as a function of the local wall temperature. In this regime, two fundamental dimensionless numbers are introduced: the Grashof number, which quantifies the relative importance of buoyancy forces compared to viscous forces, and the Rayleigh number Ra, which combines the effects of buoyancy and thermal diffusivity to characterize the onset and intensity of natural convection. Both numbers are expressed as functions of the air properties calculated at the film temperature and of the characteristic wall length L:

$$Ra = Gr \cdot Pr = \frac{g\beta(T_2 - T_{air})L^3}{\mu\rho}\frac{\mu C_p}{k_{gas}} \tag{C.34}$$

The correlation for the Nusselt number also changes under natural convection conditions. From this modified expression, the convective heat transfer coefficient h_{nat} can be derived in accordance with eqs. (C.35) and (C.36), thereby providing a rigorous estimate of the heat exchange due to natural convection at the outer wall:

$$Nu = \left\{ 0.60 + \frac{0.387 Ra^{\frac{1}{6}}}{\left[1 + \left(\frac{0.559}{Pr}\right)^{\frac{9}{16}}\right]^{\frac{8}{27}}} \right\} \tag{C.35}$$

$$h_{nat} = \frac{Nuk_{air}}{L} \tag{C.36}$$

The combined effect of these phenomena is expressed in the energy balance for the wall of the reactive chamber:

$$\begin{aligned} 0 = \frac{\delta}{\delta z}\left(k\frac{\delta T_2}{\delta z}\right) &- \frac{h_2 P_{2,In}}{S_2}\frac{\delta}{\delta z}\left(T - T_{gas}\right) \\ &- \frac{h_{air} P_{2,Out}}{S_2}\frac{\delta}{\delta z}(T - T_{air}) \\ &+ \frac{e\sigma P_2}{S_2}(T_1^2 + T_2^2)(T_1 + T_2)\frac{\delta}{\delta z}(T_1 - T_2) \end{aligned} \tag{C.37}$$

in which the geometric parameters relating to the internal and external perimeter, respectively $P_{2,In}$ and $P_{2,Out}$, and the section S_2 relating to this portion of the reactive chamber appear.
This expression defines the temperature distribution along the vertical direction of the in the entire region beneath the cooling chamber.

Appendix D

DAQ accuracy

For the USB-6341 X-Series DAQ (16 AI, 24 DIO, 2 AO) the key specifications relevant to evaluating its performance during the acquisition phase are listed in Table D.1.

Table D.1 Key relevant specifications for NI USB-6341.

ADC resolution:	16 bits
Input ranges:	±1 V, ±2 V, ±5 V, ±10 V
Gain error (maximum):	±80 ppm of reading
Offset error (typical):	±20 µV
Offset error (maximum):	±60 µV
Input noise (typical, ±10 V range):	30–50 µV RMS
Integral nonlinearity (INL):	±80 ppm of full scale
Differential nonlinearity (DNL):	±1 LSB
Quantization step (±10 V range):	305 µV
Input impedance:	1 GΩ
Input noise (RMS, ±10 V range)	30–50 µV
acquisition frequency:	500 kS/s

For this unit, the Maximum Absolute Accuracy is computed as follows:

Gain error uncertainty:

$$U_{gain} = 10V * Gain\ eorr = 800 * 10^{-6}\ V \quad \text{(A.1)}$$

Offset error uncertainty:

$$U_{offset} = 60 * 10 - 6\ V \quad \text{(A.2)}$$

Noise uncertainty:

$$U_{noise} = \frac{3 * Input\ noise}{\sqrt{N}} = \frac{3 * 50 * 10^{-6}V}{\sqrt{30}} = 27.4 * 10^{-6}\ V \quad \text{(A.3)}$$

where the number of samples N was selected to remain consistent with the analyses later performed on the sensor-derived signals.

Therefore, the extended uncertainty U_{DAQ} associated with the DAQ is given by the sum of the previous three:

$$U_{DAQ} = \pm 887.4 * 10^{-6}\, V \quad \text{(A.4)}$$

While the instrument resolution is given by the Least Significant Bit, estimated as:

$$LSB = \frac{V_{max} - V_{min}}{2^n} = \frac{20}{65536} = 305 * 10^{-6}\, V \quad \text{(A.5)}$$

In all cases examined, the expanded uncertainty of the DAQ is at least one order of magnitude smaller than the estimated sensor uncertainty. For this reason, it is considered negligible when compared with the uncertainty obtained from the analysis of the voltage-to-measurand relationship.

Sensors

For the position sensor and the torque transducer, the uncertainty estimation procedure was carried out by monitoring the voltage signal acquired by the DAQ while applying a reference measurand of known value. Each component was evaluated across its full operating range to ensure that the resulting calibration and uncertainty estimates were representative of all measurement conditions encountered during testing.

The procedure consisted of imposing a controlled stepwise variation of the measured entity. During the ascending phase, a positive step function was applied, incrementing the input quantity in discrete steps while continuously recording the corresponding voltage output. The same sequence was then repeated in reverse during the descending phase, applying a negative step function to reduce the measured entity in identical increments. This bidirectional approach allowed the identification of potential hysteresis effects, nonlinearities, or drift phenomena, and ensured that the calibration captured both loading and unloading behaviour.

By analysing the voltage response over the entire measurement range and under both monotonic trends, a robust dataset was obtained to derive the calibration curve and assess repeatability.

For each reference value of the measured entity, the voltage signal was recorded for a sufficiently long duration to ensure the system reached steady state. As confirmed by subsequent analyses, the sensors' response time is effectively negligible, and the steady state is attained almost instantaneously after each step change. For each imposed level of the measured entity, the final portion of the acquired dataset was used for statistical evaluation. Specifically, the last 30 samples, N, were selected to compute the arithmetic mean, $\bar{V}$, and variance based on the entire population σ of the voltage signal, from which the standard measurement uncertainty, u, and the corresponding expanded uncertainty, U, were derived. This approach ensures that the uncertainty

estimation is based solely on stable, noise-dominated signal behaviour, free from transient effects.

$$\bar{V} = \sum_{i=1}^{N=30} \frac{V_i}{N} \tag{D.6}$$

$$\sigma = \sqrt{\sum_{i=1}^{N=30} \frac{(V_i - \bar{V})^2}{N-1}} \tag{D.7}$$

$$u = \frac{\sigma}{\sqrt{N}} \tag{D.8}$$

$$U = k * u = 3u \tag{D.9}$$

For the estimation of the expanded uncertainty, a coverage factor k equal to 3 was adopted. This choice corresponds to a confidence level of approximately 99.7% under the assumption of an underlying normal distribution and is commonly used in engineering applications where a conservative uncertainty bound is required.

Once the expanded uncertainty expressed in terms of voltage had been determined, the corresponding uncertainty of the measured entity was obtained by propagating this contribution through the calibration model. Given the linear relationship between voltage and the measured entity this propagation reduces to multiplying the expanded voltage uncertainty by the slope of the calibration line, thereby converting the uncertainty from voltage units into the physical units of the measurand.

Position sensor

The main technical specifications of the PMA12 self-supporting rectilinear magnetic-drive position transducer by Grafen , relevant to the present analysis, are reported in Table D.2.

Table D.2 PMA12 self-supporting rectilinear magnetic- drive position transducer properties.

Electrical Stoke:	100 mm
Independent Linearity:	±0.1 mm
Repeatability:	0.08 mm
Resolution:	0.01 mm
Nominal Resistance:	5 kΩ
Temperature Coefficient:	0.02 mm/°C
Supply Voltage:	10 V
Nominal Sensitivity:	10 mm/V
Voltmeter Resolution:	0.001 V

The uncertainties associated with the intrinsic properties of the sensor arise primarily from its specified linearity, u_{lin} , and repeatability, u_{rep}, limits. This manufacturer-provided performance metrics represent additional contributions to the overall measurement uncertainty and must be incorporated alongside the uncertainties derived from the calibration procedure.

$$u_{lin} = \frac{0.1}{\sqrt{3}} = 0.058\ mm \tag{D.10}$$

$$u_{rip} = \frac{0.08}{\sqrt{3}} = 0.046\ mm \tag{D.11}$$

Figure D.1.a presents the voltage–time response acquired during the calibration of the position sensor. The sequence corresponding to the positive step function is shown in blue, while the negative step sequence is shown in orange. As described previously, the average voltage values computed for each step are reported in Figure D.1.b. The resulting voltage–extension plot clearly exhibits a linear relationship, through the corresponding regression equations and the coefficient of determination R^2, over the entire measurement range. Moreover, the two calibration curves (ascending and descending) show an almost perfect overlap. This high degree of agreement confirms the absence of hysteresis in the sensor response.

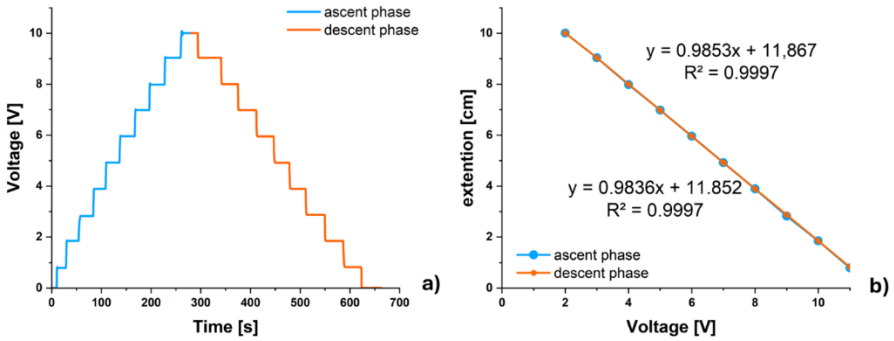

Figure D.32 Response analysis of the Position sensor: a) voltage-time response recorded during the calibration of the position sensor; b) extension-voltage relationship, where the mean voltage values are extracted from the steady-state portion of each calibration step.

The procedure described in the previous paragraph was applied to all calibration steps. Among the statistical quantities estimated for each imposed measurand level, the maximum values were selected for the uncertainty evaluation, ensuring that the final estimate reflects the most conservative and representative operating condition. These values are reported below.

$$\bar{V}_{max} = 4.92\ V \tag{D.12}$$

$$\sigma_{max} = 0.0054\,V \quad \text{(D.13)}$$

$$u_{position\ sensor} = 9.78 * 10^{-4}\,V \quad \text{(D.14)}$$

The expanded uncertainty expressed in voltage units is converted into the corresponding uncertainty on the torque measurement, x_u, by applying the slope of the calibration curve.

$$x_u = \pm 0.003\text{mm} \quad \text{(D.15)}$$

Therefore, the overall measurement error, u_c, of the position sensor was estimated by combining the uncertainty contributions arising from the calibration procedure with those associated with the intrinsic sensor specifications (linearity and repeatability). The resulting total error can thus be expressed as:

$$u_c = \sqrt{u_{lin}^2 + u_{rip}^2 + x_u^2} = 0.075\,mm \quad \text{(D.17)}$$

And the expanded uncertainty is equivalent to:

$$U_{position\ sensor} = \pm 0.225\,mm \quad \text{(D.18)}$$

Torquemeter

The principal technical specifications for the torque transducer of MTR series, relevant to the present analysis, are summarized in Table D.3.

Table D.3 MTR torque transducer properties.

Full scale:	100 Nm
Accuracy class:	±0.1 Nm
Linearity and hysteresis:	±0.1 Nm
Repeatability:	±0.03 Nm
Zero Thermal Drift:	±0.02 Nm/10°C
Sensitivity Thermal Drift:	0.02 mm/°C
Long-term Stability:	<0.003/year
Supply Voltage:	10 V
Nominal Sensitivity:	2 mV/V

The linearity of the uncertainties, u_{lin}, and repeatability, u_{rep}, limits are estimated:

$$u_{lin} = \frac{0.1}{\sqrt{3}} = 0.058\,Nm \quad \text{(D.19)}$$

$$u_{rip} = \frac{0.03}{\sqrt{3}} = 0.017\,Nm \quad \text{(D.20)}$$

Figure D.2.a illustrates the voltage–time response recorded during the calibration of the torque transducer. The blue curve corresponds to the ascending (positive-step) sequence, while the orange curve represents the

descending (negative-step) sequence. The mean voltage values extracted from the steady-state portion of each step are shown in Figure D.2.b, where the resulting torque–voltage relationship displays an exact linear trend. The regression analysis yields a coefficient of determination R^2 euqal to 1, and the ascending and descending curves overlap perfectly. This complete superposition confirms the absence of hysteresis and demonstrates the excellent linearity of the transducer over the entire calibration range.

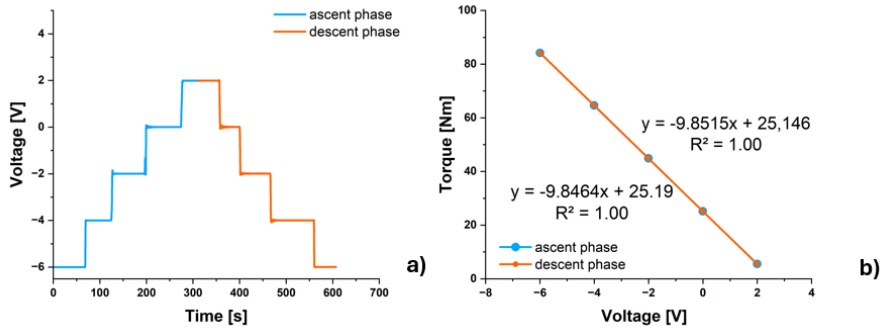

Figure D.33 Response analysis of the Torsiometer: a) voltage-time response recorded during the calibration of the torque transducer; b) extension-voltage graph, where the mean voltage values are extracted from the steady-state portion of each calibration step.

Also, for the torque transducer's uncertainty estimation, the maximum values were selected for a given torque, ensuring the final estimate reflects the most conservative and representative operating condition.

$$\bar{V} = 0.006\,V \quad \text{(D.21)}$$

$$\sigma_{max} = 0.0018\,V \quad \text{(D.22)}$$

$$u_{position\ sensor} = 3.24 * 10^{-4}\,V \quad \text{(D.23)}$$

The expanded uncertainty expressed in voltage units is converted into the corresponding uncertainty on the torque measurement, T_u:

$$T_u = \pm 0.003\ \text{Nm} \quad \text{(D.24)}$$

Therefore, the combined measurement uncertainty of the torque transducer, u_c, was obtained by aggregating the uncertainty contributions derived from the calibration procedure together with those associated with the intrinsic sensor specifications, namely linearity and repeatability. The resulting total measurement error can thus be expressed as:

$$u_c = \sqrt{u_{lin}^2 + u_{rip}^2 + T_u^2} = 0.06\,Nm \quad \text{(D.25)}$$

And the expanded uncertainty is equivalent to:

$$U_{torquemeter} = \pm 0.18\,Nm \quad \text{(D.26)}$$

The uncertainty associated with the torque measurement can be converted to the corresponding uncertainty in shear stress by applying the appropriate geometric relationship for the tested specimen.

$$U_T = \frac{3 * U_{torquemeter}}{2\pi(R_o^3 - R_i^3)} = \pm 2.05\ kPa \quad \text{(D.27)}$$

where R_o denotes the external diameter of the lid, and R_i represents the internal diameter that defines the effective measuring surface.

Propotional valve

To apply the desired force on the lid and, consequently, the stress transmitted to the sample, a pneumatic actuation system was employed: the VPP-series proportional pressure control valve, which ensures precise and stable control of the fluid pressure delivered to the cylinder throughout the test. The main technical specifications of the valve are reported in Table D.4.

Table D.4 VPP proportional pressure control valve properties.

Pressure range:	0 ÷ 6 bars
Linearity:	±0.054 bar
Hysteresis:	±0.024 bar
Repeatability:	±0.024 bar
Overall Accuracy:	±0.066 bar
Sensitivity Thermal Drift:	±0.024 / K

Therefore, the uncertainty estimate is derived directly from the device's overall accuracy, which accounts for its intrinsic performance characteristics.

$$u_{overall} = \frac{0.066}{\sqrt{3}} = 0.038\ bar \quad \text{(D.28)}$$

The measurement sequence used to derive the calibration curve for interpreting the valve signal is shown in Figure D.3. Because the valve also functions as a controller, an input voltage is applied, and the corresponding gas pressure delivered to the system is measured. Following the analysis of the positive step response, the steady-state values were averaged to establish the relationship between the applied pressure and the valve input voltage.

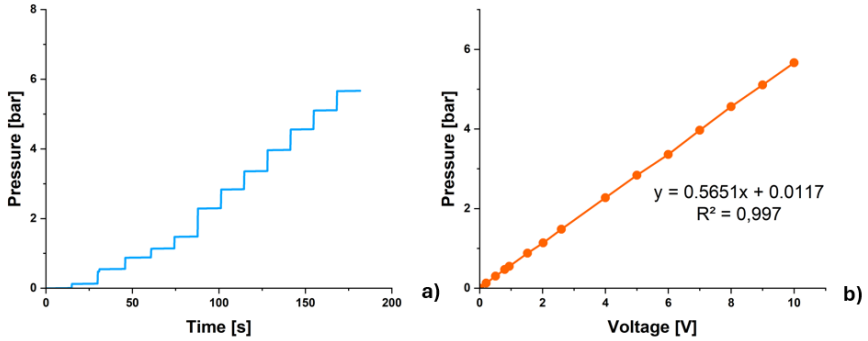

Figure D.34 Response analysis of the proportional valve: a) pressure–time response recorded during the calibration of the proportional valve. b) pressure-voltage graph, where the mean voltage values extracted from the steady-state portion of each calibration step are represented.

When acquiring the calibration data, particular attention was devoted to the lower pressure range, as these values represent operating conditions frequently encountered during testing. Owing to the 3:1 ratio between the internal surface area of the pneumatic cylinder and that of the lid, a measurement range of 6 bar is sufficient to generate the maximum stress of 800 kPa applied to the sample.

The resulting calibration curve displays a linear trend, with a coefficient of determination R^2 approaching unity, confirming the excellent agreement between the measured data and the regression model. Based on the calibration dataset, the next step was to estimate the associated measurement uncertainty under worst-case conditions.

$$\bar{P} = 1.140\ bar \tag{D.29}$$

$$\sigma_{max} = 9.95 * 10^{-4}\ bar \tag{D.30}$$

$$u_{propotional\ valve} = 0.00545\ bar \tag{D.31}$$

By combining the individual uncertainty contributions reported above, the expanded uncertainty associated with the proportional valve can be determined.

$$u_c = \sqrt{u_{overall}^2 + u_{propotional\ valve}^2} = 0.0383\ bar \tag{D.32}$$

$$U_{valve} = \pm 0.12\ bar \tag{D.33}$$

Thermocouples

For the thermocouple, the lack of suitable equipment to perform a full-range calibration meant relying solely on the manufacturer-specified accuracy. Consequently, the uncertainty evaluation is based solely on the Type B contribution. The calibration curve used to convert the measured voltage

signal into temperature is reported in Figure D.4, while the accuracy of a K-type thermocouple can be reasonably assumed to correspond to 0.75% of the full-scale value.

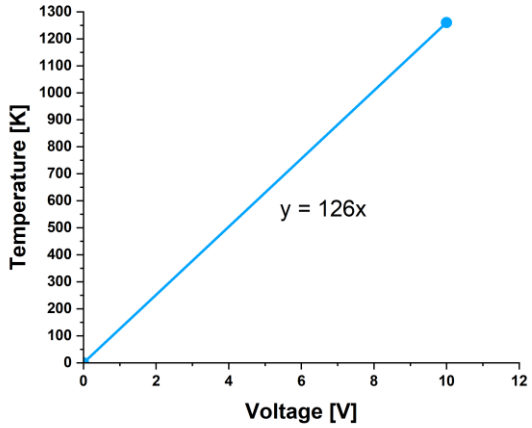

Figure D.35 pressure-voltage relationship

Thermocouple uncertainty, $u_t(T)$, obtained from vendor:

$$\Delta_t(T) = 0.0075 * T_{max} = 0.0075 * 1100 = 8.25°C \quad \text{(D.34)}$$

from which the expanded uncertainty can be obtained by applying a coverage factor equal to 3.

$$u_c = \frac{8.25°C}{\sqrt{3}} = 4.76°C \quad \text{(D.35)}$$

$$U_{thermocouple} = \pm 14.28°C \quad \text{(D.36)}$$